THÈSE DE DOCTORAT

de l'Université de recherche Paris Sciences et Lettres
PSL Research University

Préparée à MINES ParisTech

Full field and mean field modeling of dynamic and post-dynamic recrystallization in 3D – Application to 304L steel

Modélisation 3D en champ complet et champ moyen de la recristallisation dynamique et post-dynamique – Application à l'acier 304L

Ecole doctorale n°364 Sciences fondamentales et appliquées
Spécialité Mécanique Numérique et Matériaux

COMPOSITION DU JURY :

M. Lukasz MADEJ
AGH University, Rapporteur

M. Frank MONTHEILLET
CNRS, Rapporteur

M. Carl KRILL
Ulm University, Examinateur

M. Pascal DE MICHELI
Transvalor SA, Examinateur

M. Marc BERNACKI
MINES ParisTech, Examinateur

M^{me} Nathalie BOZZOLO
MINES ParisTech, Examinateur

M. Charbel MOUSSA
MINES ParisTech, Examinateur

Soutenue par **Ludovic MAIRE**
le **23 Novembre 2018**

Dirigée par **Marc BERNACKI**
Nathalie BOZZOLO
Charbel MOUSSA

MINES ParisTech | PSL RESEARCH UNIVERSITY PARIS

CONFIDENTIEL

Acknowledgments

First of all, I would like to thank all the academic and industrial partners of the DIGIMU project that contributed to this work. I am also very grateful to the CEMEF MINES ParisTech for providing me all the tools and knowledges so that my PhD goes as well as possible. I would also like to thank all the members of the jury for agreeing to judge my work. A particular thank to Lukasz Madej and Frank Montheillet for accepting to be my reporters and to Carl Krill and Pascal de Micheli for accepting to be my examiners. I would also like to thank Pascal de Micheli and Julien Barlier from Transvalor SA for the industrial collaboration and all the interesting discussions we had together.

I would like to express my deepest sense of gratitude to my supervisors, Marc Bernacki, Charbel Moussa and Nathalie Bozzolo for their sympathy, their constructive advices and their availability in correcting my articles and my PhD manuscript. I would especially like to thank Charbel Moussa and Nathalie Bozzolo for enriching my knowledges in the metallurgical field and Marc Bernacki for improving my knowledges and my autonomy in multi-scale modeling and programming fields.

I would like to thank all my colleagues, especially those of the MSR and MSM teams who made my three years very pleasant. I would also like to thank Daniel and Thomas, for their constructive advices at the beginning of my PhD. A particular thank to my first office colleague, Benjamin, for training and assisting me during all my first year of PhD. I would also like thank my second office colleague, Sebastian, for all the good times and the laughs we spent together and to my other colleagues, Julien, Alexis, Suzanne and Romane, for making my three years awesome and full of good memories. Thank you also to the CEMEF staff, Suzanne, Gilbert and Cyrille for their availability, especially at the end of my PhD.

Last but not least, I would especially like to thank my girlfriend, Laetitia, for always being there for me and for supporting me in my everyday life and my parents, my sister and my in-laws for encouraging me in this adventure.

Contents

1 Litterature review **7**

1.1 Dynamic and post-dynamic recrystallization 9

1.1.1 Introduction 9

1.1.2 Austenitic stainless steel 304L 9

1.1.3 Strain hardening 11

1.1.4 Recovery 11

1.1.5 Grain boundary migration 12

1.1.6 Nucleation 14

1.1.7 Influence of recrystallization on the flow behavior 17

1.2 Modeling of dynamic and post-dynamic recrystallization 18

1.2.1 Phenomenological models 19

1.2.2 Mean field models 22

1.2.3 Full field models 35

2 The Level-Set method in a finite element framework for modeling of microstructure evolutions **47**

2.1 Introduction to the Level-Set method for polycrystals 49

2.1.1 Generation and immersion of a virtual polycrystal within a finite element mesh 50

2.1.2 Grain boundary migration 54

2.2 Full field simulations of grain growth and improvements of two existing models in the state of the art 56

2.2.1 Introduction 56

2.2.2 Initial polycrystal and material parameters 57

2.2.3 Full field simulation results 58

2.2.4 Confrontation of full field simulation results with Hillert/Abbruzzese model 62

2.2.5 Confrontation of full field simulation results with Burke & Turnbull model 68

3 Modeling of dynamic and post-dynamic recrystallization by coupling a full field approach to phenomenological laws **75**

3.1 Introduction 77

3.2 Modeling of dynamic and post-dynamic recrystallization 78

3.2.1 Initial polycrystal . . . 78
3.2.2 Grain boundary migration . . . 78
3.2.3 Strain hardening and recovery . . . 78
3.2.4 Nucleation . . . 81
3.3 Sensitivity study of the model . . . 86
3.3.1 Dynamic recrystallization . . . 86
3.3.2 Post-dynamic recrystallization . . . 93
3.4 Comparison with predictions of a mean field model . . . 95
3.4.1 Dynamic recrystallization . . . 95
3.4.2 Post-dynamic recrystallization . . . 102

4 A new topological approach for the mean field modeling of dynamic and post-dynamic recrystallization : the NHM 109
4.1 Introduction . . . 111
4.2 Mean field modeling of dynamic recrystallization . . . 112
4.2.1 Constitutive laws . . . 112
4.2.2 Neighborhood choice during DRX . . . 113
4.2.3 Modeling of grain elongation . . . 119
4.2.4 Comparison with DRX full field predictions . . . 123
4.3 Mean field modeling of post-dynamic recrystallization . . . 130
4.3.1 Constitutive laws . . . 130
4.3.2 Neighborhood choice during PDRX . . . 130
4.3.3 Comparison with PDRX full field predictions . . . 131

5 Identification of DRX model parameters for the 304L steel and comparison between model predictions and experimental results. 137
5.1 Thermomechanical testing . . . 139
5.1.1 Compression process . . . 140
5.1.2 Sample geometries . . . 141
5.1.3 Finite element simulations . . . 141
5.1.4 Repeatability study . . . 145
5.2 Identification of strain hardening (K_1) and dynamic recovery (K_2) parameters . . . 146
5.2.1 Stress-strain curves . . . 146
5.2.2 Method for the identification of K_1 and K_2 . . . 148
5.3 Identification of the parameter describing the strain rate dependence of boundary migration (δ) and of the nucleation parameter (K_g) . . . 156
5.3.1 Microstructure investigations . . . 156
5.3.2 Identification procedure for δ and K_g . . . 168
5.4 Comparison between experimental data and results issued from the NHM after calibration . . . 171
5.5 Comparison between experimental data and results issued from the NHM and the full field model after calibration . . . 174

6 Conclusions and prospects **181**

Abbreviations and Symbols

Abbreviations

RX	Recrystallized
NR	Non-recrystallized
GG	Grain growth
DRX	Dynamic recrystallization
SRX	Static recrystallization
PDRX	Post-dynamic recrystallization
EBSD	Electron backscattered diffraction
SEM	Scanning electron microscopy
HEM	Homogeneous equivalent medium
FE	Finite elements
CA	Cellular automata
LS	Level-Set
MC	Monte-Carlo
PF	Phase-Field

Physical variables

ε	Strain level
ε_{p}	Peak strain
$\varepsilon_{\mathrm{cr}}$	Critical strain for onset of DRX
$\dot{\varepsilon}$	Strain rate (s^{-1})
Z	Zener-Hollomon parameter
τ	Energy per unit dislocation line ($\mathrm{J.m}^{-1}$)
M_{b}	Grain boundary mobility ($\mathrm{m}^4.\mathrm{s}^{-1}.\mathrm{J}^{-1}$)
θ	Misorientation angle ($^\circ$)
γ_{b}	Grain boundary energy per unit area ($\mathrm{J.m}^{-2}$)
b	Norm of Burgers vector (m)
R	Perfect gaz constant ($\mathrm{J.mol}^{-1}.\mathrm{K}^{-1}$)
R_i	Equivalent sphere radius of the i^{th} grain (μm)
D_i	Equivalent sphere diameter of the i^{th} grain (μm)
S_i	Surface of the i^{th} grain ($\mu\mathrm{m}^2$)
V_i	Volume of the i^{th} grain ($\mu\mathrm{m}^3$)
$\langle R \rangle$	Mean grain radius (μm)
$\langle D \rangle$	Mean grain diameter (μm)

$\langle R_0 \rangle$	Initial mean grain radius (μm)
$\langle D_0 \rangle$	Initial mean grain diameter (μm)
ρ_i	Mean dislocation density in the i^{th} grain (m^{-2})
$\langle \rho \rangle$	Mean dislocation density (m^{-2})
E_i	Stored energy in the i^{th} grain ($J.mm^{-3}$)
$\langle E \rangle$	Mean stored energy ($J.mm^{-3}$)
σ_R	Standard deviation of grain radius (μm)
σ_E	Standard deviation of stored energy ($J.mm^{-3}$)
ρ_{cr}	Critical dislocation density for onset of DRX (m^{-2})
r_{cr}	Critical nucleus radius (μm)
X	Recrystallized fraction
T	Temperature (K)
Q_{def}	Activation energy for hot deformation ($J.mol^{-1}$)
Q_m	Activation energy for boundary migration ($J.mol^{-1}$)
Q_n	Activation energy for nucleation ($J.mol^{-1}$)
P_e	Pressure exerted on a grain boundary due to stored energy ($N.m^{-2}$)
P_c	Pressure exerted on a grain boundary due to local curvature ($N.m^{-2}$)
P_b	Total pressure exerted on a grain boundary ($N.m^{-2}$)
v_b	Grain boundary velocity ($m.s^{-1}$)
$\dot{V}$	Volume of nuclei per unit time (s^{-1})
σ_i	Flow stress in the i^{th} grain (MPa)
σ	Macroscopic flow stress (MPa)
σ_0	Yield stress (MPa)
M_T	Taylor factor
μ	Shear modulus (MPa)
κ	Grain boundary curvature (m^{-1})
Model parameters	
K_1	Parameter related to strain hardening (m^{-2})
K_2	Parameter related to dynamic recovery
K_s	Parameter related to static recovery
δ	Parameter related to grain boundary mobility under dynamic conditions
δ_s	Parameter related to grain boundary mobility under static conditions
K_g	Parameter related to nucleation ($m.s^{-1}$)

Introduction

A metal alloy is composed of several *grains*, each grain having its own crystallographic orientation describing the atoms arrangement in space. The grain size is typically between 1 and 100 μm and the frontier between one grain to another is called *grain boundary*. The properties of a metal alloy (e.g. toughness, strength, conductivity) directly depend on its *microstructure*, that is to say the chemical composition, crystalline structure, as well as size, shape and orientation of the different grains.

To obtain an intermediate or final product, the metal alloy is generally cold-worked after casting by different processes such as forging, rolling, extrusion etc. During these processes, a large part of the energy is dissipated as heat. However, a small part remains in the microstructure in the form of crystallographic defects, mainly *dislocations*. If the material is subsequently heated at high temperatures, thermally activated mechanisms tend to reorganize and anneal these defects to decrease the global energy: this phenomenon is called *static recrystallization*.

However, casting products can also be directly hot-worked, therefore microstructure mechanisms tending to increase and decrease defects in the microstructure occur simultaneously during deformation: this phenomenon is called *dynamic recrystallization*. After deformation when the material is still at high temperatures, some mechanisms tending to decrease defects are still activated, leading to *post-dynamic recrystallization*.

Even if most of dislocations are annihilated by recrystallization, the presence of grain boundaries in the microstructure still leads to a thermodynamically unstable state. Therefore under the effect of temperature, microstructure naturally tends to decrease the total surface of grain boundaries, leading to a shrinkage of small grains and a growth of coarse grains: this mechanism is called *grain growth*.

Given this large number of mechanisms occurring simultaneously in a microstructure during and after deformation, a huge challenge for industrials is to control and predict microstructure evolutions occurring during and after processes, whatever the initial state of the microstructure (grain size distribution, dislocation density distribution, second-phase particles etc.). Finite element software are widely used to predict the macroscopic behavior (strain field, temperature field, stress field) of metal alloys during forging. However, industrials and researchers have quickly understood that macroscopic simulations are not always sufficient to correctly understand and optimize local behaviors of metal alloys, and knowledges on microstructure evolutions are of prime importance in some cases. Therefore, simulations at a polycrystalline scale, called *full field* simulations, were proposed in the last decades to predict local microstructures of metal alloys. These simulations showed good interests, in particular for discussing assumptions made in higher scale models. Since full field models are generally greedy in terms of computational costs, *phenomenological* laws can be used as an alternative to predict mean quantities such as recrystallized fractions or mean grain sizes but these models are often

based on many assumptions. Therefore, *mean field* models emerged as a compromise between full field models and analytical laws. Mean field models are based on a an implicit description of the microstructure by considering grains as spherical entities.

In this context, a project called DIGIMU was created at CEMEF in collaboration with many R&D research centers: Safran, Aubert & Duval, Framatome, CEA, Timet, ArcelorMittal and Ascometal, to develop a full field numerical software package called DIGIMU® and aiming to model microstructure mechanisms occurring at the polycrystalline scale during and after hot forging processes. The DIGIMU® software package version pre-existing to this PhD work was able to handle only the mechanisms of grain growth and static recrystallization, and was limited to two-dimensional simulations.

The first contribution of my PhD work in this project was to develop and integrate a three-dimensional full field model of dynamic and post-dynamic recrystallization into the DIGIMU® software package. Thereafter, my second contribution was to use this full field model as a reference to propose a new mean field approach, aiming to perform three-dimensional simulations of dynamic and post-dynamic recrystallization in a very short time. Finally, my last contribution was to propose a method of calibration for these two models and to test this method based on experimental data of a 304L austenitic steel.

This PhD book is subdivided into five main chapters :

- **Chapter 1 :** The first chapter is dedicated to the literature review of this work. The 304L austenitic stainless steel considered in this study is first presented. Then the mechanisms of dynamic and post-dynamic recrystallization are introduced with their influence on the flow behavior of metals. Finally, the main three different scales for modeling of dynamic and post-dynamic recrystallization are mentioned and different models of literature are described with their advantages and drawbacks.

- **Chapter 2 :** In this second chapter, the formalism of full field modeling considered at CEMEF and used in the DIGIMU® software for microstructure evolutions is introduced. This latter is based on the Level-Set approach in a finite element framework. In a second part, three-dimensional full field simulations of grain growth (i.e. without stored energy and deformation) are performed using this framework. More particularly, the influence of the initial grain size distribution on microstructure evolutions occurring during the transient grain growth regime is discussed thanks to full field simulations, and these results are used to enhance two analytical grain growth models of the literature.

- **Chapter 3 :** This third chapter is dedicated to the development of a new full field model for dynamic and post-dynamic recrystallization. Contrary to full field models in the state of the art, this latter aims to describe microstructure evolutions in three-dimensions, for large deformations and with relatively low computational

costs. Modeling of microstructure and grain boundary migration is based on the Level-Set method in a finite element framework presented in chapter 2 while other mechanisms are simulated by phenomenological laws. First, the constitutive laws for modeling strain hardening, recovery and nucleation are introduced. Then, a sensitivity study about the model is made and finally, results are compared with a mean field model of the literature to discuss limitations of existing mean field models.

- **Chapter 4 :** In this fourth chapter, a new topological approach, called "NHM" for NeighborHood Model, is proposed for mean field modeling of dynamic and post-dynamic recrystallization. The NHM is based on two major improvements with respect to the literature. A major advantage is related to the fact that constitutive laws (and thus model parameters) for dynamic and post-dynamic recrystallization are the same as those considered in the full field model of chapter 3. Therefore the full field model introduced in chapter 3 can be used as a reference to validate improvements made in the NHM. Furthermore, since mean field simulations can be perform in few seconds, the NHM can be used to identify very quickly by inverse analysis the model parameters used in both the full field model and the NHM. In a first part, the two major improvements considered in the NHM are introduced. Then a sensitivity study of this model is made. Finally this model is compared to the full field model of chapter 3 considering same model parameters.
- **Chapter 5 :** In this last chapter, experimental investigations are performed on 304L steel samples. More precisely, compression tests are performed on two different sample geometries. First, the compression framework is introduced and results in terms of stress-strain curves are presented and then used to identify both hardening K_1 and recovery K_2 model parameters. Then, microstructure investigations are introduced and results in terms of mean grain sizes, grain size distributions as well as recrystallized fractions are presented and used to identify both nucleation K_g and strain rate dependence of grain boundary migration δ model parameters. After identification of these four model parameters, predictions of the full field model and the NHM are compared to experimental data. Finally, two-dimensional slices are performed from three-dimensional representative elementary volumes of full field simulations and results are qualitatively compared to electron backscatter diffraction maps.

Oral and written communications

This PhD work led to several publications reported below :

Articles

L. Maire, N. Bozzolo, M. Bernacki, C. Moussa, Full field and mean field modeling of dynamic recrystallization: Application to 304L steel. *Ready to be submitted*, 2018.

A. Settefrati, P. de Micheli, L. Maire, B. Scholtes, N. Bozzolo, C. Moussa, E. Perchat, M. Bernacki. Prédiction de l'évolution de taille de grains à l'échelle mésoscopique lors des traitements thermiques: un cadre numérique et des exemples industriels. Matériaux & Techniques, vol. 106, pp. 105-112, 2018.

L. Maire, J. Fausty, M. Bernacki, N. Bozzolo, P. De Micheli, and C. Moussa. A new topological approach for the mean field modeling of dynamic recrystallization. Materials & Design, vol. 146, pp. 194-2017, 2018.

L. Maire, B. Scholtes, C. Moussa, N. Bozzolo, D. Pino Muñoz, A. Settefrati, and M. Bernacki. Modeling of dynamic and post-dynamic recrystallization by coupling a full field approach to phenomenological laws. Materials & Design, vol. 133, pp. 489-519, 2017.

L. Maire, B. Scholtes, C. Moussa, N. Bozzolo, D. Pino Muñoz and M. Bernacki. Improvement of 3D mean field models for capillarity-driven grain growth based on full field simulations. Journal of Materials Science, vol. 51, pp. 10970-10981, 2016.

Conference proceeding

L. Maire, B. Scholtes, C. Moussa, N. Bozzolo, A. Settefrati, I. Poitrault, A. Karch, and M. Bernacki. 3D full field modeling of recrystallization in a finite element framework application to 304L. In CSMA 2017-13eme Colloque National en Calcul des Structures, Giens, France, 2017.

A. Settefrati, P. de Micheli, L. Maire, B. Scholtes, N. Bozzolo, C. Moussa, E. Perchat, M. Bernacki. Prediction of the grain size evolution during thermal treatments at the mesoscopic scale: a numerical framework and industrial examples. In 24th IFHTSE Congress, Nice, France, 2017.

Conferences

This PhD work also led to international and national conferences :

International

L. Maire, J. Fausty, M. Bernacki, N. Bozzolo, P. De Micheli, C. Moussa. A new topological approach for the prediction of dynamic recrystallization. In European Conference on Computational Mechanics (ECCM 6), Glasgow, UK, 2018.

L. Maire, C. Moussa, N. Bozzolo, and M. Bernacki. Modeling of dynamic recrystallization in austenitic stainless steel 304L by coupling a full field approach in a finite element framework with mean field laws. In 2017 MRS Spring Meeting & Exhibit,

Phoenix, USA, 2017.

D. Pino Muñoz, M. Bernacki, N. Bozzolo, T. Toulorge, C. Moussa, L. Maire, and J. Fausty. Recent advances in the full field modeling of recrystallization and grain growth using the level set approach. In 14th U.S. National Congress on Computational Mechanics (USNCCM14), Montreal, Canada, 2017.

National

L. Maire, J. Fausty, N. Bozzolo, M. Bernacki, D. Pino Muñoz, C. Moussa, Mean field and full field simulations of dynamic recrystallization of austenitic 304L steel, MATERIAUX 2018, Strasbourg, France, 2018.

Marc Bernacki, Ludovic Maire, Julien Fausty, Nathalie Bozzolo, Charbel Moussa, Daniel Pino Muñoz, Thomas Toulorge, Pascal De Micheli, Isabelle Poitrault, Rémy Besnard, Jean-Michel Franchet, Christian Dumont, Towards the full field modeling of microstructural evolutions during metal forming industrial processes, MATERIAUX 2018, Strasbourg, France, 2018.

L. Maire, C. Moussa, N. Bozzolo, D. Pino Muñoz, and M. Bernacki. Full field simulation of dynamic and post-dynamic recrystallization in 304L steel. Journées annuelles SF2M, Lyon, France, 2017.

L. Maire, C. Moussa, N. Bozzolo, and M. Bernacki. Modeling of dynamic recrystallization in austenitic stainless steel 304l by coupling a full field approach in a finite element framework with mean field laws. 3ème Journées Matériaux Numériques, Tours, France, 2017.

L. Maire, B. Scholtes, C. Moussa, D. Pino Muñoz, N. Bozzolo, and M. Bernacki. Simulation of static recrystallization and grain growth phenomena by mean field and full field modeling. Colloque Métallurgie, quel avenir! Saint-Etienne, France, 2016.

Chapter 1

Litterature review

Contents

1.1 Dynamic and post-dynamic recrystallization 9

1.1.1 Introduction 9

1.1.2 Austenitic stainless steel 304L 9

1.1.3 Strain hardening 11

1.1.4 Recovery 11

1.1.5 Grain boundary migration 12

1.1.6 Nucleation 14

1.1.7 Influence of recrystallization on the flow behavior 17

1.2 Modeling of dynamic and post-dynamic recrystallization 18

1.2.1 Phenomenological models 19

1.2.2 Mean field models 22

1.2.3 Full field models 35

Résumé en français

Ce premier chapitre est consacré à l'étude bibliographique de mon sujet de thèse. Premièrement, la composition ainsi que les propriétés physiques du matériau considéré dans cette étude, c'est-à-dire l'acier 304L, sont données. Par la suite les mécanismes de recristallisation dynamique et post-dynamique sont physiquement décris et l'influence de la recristallisation dynamique sur le comportement global du matériau est évoquée. Finalement, les différents types de modèles métallurgiques existants dans la littérature sont introduits. Pour chaque type, des modèles de recristallisation dynamique et post-dynamique de la littérature sont décrits, avec leurs avantages et leurs faiblesses.

1.1 Dynamic and post-dynamic recrystallization

1.1.1 Introduction

Hot deformation of metals is responsible of a wide range of phenomena occurring in the microstructure. At high deformation temperatures, the dislocation density is the result of a competition between the increase of the amount of dislocations due to strain hardening and its decrease due to dynamic recovery. In general, the increase is faster than the decrease and the dislocation density globally goes up. Once a critical dislocation density is locally reached, the recrystallization mechanism, characterized by the appearance of recrystallized (RX) grains, occurs in the microstructure. These RX grains have a low content of dislocations and therefore a low stored energy value compared to the deformed ones. Because of stored energy differences between RX and non-recrystallized (NR) grains, RX grains grow by grain boundary migration at the expense of deformed grains. Simultaneously, dislocation density increases in the RX grains because of plastic deformation. In addition to stored energy differences, capillarity effect is also a driving force for grain boundary migration. This force tends to decrease the total grain boundary energy and its contribution is particularly important at multiple junctions. All these mechanisms acting during hot deformation constitute the so-called *discontinuous dynamic recrystallization* mechanism [1–10], which is the classical dynamic recrystallization (DRX) mechanism occurring in low/medium stacking fault energy (SFE) metal alloys, such as the 304L austenitic steel considered for application in this work. If the plastic deformation is stopped and the material is still at high temperature, grain boundary migration is still active because of stored energy differences and capillarity effects, which is called *metadynamic recrystallization*. Furthermore, the nucleation mechanism can also occur in some hardened grains, which is then called *static recrystallization* (SRX). Both SRX and MDRX appearing after hot deformation constitute the so-called *post-dynamic recrystallization* mechanism (PDRX) [11, 12]. Finally, if the material is left at high temperature and microstructure is almost free of stored energy, the only mechanism occurring is boundary migration due to capillarity effects: this regime is called *grain growth* (GG). A well-known review of recrystallization phenomena occurring in metal alloys can be found in [5]. More recently, Huang et al. [10] proposed a review of mechanisms acting during DRX.
In the following section, the 304L austenitic steel which is the material considered in this work for application is first presented. Then, the individual mechanisms involved in DRX and PDRX, i.e. strain hardening, recovery, nucleation and grain boundary migration, are described.

1.1.2 Austenitic stainless steel 304L

Chemical composition

Among the large number of metal alloys, stainless steels are widely used for their good corrosion resistance due to a large amount of chrome ($>11\%$), as well as good mechanical properties at high temperatures. Depending of the nature of the phases formed

in a steel, several classes are defined: martensitic, ferritic, austenitic and also duplex austenitic + ferritic steels. 304L is an austenitic stainless steel that is widely used. We can find this alloy in a large variety of applications such as automotive, aerospace and nuclear structure constructions. The crystalline structure of the 304L steel is face-centered cubic, with a lattice parameter a equal to $3.586.10^{-10}$m [13] and a Burgers vector magnitude b equal to $a/\sqrt{2} \simeq 2.5.10^{-10}$m. In addition to the high amount of Chrome, Nickel is also added in high proportions in 304L steel so as to stabilize the austenite at low temperatures. The general chemical composition of the 304L steel is reported in Tab. 1.1.

Element	Carbon	Mn	P	S	Si	Cr	Ni	N	Fe
w% 304L	<0.03	<2.00	<0.045	<0.03	<0.75	18- 20	8-12	<0.10	Bal.

Tab. 1.1. *Chemical composition of austenitic stainless steel 304L (weight %).*

Physical properties

The volumic mass of the 304L steel is about 7900 kg/m^3 and its melting temperature is about 1673K [14]. Concerning its mechanical properties at ambient temperature, the Young's modulus is about 200 GPa, the elongation to rupture is about 60% and the failure strength is under 600 MPa. Numerous papers and studies exist concerning the flow behavior of the 304L steel. In [15], the authors performed several compression tests on 304L steel at different temperatures (from 300K to 1500K) and at very low strain rates ($< 0.003\text{s}^{-1}$). The thermomechanical conditions as well as measured elastic modulus and yield stress are presented in Tab. 1.2.

T (K)	$\dot{\varepsilon}$ (s^{-1})	Max Strain	Young's modulus (GPa)	Yield stress (MPa)
293K (20°C)	0.00183	0.1131	228	447.8 8
600K (327°C)	0.00196	0.1748	208	320.1
700K (427°C)	0.00189	0.1803	195	322.2
800K (527°C)	0.00184	0.2728	163	294.2
900K (627°C)	0.00161	0.4569	156	264.5
1000K (727°C)	0.00172	0.4967	132	231.2
1100K (827°C)	0.00170	0.6144	107	162.1
1200K (927°C)	0.00183	0.6891	72	96.9
1300K (1027°C)	0.00263	0.7505	45	55.3
1400K (1127°C)	0.00182	0.6963	45	27.3
1500K (1227°C)	0.00197	0.6591	16	12.5

Tab. 1.2. *Temperatures, strain rates and maximum strain levels achieved for compression tests on a 304L steel. The resulting Young's modulus and yield stresses measured on stress-strain curves are also reported from [15].*

1.1.3 Strain hardening

When a metal alloy is plastically deformed, a large quantity of energy is dissipated in the form of heat and the remaining energy, typically 1% [5], is stored in the material under the form of crystallographic defects, mainly *dislocations*. During plastic deformation, dislocations move in the material until they interact with each other or with barriers (e.g. dislocation pile-up at grain boundaries, twins, inclusions etc.) in the polycrystal. Therefore the more dislocations in the metal, the more they interact and become pinned or tangled, resulting in a decrease of their mobility and consequently a strengthening of the metal alloy: this strengthening during plastic deformation is called *strain hardening*. The typical dislocation density of an annealed microstructure is between $10^{10}\mathrm{m}^{-2}$ and $10^{11}\mathrm{m}^{-2}$ and can increase up to $10^{15}\mathrm{m}^{-2}$ for a cold-worked metal [16].

1.1.4 Recovery

The presence of a dislocation induces an elastic strain field around the dislocation core. This strain field is in compression and tension on one side and the other of the dislocation line. In order to reduce those stress fields (i.e. the energy per dislocation), attraction and repulsion of dislocations take place between each other. Although at low temperatures dislocations are not mobile, at high temperatures dislocations move in order to reduce the energy associated to their strain field. *Dislocation glide* and *cross slip*, as illustrated on Fig. 1.1(a) and (b), respectively, are the main mechanisms occurring at high temperatures. Dislocation glide allows a dislocation to move on its slip plane by broken atomic bonds while cross slip allows a dislocation to change slip plane and hence move in 3D. For some materials, at very high temperatures, *dislocation climb* may also occur.

All these thermally activated mechanisms concerning mobility of dislocations allow them to adopt minimal energy configurations. Dislocations with opposite Burgers vector annihilate, dislocations with same Burgers vector group together forming subgrains: this global mechanism is called *recovery*. Dynamic and static recovery may occur depending whether it takes place during deformation or not.

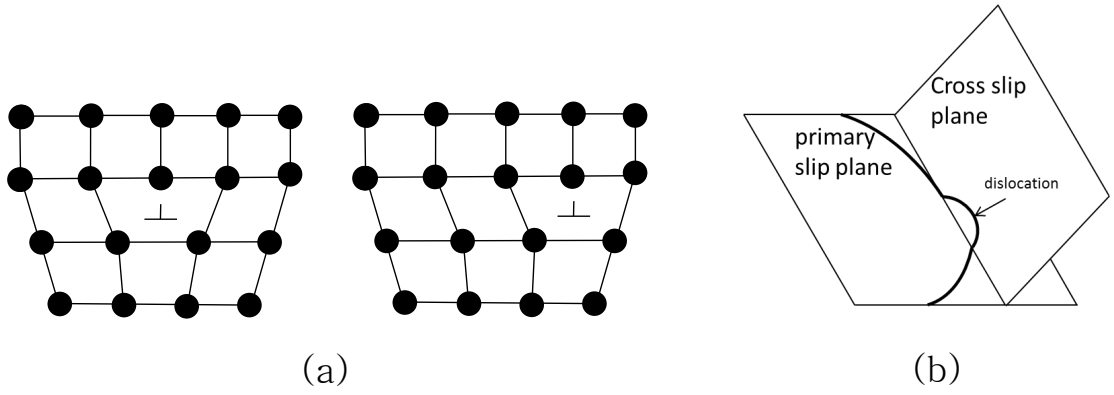

Fig. 1.1. *a) Glide of a edge dislocation: a bond is broken per plane for each glide and b) cross slip of a dislocation: a dislocation moved from a slip plane to another.*

1.1.5 Grain boundary migration

At high temperatures, grain boundaries migrate due to driving forces. This mechanism occurs to decrease the Gibbs free energy of the system and is based on the simple theory that atoms cross boundaries with net energy gain. The grain boundary velocity $\vec{v_b}$ is generally assumed as a linear function of a driving pressure, noted P_b, leading to :

$$\vec{v_b} = M_b P_b \vec{n}, \tag{1.1}$$

where $\vec{n}$ is the unit outward vector normal to the grain boundary and M_b is the grain boundary mobility. Furthermore, it is generally assumed that the total pressure exerted on the boundary P_b is the sum of a pressure due to capillarity effects noted P_c and a pressure due to a jump in stored energy across the grain boundary noted P_e :

$$P_b = P_c + P_e. \tag{1.2}$$

In a highly deformed material, forces due to stored energy are much higher than capillarity forces. In the case where second phase particles exist in the microstructure, grain boundaries can be pinned by these particles and their velocity is thus decreased: this mechanism is called the *Smith-Zener pinning* effect [17] but is not considered in this report since the investigated 304L steel is quasi single-phased.

The pressure P_c on a boundary is usually assumed to be directly proportional to its mean curvature, which is the trace of the curvature tensor in 3D, and the pressure P_e is generally assumed to be driven by a jump in stored energy across the grain boundary, leading to :

$$P_c = -\gamma_b \kappa, \tag{1.3}$$

$$P_e = [\![E]\!] = \tau [\![\rho]\!], \tag{1.4}$$

where γ_b is the grain boundary energy, κ is the local mean curvature, and $[\![E]\!]$ is the jump in stored energy across the grain boundary. The stored energy E in a grain is generally estimated with the relation $E = \tau \times \rho$ where τ is the energy per unit dislocation line. The parameter τ is often estimated by the relation $\mu b^2/2$ where μ is the shear modulus and b is the norm of the Burgers vector. A schematic illustration of a grain boundary submitted to the pressures P_c and P_e is presented on Fig. 1.2 in the case where the grain 2 has a dislocation density higher than that of grain 1 (i.e. $\rho_2 >> \rho_1$).

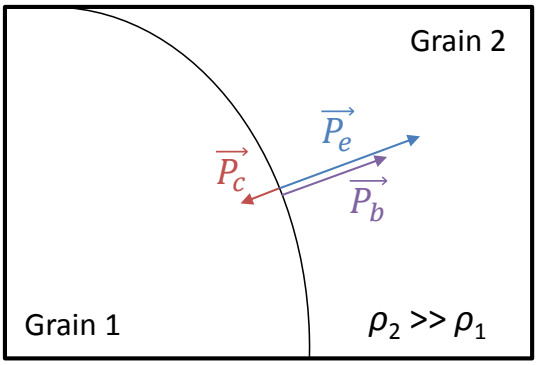

Fig. 1.2. *Schematic illustration of a grain boundary submitted to a pressure P_c due to capillarity effects and a pressure P_e due to the jump in stored energy across the grain boundary. P_b is the total pressure exerted on the grain boundary. The grain 2 has a dislocation density noted ρ_2 higher than that of the grain 1 noted ρ_1.*

A boundary separating two grains can be physically described by a misorientation of the lattice between these two grains and by the normal to the boundary plane $\vec{n}$. Depending on these two factors, the grain boundary energy γ_b can change. However, the effect of boundary plane on its energy is still poorly understood which explains why this effect is rarely considered in the state of the art concerning grain boundaries. Usually, the crystallographic mismatch between two grains at a grain boundary is quantified using a misorientation angle, also called disorientation and noted θ. Furthermore, the Read-Shockley relation [18, 19] is generally used to describe the dependence of the disorientation θ on γ_b :

$$\gamma_b(\theta) = \begin{cases} \gamma_0 \dfrac{\theta}{\theta_{\text{ref}}} \left(1 - \ln\left(\dfrac{\theta}{\theta_{\text{ref}}}\right)\right) & \text{if } \theta \leq \theta_{\text{ref}}, \\ \gamma_0 & \text{if } \theta \geq \theta_{\text{ref}}, \end{cases} \tag{1.5}$$

where γ_0 is the energy of high misorientation angle grain boundaries (HAGB) and θ_{ref} is the misorientation angle that defined a HAGB, generally close to 15°. This relation assumes that grain boundary energy is not affected by misorientation angles above 15°. A modified Read-Shockley relation was proposed and used in [20, 21] for large values of misorientation angles. Recently, using Olmsted molecular dynamic simulation results [22], Bulatov et al. [23] proposed an analytical function to describe qualitatively the grain boundary energy variations in the 5-space of macroscopic parameters defining a grain boundary (3 parameters for describing the misorientation and 2 for the plane inclination).

Eq. 1.3 is widely used in literature for modeling of grain boundary migration under the assumption of isotropic (i.e. constant in the microstructure) or anisotropic (i.e. constant per grain boundary) grain boundary energies. In the context of anisotropic grain boundary energies, Eq. 1.5 can be used as a first approximation to define constant per grain boundary γ_b values. In [24], a novel formulation was proposed for modeling GG with anisotropic energies. To our knowledge, there exists no models able to consider

the dependence of $\vec{n}$ on the grain boundary energy. However in this case, the capillarity pressure given by Eq. 1.3 would become a large assumption and based on Herring's equation [25], the capillarity pressure should be expressed as :

$$P_c = -\kappa_1 \left(\gamma_b + \frac{\partial^2 \gamma_b}{\partial \xi_1^2} \right) - \kappa_2 \left(\gamma_b + \frac{\partial^2 \gamma_b}{\partial \xi_2^2} \right), \tag{1.6}$$

where κ_i is the curvature in the i^{th} principal direction of the grain boundary and (ξ_1, ξ_2) are the angles parametrizing the grain boundary normal $\vec{n}$.

The boundary mobility M_b, reflecting the ability of the boundary to move, is material and temperature dependent and is generally assumed to follow a law close to Arrhenius type [5] :

$$M_b = M_0 \exp\left(\frac{-Q_m}{RT} \right), \tag{1.7}$$

where M_0 is a pre-exponential term, T is the temperature, Q_m is the activation energy for grain boundary migration, which is dependent on the material, and R corresponds to the perfect gaz constant. M_0 can also be considered inversely proportional to the temperature.

1.1.6 Nucleation

Nucleation has a primordial role in understanding the microstructure evolution by recrystallization phenomena. It consists in the appearance of new grains with very low stored energy. It is generally assumed that nucleation occurs at high temperatures in regions with high dislocation content, i.e. high stored energy level (the concept of critical strain is sometimes used). Hence, nucleation appears mainly at grain boundaries during DRX . Some accepted mechanisms found in the literature for nucleation are presented in the following: nucleation by subgrain coalescence, nucleation by strain induced boundary migration (SIBM) and nucleation by low angle boundary migration. A review of these major mechanisms can be also found in [26].

Subgrain coalescence
This mechanism was first proposed by Smith in 1948 [27]. Then, Hu [28, 29] studied nucleation occurring during annealing of a Fe-3%Si single crystal using TEM and observed that it mainly occurs by subgrain coalescence as seen on Fig. 1.3.

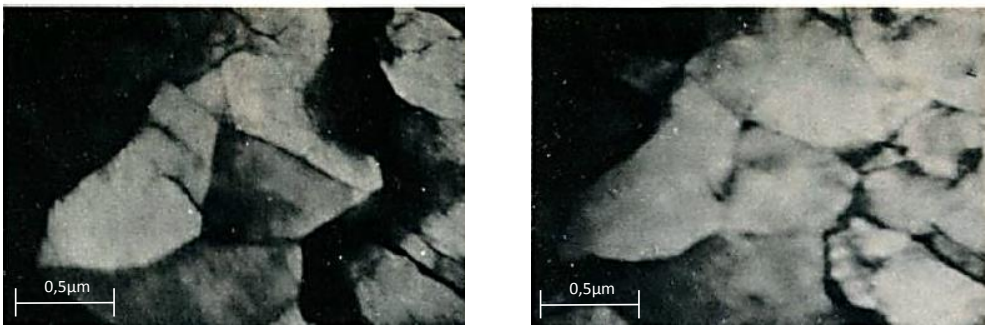

Fig. 1.3. *Coalescence of subgrains in Fe-3%Si alloy cold rolled to 70% seen by the gradual disappearance of several subgrain boundaries, and a decrease of the contrast between grains during annealing at 1000K after (a) 2min and (b) 3min. Reproduced from [28].*

Few years later, Jones [30] and [31] observed the same mechanism in aluminium alloys. The theory of this mechanism is based on the rotation of one subgrain lattice up to coalescence with a neighboring subgrain lattice. The subgrain boundaries slowly disappear and a high angle boundary is formed. Then, the coalesced subgrains grow by boundary migration. This mechanism is mainly observed in metal alloys with well organized deformation substructures, which is not the case of the 304L steel. Furthermore, this mechanism is favoured at moderate strain and low annealing temperatures.

Strain induced boundary migration (SIBM)
This mechanism is the common nucleation mechanism observed in most of metal alloys. It was first observed by Beck and Sperry in 1950 [32] in high purity aluminium, as shown on Fig. 1.4 and schematized on Fig. 1.5. It was then validated thanks to experiments on a large number of other metal alloys [33–35]. This mechanism is characterized by the migration of a pre-existing grain boundary (position 1 on Figs. 1.4 and 1.5) toward the interior of a highly strained grain (grain B on Figs. 1.4 and 1.5). The new position of the boundary (position 2 on Figs. 1.4 and 1.5) swept an area almost free of defects, defined as a nucleus. A particularity of this mechanism is that the nucleus formed has an orientation close to its parent grain.

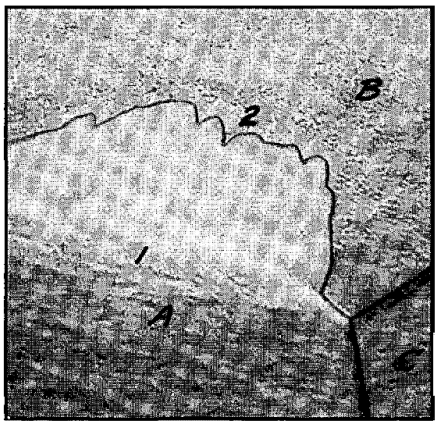

Fig. 1.4. *SIBM in high purity aluminium from position 1 to position 2. Orientation in the swept area is almost identical to that of the deformed grain A [32].*

Since SIBM occurs at grain boundaries, it often leads to a necklace nucleation characterized by several small nuclei along former grain boundaries. The condition for those nuclei to survive is given by a positive energy-balance between the stored energy and the surface energy of the migrating boundary surface. This condition, known as the Bailey-Hirsch criterion [36], leads to a critical grain size r_{cr} for the subgrain to be viable as a nucleus :

$$r_{\mathrm{cr}} = \frac{2\gamma_{\mathrm{b}}}{\tau\Delta\rho}, \tag{1.8}$$

where γ_{b} is the grain boundary energy, τ is the energy per unit dislocation line, and $\Delta\rho$ is the difference of dislocation density $\Delta\rho = \rho_B - \rho_A$ as seen on Figs. 1.4 and 1.5. Investigations on deformed metals suggested that SIBM is the dominant mechanism occurring for hot deformations lower than 20% [36,37], even if it also occurs for higher deformations.

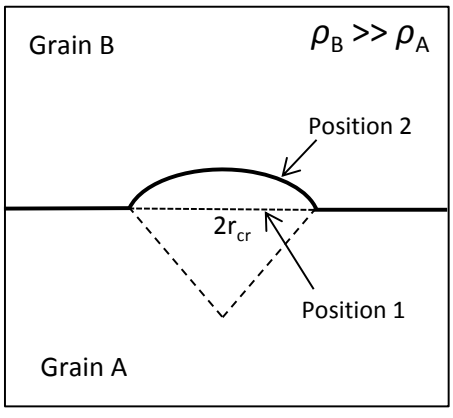

Fig. 1.5. *SIBM of a boundary separating a grain of low stored energy (Grain A) from one of higher energy (Grain B). The positions 1 and 2 denote the positions of the grain boundary before and after SIBM, respectively.*

Low angle boundary migration

This nucleation mechanism was independently proposed by Beck in 1949 [38] and Cahn [39] in 1950. Then, additional explanations were brought by Cottrel in 1953 [40] leading to the *Cahn-Cottrell* nucleation model. This model is based on the growth of a subgrain at the expense of its neighbors by thermally assisted subgrain boundary migration. During migration, the subgrain boundary absorbs dislocations, increasing its misorientation angle and transforming into a mobile high angle boundary, as illustrated on Fig. 1.6. For this mechanism, the condition for a subgrain to become a stable nucleus can also be given by the Bailey-Hirsch condition (Eq. 1.8). This mechanism is mainly observed in materials with a low stacking fault energy and during processes at high temperatures and high strain levels [26, 41].

Fig. 1.6. *Schematic illustration showing the nucleation of a RX grain starting from a subgrain: a) initial substructure, b) the growth of the larger (middle) subgrain over the other (smaller) ones and c) an area free of defects associated to a large angle boundary that is being formed [26].*

1.1.7 Influence of recrystallization on the flow behavior

The flow behavior of a metal alloy is driven by its microstructure. During the first stage of deformation, strain hardening and dynamic recovery, characterized by an increase and a decrease of the stored energy, respectively, act in the microstructure. Globally, strain hardening is preponderant and the global stored energy increases in the microstructure, inducing an increase of the macroscopic flow stress. As soon as nucleation occurs (around 80% of the peak strain), new small grains with low energy contents appear in the microstructure, leading to a decrease of the global stored energy and consequently to macroscopic softening. Typical stress-strain curves obtained during hot deformation of a metallic alloy are presented on Fig. 1.7. It is well known in literature [5] that an increase in temperature or a decrease in strain rate leads to a decrease in the flow stress and conversely. This sensitivity of the flow behavior to temperature and strain rate led to the introduction of the Zener-Hollomon parameter [42] noted Z. This parameter is also called temperature-compensated strain rate and is defined by the following relationship

:

$$Z = \dot{\varepsilon} \exp\left(\frac{Q_{\text{def}}}{RT}\right), \tag{1.9}$$

where $\dot{\varepsilon}$ is the strain rate, Q_{def} is the apparent activation energy for deformation (J.mol^{-1}), R the perfect gas constant (J.mol^{-1}.K^{-1}) and T is the deformation temperature (K).

The parameter Z is used by several authors to describe the shape of the stress-strain curve [1, 19, 43]. Usually, at high Z values, i.e. high strain rates and low temperatures, a very pronounced single-peak flow is observed (Fig. 1.7 (a)), whereas at low Z values, a multi-peak is observed (Fig. 1.7 (b)). Such oscillations can be explained by the fact that at low strain rates and high temperatures, most of the microstructure is recrystallized before the first RX grains hardened enough to start a new cycle of nucleation. So one oscillation means that the major part of the microstructure was one time almost fully recrystallized. If the strain rate is increased and/or temperature decreased, strain hardening and nucleation are more simultaneous, damping out the flow curve oscillations.

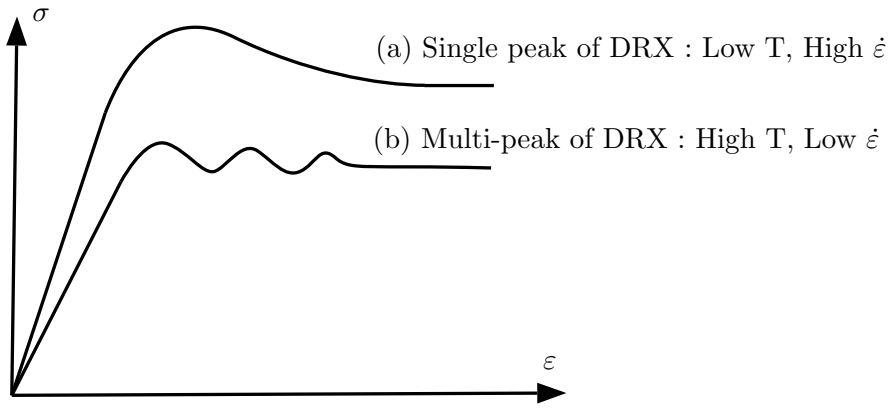

Fig. 1.7. *Schematic illustration of the typically observed stress-strain curves during hot deformation. The two cases (a) and (b) show the transition from single to multi-peak for DRX, respectively.*

1.2 Modeling of dynamic and post-dynamic recrystallization

Several kinds of model were reported in the literature to simulate the recrystallization phenomenon :

- *Phenomenological models* can be used to reproduce experimental observations by using analytical laws. However such models are based on a large number of assumptions and do not describe explicitly the physical mechanisms taking place, which makes them dependent on materials and thermomechanical conditions. Furthermore, they use a large number of calibration parameters, which requires

a large number of experimental data. Most of these DRX and PDRX models are based on the well-known Johnson-Mehl-Avrami-Kolmogorov (JMAK) [44–46] and aim at predicting the evolution of the RX fraction during hot deformation.

- *Mean field models* are based on an implicit description of the microstructure by considering grains as spherical entities with an equivalent radius and dislocation density. To further decrease computational costs of mean field models, grains having same characteristics (in terms of grain radius and dislocation density) can be gathered into grain classes. Each grain is considered into a homogeneous equivalent medium (HEM) and its evolution is governed by its interaction with the HEM [47–50]. In those models, each individual physical mechanism taking place during DRX (i.e. strain hardening, dynamic recovery, grain boundary migration etc.) is described by a phenomenological or physical law. Hence they are more versatile than phenomenological laws.

- *Full field models* are more sophisticated and are able to explicitly reproduce microstructure evolutions. Full field models can be based on different numerical methods such as Phase-Field (PF) [51], Level-Set (LS) [52], Vertex [53], Monte Carlo (MC) [54,55] or Cellular Automata (CA) [56,57]. Contrary to phenomenological and mean field models, full field models are based on an explicit description of the microstructure. However, a major limitation of these models remains their computational cost, especially when crystal plasticity is implemented or when aiming at a direct coupling with macroscale simulations.

The following part describes the state of the art of the different DRX and PDRX models existing in the literature. First several models based on the JMAK equation are presented. Then mean field models of the literature are described with their advantages and limitations. Finally, the different frameworks used for full field modeling of DRX and PDRX are reviewed.

1.2.1 Phenomenological models

The JMAK [44–46] equation is often used as an empirical approach to describe the RX fraction obtained during SRX. This well-known equation and its sigmoidal shape are based on many assumptions such as a constant temperature, uniformity of nucleation and growth rates, and location of the nucleation sites. The basic expression of the JMAK law is the following [5] :

$$X(t) = 1 - \exp\left(\frac{-f\dot{N}\dot{G}^3 t^4}{4}\right), \tag{1.10}$$

where X is the RX fraction, $\dot{N}$ is the nucleation rate (number of nuclei per unit time and volume), $\dot{G}$ is the grow rate (assumed to be constant), f is a shape factor (equal to $4\pi/3$ for spherical grains) and t is time. Eq. 1.10 can also be found in a more general form :

$$X(t) = 1 - \exp(-B \times t^n). \tag{1.11}$$

Since people observed that the evolution of the RX fraction during DRX and PDRX plotted as a function of the strain level has a sigmoidal shape, the same form of JMAK equation was adapted to these two regimes. In the following, the literature review will be limited to the materials close to that of interest of this work (304 steel).

In 2001, Kim et al. [58] proposed these expressions for the modeling of DRX in a AISI 304 steel based on the JMAK equation :

$$X^{\mathrm{drx}} = 1 - \exp(-((\varepsilon - \varepsilon_{\mathrm{cr}}^{\mathrm{drx}})/\varepsilon^*)^m), \tag{1.12}$$

$$\varepsilon_{\mathrm{cr}}^{\mathrm{drx}} = 0.27 \left(\frac{Z}{A}\right)^{0.0115}, \tag{1.13}$$

$$\varepsilon^* = 0.61 \left(\frac{Z}{A}\right)^{0.007}, \tag{1.14}$$

$$\langle D \rangle = 67.8 \left(\frac{Z}{A}\right)^{-0.017}, \tag{1.15}$$

where $\varepsilon_{\mathrm{cr}}^{\mathrm{drx}}$ is the critical strain for DRX, i.e. the strain level at which nucleation is triggered, ε^* is the strain for maximum softening rate, $\langle D \rangle$ is the mean grain diameter, Z is the Zener-Hollomon parameter and A is a constant. These equations were proposed in the temperature range of 1173-1373K and the strain rate range of 5.0×10^{-2}-5.0×10^{0} s^{-1}. In 2002, Venugopal et al. [59] proposed the following expressions for modeling of DRX during hot deformation of a 304L steel in the temperature range of 1223-1523K and strain rate range of 0.1-20s^{-1}, representative of the extrusion process :

$$X^{\mathrm{drx}} = 1 - \exp(\ln 2(\varepsilon - \varepsilon_{\mathrm{cr}}^{\mathrm{drx}})/(\varepsilon_{0.5})^2), \tag{1.16}$$

$$\varepsilon_{\mathrm{cr}}^{\mathrm{drx}} = 5.32 \times 10^{-4} \exp(8700/T), \tag{1.17}$$

$$\varepsilon_{0.5} = 1.264 \times 10^{-5} \langle D_0 \rangle^{0.31} \varepsilon^{0.05} \exp(6000/T), \tag{1.18}$$

$$\langle D \rangle = 20560 \dot{\varepsilon}^{-0.3} \exp(-0.25(Q_{\mathrm{def}}/RT)), \tag{1.19}$$

where $\varepsilon_{0.5}$ is the plastic strain for 50% of RX fraction and T is the deformation temperature. More recently in 2008, Dehghan-Manshadi et al. [60] proposed these expressions for DRX modeling in 304L steel in the temperature range of 1173-1373K and strain rate range of 0.01-1s^{-1} :

$$X^{\mathrm{drx}} = 1 - \exp(-k(\varepsilon - \varepsilon_{\mathrm{cr}}^{\mathrm{drx}})^{1.3}), \tag{1.20}$$

$$\varepsilon_{\mathrm{cr}}^{\mathrm{drx}} = 2.2 \times 10^{-3} Z^{0.15}, \tag{1.21}$$

$$\langle D \rangle = 5.2 \times 10^3 Z^{-0.17}. \tag{1.22}$$

Several phenomenological models of PDRX based on the JMAK law were also proposed in the literature. In 2001, Cho et al. [61] proposed these expressions for modeling of PDRX in a AISI 304 steel, in the temperature range of 1173-1373K and a strain rate of 0.5s^{-1} :

$$X^{\text{pdrx}} = 1 - \exp(-0.693(t/t_{50})^{1.06}), \tag{1.23}$$

$$t_{50} = 1.33 \times 10^{-11} \dot{\varepsilon}^{-0.41} \langle D_0 \rangle \exp(230300/RT), \tag{1.24}$$

where t_{50} is the time for 50% softening. In 2003, Uranga et al. [62] proposed these expressions for modeling of PDRX in a coarse Nb microalloyed austenite in the strain rate range of $0.2\text{-}5\text{s}^{-1}$ and a temperature of 1373K :

$$X^{\text{pdrx}} = 1 - \exp(-0.693(t/t_{50})), \tag{1.25}$$

$$t_{50} = 1.77 \times 10^{-6} \dot{\varepsilon}^{-0.62} \exp(153000/RT). \tag{1.26}$$

Finally in 2008, Dehghan-Manshadi [63] proposed these expressions for PDRX modeling in 304 steel at a temperature of 1173K and a strain rate of 0.01s^{-1} :

$$X^{\text{pdrx}} = 1 - \exp(-0.693(t/t^{50})^{1.1}), \tag{1.27}$$

$$t_{50} = 8 \times 10^{-9} \varepsilon^{-1.48} Z^{-0.42} \exp(375000/RT). \tag{1.28}$$

Other models can be found for GG regime, i.e grain boundary migration with no stored energy within the microstructure. Burke & Turnbull (B&T) proposed an analytical law aiming to predict a parabolic evolution of the mean grain size as a function of time during GG :

$$\langle R \rangle^2 - \langle R_0 \rangle^2 = \alpha M_\text{b} \gamma_\text{b} t, \tag{1.29}$$

where α is a constant close to 0.5 according to [64, 65], M_b is a function of temperature and γ_b is assumed isotropic (i.e. constant in the microstructure). Cruz-Fabiano et al. [66] recently proposed a modified B&T law where the grain size distribution (GSD) characteristics are considered, leading to a more realistic prediction of 2D mean grain size, in particular during the transient regime.

Conclusion of phenomenological laws

Despite their very low numerical cost and ease of use, phenomenological approaches are limited by the fact that they generally do not take the heterogeneities of energy and grain size into account. Furthermore, in these models, the nucleation occurring during

hot deformation is considered to be with a constant rate and to be topologically random but these assumptions are far from reality. We can even speak of "blind" models concerning the involved physical mechanisms. Finally phenomenological models cannot be generalized and must be discussed and parametrized each time thermomechanical conditions or materials evolve.

1.2.2 Mean field models

Several mean field models can be found in the literature to model DRX and PDRX. The structure of these models is always the same: the microstructure is implicitly described by considering spherical grains with a given dislocation density (uniform per grain). To further decrease computational costs, grains with same characteristics (in terms of radius and dislocation density) can be gathered into grain classes. This concept was already used in few mean field models but can be easily extended to any other ones. The main drawback of this concept is related to the fact that all grains belonging to the same class follow the same behavior during the simulation. The individual physical mechanisms taking place during DRX, i.e. strain hardening, dynamic recovery, dynamic nucleation and grain boundary migration and those taking place during PDRX, i.e. static recovery, static nucleation and grain boundary migration, are independently described by analytical laws. The main advantage of mean fields models as compared to phenomenological laws is the modeling of each underlying physical mechanism, which makes them more versatile. In addition, not only the mean grain size but also the grain size distribution can be predicted along the hot deformation process. The first mean field model was proposed by Hillert and Abbruzzese [47, 67–69] for modeling GG. This model was extended to DRX in 2009 by Montheillet et al. [48]. In Montheillet's model, each grain is considered inside a HEM composed of all grains of the microstructure. Also in 2009, Cram & Zurob [70] proposed another kind of mean field model for DRX based on another assumption: during deformation, each grain undergoes the same mechanical work meaning that softer grains deform more than harder ones. Following Montheillet's approach, Bernard et al. [49] proposed two years later another physically-based mean field model, for both DRX and PDRX mechanisms, whose main novelty lies in the fact that the HEM is subdivided into two different media composed of RX and NR grains respectively. In 2015, Beltran et al. [50] proposed an improvement of Bernard's model to handle multi-pass deformation routes. Very recently, Smagghe [71] developed in his PhD work a new approach for DRX and PDRX modeling in which each grain interacts with only one randomly-selected grain all along the process. All the quoted mean field models are detailed below.

Model of Hillert/Abbruzzese [47, 67–69]

Description of the microstructure

In this GG model, the microstructure is modeled by considering grain classes as spherical entities, each composed of an equivalent sphere radius R_i and an equivalent number

of grains N_i as illustrated on Fig. 1.8. Then each grain class is immersed into a HEM with an equivalent radius R_{cr}, considering the assumption that all grain classes smaller than R_{cr} shrink while those larger than R_{cr} grow.

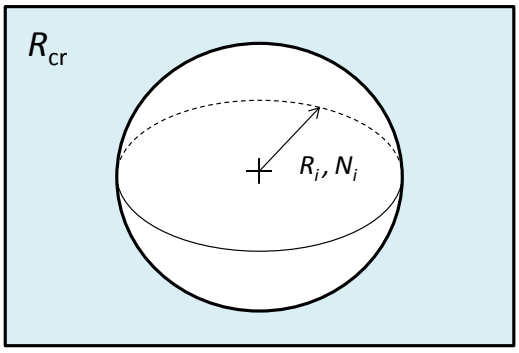

Fig. 1.8. *A grain class immersed into a HEM as considered in the model of Hillert/Abbruzzese.*

Grain boundary migration

This model is based on a single central equation for the modeling of boundary migration :

$$\frac{dR_i}{dt} = \beta M_{\text{b}} \gamma_{\text{b}} \left(\frac{1}{R_{\text{cr}}} - \frac{1}{R_i} \right), \tag{1.30}$$

where β is a geometrical dimensionless constant close to unity in 3D, which refers to the inherent approximations concerning the assumed idealized grain geometry and R_{cr} is relative to the mean grain size. By applying the volume conservation equation, it can be demonstrated that $R_{\text{cr}} = \langle R^2 \rangle / \langle R \rangle$ [72–74]. Therefore at each time increment, grain classes undergo Eq. 1.30 and all equivalent radius are updated simultaneously at the end of the time increment, leading to a new grain size distribution.

Model of Montheillet et al. [48]

Description of the microstructure

In the DRX model of Montheillet et al. [48], the microstructure is described by spherical grains having an equivalent sphere radius R_i and a dislocation density ρ_i. Although the concept of grain classes was not initially considered in this model, it could be done by adding an additional scalar value N_i accounting for the number of grains in each class. In that case, the index i used in all the constitutive equations would denote the i^{th} grain class instead of the i^{th} grain. In this model, each grain is immersed into a HEM composed of all the grains in the microstructure as shown on Fig. 1.9. This HEM is characterized by a mean dislocation density noted $\langle \rho \rangle_{\text{surf}}$ (weighted by grain surface).

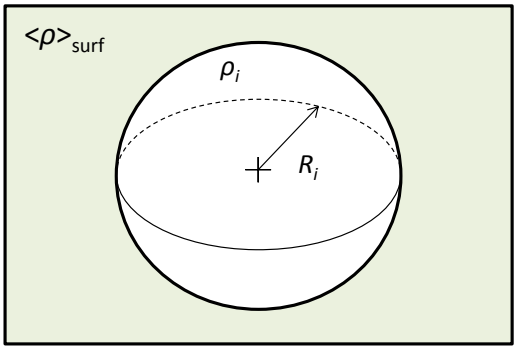

Fig. 1.9. *A grain immersed into a HEM as considered in the model of Montheillet.*

Strain hardening and dynamic recovery

Strain hardening and dynamic recovery are both described in this model within the same differential equation. In other words, the dislocation density in each grain is updated at each time increment following a differential equation. Three different differential equations, summarized in Tab. 1.3, were tested in this model: the power-law (PW) equation [48], the Yoshie-Lasraoui-Jonas (YLJ) equation [75, 76] and the Kocks-Mecking (KM) equation.

Name	Equation
PW	$d\rho_i/d\varepsilon = H/\rho_i^{\nu}$
YLJ	$d\rho_i/d\varepsilon = K_1 - K_2\rho_i$
KM	$d\rho_i/d\varepsilon = K_1\sqrt{\rho_i} - K_2\rho_i$

Tab. 1.3. *The three differential equations compared in [48] for strain hardening and dynamic recovery modeling.*

K_1 and K_2 are the strain hardening and dynamic recovery parameters respectively, H is a parameter accounting for both strain hardening and recovery balance effects and ν is a constant.

The macroscopic flow stress of the material is computed at any instant in this model according to this form of Taylor's equation :

$$\sigma = \alpha\mu b\sqrt{\langle\rho\rangle_{\text{vol}}}, \tag{1.31}$$

where α is a constant close to unity [48], μ is the shear modulus, b is the Burgers vector magnitude and $\langle\rho\rangle_{\text{vol}}$ is the mean dislocation density (weighted by grain volume), i.e. :

$$\langle\rho\rangle_{\text{vol}} = \frac{\sum\rho_i R_i^3}{\sum R_i^3}. \tag{1.32}$$

Grain boundary migration

Grain boundary migration is assumed to be driven only by the stored energy difference between each grain and the HEM, leading to the following equation :

$$\frac{dR_i}{dt} = M_\mathrm{b}\tau(\langle\rho\rangle_\mathrm{surf} - \rho_i), \tag{1.33}$$

where M_b is the grain boundary mobility, τ is the energy per unit dislocation line and $\langle\rho\rangle_\mathrm{surf}$ is the mean dislocation density of the whole set of grains, weighted by grain surface to ensure volume conservation :

$$\langle\rho\rangle_\mathrm{surf} = \frac{\sum \rho_i R_i^2}{\sum R_i^2}. \tag{1.34}$$

The capillarity term is not considered in the grain boundary migration equation of this model. If capillarity effects would be considered, the nuclei would have to be generated with a minimum radius to counter capillarity effects and survive after their appearance (Bailey-Hirsch criterion in section 1.1.6). On the contrary, the omission of the capillarity term in this model enables the creation of nuclei with no limitation in terms of minimal size. However, it was shown that capillarity effects play a role in microstructure evolutions, not only during GG but also during DRX and PDRX, in particular at multiple junctions [77]. Omitting the capillarity term could thus lead to non-physical results in particular cases. Another drawback is that GG can of course not be modeled with this model.

Nucleation

Several mechanisms of nucleation were reported in section 1.1.6. Since it is not straightforward to investigate and model independently each nucleation mechanism, the authors propose a nucleation rate equation accounting for any physical type of nucleation :

$$\frac{dN}{dt} = B_\mathrm{n} \times \langle\rho\rangle^p \sum S_i, \tag{1.35}$$

where N is the number of nuclei, B_n is a nucleation parameter depending on temperature and p is a positive exponent. The term $\sum S_i$ is due to the fact that nucleation mainly occurs at grain boundaries and the nucleation rate is assumed to be proportional to the total grain boundary surface.

Model of Cram & Zurob [70]

Description of the microstructure

The same year, Cram & Zurob [70] proposed a mean field model of DRX with a similar but richer microstructure description compared to that of Montheillet et al. [48], as shown on Fig. 1.10. The concept of grain classes is not considered in this model but this

concept can be easily integrated to this model in the same manner as already discussed for the model of Montheillet. In addition to the equivalent sphere radius R_i and the dislocation density ρ_i, each grain is also characterized by a Taylor factor $M_T(i)$ and a parameter P_i describing the subgrain size distribution.

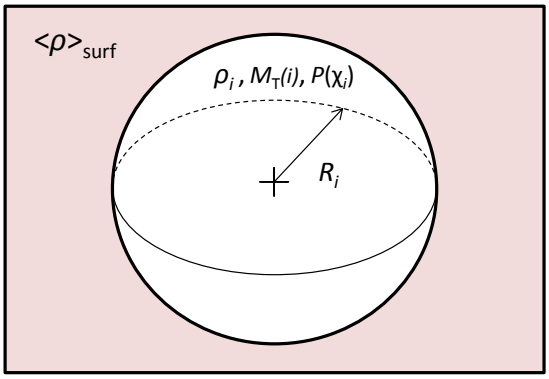

Fig. 1.10. *A grain immersed into a HEM as considered in the model of Cram & Zurob.*

Strain hardening and dynamic recovery

Strain hardening and dynamic recovery are based on the "iso-work increment assumption" in this model. For modeling of strain hardening and dynamic recovery, two assumptions can actually be done. The first one, called *Taylor's* assumption, consists in assuming that all grains undergo the same homogeneous strain. This assumption is considered in the model of Montheillet et al. [48] and ensures strain compatibility between grains. The second one, called *static* assumption, consists in assuming that all grains are submitted to the same homogeneous stress. In a real microstructure during deformation, two conditions should be fulfilled: the softer grains should deform more than the hard ones (which is not fulfilled with the Taylor's assumption) and the flow stress should vary from grain to grain (which is not the case with the static assumption). Therefore a compromise between these two conditions was proposed by Bouaziz et al. [78] by assuming that mechanical work noted K is equal from grain to grain. This assumption, called "iso-work increment assumption", is used to decompose each macroscopic strain increment noted $d\varepsilon_{\text{mac}}$ in individual strain increments $d\varepsilon_i$ using the following relationship :

$$d\varepsilon_i = \frac{K}{\sigma_i}, \tag{1.36}$$

where $d\varepsilon_i$ and σ_i are the strain increment and the stress in grain i, respectively. In this way, softer grains deform more than harder ones in the same macroscopic increment $d\varepsilon$. The mechanical work K is chosen so as to maintain a relatively low macroscopic strain increment $d\varepsilon$. The macroscopic strain $d\varepsilon$ and the macroscopic stress σ are calculated by the respective relationships :

$$d\varepsilon = \frac{\sum V_i d\varepsilon_i}{\sum V_i}, \tag{1.37}$$

$$\sigma = \frac{\sum V_i \sigma_i}{\sum V_i}. \tag{1.38}$$

Finally, in the model proposed by Cram & Zurob, a Voce hardening law [79] is used as constitutive equation between the stress increment and the strain increment to describe strain hardening and dynamic recovery :

$$\frac{d\sigma_i}{d\varepsilon_i} = \Theta_{\mathrm{II}} \left(1 - \frac{\sigma_i}{\sigma_{s,i}} \right), \tag{1.39}$$

where $\sigma_{s,i}$ is the steady-state stress of grain i and Θ_{II} is the stage II work-hardening rate. The flow stress of grain i is related to its mean dislocation density by the following relationship :

$$\sigma_i = \alpha M_{\mathrm{T}}(i) \mu b \sqrt{\rho_i} \left(\frac{\dot{\varepsilon}_i}{\dot{\varepsilon}_{\mathrm{ref}}} \right)^m, \tag{1.40}$$

where α is a constant, μ is the shear modulus, b is the Burgers vector magnitude, $\dot{\varepsilon}_{\mathrm{ref}}$ is a reference strain rate and m is the strain rate sensitivity.

Grain boundary migration

The boundary migration is driven by the same equation as considered in the model of Montheillet et al. [48] (Eq. 1.33). The grain boundary mobility M_{b} is estimated in this model based on the relation proposed in [80] :

$$M_{\mathrm{b}} \approx \frac{\delta D_{\mathrm{gb}}(T) V_{\mathrm{m}}}{5 b^2 R T}, \tag{1.41}$$

where δ is the grain boundary width, V_{m} is the molar volume, R is the perfect gas constant and $D_{\mathrm{gb}}(T)$ is the grain boundary diffusivity.

Nucleation

The nucleation mechanism modeled in this work is the SIBM mechanism introduced in section 1.1.6. which is based on the fact that a subgrain can grow into a more hardened grain until reaching the critical radius to become a viable nucleus. Therefore it is considered in this model that each grain owns a Rayleigh distribution of subgrain sizes and the evolution of the mean subgrain size noted $\langle r_i \rangle$ of a grain i evolves according to two components. The first one accounts for the growth of subgrains :

$$\left(\frac{d\langle r_i \rangle}{dt} \right)^+ = M_{\mathrm{b}} \frac{2\gamma_{\mathrm{b}}}{\langle r_i \rangle}. \tag{1.42}$$

The second one accounts for the shrinkage of subgrains due to the stress applied onto dislocation structures. The subgrain shrinkage term is derived from the work of Raj et al. [81] and leads to :

$$\left(\frac{d\langle r_i \rangle}{dt} \right)^- = \left(\frac{d\langle r_i \rangle}{d\sigma_i} \right) \left(\frac{d\sigma_i}{d\varepsilon_i} \right) \left(\frac{d\varepsilon_i}{dt} \right) = -\frac{1}{2} K_{\mathrm{sub}} b \left(\frac{\mu}{\sigma_i^2} \right) \Phi_{\mathrm{II}} \left(1 - \frac{\sigma_i}{\sigma_{s,i}} \right) \dot{\varepsilon}_i, \tag{1.43}$$

where K_{sub} is a constant. Then for each time increment, grains have a part of their subgrains (i.e. those with a size larger than a critical radius r_{cr}) that transform into nuclei (i.e. into new grains).

Model of Beltran et al. [50]

The Model of Beltran et al. [50] is quite similar to the model of Bernard et al. [49]. The main improvement results in the fact that the model of Beltran is able to model multi-pass deformation routes (DRX + PDRX), therefore only the model of Beltran et al. is introduced below.

Description of the microstructure

The microstructure is represented by spherical grain classes characterized by an equivalent sphere radius R_i, a dislocation density ρ_i and a number of grains N_i. Contrary to the models of Montheillet et al. [48] and Cram & Zurob [70] previously introduced, this model considers two different HEM composed of RX and NR grain classes, respectively, in order to obtain more physical results (Fig. 1.11).

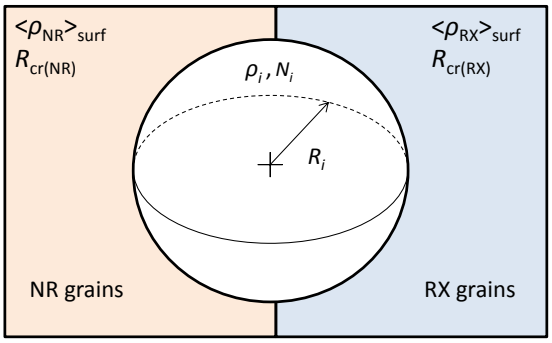

Fig. 1.11. *A grain class immersed into two HEM, respectively composed of NR and RX grain classes, as considered in the model of Beltran.*

Strain hardening and recovery

The law used in Beltran's model to describe the dislocation density evolution (i.e. strain hardening and dynamic recovery) in each grain class during deformation is the YLJ law [76] :

$$\frac{d\rho_i}{d\varepsilon} = K_1 - K_2\rho_i, \tag{1.44}$$

where K_1 and K_2 are two parameters accounting for strain hardening and dynamic recovery. Right after deformation while the material is still at high temperature (i.e. PDRX regime), static recovery occurs in the microstructure. Static recovery is modeled by the following relationship :

$$\frac{d\rho_i}{dt} = -K_s\rho_i, \tag{1.45}$$

where K_s is a static recovery parameter. When a grain boundary migrates, the swept volume is almost free of dislocations, reducing the stored energy per unit volume in the growing grain. This consideration, omitted in most of mean field models, is taken into account in Beltran's model using the Eq. 1.46. The latter aims to decrease the dislocation density in a grain class when its size increases using the following relationship :

$$\frac{\Delta\rho_i}{\rho_i} = -\frac{\Delta V_i}{V_i}. \tag{1.46}$$

The individual flow stress in any grain of the i^{th} class is calculated at any instant using the Taylor's equation :

$$\sigma_i = \sigma_0 + M_T \alpha \mu \sqrt{\rho_i}, \tag{1.47}$$

where σ_0 denotes the yield stress, α is a constant, μ is the shear modulus and M_T is the Taylor factor. The macroscopic flow stress is deduced from individual grain stresses by a volume weighted average :

$$\sigma = \frac{\sum \sigma_i V_i N_i}{\sum V_i N_i}. \tag{1.48}$$

Grain boundary migration

Contrary to the previous models of Montheillet et al. [48] and Cram & Zurob [70], a capillarity term is considered in grain boundary migration equations of this model. Furthermore, since two different HEM made of RX and NR grain classes are considered, two equations are used for boundary migration. The first one, defined by Eq. 1.49, represents the interaction between any grain class and the HEM composed of RX grain classes. In the same manner, the second one, defined by Eq. 1.50, represents the interaction between any grain class and the HEM composed of NR grain classes.

$$\frac{dR_{i/\mathrm{RX}}}{dt} = M_b \Delta E_i^{\mathrm{RX}} = M_b(\tau(\langle\rho_{\mathrm{RX}}\rangle_{\mathrm{surf}} - \rho_i) + \gamma_b\left(\frac{1}{R_{\mathrm{cr(RX)}}} - \frac{1}{R_i}\right)), \tag{1.49}$$

$$\frac{dR_{i/\mathrm{NR}}}{dt} = M_b \Delta E_i^{\mathrm{NR}} = M_b(\tau(\langle\rho_{\mathrm{NR}}\rangle_{\mathrm{surf}} - \rho_i) + \gamma_b\left(\frac{1}{R_{\mathrm{cr(NR)}}} - \frac{1}{R_i}\right)), \tag{1.50}$$

where $R_{\mathrm{cr(RX)}}$ and $R_{\mathrm{cr(NR)}}$ are respectively defined by $\langle R_{\mathrm{RX}}^2\rangle/\langle R_{\mathrm{RX}}\rangle$ and $\langle R_{\mathrm{NR}}^2\rangle/\langle R_{\mathrm{NR}}\rangle$ in order to ensure volume conservation.

Each grain class has a surface fraction in contact with the two different HEM. Thus the quantities γ_{NR} and γ_{RX}, presented on Fig. 1.12, are used to describe the surface fraction of NR and RX grain classes in contact with the HEM composed of RX and NR grain classes, respectively.

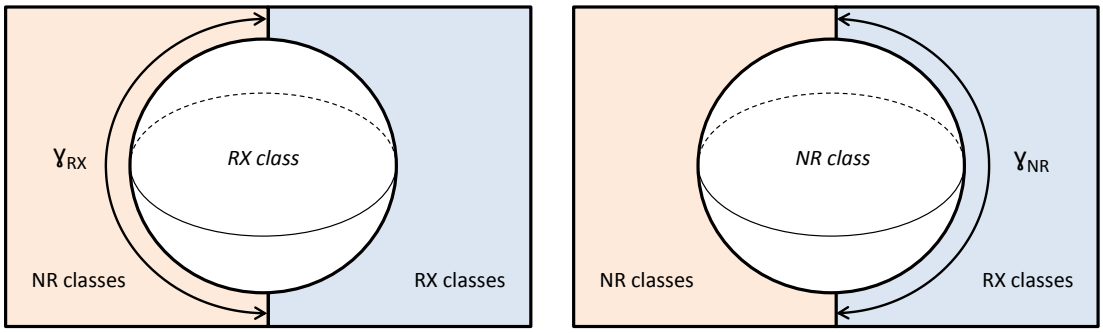

Fig. 1.12. *Representation of surface fractions between grain classes and HEM in the model of Beltran.*

Therefore the total volume variation of a i^{th} NR grain class noted $(\Delta V_{i,\mathrm{NR}})$ or a i^{th} RX grain class noted $(\Delta V_{i,\mathrm{RX}})$ is expressed as follows :

$$\Delta V_{i,\mathrm{NR}} = \left(\frac{dR_{i/\mathrm{RX}}}{dt} \gamma_{\mathrm{RX}} + \frac{dR_{i/\mathrm{NR}}}{dt} (1 - \gamma_{\mathrm{RX}}) \right) S_i \Delta \mathrm{t}, \tag{1.51}$$

$$\Delta V_{i,\mathrm{RX}} = \left(\frac{dR_{i/\mathrm{NR}}}{dt} \gamma_{\mathrm{NR}} + \frac{dR_{i/\mathrm{RX}}}{dt} (1 - \gamma_{\mathrm{NR}}) \right) S_i \Delta \mathrm{t}. \tag{1.52}$$

A major drawback of this model is the calculation of γ_{NR} and γ_{RX} that is not straightforward. By applying volume conservation equations, a relation between γ_{NR} and γ_{RX} can be found as seen in Eq. 1.53 :

$$\gamma_{\mathrm{RX}} = \frac{-\gamma_{\mathrm{NR}} (\sum_{\mathrm{NR}} N_j S_j \Delta E_j^{\mathrm{RX}} - \sum_{\mathrm{NR}} N_j S_j \Delta E_j^{\mathrm{NR}}) - (\sum_{\mathrm{NR}} N_j S_j \Delta E_j^{\mathrm{NR}} - \sum_{\mathrm{RX}} N_i S_i \Delta E_i^{\mathrm{RX}})}{(\sum_{\mathrm{RX}} N_i S_i \Delta E_i^{\mathrm{NR}} - \sum_{\mathrm{RX}} N_i S_i \Delta E_i^{\mathrm{RX}})}. \tag{1.53}$$

For the determination of these two fractions during the simulation, a first value of γ_{NR} or γ_{RX} is estimated using the RX fraction and the second term is deduced from the first using Eq. 1.53.

Nucleation

In the same manner as the model of Cram & Zurob [70], nucleation is modeled here by the SIBM mechanism introduced in section 1.1.6., similarly to the model of Cram & Zurob [70]. This mechanism postulates a necklace nucleation. In the considered model, these nucleation regions are defined by the grain boundaries of classes having a dislocation density higher than a critical dislocation density noted ρ_{cr}. The computation of ρ_{cr} is done following this method: a first estimation is done according to Eq. 1.54

(see [43]) and an iterative solution is found according to Eq. 1.55 (see [50]):

$$\rho_{\mathrm{cr}} = \left(\frac{20 K_1 \gamma_{\mathrm{b}} \dot{\varepsilon}}{3 K_3 \tau} \right)^{1/3}, \tag{1.54}$$

$$\rho_{\mathrm{cr}} = \left[\frac{-2\gamma_{\mathrm{b}} \dot{\varepsilon} \dfrac{K_2}{K_3 \tau}}{\ln\left(1 - \dfrac{K_2}{K_1}\rho_{\mathrm{cr}}\right)} \right]^{1/2}. \tag{1.55}$$

Since nuclei mainly appear at grain boundaries, the nucleation rate in each grain class i is assumed to be proportional to the total grain boundary surface of all grain classes having $\rho_i \geq \rho_{cr}$ multiplied by a nucleation parameter K_{g}. Furthermore, the nucleation rate in each i^{th} grain class is weighted by its number of grains as well as its size and its dislocation density, leading to the final relationship :

$$\frac{dN_i}{dt} = K_{\mathrm{g}} S_{\mathrm{cr}} \frac{N_i r_i^q (\rho_i - \rho_{\mathrm{cr}})^m}{\sum_{\rho_k \geq \rho_{\mathrm{cr}}} N_k r_k^q (\rho_k - \rho_{\mathrm{cr}})^m}, \tag{1.56}$$

where q is a constant equal to 2 for necklace nucleation and 3 for bulk nucleation, m is a constant close to 3 and $\mathrm{S_{cr}}$ is the total surface of grains having $\rho_i > \rho_{\mathrm{cr}}$.

The SIBM mechanism also postulates that a subgrain must have a critical radius to become viable as a nucleus. This condition, known as the Bailey-Hirsch criterion introduced in section 1.1.6, is calculated as following in this model :

$$r_{\mathrm{cr}} = \frac{2\gamma_{\mathrm{b}}}{\rho_{\mathrm{cr}} \tau}. \tag{1.57}$$

After hot deformation, within the PDRX regime, nucleation can still occur due to rearrangement of dislocations. However in this model, it is assumed that all nuclei appeared during hot deformation and therefore only static recovery and boundary migration are modeled during PDRX. In spite of many assumptions, this model showed good results in terms of mean quantities such as RX fraction and mean grain size [50].

Model of Smagghe [71]

All models presented above have the same drawback inherent to the implicit microstructure description, to not consider topology. Recently, Smagghe [71] developed in his PhD work a semi-topological approach for the mean field modeling of DRX and PDRX published in [82]. The motivations for developing this new model was the fact that even if mean quantities can be correctly described by the pre-existing mean field models, predicted grain size distributions were generally unrealistic. Comparisons between experimental grain size distributions and grain size distributions predicted by the model of Montheillet et al. [48] are introduced in [82] and illustrated on Fig 1.13. Distributions

were obtained after one hot torsion test on a 304L steel at a strain rate of $0.01s^{-1}$ and a temperature of 1323K.

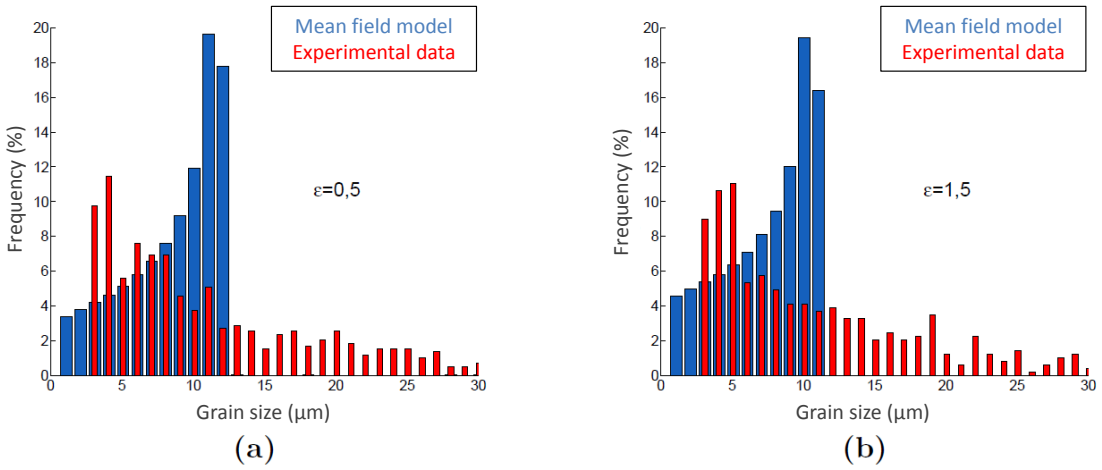

Fig. 1.13. *A comparison between experimental grain size distributions and grain size distributions predicted by the model of Montheillet et al. [48] at two different strain levels (a) $\varepsilon = 0.5$, (b) $\varepsilon = 1.5$, and for a temperature of 1323K and a strain rate of $0.01s^{-1}$ [82].*

It is clearly seen that grain size distributions predicted by the mean field model of Montheillet et al. [48] are far from experimental distributions. The numerical distributions tend to a vertical asymptote with a maximal grain size, whereas a high number of large grains are still observed in experimental distributions. Piot et al. [83] already discussed this kind of limitation in mean field modeling of DRX and showed that this issue of distributions is directly related to the grain boundary migration equation (Eq. 1.33) and the consideration of the same HEM for each grain. During the steady-state regime, the mean dislocation density $\langle\rho\rangle$ is constant. Thus, according to Eq. 1.33, the softest grains rapidly grow until their dislocation density reaches the mean value $\langle\rho\rangle$. Then, these grains continue to hardened and their dislocation density becomes higher than $\langle\rho\rangle$, leading to a shrinkage of these grains. However, the time spent by the grains when they had a dislocation density close to the mean dislocation density $\langle\rho\rangle$ is much higher than the time spent when they had a low dislocation density. Therefore, they spent a long time with the maximal grain size, which leads to the typical distributions on Fig. 1.13 with more and more high peak when grain size increases and a vertical asymptote. Smagghe [71] recently tackled this issue in his PhD work by making each grain evolves with a random-selected grain as neighbor. It is worth noticing that his new model considerably leads to a best prediction of grain size distributions during DRX.

Description of the microstructure

As in the model of Montheillet et al. [48], each grain is defined in Smagghe's model by its equivalent sphere radius R_i and mean dislocation density ρ_i. However, the main

difference between this model and other mean field models lies in the omission of the HEM. In the mean field models previously introduced, each grain is immersed into a HEM composed of all the grains in the microstructure [48, 70] or two HEM composed of RX and NR grains, respectively [49,50]. In his mean field model, Smagghe proposed to make each grain evolves with a unique randomly-selected grain as neighbor in order to include a stochastic effect in the model, as presented on Fig. 1.14.

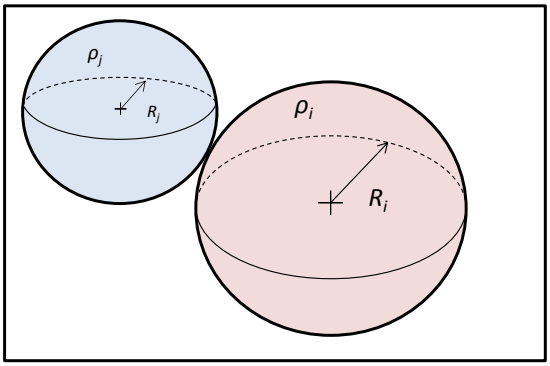

Fig. 1.14. *Principle of the semi-topological approach considered in the model of Smagghe: each grain evolves with a unique randomly-selected grain as neighbor.*

At the first stage of the simulation, a neighborhood (i.e. one neighbor) is chosen for each grain, and this connection is maintained until one of the two grains disappears. However, this connection is not reciprocal, meaning that if a grain i has the grain j as neighbor, the grain j has not necessarily the grain i as neighbor. Furthermore, each grain has only one neighbor but can be chosen as neighbor of several grains.

Grain boundary migration

The boundary migration between one grain i and its neighbor j is considered to be driven only by the difference of stored energy between these two grains, and the capillarity effects are neglected as in the models of Montheillet et al. [48] and Cram & Zurob [70], leading to :

$$\frac{dR_i}{dt} = M_\mathrm{b}\tau(\rho_j - \rho_i), \tag{1.58}$$

with M_b the grain boundary mobility, τ the energy per unit dislocation line, ρ_i the dislocation density of the grain i and ρ_j the dislocation density of the neighbor grain j. Volume conservation is not necessarily fulfilled with this new configuration, therefore the volume variation of the grain i is automatically transferred to the grain j for the sake of volume conservation.

Right after deformation, within the PDRX regime, boundary migration still occurs. The latter is then described using a modified Eq. 1.58 accounting for capillarity effects :

$$\frac{dR_i}{dt} = M_\mathrm{b}\left[\tau(\rho_j - \rho_i) + \gamma_\mathrm{b}\left(\frac{1}{R_j} - \frac{1}{R_i}\right)\right], \tag{1.59}$$

were γ_b is the grain boundary energy.

Strain hardening and recovery

In the considered model, a power law (PW) close to that proposed by Montheillet et al. [48] is used to describe strain hardening and dynamic recovery during deformation :

$$\frac{d\rho_i}{d\varepsilon} = \frac{H^{\nu+1}}{\rho_i^{\nu}}, \tag{1.60}$$

with H a parameter accounting for both strain hardening and dynamic recovery, and ν is a constant. The macroscopic flow stress is calculated at any instant by the following relationship derived from the Taylor's equation :

$$\sigma = \alpha\mu b\frac{\sum(\sqrt{\rho_i}R_i^3)}{\sum R_i^3}, \tag{1.61}$$

where α is a constant, μ is the shear modulus and b is the Burgers vector magnitude.

Static recovery occurring in the PDRX regime is modeled using the following relationship :

$$\frac{d\rho_i}{dt} = r_s(\rho_s - \rho_i), \tag{1.62}$$

where r_s is a recovery parameter and ρ_s is a threshold density. This equation only applies to grains with a mean dislocation density higher than ρ_s.

Nucleation

The nucleation mechanism is modeled here using the same nucleation law as used in the model of Montheillet et al. [48] (Eq. 1.35). Some rules are imposed concerning the choice of neighbors for nuclei. For instance when a nucleus appears in the microstructure, this latter can only have a neighbor which is not a nucleus to ensure that the difference in dislocation density between the nucleus and its neighbor is high enough to promote its growth. Additional rules, presented in [71], are used to integrate more quickly the nucleus into the neighborhood system.

In the same manner as in the model of Beltran et al. [50], all nuclei are assumed to appear dynamically and no nucleation is assumed to occur after deformation. Therefore, the PDRX regime is only described in this model by boundary migration using Eq. 1.59 and static recovery using Eq. 1.62.

Conclusions on mean field models

Several mean field models showed good ability to predict microstructure quantities such as mean grain size and RX fraction during and after hot deformation, or even during multi-pass deformation routes. In addition to their low numerical cost, these kinds of

model have no numerical limitations in terms of maximal strain level that can be modeled, which makes them widely used to model industrial processes at high strain levels ($\varepsilon > 2$). However these models still have some drawbacks. First, the grain morphology is not considered, which can have an effect on the effective grain boundary surface and therefore on the nucleation rate predicted by the model. Furthermore, although grain size distributions are obtained with these models, comparisons with experimental data showed poor predictions of these distributions [84]. This limitation is due to the fact that all grains are immersed into the same HEM and boundary migration equation imposes the same evolution for each grain. A first step in the improvement of predicted grain size distributions was recently made with the PhD work of Smagghe [71] by making each grain evolves with a particular random-selected grain as neighbor. However, this consideration of particular neighborhood for each grain can still be improved. Both improvements (grain shape evolution and a particular neighborhood for each grain) will be implemented into a new mean field model proposed in this PhD work and presented in chapter 4.

1.2.3 Full field models

Stochastic approaches

Stochastic approaches were introduced long time ago, by Potts in 1952 [85]. This kind of approach is still widely used for modeling microstructure evolutions. In stochastic approaches can be found MC and CA approaches. These approaches are based on an explicit microstructure representation considering a regular grid of lattice sites (i.e. cells).

Monte Carlo

The first metallurgical models based on the MC method were proposed in the 1980's by Anderson and co-workers for modeling GG [86], grain size distribution and topology [87], influence of particle dispersions [88], anisotropic grain boundary energies [89] as well as abnormal GG [90]. Few years later, several models based on the MC approach were also developed for SRX [91, 92], leading to a major improvement in terms of microstructure evolution modeling.

In the MC approach, a grid is composed of a number N of lattice sites, and each site is characterized by an orientation number O_i as well as microstructure variables such as stored energy. Therefore, a grain i is defined by all sites having the identifier O_i and the frontier between two sites of different identifiers is the grain boundary (Fig. 1.15).

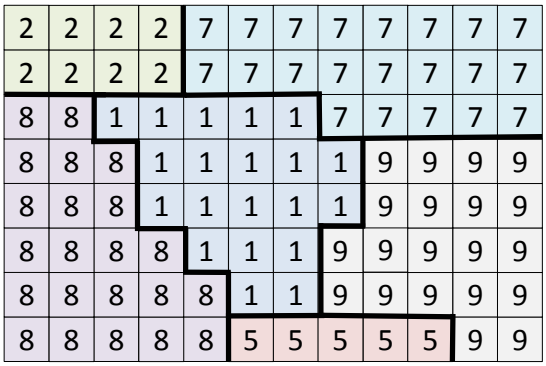

Fig. 1.15. *Representation of the microstructure with a regular grid of lattice sites as used in MC and CA approaches. Six grains are depicted, composed of square sites having the same index and grain boundaries are plotted as bold line.*

The MC algorithm for boundary migration is composed of MC steps. Furthermore, a MC step is composed of N lattice site change tests, N being the total number of sites composing the microstructure. A site change test is classically composed of four main steps : (i) random selection of a site, (ii) assignment of a new orientation number to this site, randomly selected among all the orientation numbers except the actual one, (iii) calculation of the energy variation ΔE_{tot} in the domain due to reorientation of the site, (iv) possible reorientation of the site validated with a probability p that depends on ΔE_{tot}.

In case of isotropic (i.e. constant in the microstructure) grain boundary energy assumption, the total energy E_{tot} of the MC domain is generally calculated following the relationship [93] :

$$E_{\text{tot}} = \frac{\gamma_{\text{b}}}{2} \sum_{i=1}^{N} \sum_{j=1}^{m} (1 - \delta_{ij}) + \sum_{i=1}^{N} E_i, \tag{1.63}$$

where γ_{b} is the boundary energy, m is the number of nearest neighbors of the site I_i, δ_{ij} is the Kronecker delta function and E_i is the stored energy in the site I_i, considered constant per grain. Furthermore, an example of a probabilistic law depending on ΔE_{tot} for lattice site reorientation is the following [94] :

$$p(\Delta E_{\text{tot}}) = \begin{cases} 1 & \text{if} \quad \Delta E_{\text{tot}} \leq 0, \\ \exp\left(-\dfrac{\Delta E_{\text{tot}}}{kT}\right) & \text{if} \quad \Delta E_{\text{tot}} \geq 0, \end{cases} \tag{1.64}$$

where k is the Boltzmann constant and T is a simulation temperature term introduced to manage the lattice site evolution kinetic in some particular cases. After testing N site changes, a MC step is reached and a new increment starts. Even though N site changes are done for N sites, because of the random choices, the N changes do not affect all N sites.

A major advantage of using the MC method is the ability to easily parallelize calculations, which enables to model microstructure evolutions with a huge number of

grains and with relatively low computational costs. Furthermore, the MC framework is straightforward to implement since it is based on a simple grid of lattice sites coupled to analytical laws. Finally, the creation of nuclei during DRX can be easily implemented by simply adding a new orientation number at a given place where a criterion is validated. However, although this kind of model proved its efficiency, some drawbacks may still limit its use. First a major drawback of the MC approach is the difficulty to link MC increment to a physical time. Experimental or other computational methods are generally used to calibrate the "MC time" scale. Furthermore, the grain boundary curvature is not straightforward to calculate in MC models due to the consideration of regular lattice sites to model microstructure. Finally, due to the discrete nature of the MC method, the description of the domain deformation during DRX is a limitation and major assumptions, or even a total omission, are generally made with these regards.

To our knowledge, only few models of DRX based on the MC method were proposed in the literature. The first ones were proposed by Rollet in 1992 [93] and Peczak in 1995 [95] but the deformation of the domain is omitted in these models. More recently in 2010, Li et al. [96] proposed a model based on the MC method for the prediction of DRX in solder interconnections. This model is coupled to a finite element (FE) algorithm for modeling of stress and strain fields. However, none information were given concerning the grid deformation and many assumptions were probably made on this topic.

Cellular automata

The CA method was first introduced by von Neumann in 1963 [97] for the simulation of self-reproducing Turing automata and population evolution. This approach was then extended to another scientific field in 1986 by Wolfram [98]. It became a major approach for modeling microstructure evolutions in terms of phase transformation [99], dendrite growth during solidification [100] as well as recrystallization [101].

Like the MC approach, the CA approach consists in partitioning the microstructure into a regular grid of lattice sites as presented on Fig. 1.15, each lattice site being characterized by internal variables (crystalline orientation, dislocation density etc.). Although CA models can be formulated as either stochastic or deterministic, most of CA models for recrystallization are stochastic and use cell state switches as introduced in [54, 56] to model grain boundary kinetics in a physical time scale. In stochastic CA models, the computation of boundary kinetics is mainly composed of four main steps: (i) random selection of a lattice site, (ii) consideration of a local neighborhood [102], (iii) a switching rule is defined as a function of the state of the considered site prior to switch and the states of the neighboring sites, (iv) updating of state variables through the local switching rule.

The switching rule, used in stochastic CA models, consists in estimating a probability

P for the reorientation of a lattice site :

$$P = \frac{v}{v_{\max}}, \tag{1.65}$$

where v is the velocity in the considered lattice site and $v_{\max}$ is the maximum velocity in all the domain. Then the probability P is compared to a random number between 0 and 1. If this random number is inferior to P, the site adopts the orientation number of the growing adjacent grain, otherwise it remains unchanged. The updated state of all sites is calculated as a discrete solution but no change is made until the switching rule was applied to all sites. Then, all the sites are updated simultaneously to avoid multiple sites covering.

A major advantage of the CA over MC approach is the consideration of an explicit velocity which defines the propagation rate between two lattice sites. Furthermore, the CA algorithm is able to capture local effects and shows a good efficiency for parallelling since only a small amount of data has to be passed between sites [103]. However, similarly to the MC method, a major limitation of this approach is the estimation of the grain curvature that is not straightforward since the grain boundary is composed of square sites. A formulation was proposed by Kremeyer in 1998 to estimate a curvature by use of kink-template [104] and was applied in several CA studies [57, 103, 105]. Furthermore, the problem of domain deformation mentioned above in the description of the MC method is also a limitation in CA models and most of models are based on many assumptions when dealing with the CA space deformation issue [106].

A large number of DRX models based on a coupling between the CA method to model microstructure and phenomenological laws to model recrystallization mechanisms were proposed in the last decades. The first one was proposed in 2001 by Ding and Guo [107] where CA method is used to model 2D microstructure and phenomenological laws are used to model strain hardening, dynamic recovery and nucleation. The CA space deformation is not modeled in this paper, which allows to reach high strain levels. In 2010, Hallberg et al. [105] proposed a 2D stochastic CA model for modeling of DRX in pure Cu. Strain hardening and dynamic recovery are modeled using phenomenological laws while nucleation is modeled using a probabilistic law depending on the local dislocation density and the maximal dislocation density in the microstructure. Furthermore, even if CA space deformation is not directly considered in this model, a post-processing step is performed on results to observe grain elongations. In 2014 [108], Hallberg extended its model to 3D modeling of DRX occurring in particle-containing Cu. These models showed a good correlation with experimental data in terms of macroscopic flow stress and mean grain size. In 2014 [109], Sitko developed a deterministic CA model coupled to a probabilistic nucleation law for 2D modeling of DRX with validation on a deformed copper. In this model, the CA space deformation is modeled by an elongation of the domain along the selected axis. However, this technique transforms square sites into rectangle ones, affecting proper interactions with other neighboring CA sites and leading to non-physical elongated grains. All previously cited models lead to a good description of experimental data. However, they are all based on phenomenological laws

for dislocation density evolutions, meaning that the texture evolution cannot be predicted. The crystal plasticity FE method (CPFEM) became a major tool for modeling dislocation density evolutions inside grains. However, computational costs are prohibited when using this kind of model, which generally limits the maximal true strain that can be reached. In 2013, Chuan et al. [110] proposed to couple a stochastic CA model with CPFEM for 2D modeling of DRX in a near-α titanium alloy and results showed a good match with experimental data. In this model, a maximal true strain of 0.5 is reached. Furthermore the initial grain size distribution was generated by the CA model and was quite far from a real microstructure. Two years later, Popova et al. [111] also proposed a coupling between a stochastic CA model and CPFEM to model 2D DRX in hexagonal closed packed metals, particularly magnesium alloys, and the initial microstructure can be generated from EBSD data in order to lead to more convincing results. In this model, a maximal true strain of 0.35 is reached. Recently, Madej et al. [106] proposed a coupled CA model with FE method to model DRX in 2D. A major advantage of this model is to tackle the problem of domain deformation, leading to more physical results contrary to most of other CA models for DRX. A maximal true strain of 0.25 is reached in this model. All these CA models coupled to CPFEM were developed in 2D because of computational time limitations and algorithm complexity. However, real microstructure evolutions are three-dimensional and results obtained with simulations on 2D microstructures may not always be compared to 2D sections of real 3D microstructures. Recently in 2016 [101], Hongwei et al. proposed a coupling between a semi-stochastic CA model and CPFEM to model 3D DRX in titanium alloys. The maximal true strain reached in this model is 0.4.

Deterministic approaches

Other kinds of full field model are based on deterministic approaches. Those are more precise than stochastic approaches since they do not introduce probabilistic laws. However, they often lead to high computational costs when used with FE meshes since they involve the resolution of partial differential equations. In deterministic approaches can be found vertex, PF and LS approaches.

Vertex

The vertex method belongs to the front tracking approaches and was established at the end of the 1980's by several authors [112–114]. The basic idea of the vertex model is that the minimization of the free energy can be achieved exclusively by the motion of multiple junctions. Therefore in vertex models, the state of the microstructure is given by the position and velocity of real nodes, also called vertices, placed at multiple junctions. Boundary curvature was initially not considered in vertex models, but the method was then improved by considering additional nodes, called virtual nodes, placed along grain boundaries to be able to estimate the grain boundary curvature [113]. A schematic representation of a microstructure with real and virtual nodes is presented on Fig. 1.16.

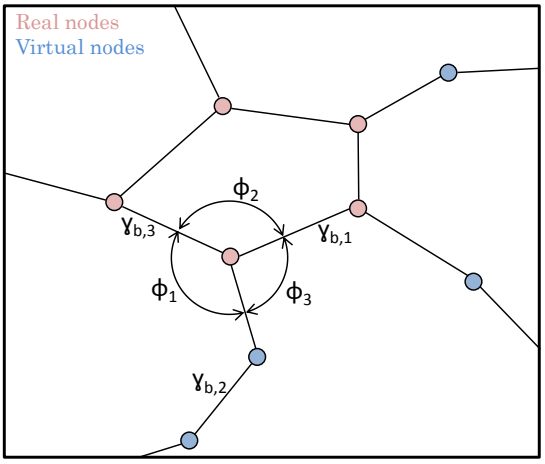

Fig. 1.16. *Explicit representation of grain boundaries as used in the vertex approach. The network is defined by real nodes on multiple junctions and virtual nodes on grain boundaries.*

The principle of vertex models for modeling GG is the following: let's denote the position $\vec{r}$ and velocity $\vec{v}$ of a grain boundary. A potential term noted $E(\vec{r})$ represents the total surface energy and a dissipative term noted $R(\vec{r},\vec{v})$ represents the energy dissipation due to the movement of grain boundaries. These terms are given by :

$$E(\vec{r}) = \int \gamma_{\mathrm{b}}(p)dp, \tag{1.66}$$

$$R(\vec{r},\vec{v}) = \frac{1}{2}\int \frac{v(p)^2}{M_{\mathrm{b}}(p)}dp, \tag{1.67}$$

where p represents the curvilinear coordinates of the grain boundary and $\gamma_{\mathrm{b}}(p)$, $v(p)$, $M_{\mathrm{b}}(p)$ are the surface energy, normal velocity and mobility of the grain boundary at the position p, respectively. The positions and velocities of all nodes are noted $\{\vec{r}_{\mathrm{n}}\}$ and $\{\vec{v}_{\mathrm{n}}\}$, respectively. Therefore the equations for the motion of the nodes are of dissipative character and can be derived from the Lagrange equation :

$$\frac{\partial R(\{\vec{r}_{\mathrm{n}}\},\{\vec{v}_{\mathrm{n}}\})}{\partial \vec{v}_i} + \frac{\partial E(\{\vec{r}_{\mathrm{n}}\})}{\partial \vec{r}_i} = 0. \tag{1.68}$$

Solving this system during a time increment dt leads to new positions of nodes given by :

$$\vec{r}(t+dt) = \vec{r}(t) + \vec{v}_i(t)dt. \tag{1.69}$$

In general, a benefit of vertex models, when compared to others, is the low memory requirement for the implementation. However, a major drawback of vertex models, as compared to MC or CA models, is the need to take all possible topology changes of a microstructure into account. Therefore, a set of topological rules has to be incorporated into the model. Typical topological changes used in a recent 2D vertex model [115] are presented on Fig. 1.17. Lazar et al. [116] recently proposed an overview of topological

operations that need to be handled in a 3D vertex model. A major drawback of these topological rules is the required computational resources which can be high, especially in 3D cases. Furthermore these rules are often based on criteria that have no physical meaning. For instance, if a grain is growing but its size is below a critical size, the topological rule can remove it without any reversibility.

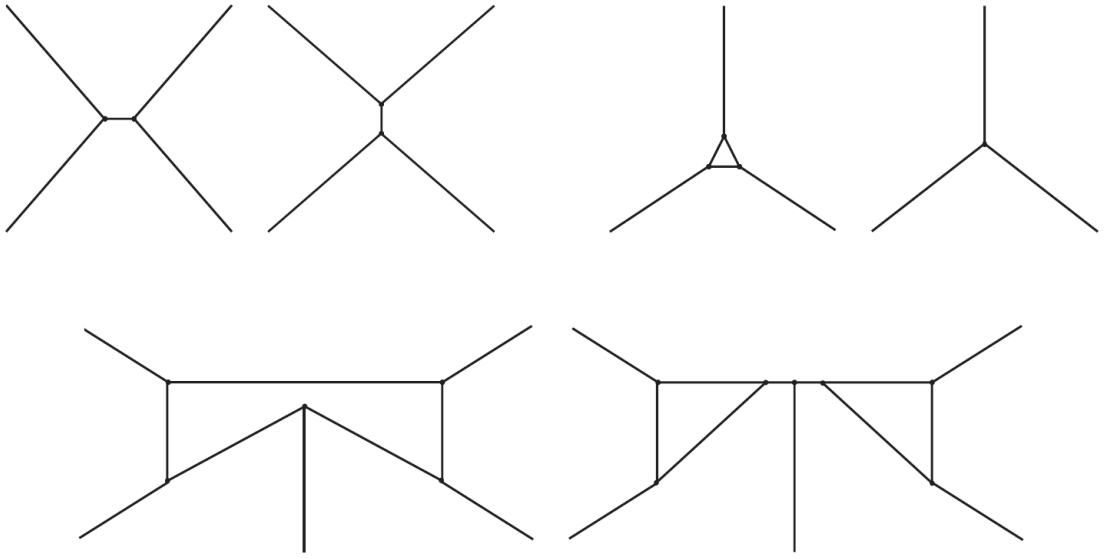

Fig. 1.17. *Some topological operations that need to be taken into account in 2D vertex models [115].*

Vertex models of DRX are not numerous in the literature and most of them only concern GG mechanism. This is due to the modeling of nucleation that is a big issue in vertex models due to topological events and the presence of nodes only at multiple junctions. However in 2008, Piękoś et al. [117] extended for the first time vertex models in order to take the effect of stored energy and nucleation into account. In 2015, a vertex model for DRX was proposed by Mellbin et al. [53]. This model was developed in 2D and to our knowledge, there is currently no vertex model able to model DRX in 3D. In this model, grain boundary migration is driven by Eqs. 1.66, 1.67 and 1.68 introduced previously and an additional term is considered in the potential term to account for stored energy. The vertex model is coupled to a crystal plasticity algorithm in order to model strain hardening and recovery. Furthermore, nucleation is assumed to occur only at multiple junctions where the stored energy in any of the surrounding grains is higher than a threshold energy. The creation of a new grain is possible thanks to the topological change presented on Fig. 1.18.

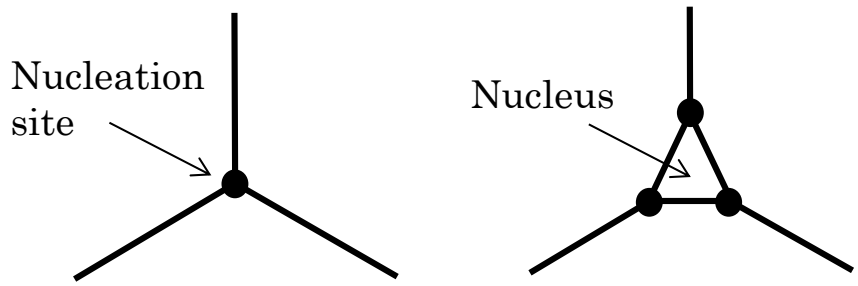

Fig. 1.18. *Creation of a nucleus as considered in a vertex model of DRX [53].*

The same model was applied in another work [115] for studying texture evolution during hot rolling of copper. In 2017 [118], this model was still improved to account for the Smith-Zener pinning effect due to the presence of second phase particles. Second phase particles are modeled by adding additional vertices in the microstructure, which means that their size cannot be controlled, nor evolve. Finally, this last model also uses virtual nodes on grain boundaries to have a more explicit description of grain boundary curvature.

Contrary to previously cited CA-CPFEM models, the crystal plasticity-vertex models do not require mesh in simulations and consequently are a memory efficient method. Furthermore, paralleling is quite easy to implement with this method, which explains why DRX simulations were performed up to a true strain of 1.25 in [53]. Although high strain levels can be achieved with this kind of model, many improvements are still required to perform 3D simulations. Furthermore, since nodes only exist on grain boundaries, many information, such as dislocation density fields, crystalline orientation fields, or any other intragranular heterogeneity cannot be tackled.

Phase-Field

The PF method was first devoted to the modeling of dendrite formation [119,120], where different phases, for instance solid/liquid have to be considered. Then, the PF approach was applied to various problems in materials science, such as recrystallization and GG. Recrystallization PF models are based on continuous functions of spatial coordinates and time, called PF variables, representing the grains of the microstructure. Each grain is described by a PF variable equal to 1 in the grain and 0 elsewhere (see Fig. 1.19(a)). However, the transition from 0 to 1 leads to sharp gradients at boundaries resulting in discontinuities and poorly conditioned problems. To obtain a continuous transition of the PF variable at grain boundaries, the PF variable is generally smoothed at the grain boundary as seen on Fig. 1.19(b): this concept is called *diffuse interface* [121] .

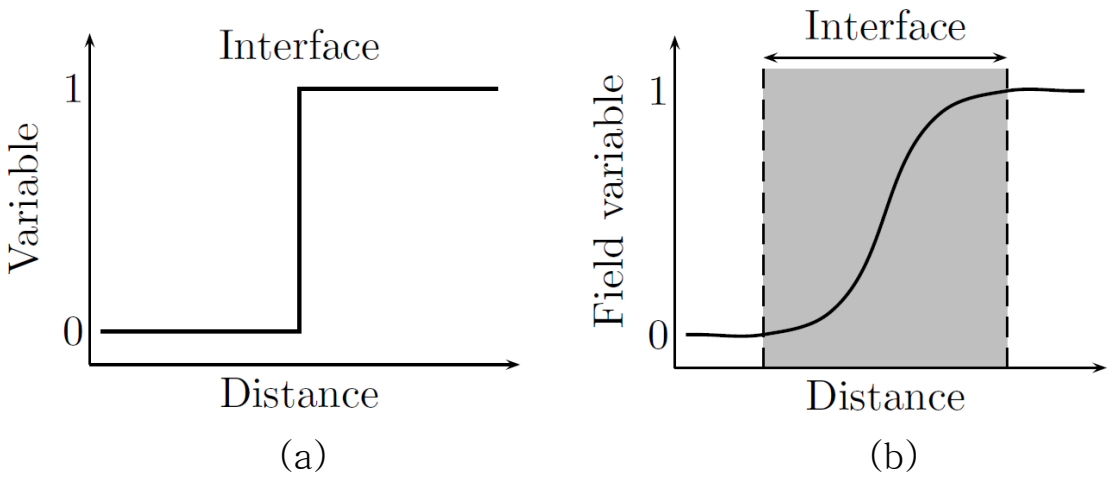

Fig. 1.19. *(a) Sharp and (b) diffuse interface descriptions related to the PF approach.*

Two different kinds of PF approach exist in the literature: the first one, referred to the continuum-field (CF) model, was proposed by Chen et al. [122] and Fan et al. [123]. The second one, referred to the Multi-Phase-Field (MPF) model, was proposed by Steinbach et al. [124] and Garcke et al. [125]. In both models, grain orientations are described using several PF variables. The major difference between CF and MPF models is due to the fact that in CF models, the PF variables are treated independently and can have any value at the diffuse interface without any restrictions. In MPF models, PF variables represent volume fractions, thus the sum of all PF variables at a given place of the microstructure must verify the unity. However, a common point exists between all PF models: they all employ a functional to describe the free energy of the system and PF variables evolve in order to minimize this functional. The functional F is given by a volumic integral of the local free-energy density.

Several PF models were proposed for recrystallization in the literature. In 2013, Moelans et al. [126] extended the initial GG model of Chen et al. [122] to account for the grain stored energy, which consists in adding an additional term in the functional. Furthermore, authors used two additional parameters η_{rex} and η_{def} to separate RX and NR grains. This PF model was used for 2D modeling of SRX. Then in 2008, Takaki et al. [127] proposed a MPF model for DRX in 2D where strain hardening and dynamic recovery are modeled by phenomenological laws. One year later, Takaki et al. [128] improved their model to improve the consideration of polycrystal deformation. In 2014, Takaki et al. [129], further extended his model by considering an elasto-plastic FE method to take non-uniform deformation fields into account, although the dislocation density is still averaged in each grain and evolves with a phenomenological law. Since PF models generally consider regular grids, it is common to use fast Fourier transform (FFT) based algorithms for a high efficiency. Therefore in 2015, Chen et al. [130] proposed a DRX model where a FFT-based crystal plasticity algorithm is used for modeling strain hardening and dynamic recovery. Using this model, a maximal von Mises strain of 0.1 was reached. In 2016, Zhao et al. [131] also used the PF method to model the 3D

microstructure and a FFT based elasto-viscoplastic algorithm to model strain hardening and dynamic recovery. In this work, a maximal true strain of 0.5 was reached.

PF models coupled to FFT methods generally reach only low strain levels, which can be explained by the fact that FFT methods impose working with regular grids. In the model of Zhao et al. [131], simulations up to a maximal true strain of 0.5 were performed but in this model, the domain is only "virtually" deformed, which leads to non physically based results.

Level-set method

The Level-Set method is the approach considered at CEMEF for modeling of microstructure evolutions and is also the approach considered in this PhD work. This latter is introduced and described in details in the next chapter.

Only few DRX models are based on the LS method. To our knowledge, the first LS based DRX model was proposed in 2013 by Hallberg [132]. This 2D model of DRX uses the LS approach for the representation of the microstructure and the modeling of boundary migration, and it considers phenomenological laws to model strain hardening, dynamic recovery and nucleation. Simulation results were in good agreement with experimental data in terms of macroscopic flow stress even if no comparisons were made about grain size distributions and recrystallization kinetics.

Conclusion of full field models

Quite a large number of full field models for DRX and PDRX were already proposed in literature. These models are based on different methods such as Monte Carlo, Cellular Automata, Phase-Field, Vertex and Level-Set methods, which all have their advantages and their drawbacks. Some methods, such as Monte Carlo and Cellular Automata, are based on the consideration of regular grids, leading to relatively low computational costs but also leading to many limitations when aiming to model large strains. Vertex method is also a very efficient method for modeling of microstructure evolutions. However, topological transformations (e.g. appearance and disappearance of grains) are not straightforward to implement, in particular in 3D. Finally other methods such as Phase-Field and Level-Set are quite complicated to implement and generally lead to high computational costs due to the use of solvers for the resolution. However, since grain boundaries are implicitly described with these methods, complex geometries can be modeled. Furthermore, these methods are able to reach large strains when coupling with an efficient meshing/remeshing tool. In order to model strain hardening and dynamic recovery during deformation, full field models are generally coupled either to phenomenological laws or to a crystal plasticity formulation. The first possibility enables to predict mean dislocation densities at high level of strains in a relatively short time. The second possibility can be computationally expensive in the case of a FE formulation. Furthermore it requires a good quality of mesh or grid all along the simu-

lation, which can still limit the maximal level of strain that can be reached. In practice, the maximal strain level reached with models using a crystal plasticity formulation is generally below 0.5, which is much lower than the typical strain applied in classical industrial forming processes.

Summary

DRX and PDRX occurring during and after hot deformation, respectively, play a primordial role as they control the final microstructure and therefore final properties of metal alloys. Those recrystallization phenomena result from the combination of several physical mechanisms. In single phase materials, those mechanisms are hardening, recovery, grain boundary migration and nucleation. All these mechanisms occur in parallel in the material, explaining why it is a challenge to be able to predict locally the microstructure evolutions.

Many kinds of model exist to describe microstructure evolutions due to DRX and PDRX. Phenomenological models, in particular those derived from the JMAK model, were proposed to describe recrystallization kinetics without a real understanding of the underlying physical mechanisms. Phenomenological models are still very used nowadays, in particular for coupling with a FE software since they can be used to predict mean quantities (RX fraction, mean grain size) over an entire forged part within a few minutes. On the other hand, full field models were developed to explicitly represent microstructure and physical mechanisms. Although these models are undoubtedly more accurate and richer than phenomenological laws, they require high computational resources and therefore cannot be easily coupled to a FE software. However, full field models keep being very attractive since they can provide a lot of information regarding for example the grain size distribution, the dislocation density distribution, the crystallographic texture and their evolution all along the simulation. As a compromise between phenomenological and full field models, mean field models were proposed in the last decades to model DRX and PDRX. They are based on an implicit description of the microstructure and include analytical laws for each individual physical mechanism occurring during and after deformation. However, mean field models are based on assumptions and basically do not account for grain topology, which indirectly leads to poor predictions of the grain size distributions.

In chapter 2, the formalism of Level-Set in a finite element framework considered in this PhD work for full field simulations is presented. This formalism enables to simulate all microstructure mechanisms in a single numerical framework. Furthermore, thanks to the large number of previous developments already made on this formalism, some 3D simulations of GG are performed and results are used to discuss predictions of two existing analytical GG models, in particular during the transient regime.

Chapter 2

The Level-Set method in a finite element framework for modeling of microstructure evolutions

Contents

2.1 Introduction to the Level-Set method for polycrystals 49

2.1.1 Generation and immersion of a virtual polycrystal within a finite element mesh 50

2.1.2 Grain boundary migration 54

2.2 Full field simulations of grain growth and improvements of two existing models in the state of the art 56

2.2.1 Introduction 56

2.2.2 Initial polycrystal and material parameters 57

2.2.3 Full field simulation results 58

2.2.4 Confrontation of full field simulation results with Hillert/Abbruzzese model 62

2.2.5 Confrontation of full field simulation results with Burke & Turnbull model 68

Résumé en français

Ce chapitre introduit le formalisme champ complet développé au CEMEF et utilisé lors de ma thèse pour la modélisation de la recristallisation. Ce formalisme est basé sur la méthode Level-Set dans un contexte éléments finis, permettant une description implicite des joints de grains. Cette description implicite permet d'immerger puis de suivre le mouvement de géométries complexes, ce qui est un avantage considérable dans le cas des évolutions microstructurales. La méthode Level-Set est donc tout d'abord présentée puis les équations modélisant la cinétique des joints de grains sont introduites. De plus, les différents outils développés au CEMEF ces dernières années afin d'accélérer les temps de calcul sont également introduits. Dans un second temps, ce formalisme est utilisé afin de modéliser la croissance de grains en trois dimensions. Plus particulièrement, l'impact de la distribution initiale de tailles de grains sur l'évolution de la microstructure durant le régime transtitoire est discuté. A partir de ces résultats champ complet, deux modèles analytiques de croissance de grains de la littérature sont améliorés afin de prendre en compte l'influence de la distribution initiale durant le régime transitoire.

In this chapter, the formalism for 3D full field modeling of microstructure evolutions, considered in this PhD work, is firstly presented. This formalism, based on the Level-Set method in a finite element framework, was established by Bernacki [52, 133] few years ago and is the result of a large number of previous studies as well as PhD work [77, 134–136]. Then, several full field simulations of grain growth were launched based on this formalism and results were used to discuss and improve two existing grain growth models in the state of the art during the transient regime.

2.1 Introduction to the Level-Set method for polycrystals

The LS method was introduced for the first time in 1988 [137] as a numerical tool to trace the spatial and temporal evolution of interfaces. Several authors extended this method to interfaces with multiple junctions [138, 139] and a framework for modeling the GG mechanism in metal alloys was proposed in [138]. Then, several authors used the Level-Set method in a finite element (LS-FE) framework for modeling of GG in 2D and 3D [52, 66, 103, 140–142]. This method was also extended to SRX by Scholtes et al. [143]. Recently, the Smith-Zener pinning mechanism was successfully modeled in 2D and 3D using the LS-FE approach [143, 144]. The LS method has many common points with the PF method, especially both methods avoid the difficulty of tracking interfaces.

The principle of the LS method for modeling of polycrystals is the following: each grain is, a priori, defined by a function ψ, called LS function. As a definition, a LS function ψ of a grain, defined over a domain ω, corresponds to the distance from any point of ω to the grain boundary. In other words, the grain boundary can be captured at any instant by the zero-isovalue of the function ψ. This leads to the following expression of the LS function ψ :

$$\begin{cases} \psi(x) = d(x,\Gamma), x \in \Omega, \\ \Gamma = \{x \in \Omega, \psi(x) = 0\}. \end{cases} \tag{2.1}$$

Furthermore, this distance is generally signed, meaning that the distance is generally taken as positive ($\psi > 0$) inside the grain and negative ($\psi < 0$) outside. As an illustration, the LS function ψ of a 2D schematic grain is given at three different points of space on Fig. 2.1.

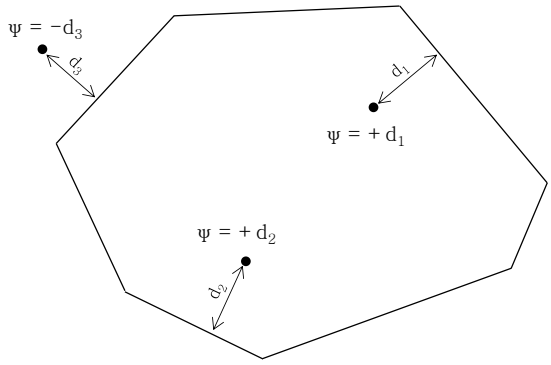

Fig. 2.1. *LS function ψ of a 2D schematic grain given at three different points of space.*

2.1.1 Generation and immersion of a virtual polycrystal within a finite element mesh

At early stage of full field simulations thanks to LS functions, a virtual polycrystal, representative of a real microstructure, can be generated and immersed into a FE mesh to constitute a Representative Volume Element (RVE). Several methods can be found in literature for the generation of polycrystals in a FE mesh. These methods are based either on experimental pictures or on more statistical methods. Recently, an interesting review on the generation of virtual microstructures for metal alloys was published by Madej [145].

Some authors have already immersed experimental pictures in a FE mesh thanks to an implicit description of grain boundaries using LS or PF functions. In [131], an experimental picture was interpolated on a homogeneous FE mesh and mesh was then refined close to grain boundaries. Then LS functions were initialized with a reinitialization procedure. More recently in the PhD work of Scholtes [135], a new approach was proposed based on developments of Shakoor et al. [146] for immersion of 2D and 3D polycrystals using LS functions. These methods are able to tackle efficiently the immersion of real polycrystals in a LS-FE framework. Of course it is also possible to immerse microstructures in a FE mesh thanks to a conform mesh strategy [147,148]. In this context, a surface mesh of the grain boundaries is generally first considered and the volume mesh is then generated inside grains based on surface meshes. This method has the particularity to generate a mesh coincident with grain boundaries, which is interesting when aiming to model polycrystal deformation. Furthermore, a very good description of grain boundaries is generally obtained with this method, even with relatively large mesh sizes. A major drawback of having a coincident mesh is the modeling of particular events such as grain disappearance as well as nucleation, which are not straightforward to take into considerations as already mentioned in vertex models.

Experimental data can be difficult to obtain, especially in 3D or when aiming to model a very large number of grains. Therefore in this PhD work, statistical methods are used for the generation of polycrystals in a FE mesh.

Statistical methods such as Voronoï and Laguerre-Voronoï methods are widely used to generate 2D and 3D virtual polycrystals in a FE mesh. In the same manner as with experimental data, two different mesh strategies (i.e. a conform or an implicit description of grain boundaries) can be considered. In this PhD work, an implicit description of grain boundaries using LS functions is considered since it enables to reach large level of polycrystal deformation without having to deal with topological events encountered when using a conform mesh.

The Voronoï tessellation method [133, 149–151] consists in generating a diagram composed of a set of N_{v} Voronoï nuclei (S_i). Then, a single Voronoï cell V_i per nucleus is defined following this rule: each Voronoï cell is composed of all points closer to S_i than to any other nuclei :

$$V_i = \left\{ X \in \mathbb{R}^d / d(x,S_i) = \min_{1<j<N_{\mathrm{v}}} d(x,S_j) \right\}, \tag{2.2}$$

with d the space dimension. Thus, the number of grains N_{g} in the generated polycrystal corresponds to the imposed number of Voronoï nuclei N_{v}. A 2D schematic Voronoï tessellation is represented on Fig. 2.2(a). A major drawback of the Voronoï method is related to the fact that even if it respects a given number of grains, it cannot respect a given grain size distribution. Thus, a second method called Laguerre-Voronoï exists [150–153]. This method consists in generating a diagram where the locations of the cell faces are constrained by a given non-intersecting spherical packing as illustrated in 2D on Fig. 2.2(b). Thus, the diagram is composed of N_{v} weighted seeds $(S_i;W_i)$. Then, a single Laguerre-Voronoï L_i is created per seed following this new rule: each Laguerre-Voronoï cell is composed of all points closer to S_i than to any other nuclei, via the power distance Π:

$$L_i = \left\{ X \in \mathbb{R}^d / \Pi(x,S_i) = \min_{1<j<N_{\mathrm{v}}} \Pi(x,S_j) \right\}, \tag{2.3}$$

where $\Pi(x,S_i) = d(x,S_i)^2 - W_i^2$. The cell weights can be determined thanks to the generation of a dense sphere packing with highest possible density which obeys the prescribed grain size distribution [151, 152]. The weight W_i of the i^{th} site is then related to the radius of the corresponding sphere. A review about dense packing can be found in [134, 151].

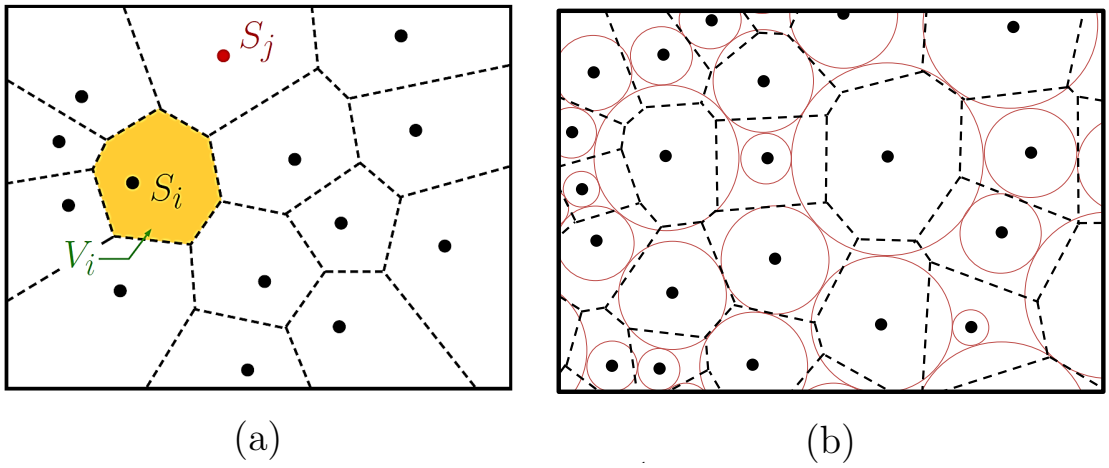

Fig. 2.2. *(a) A Voronoï and (b) Laguerre-Voronoï 2D tessellation.*

The Voronoï and Laguerre-Voronoï methods were the two methods used during this PjD work for the generation of polycrystals since they easily allow to immerse generated polycrystals in an unstructured FE mesh thanks to LS functions. Therefore, by considering, a priori, one LS function per Voronoï/Laguerre cell (i.e. per grain), the LS functions values are computed at every mesh node thanks to the relationship :

$$\psi_i(x) = \min_{j \in \text{Graph}(S_i)} (\alpha_{ij}(x)) \;\; \forall i \in \{1, ..., N_\text{v}\}. \tag{2.4}$$

In the Voronoï method, $(\alpha_{ij}(x))$ represents the signed distance between a point $X \in \Omega$ and the perpendicular bisector of $[S_i S_j]$:

$$\alpha_{ij}(x) = \frac{1}{2}||\overrightarrow{S_iS_j}|| - \frac{\overrightarrow{S_iS_j}.\overrightarrow{S_iX}}{||\overrightarrow{S_iS_j}||}. \tag{2.5}$$

When using the Laguerre-Voronoï method, the quantity $(\alpha_{ij}(x))$ is computed according to this relationship :

$$\alpha_{ij}(x) = \frac{1}{2}\left(||\overrightarrow{S_iS_j}|| + \frac{W_i^2 - W_j^2}{||\overrightarrow{S_iS_j}||}\right) - \frac{\overrightarrow{S_iS_j}.\overrightarrow{S_iX}}{||\overrightarrow{S_iS_j}||}. \tag{2.6}$$

In order to limit the number of LS functions and thus the computational cost in our simulations, a coloring/recoloring technique was recently developed and applied in this LS-FE formalism [154]. This technique consists in gathering several grains in the same LS function provided that they are far enough from each other. This way, the number N_f of LS functions can be significantly lower than the number of grains ($N_\text{f} << N_\text{g}$) and independent of the total number of grains all along the simulation. To illustrate this technique, a 2D polycrystal is schematically presented on Fig. 2.3(a) with a number of 25 grains represented by only four LS functions. A major inconvenient to this improvement is the possibility to have grain coalescence during boundary migration between two neighbor grains, as presented on Fig. 2.3(b). To avoid grain coalescence,

Scholtes [135] proposed a swapping method in his PhD work aiming to dynamically redistribute grains in other LS functions. All these features (i.e. coloring/recoloring as well as swapping) are considered in this LS-FE framework.

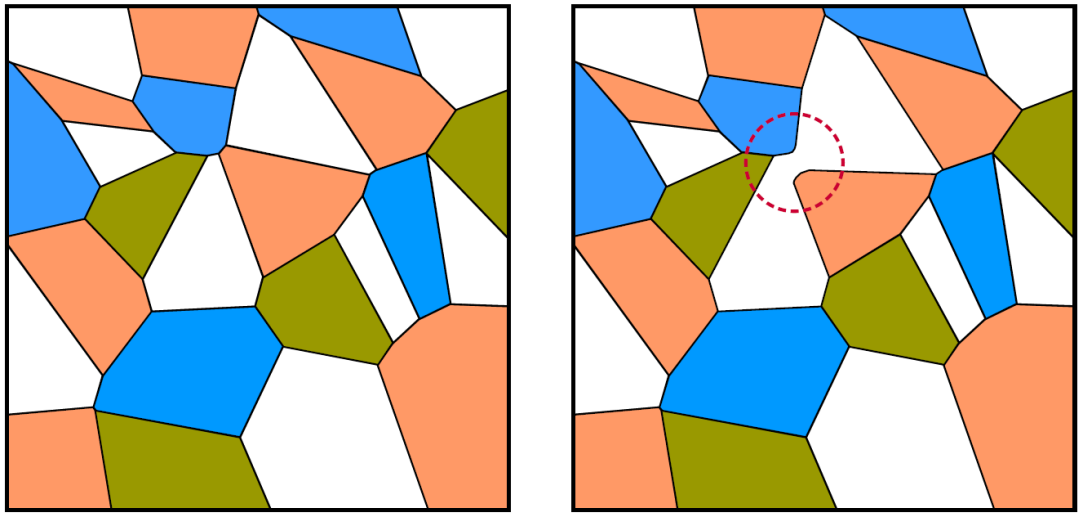

Fig. 2.3. *(a) 2D polycrystal composed of 25 grains represented by only four LS functions. (b) A case of grain coalescence between two grains in white color. [135]*

As an illustration, two polycrystals generated from statistical methods with a different mesh strategy (conform and non-conform description of grain boundaries) are presented on Fig. 2.4. A 3D polycrystal composed of 100 grains generated from the Voronoï method with a coincident FE mesh is presented on Fig. 2.4(a). On the other hand, a 3D polycrystal composed of 184 grains generated from the Laguerre-Voronoï algorithm and immersed into a FE mesh thanks to 18 LS functions is presented on Fig. 2.4(b). It is worth noticing that the number of mesh elements needs to be much higher in case of non-coincident mesh to obtain a correct description of grain boundaries. An alternative is to adapt the mesh size at grain boundaries, in order to reach a coarse mesh size inside grains but a small mesh size at grain boundaries. This method is considered in 2D simulations due to the low computational cost of 2D remeshing operations [135]. However, due to prohibitive costs of 3D remeshing operations, we preferred to consider in this work a uniform isotropic unstructured FE mesh with a small mesh size everywhere in the RVE, as illustrated on Fig. 2.4(b).

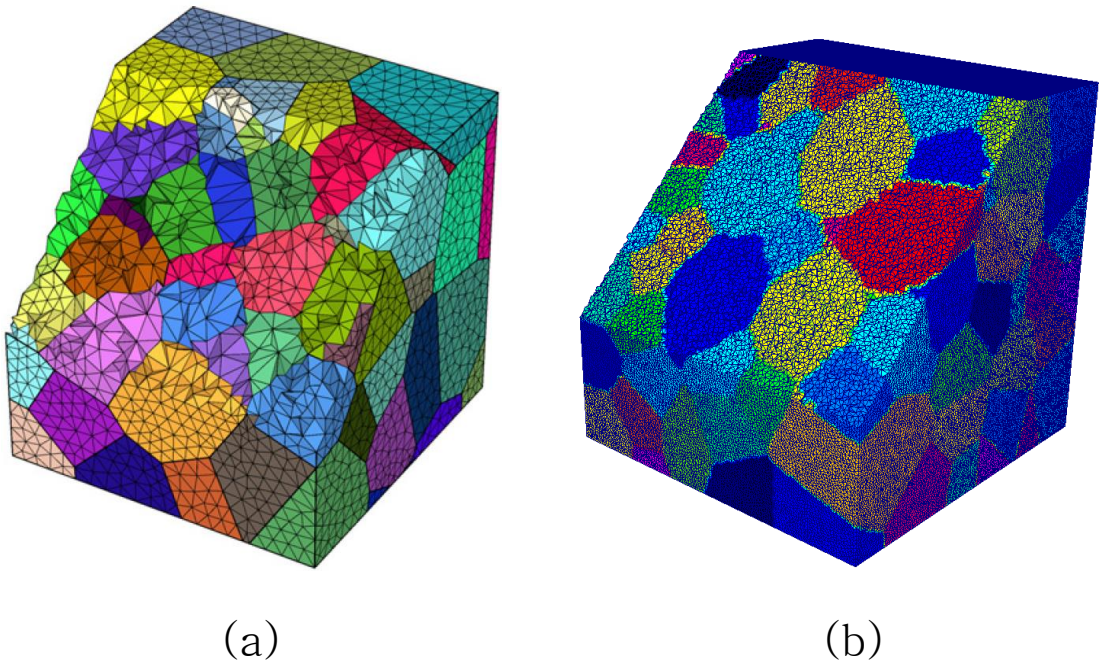

Fig. 2.4. *(a) 3D polycrystal composed of 100 grains where boundaries are coincident with the unstructured tetrahedral mesh [150], (b) 3D polycrystal composed of 184 grains generated using the Laguerre-Voronoï method and immersed into an unstructured tetrahedral mesh using 18 LS functions.*

2.1.2 Grain boundary migration

After the generation of the 2D or 3D polycrystal by initializing the LS functions, grain boundaries can be displaced according to a velocity field $\vec{v}_i$ by solving a set of transport equations :

$$\begin{cases} \dfrac{\partial \psi_i(x,t)}{\partial t} + \vec{v}_i.\vec{\nabla}\psi_i(x,t) = 0 \\ \psi_i(t=0,x) = \psi_i^0(x) \end{cases} \quad \forall i \in \{1,...,N_f\}\,, \tag{2.7}$$

where ψ_i^0 is the initial value of ψ_i. Furthermore the normal $\vec{n}_i$ to the boundary as well as the grain boundary curvature κ_i can be calculated in the considered framework thanks to the relations :

$$\vec{n}_i = \frac{\nabla \psi_i}{||\nabla \psi_i||}, \tag{2.8}$$

$$\kappa_i = -\nabla \cdot \vec{n}_i, \tag{2.9}$$

with $\nabla\cdot$ the divergence operator. Therefore by combining Eqs. 1.1, 2.7, 2.8 and 2.9 and by considering that LS functions satisfy the metric property $||\nabla \psi_i|| = 1$ at least in a thin layer around the grain boundary, a convective-diffusive equation is obtained to model boundary migration of each considered grain in context of isotropic or anisotropic grain

boundary energy and mobility :

$$\begin{cases} \dfrac{\partial \psi_i(x,t)}{\partial t} - M_{\mathrm{b}}\gamma_{\mathrm{b}}\Delta\psi_i + \overrightarrow{v_i^e}.\nabla\psi_i = 0 \\ \psi_i(t=0,x) = \psi_i^0(x) \end{cases} \quad \forall i \in \{1,...,N_{\mathrm{f}}\}\,, \tag{2.10}$$

with $\overrightarrow{v_i^e}$ the velocity due to the jump in stored energy across the grain boundary. This term can be computed thanks to different approaches [52, 133, 135, 155]. To avoid kinematic incompatibilities and deal with the considered coloring/recoloring scheme, the velocity term $\overrightarrow{v_i^e}$ is evaluated here as common for all the LS functions and thanks to the strategy described by Scholtes et al. (sections 3.2, 3.3 and Equation (8) of [143] but where the corresponding mobility M_{b} is defined here as $M_{\mathrm{b}}\delta$). The additional term δ, related to strain rate dependence of grain boundary migration, was added in the velocity term $\overrightarrow{v_i^e}$ to tackle the assumption of stored energy averaged per grain. Indeed, in reality, most of dislocations are located close to grain boundaries, generating high stored gradients and therefore high velocities. However, in our case, the stored energy is averaged per grain and the differences of stored energy across boundaries are consequently underestimated, which can be corrected by adding this artificial parameter noted δ. Since the quantity of stored energy depends on strain rate, this additional parameter should be mainly dependent on strain rate. This correction was already made in few mean field models by considering directly the product $M_{\mathrm{b}}\tau$ as dependent on the strain rate [49, 50, 156]. The grain boundary mobility M_{b}, appearing in the set of Eqs. 2.10 is calculated according to Eq. 1.7. Then the set of Eqs. 2.10 can be solved either using a spectral method relying on Fourier transforms in the context of regular Cartesian grids [140, 141, 157] or by using a FE approach in the context of structured or unstructured mesh [52, 133]. Given that first method is not really adapted for large polycrystal deformations as already mentioned in the chapter 1, we considered the second approach in this work. A P1 solver is considered and a Streamline Upwind/Petrov-Galerkin formulation is used for the stabilization of the solution. The Generalized Minimal Residual Method is used as iterative method for the resolution of the linear system of equations. Boundary conditions must be applied on the RVE frontiers $\partial\Omega$ during simulations. In this work, the following Neumann boundary conditions are applied :

$$\nabla\psi_i.\overrightarrow{m} = \sin(\theta) \;\; \forall x \in \partial\Omega, \tag{2.11}$$

with $\overrightarrow{m}$ the unit outward vector normal to $\partial\Omega$ and θ the angle between the grain boundaries and RVE frontiers $\partial\Omega$, defined as 90° in this work (null Neumann boundary conditions). These boundary conditions play a role on the behavior of grain boundaries interacting with $\partial\Omega$, therefore large polycrystals (i.e. with a large number of grains) are considered in simulations to limit the effect of boundary conditions on results.

After the resolution of the set of Eqs. 2.10, incompatibilities can occur between LS functions, in particular at multiple junctions due to infinite curvature. These problems are called here *vacuum* if LS functions are all negative at a given mesh node and *overlapping* if more than one LS function is positive at a given mesh node. To solve these

incompatibilities, the following treatment proposed in [142] is applied at each mesh node after solving the set of Eqs. 2.10 :

$$\psi_i(x) = \frac{1}{2}\left(\psi_i(x) - \max_{j\neq i}\left(\psi_j(x)\right)\right). \tag{2.12}$$

Although this treatment solves vacuum and overlapping, it leads to altered LS functions, in particular close to grain boundaries. Another limitation intrinsic to the LS method is related to the fact that after solving the set of Eqs. 2.10, the LS functions lose their metric properties, meaning that the condition $||\nabla\psi|| = 1$ of each LS function is no longer satisfied. This limitation is particularly important since if LS functions loose their metric properties, the diffusive part in the set of Eqs. 2.10 is no longer equivalent to the capillarity term. Therefore, after solving the set of Eqs. 2.10 and applying vacuum/overlapping treatment given by Eq. 2.12, the metric properties of the LS functions must be recalculated, which is called the reinitialization procedure. To reinitialize the metric properties of the LS functions, one approach consists in solving the Hamilton-Jacobi equation for each LS function until their respective metric properties are restored [158–160]. However, this approach is rather inefficient computationally and is very limiting in 3D simulations. Recently, Shakoor et al. [146] proposed a new reinitialization method, called Direct Reinitialization with Trees (DRT) method. This method was proved to be as accurate as the classical reinitialization methods, while being up to 20 times faster, even if a small percentage of error, in context of non-conform mesh, is still accumulated at each reinitialization step and its use has to be as reduced as possible [161]. The DRT method is the one considered in this LS-FE approach.

2.2 Full field simulations of grain growth and improvements of two existing models in the state of the art

2.2.1 Introduction

Single-phase fully dense polycrystals can generally be described by a log-normal grain size distribution [162–164], defined by $\langle R\rangle$ and a standard deviation (σ_{R}). The standard deviation is related to the width of the grain radius dispersion around $\langle R\rangle$. During GG mechanism, grain boundaries migrate under capillarity effects which results in an increase of $\langle R\rangle$ and σ_{R}. It is well-known that during GG, grain size distribution evolves to a steady-state [165]. However, the reported steady-states in literature often exhibit large discrepancies, even for studies employing the same numerical models [166, 167]. A major reason given to these discrepancies is the use of a too small initial number of grains in simulations. Therefore ultra-large scale GG simulations were recently proposed in literature to discuss steady-state regimes of GG when considering a very high number of grains. For instance in 2017, Baskaran et al. [168] studied the influence of the heterogeneity of the initial grain size distribution on the growth rate using a FE based front tracking approach. Authors performed full field simulations of GG considering 9 different initial grain size distributions and an initial number of 38000 grains. It was

shown that distributions with the highest deviation evolve at the highest growth rate and vice versa, but this study was based on 2D considerations. The same year, Miyoshi et al. [169] reached a new step in terms of 3D-GG simulations by performing full field simulations on polycrystals composed of 3 millions of initial grains, which is largely higher than previous 3D-GG full field simulations in the state of the art. A MPF model with 2560^3 grid points was used and authors showed the good ability of the B&T model during the steady-state regime as well as the existence of a steady-state distribution during GG. Finally in [141], Miessen et al. also performed 3D-GG large-scale full field simulations, by considering 959^3 grid points and a maximal number of 500 000 initial grains. This model is based on the LS method and diffusive equations are solved using a spectral method relying on FFT in the context of regular Cartesian grids. The influence of the initial number of grains on the identification of the growth exponent in the B&T model was highlighted and authors showed that variations of growth exponent are due to the consideration of too small initial populations ($<$ 50 000 grains).

These ultra-large scale models of GG are essential to discuss the validity of analytical GG models during the steady-state regime. However the transient regime is generally neglected in these studies and only the steady-state regime is discussed. In an industrial point of view, the prediction of microstructure evolutions (i.e. mean grain size as well as grain size distribution) during the transient regime (i.e. few hours) are essential, and customized models can be proposed for predictions in this regime. In this section the LS-FE formalism previously introduced is used to perform 3D full field simulations of pure capillarity driven GG (i.e. with a velocity term $\overrightarrow{v_i^e}$ equal to zero in the set of Eqs. 2.10) without neglecting the transient regime, and considering an initial number of 8000 grains. More particularly, the effect of non-uniform grain size distributions on the growth rate are studied and two analytical GG models (i.e. Hillert/Abbruzzese [47, 67–69] and Burke-Turnbull (B&T) [64] models) are discussed and improved during the transient regime thanks to full field results. The material parameters of a 304L austenitic stainless steel are considered in simulations. It is worth noticing that the initial number of grains considering in our simulations ($\approx$ 8000) are much lower to those recently consider in literature ($>$ 500 000). However it must be highlighted that our LS-FE formalism is not dedicated to the only GG mechanism, but also aim to model large deformation of polycrystals, as detailed in the next chapter. Therefore, a spectral method relying on FFT cannot be consider in our formalism, which considerably increases computational costs and numerical issues while reducing the initial number of grains that can be modeled.

2.2.2 Initial polycrystal and material parameters

A 5h heat treatment at a constant temperature of 1323K for a austenitic 304L steel is simulated. The pre-exponential factor M_0 and activation energy for boundary migration Q_m considered in Eq. 1.7 are taken equal to 1.56e$-$1 $\mathrm{m}^4.\mathrm{J}^{-1}.\mathrm{s}^{-1}$ and 2.8e5 $\mathrm{J.mol}^{-1}$, respectively, for the considered austenitic 304L steel [170]. By considering R = 8.3145 $\mathrm{J.mol}^{-1}.\mathrm{K}^{-1}$ and T = 1323K, the grain boundary mobility M_b calculated by Eq. 1.7

and used in the set of Eqs. 2.10 is equal to 1.38e-12 $m^4.J^{-1}.s^{-1}$. Furthermore, the grain boundary energy γ_b used in the set of Eqs. 2.10 is taken equal to 0.6 $J.m^{-2}$ [10]. The material is assumed to be free of second phase particles (no Smith-Zener pinning effect). The numerical simulations are performed on a cubic RVE whose edge length varies from 2.00 to 2.85 mm. Each simulation was performed on 60 Intel Xeon CPUs. A 3D unstructured mesh composed of 292^3 tetrahedral elements is used.

8 initial grain size distributions are considered to generate 8 initial polycrystals using the Laguerre-Voronoï approach (see Eq. 2.3). Each of them is defined by an initial mean grain radius $\langle R_0 \rangle$ and standard deviation σ_{R0}. Their characteristics are summarized in Tab. 2.1 (line 1-4). The distributions LN_i with $i \in \{1,...,7\}$ follow a log-normal distribution. The last one, referred to as BiM, is bimodal with modes $\lambda_1 = 50\mu m$ and $\lambda_2 = 100\mu m$. The initial number of grains in the RVE is close to 8000 while at least 1200 grains remain at the end of the heat treatment (see Tab. 2.1 and Fig. 2.7). The RVE dimensions, the time steps and the mesh size are chosen so as to justify a good convergence of results in terms of grain boundary kinetics [143, 154].

		LN_1	LN_2	LN_3	LN_4	LN_5	LN_6	LN_7	BiM
Initial state ($t = 0$h)									
$\langle R_0 \rangle$	(μm)	62.0	66.0	74.3	75.3	82.2	89.4	99.0	75.2
σ_{R0}	(μm)	6.90	11.8	19.4	7.50	25.9	30.9	17.7	25.5
$\ln(\sigma_{R0}/\langle R_0 \rangle)$		-2.20	-1.71	-1.35	-2.30	-1.14	-1.05	-1.71	-1.08
No. Grains		7920	7576	7474	8100	7460	7636	7588	7472
Final state ($t = 5$h)									
$\langle R_f \rangle$	(μm)	109	120	135	111	151	160	138	115
σ_{Rf}	(μm)	39.0	45.0	53.2	39.8	59.9	66.3	50.7	36.0
$\ln(\sigma_{Rf}/\langle R_f \rangle)$		-1.03	-0.98	-0.93	-1.03	-0.92	-0.88	-1.00	-1.16
No. Grains		1483	1278	1244	2552	1221	1341	2803	2092

Tab. 2.1. *Characteristics of the initial (lines 1-4) and final (lines 5-8) grain size distributions predicted by the full field simulations.*

2.2.3 Full field simulation results

An histogram representing the instantaneous grain size distribution is generated every minute of the simulated heat treatment. Each histogram is composed of 30 equally spaced intervals delimited by 0 and 300μm. Next the term *distribution curve* is introduced to denote a linear approximation of an histogram (i.e. of a grain size distribution). The objective of these distribution curves is to simplify the representation of the grain size distributions for future comparisons. Fig. 2.5 provides a schematic illustration of the distribution curve obtained by piecewise linear approximation of an histogram while Fig. 2.6 shows all the distribution curves predicted by the full field simulations for every initial grain size distribution at the early (solid curves) and final (dashed curves) stages of the simulation. These are confronted to the Hillert/Abbruzzese model predictions in

the next section.

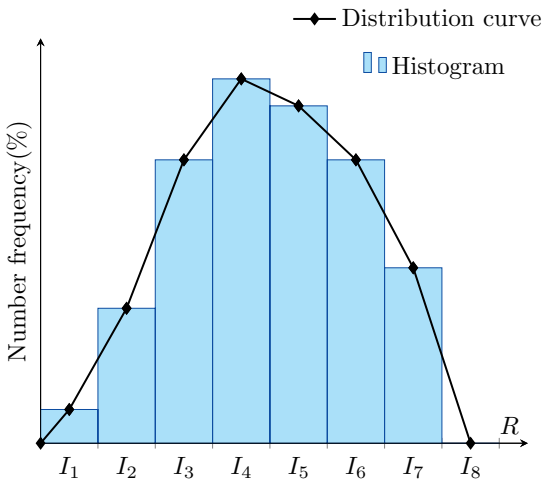

Fig. 2.5. *Distribution curve obtained by linear approximation of an histogram.*

Table 2.1 (line 5-8) presents the characteristics of the final grain size distributions predicted by the full field simulations. The ratio $\ln(\sigma_{\mathrm{Rf}}/\langle R_{\mathrm{f}}\rangle)$ is observed to tend towards the value -1.00 after 5h of treatment for every initial grain size distribution. Fig. 2.7 illustrates several RVEs of full field simulations at the beginning and at the end of the heat treatment, for the LN_1 and BiM initial grain size distributions. Among the RVEs representing the log-normal grain size distributions, only the RVE obtained for the LN_1 initial grain size distribution is depicted since this latter is representative of all the log-normal initial grain size distributions. A preponderant blue color is observed at the beginning of the heat treatment for the LN_1 initial grain size distribution, meaning that σ_{R0} is small for this distribution and most grains have sizes close to $\langle R_0\rangle$. In the BiM initial grain size distribution, two preponderant blue and green colors are observed in the RVE at the beginning of the heat treatment. These two colors depict the two modes of the bimodal distribution, centered on grain size values of 50μm and 100μm.

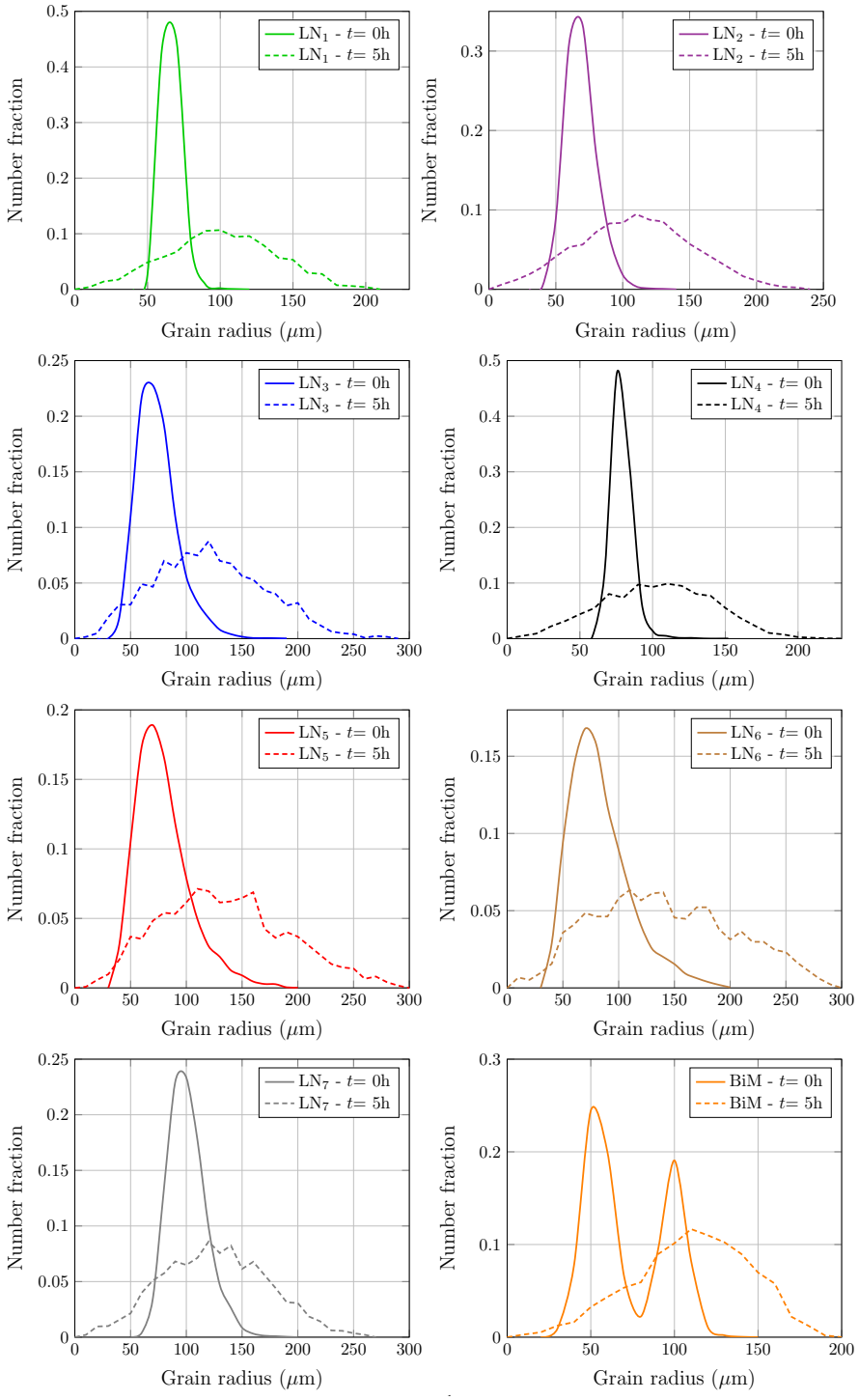

Fig. 2.6. *Initial (solid curves) and final (dashed curves) distribution curves predicted by the full field simulations for the different initial grain size distributions.*

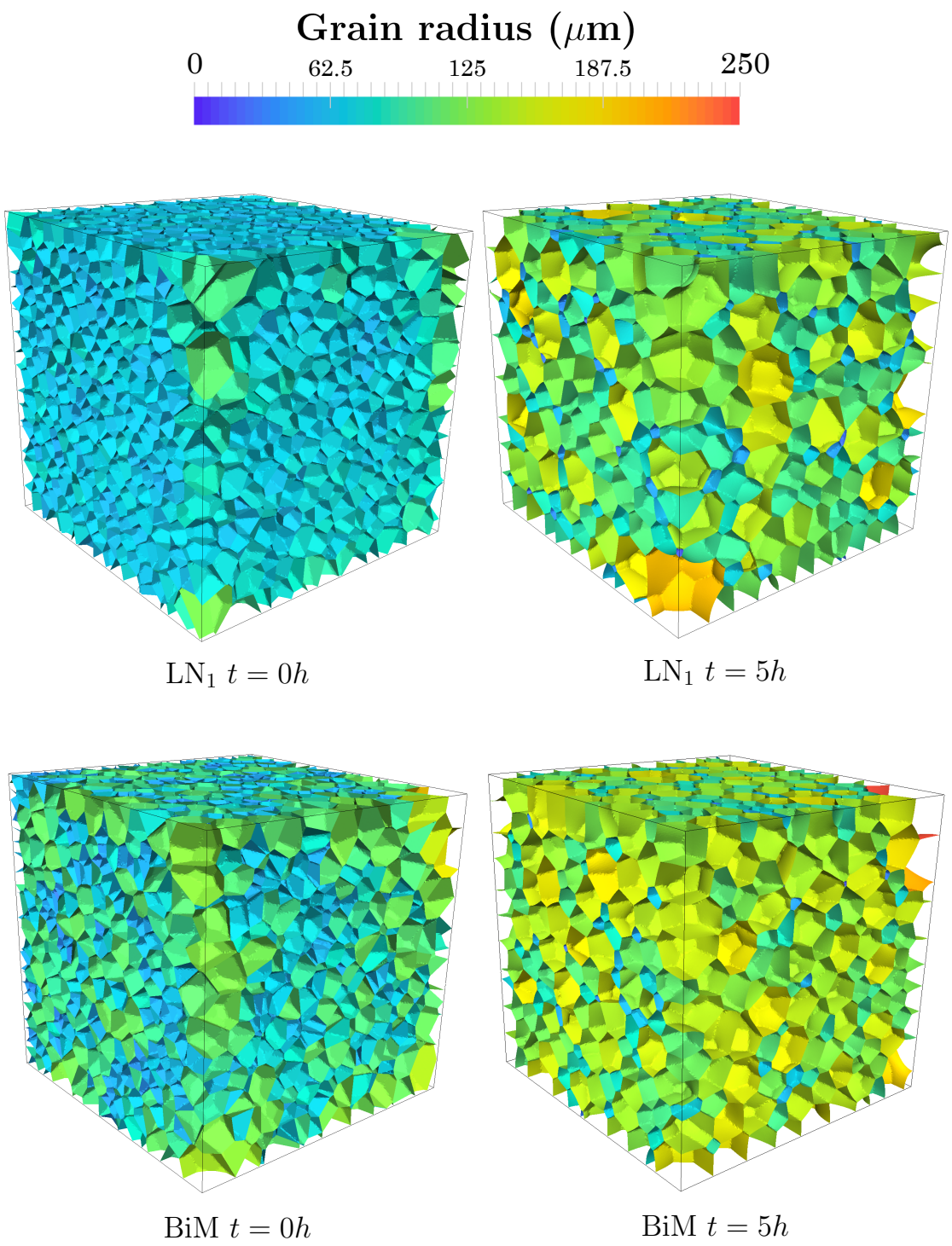

Fig. 2.7. *Grain boundary networks at initial and final stages of the simulation for the LN_1 and BiM initial grain size distributions. The color code corresponds to the equivalent sphere radius of each grain.*

2.2.4 Confrontation of full field simulation results with Hillert/Abbruzzese model

Hillert/Abbruzzese model

In 1965, Hillert/Abbruzzese proposed a mean field model [47, 67–69] for normal GG, already introduced in the first chapter. This model was discussed in many studies. Several authors [73, 74, 166, 171] recently confronted the predictions of this model with full field simulation results. Hillert/Abbruzzese model is considered to be more accurate than phenomenological GG models such as the one of B&T [64], since it is based on a discrete representation of the microstructure. This discrete microstructure is composed of N classes of spherical grains having a radius R_i ($i \in \{1,...,N\}$). Each grain class evolves according to the Hillert/Abbruzzese equation introduced in first chapter (Eq. 1.30) :

$$\frac{dRi}{dt} = \beta M_b \gamma_b \left(\frac{1}{R_{cr}} - \frac{1}{R_i} \right). \tag{2.13}$$

For each initial grain size distribution, the number of grain classes in the Hillert/Abbruzzese model was taken equal to the number of grains in the RVE of the corresponding full field simulation (see Tab. 2.1). The parameter β is a geometrical dimensionless constant which refers to the inherent approximations concerning the assumed idealized geometry in the Hillert/Abbruzzese model representation. In 3D, β is assumed to be close to unity [47, 67–69]. Other authors have nevertheless reported values above unity, such as Kamachali et al., who found $\beta \simeq 1.25$ [171]. In another work, Suwa et al. [166] also found optimal β values around 1.1. In [74], authors recently discussed a linear relationship valid in 3D between the parameter β and the index $\langle R \rangle^2 / \langle R^2 \rangle$ which aims to account for the geometrical relations between the neighbor grains for any given initial grain size distribution.

Hereafter, the notation Hi(β) designates Eq. 2.13. So Hi(1) corresponds to the classical Hillert/Abbruzzese formulation [47, 67–69]. As it employs several grain classes, this model has the advantage of being able to predict the grain size distribution evolution in addition to the $\langle R \rangle$ evolution. Previous works showed the ability of the classical Hillert/Abbruzzese model to correctly capture the GG kinetics in 2D for different initial grain size distributions [66]. In the same manner as for full field simulations, a grain size distribution is generated every minute of the Hillert/Abbruzzese simulation. The distribution curves are then deduced from the grain size distributions according to the method illustrated on Fig. 2.5.

The notation L^2_{Hi} represents the instantaneous L^2 relative error measured between the distribution curves predicted by the Hillert/Abbruzzese and full field models. This quan-

tity is computed as follows :

$$L^2_{\mathrm{Hi}}(t) = 100 \times \sqrt{\frac{\sum_{i=1}^{N} \left(S_i - S'_i\right)^2}{\sum_{i=1}^{N} (S'_i)^2}}, \tag{2.14}$$

where, as illustrated on Fig. 2.8, the distributions are approximated by a linear interpolation and S_i (resp. $S_{i'}$) denotes the surface of the i^{th} obtained trapezoid under the Hillert/Abbruzzese (resp. the full field) distribution curve. Hereafter the notation $\langle L^2_{\mathrm{Hi}} \rangle$ designates the time average of the $L^2_{\mathrm{Hi}}(t)$ errors for a given simulation :

$$\langle L^2_{\mathrm{Hi}} \rangle = \frac{1}{N_{\mathrm{incr}}} \sum L^2_{\mathrm{Hi}}(t), \tag{2.15}$$

where N_{incr} is the number of time increments (equal to 300 in this study, Δt = 1min).

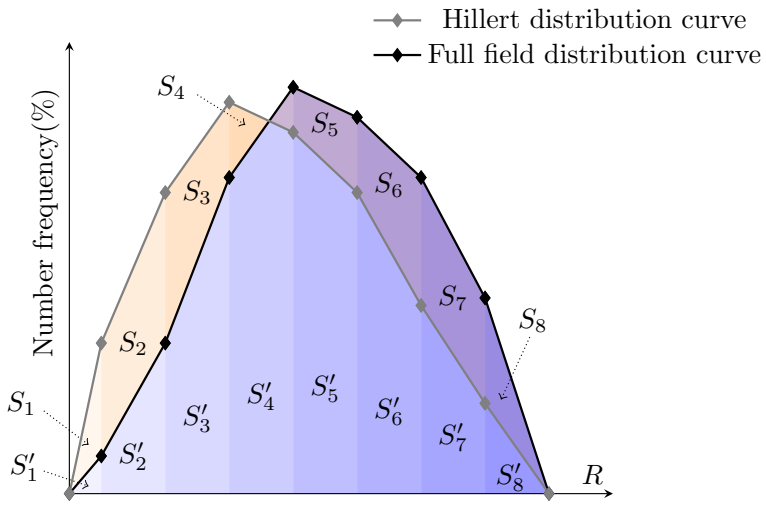

Fig. 2.8. *Computed L^2_{Hi} error between the Hillert/Abbruzzese and full field distribution curve.*

Optimization of the Hillert/Abbruzzese model

The values of $\langle L^2_{\mathrm{Hi}} \rangle$ errors obtained with the Hi(1) model are depicted by blue bars on Fig. 2.9. These errors remain globally constant and around 20% for all the initial grain

size distributions. These results confirm the versatility of this model although a difference of 26% is observed for the LN_4 and BiM initial grain size distributions. The distribution curves predicted by the Hi(1) (blue curves) and the FF model (red curves) are also compared at different stages of the heat treatment on Fig. 2.11. The kinetic of GG obtained with the Hillert/Abbruzzese model seems to be slower than that obtained with the FF model. This is observable on Fig. 2.11 at each instant of the simulation by a time shift of the Hillert/Abbruzzese distribution curves with respect to the full field distribution curves.

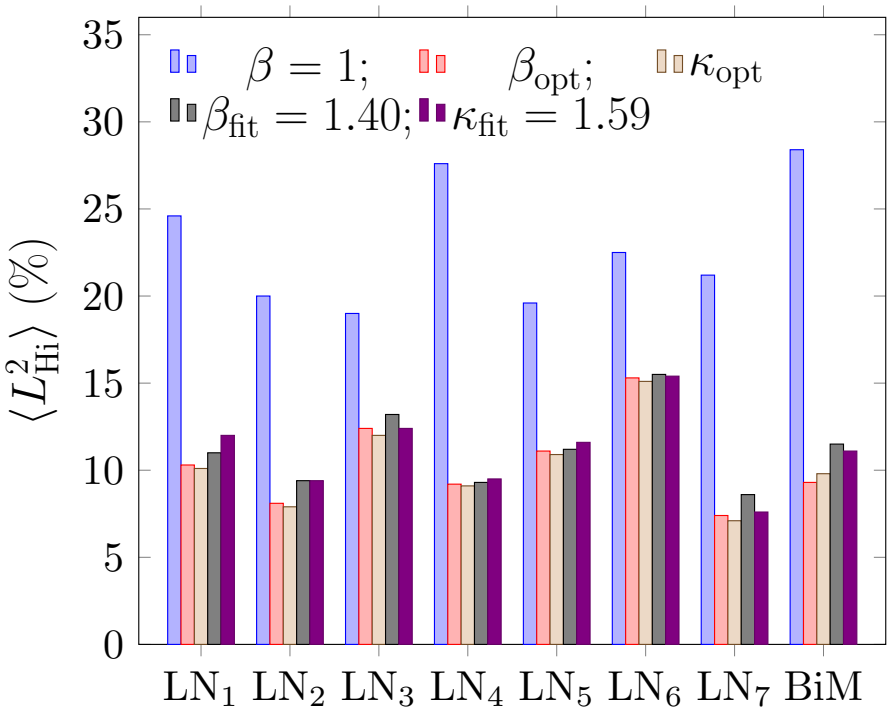

Fig. 2.9. *Comparison in terms of $\langle L^2 \rangle$ error on the distribution curves predicted by the full field and Hillert/Abbruzzese models (see Eq. 2.15 for details).*

As stated above, the value $\beta = 1$ proposed by Hillert/Abbruzzese relies on many assumptions. For example Hillert/Abbruzzese considers that each shrinking grain has four immediate neighbors just before disappearing. Furthermore he considers that the β value is two times higher in 3D than in 2D where $\beta = 0.5$ according to Hillert/Abbruzzese [47, 67–69]. Although these assumptions are judicious and justified, we propose to recalibrate this Hillert/Abbruzzese parameter based on the results of the full field simulations. Thus, several simulations using Hillert/Abbruzzese model were performed by varying the beta value from 0.5 to 2 by step of 0.01. We denote β_{opt} the value of β in Eq. 2.13 that minimizes $\langle L^2_{\text{Hi}} \rangle$ error for each initial grain size distribution. The values of β_{opt} are provided in Tab. 2.2. Red bars on Fig. 2.9 show the residual $\langle L^2_{\text{Hi}} \rangle$ error obtained with β_{opt}. These residual errors were approximately reduced by half compared to the classical value of β equal to 1. Furthermore the values of β_{opt} are distributed around a

mean value of 1.40 noted β_{fit} (see green dots on Fig. 2.10).

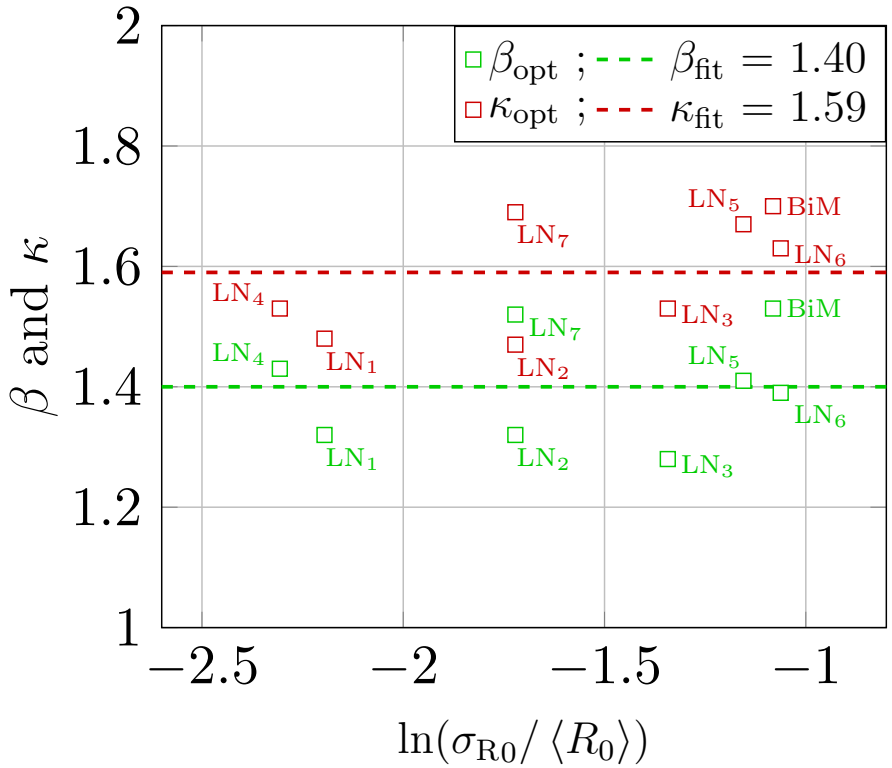

Fig. 2.10. *Optimized values β_{opt} and κ_{opt} obtained by inverse analysis from the full field simulation results and fitting values β_{fit} and κ_{fit} obtained by an average of the optimized values.*

To validate the calibrated value of $\beta = 1.40$, the distribution curves predicted by the Hi(1.40) (green curves) and the full field models (red curves) are compared at different stages of the heat treatment on Fig. 2.11. It is worth noticing that Hi(1.40) model provides non negligible improvements for the prediction of the grain size distributions compared to the initial Hi(1) model. Indeed, the time shift observed Fig. 2.11 between full field and Hi(1) distribution curves is now rectified since this new value of $\beta = 1.4$ is larger than the old one and thus logically increases the kinetic of GG. In a general way, the shapes of the grain size distributions are also in good agreement with observations made in [171]. Grain size distributions are observed to be initially sharp and then become larger during the heat treatment. After 2.5h of treatment in the BiM initial case, one single peak is observed on the distribution curve, which means that the two modes merged in the first hours of the heat treatment.

In order to investigate further the theory of [74], we define κ_0 as :

$$\kappa_0 = \frac{\beta_{\text{opt}}}{\langle R \rangle^2 / \langle R^2 \rangle_{(t=0)}}, \tag{2.16}$$

where the index $\langle R\rangle^2/\langle R^2\rangle$ is taken at the instant t = 0s of the treatment. This choice was done since this value does not significantly evolve during a simulation. The different values of κ_0 computed for every initial grain size distribution are provided in Line 3 of Tab. 2.2. These ratios are not constant between each initial grain size distribution, meaning that there is not a direct relationship between β and the index $\langle R\rangle^2/\langle R^2\rangle_{(t=0)}$ for our cases. However this index, which considers the geometrical characteristics of neighbor grains, could be useful to enrich the classical Hillert/Abbruzzese model (see Eq. 2.13).

Thus by replacing the β parameter in Eq. 2.13 by the product of an assumed constant parameter noted κ times the ratio $\langle R\rangle^2/\langle R^2\rangle$, we can consider the following Hillert/Abbruzzese model derived from the Darvishi Kamachali theory [74] :

$$\dot{R}_i = \kappa \frac{\langle R\rangle^2}{\langle R^2\rangle} M_\mathrm{b}\gamma_\mathrm{b}\left(\frac{1}{R_\mathrm{cr}} - \frac{1}{R_i}\right), \tag{2.17}$$

where κ is a constant parameter. We performed several Hillert/Abbruzzese simulations using this new formulation (see Eq. 2.17) and by varying the κ value from 1 to 2 with a step of 0.01. We denote by κ_opt the value of κ that minimizes $\langle L^2_\mathrm{Hi}\rangle$ for each initial grain size distribution. The κ_opt values are presented in Line 4 of Tab. 2.2. Grey bars on Fig. 2.9 show the residual $\langle L^2_\mathrm{Hi}\rangle$ error obtained with κ_opt. These residual errors are slightly little smaller than those obtained with β_opt. However this difference is not significant enough to affirm that the model given by Eq. 2.17 gives better predictions than Hi(1.4) model. Furthermore the κ_opt values are distributed around a mean value of 1.59 noted κ_fit (see red dots on Fig.2.10) resulting also in a low $\langle L^2_\mathrm{Hi}\rangle$ error close to that obtained with the Hi(β_fit) model (see purple bars on Fig. 2.9). These similar errors are logically due to the fact that the Hi(1.4) (Eq. 2.13) and the new Hillert/Abbruzzese formulation (Eq. 2.17) give very close predictions since the index $\langle R\rangle^2/\langle R^2\rangle$ does not change much during all our simulations. Finally, the distribution curves obtained according to the new Hillert/Abbruzzese formulation all overlay with those obtained according to the Hi(1.4) model.

	LN_1	LN_2	LN_3	LN_4	LN_5	LN_6	LN_7	BiM
β_opt	1.32	1.32	1.28	1.43	1.41	1.39	1.52	1.53
β_fit				1.40				
κ_0	1.35	1.36	1.38	1.43	1.57	1.58	1.57	1.72
κ_opt	1.48	1.47	1.53	1.53	1.67	1.63	1.69	1.7
κ_fit				1.59				

Tab. 2.2. *(Line 1-2) Optimized Hillert/Abbruzzese model parameter β_{opt} calculated by inverse analysis from the full field simulation results (see Eq. 2.13) and fitted Hillert/Abbruzzese model parameter β_{fit} obtained by averaging the values of β_{opt}. (Line 3) Values of κ_0 defined as the ratio between β_{opt} and the initial index $\langle R\rangle^2/\langle R^2\rangle$ at time = 0s of every simulation. (Line 4-5) Optimized κ values (κ_{opt}) calculated by inverse analysis from the full field simulation results (see Eq. 2.17) and fitted κ value (κ_{fit}) obtained by averaging the values of κ_{opt}.*

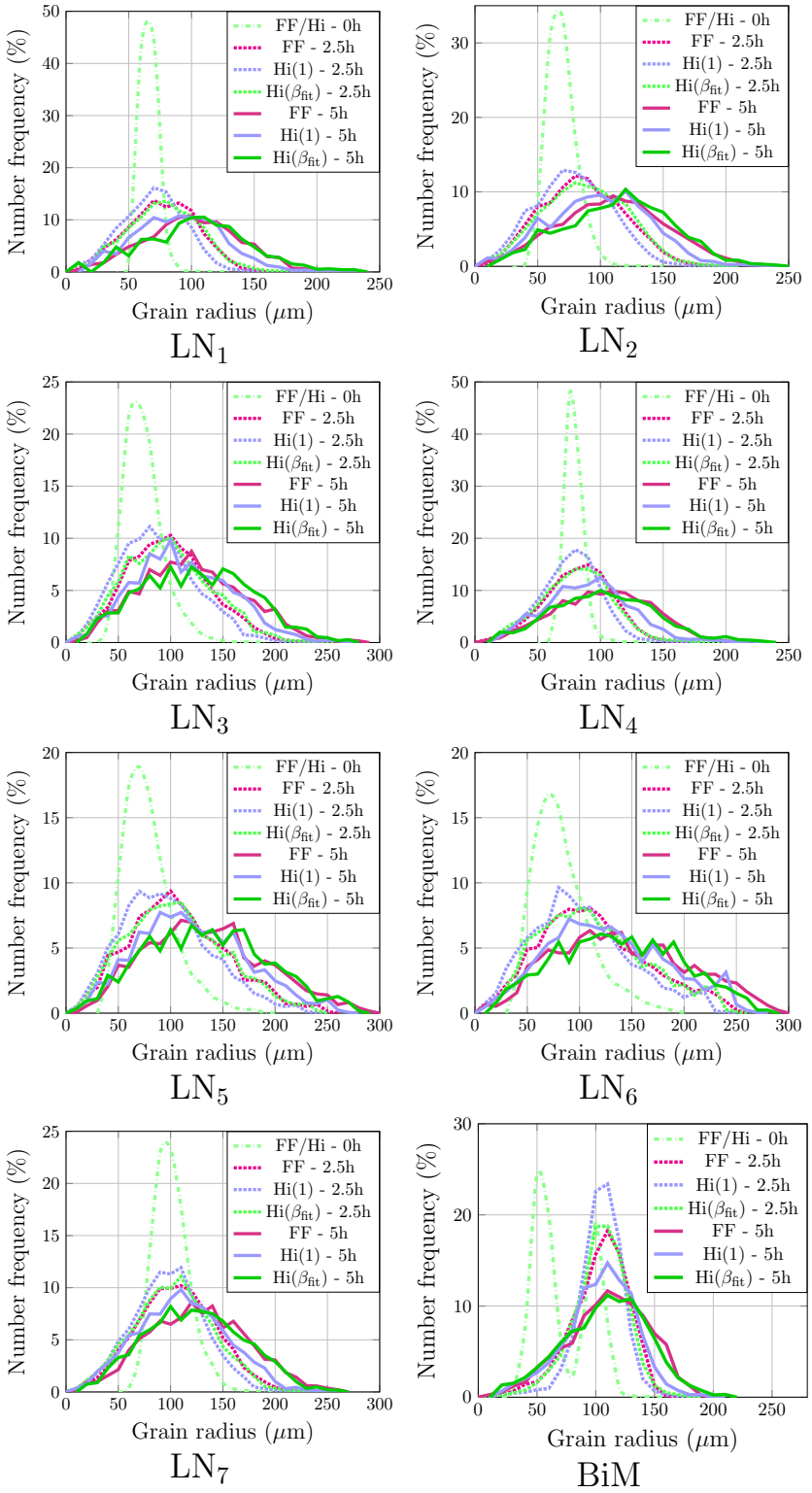

Fig. 2.11. *Distribution curves predicted by the full field (FF), Hi(1) and Hi(1.40) models for the different initial grain size distributions.*

2.2.5 Confrontation of full field simulation results with Burke & Turnbull model

Burke & Turnbull model

For materials with single mode grain size, describing the evolution of $\langle R \rangle$ could be interesting as this quantity gives information concerning the global flow behavior of the material. Especially the Hall-Petch relationship states that the Yield stress of metallic materials can be expressed as a function of $\langle R \rangle^{-0.5}$ [172]. Furthermore in such cases, the initial grain size distribution can be unknown and consequently the Hillert/Abbruzzese model can hardly be used. Thus, other mean field models can be used as a good alternative to describe the GG kinetics. In 1952, Burke and Turnbull (B&T) investigated the physical mechanisms of GG. They particularly assumed that grain boundaries migrate by atom transport toward their center of curvature, under a force due to their curved shape. These findings gave rise to the B&T model [64] mentioned in the first chapter (Eq. 1.29), which predicts a parabolic evolution of $\langle R \rangle$ as a function of the time t :

$$\langle R \rangle^2 - \langle R_0 \rangle^2 = \delta M_b \gamma_b t. \tag{2.18}$$

Some authors [171] have found a value of δ close to 0.5 when the term $\langle R_0 \rangle^2$ is neglected as compared to $\langle R \rangle^2$. This analytic mean field model has the advantage of being extremely simple to use since it requires only a value for the product $M_b \gamma_b$ and for the initial mean grain size $\langle R_0 \rangle$.

The predictions of the B&T model are confronted with the full field simulation results, using the following relative L^2 error :

$$L^2_{B\&T}(\%) = 100 \times \sqrt{\frac{\sum_{t=0}^{5h} \left(\langle R \rangle_{FF}(t) - \langle R \rangle_{B\&T}(t) \right)^2}{\sum_{t=0}^{5h} \langle R \rangle^2_{FF}(t)}}, \tag{2.19}$$

where $\langle R \rangle_{B\&T}$ and $\langle R \rangle_{FF}$ represent, respectively, the instantaneous values of $\langle R \rangle$ in the B&T and full field models.

New formulation of the Burke & Turnbull model

The resulting $L^2_{B\&T}$ measured between the classical B&T model predictions (Eq. 2.18) and the full field simulation results are illustrated by blue bars on Fig. 2.12. It is worth noticing that these $L^2_{B\&T}$ are smaller than the $\langle L^2_{Hi} \rangle$ calculated in the previous section. Indeed $L^2_{B\&T}$ relies on a single quantity which is the mean grain size of the material. On the other hand $\langle L^2_{Hi} \rangle$ reflects the difference of shape between the two distribution

curves. Results show that $L^2_{\mathrm{B\&T}}$ is globally high for any initial case. Furthermore, $L^2_{\mathrm{B\&T}}$ error globally increases when the ratio $\sigma_{R0}/\langle R_0\rangle$ decreases. This finding is actually quite logical and can be easily explained. Indeed in the case of small $\sigma_{R0}/\langle R_0\rangle$ ratios, the grain boundary kinetic slows down at the early stage of the treatment because most grains have an initial radius close to $\langle R\rangle$. Consequently the increase of $\langle R\rangle$ takes longer to initiate and a plateau or even a decrease could be observed at the beginning of the thermal treatment. These typical evolutions occurring during the transient regime are not straightforward to capture with the classical B&T model, which is more dedicated to steady-state regimes. However the transient regime can last few hours in some initial configurations and the prediction of microstructure evolutions during this regime is of prime importance for many industrials. Thus these results confirm the interest of improving the classical B&T model during the transient regime. Recent numerical investigations in 2D have also pointed out that B&T model is not accurate for all $\sigma_{R0}/\langle R_0\rangle$ initial ratios [66] during the transient regime.

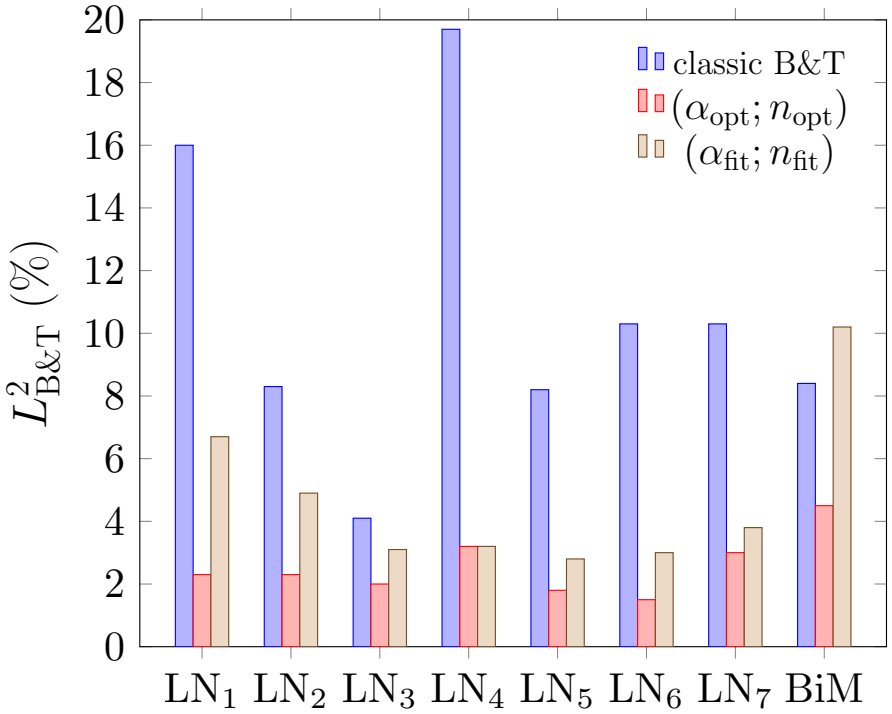

Fig. 2.12. *Comparison in term of L^2 error on the $\langle R\rangle$ values predicted by the full field simulations and the different B&T formulations (see Eq. 2.18 and Eq. 2.20 for more details).*

In order to make the classical B&T formulation more accurate, the first objective is to determine whether there exists for each initial grain size distribution, other δ values, noted δ_{opt}, that correctly describe the GG kinetics. These δ_{opt} values are obtained by minimizing the $L^2_{\mathrm{B\&T}}$ for each initial grain size distribution. The resulting fitting curves obtained by combining Eq. 2.18 and the δ_{opt} are depicted on Fig. 2.13 (dashed curves)

for the LN_4 and LN_6 initial grain size distributions, having the smallest and highest $\sigma_{R0}/\langle R_0\rangle$ ratios, respectively. It is observed that changing the values of δ does not correct the description of the transient regime. In particular for small $\sigma_{R0}/\langle R_0\rangle$ ratios, a model such as B&T model cannot be accurate enough to describe these particular mean grain size evolutions.

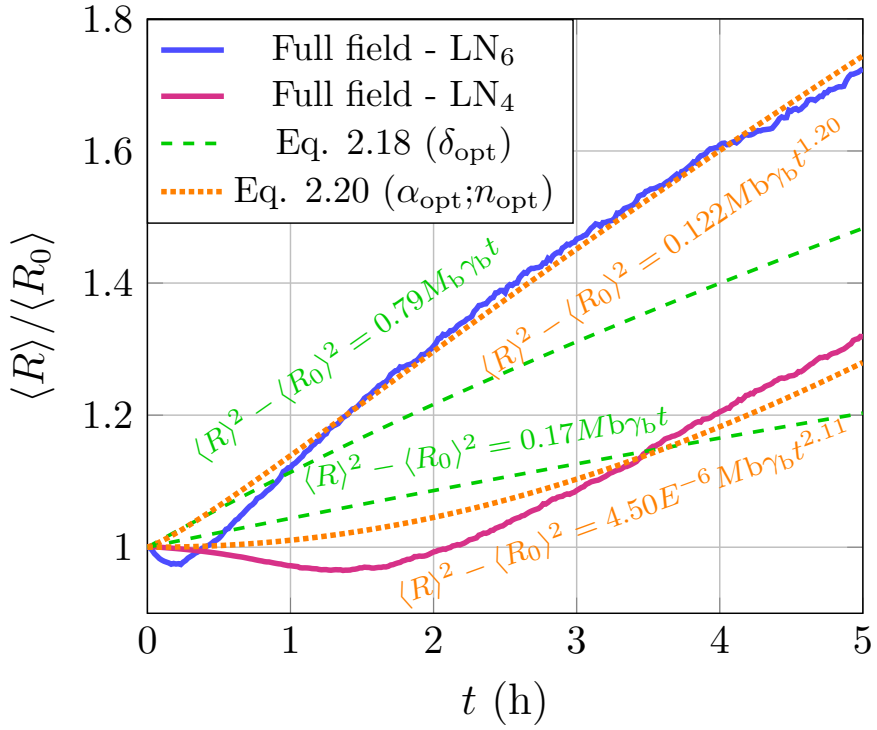

Fig. 2.13. *Evolution of $\langle R\rangle/\langle R_0\rangle$ during the heat treatment. Solid curves correspond to the full field (FF) results, dashed curves represent the B&T predictions obtained by combining Eq. 2.18 and δ_{opt} and dotted curves represent the B&T predictions obtained by combining Eq. 2.20 and the set of parameters (α_{opt};n_{opt}).*

In order to also check the consistency of this law in the transient regime, the curves $\log(\langle R\rangle^2\text{-}\langle R_0\rangle^2)$=f($\log(t)$) were plotted on Fig. 2.14 according to full field results. A linear approximation of these curves is also added. We observed that the slopes of the linear approximations are quite different for every initial grain size distribution as already observed in the work of [66], which means that the classical B&T formulation cannot be sufficient to describe the kinetic of GG for every initial grain size distribution.

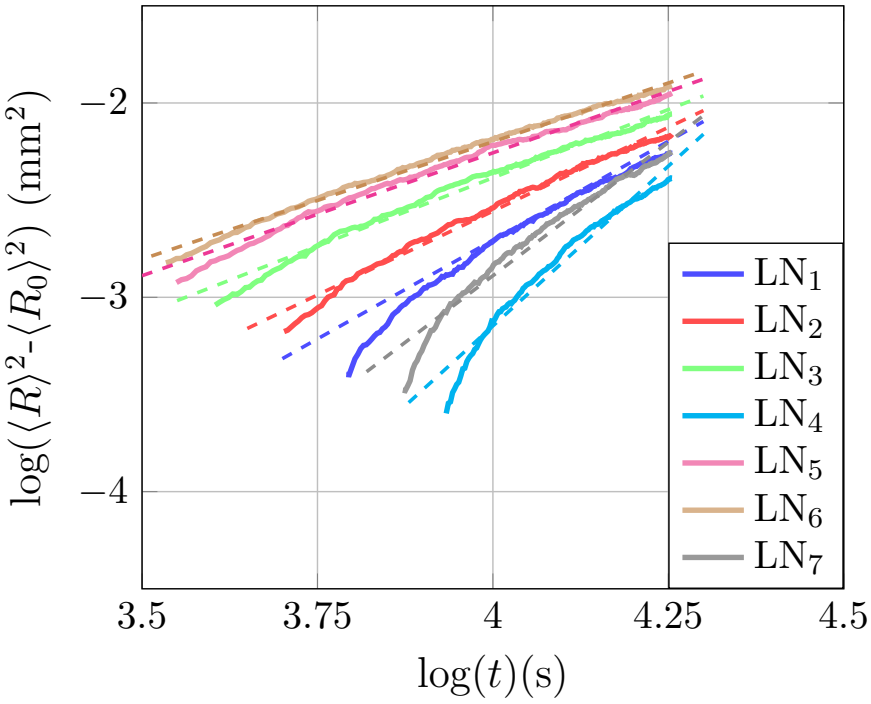

Fig. 2.14. *Evolution of $log(\langle R\rangle^2\text{-}\langle R_0\rangle^2)$ as a function of log(time) according to full field results. Linear approximations are added in dashed lines.*

Based on the previous observations, a new formulation of the B&T model was proposed in [66] including a new fitting exponent n aiming to take into account the different slopes observed on the Fig. 2.14 and the transient regimes observed on Fig. 2.13 :

$$\langle R\rangle^2 - \langle R_0\rangle^2 = \alpha M_b \gamma_b t^n, \tag{2.20}$$

where α is considered as a fitting parameter depending, in the same manner as the exponent n, on the initial grain size distribution characteristics. Thus the validity of the classical B&T model (Eq. (2.18)) can be easily verified if the slope n is equal to 1 and the fitted parameter α is equal to 0.5.

	LN_1	LN_2	LN_3	LN_4	LN_5	LN_6	LN_7	BiM
α_{opt}	6.20e-6	6.00e-4	1.66e-2	4.50e-6	7.45e-2	1.22e-1	6.18e-4	35.0
n_{opt}	2.13	1.69	1.37	2.11	1.24	1.20	1.64	0.56
α_{fit}	8.67e-6	5.67e-4	1.22e-2	3.69e-6	7.32e-2	1.58e-1	5.66e-4	1.22e-1
n_{fit}	2.06	1.67	1.39	2.13	1.23	1.16	1.67	1.18
$\ln(\sigma_{R0}/\langle R_0\rangle)$	-2.20	-1.71	-1.35	-2.30	-1.14	-1.05	-1.71	-1.08

Tab. 2.3. *Line 1-2: Optimized B&T model parameters α_{opt} and n_{opt} obtained by inverse analysis from the full field simulation results (Eq. 2.18). Line 3-4: Fitted mean field model parameters α_{fit} and n_{fit} obtained by using the new formulations of Eq. 2.21. Line 5: Ratio of the initial grain size distribution characteristics.*

Inverse analyses were performed in order to obtain optimal values of α_{opt} and n_{opt} minimizing $L^2_{\text{B\&T}}$. These values are plotted on Fig. 2.15 and the corresponding $L^2_{\text{B\&T}}$ are illustrated by red bars on Fig. 2.12. Interestingly, the results of Tab. 2.3 and Fig. 2.12 show that there exists, for each initial distribution, a set of parameters (α_{opt};n_{opt}) which predicts very accurately the evolution of $\langle R \rangle$, with $L^2_{\text{B\&T}} < 5\%$. Furthermore the LN_6 initial grain size distribution presents the set of parameters (α_{opt};n_{opt}) that is closest to the B&T classical parameters (α = 0.5; $n = 1$). This distribution has the largest ratio ($\sigma_{\text{R0}}/\langle R_0 \rangle \simeq 0.35$) of this study. It is worth noticing that increasing the ratio $\sigma_{\text{R0}}/\langle R_0 \rangle$ should lead to a new set of parameters (α_{opt};n_{opt}) even closer to the B&T parameters. In [66], authors found in 2D a set of parameters (α_{opt};n_{opt}) close to B&T parameters for initial grain size distributions having a ratio $\sigma_{\text{R0}}/\langle R_0 \rangle \simeq 0.45$.

The predictions of $\langle R \rangle$ obtained by combining Eq. 2.20 with the set of parameters (α_{opt};n_{opt}) were plotted on the Fig. 2.13 (dotted curves) for the LN_4 and LN_6 initial grain size distributions. It is clearly observed that the resulting curves obtained with Eq. 2.20 (dotted curves) are closer to full field predictions than resulting curves obtained with Eq. 2.18 (dashed curves). However, the transient regime characterized by a decrease in $\langle R \rangle$ during the first hour of treatment is not well described yet.

It is worth noticing that the α_{opt} and the n_{opt} values increase and decrease respectively with the $\sigma_{\text{R0}}/\langle R_0 \rangle$ ratio (see Tab. 2.3). This trend was already observed in the study proposed by [66]. These observations confirm that the ratio $\sigma_{\text{R0}}/\langle R_0 \rangle$ is relevant for describing the evolution of α and n. Furthermore, the sets of parameters (α_{opt};n_{opt}) are observed to be quasi identical for the two LN_2 and LN_7 initial grain size distributions with the same $\sigma_{\text{R0}}/\langle R_0 \rangle$ ratio. By plotting the parameters $\ln(\alpha_{\text{opt}})$ and n_{opt} as a function of the ratio $\ln(\sigma_{\text{R0}}/\langle R_0 \rangle)$ on Fig. 2.15, two linear relationships can be deduced for the n and α model parameters :

$$\ln(\alpha_{\text{fit}}) = 8.53 \ln\left(\frac{\sigma_{\text{R0}}}{\langle R_0 \rangle}\right) + 7.11, \qquad n_{\text{fit}} = -0.78 \ln\left(\frac{\sigma_{\text{R0}}}{\langle R_0 \rangle}\right) + 0.34, \tag{2.21}$$

where these two constant parameters are quite different from those obtained in [66] probably due to the fact that this study is investigated in 3D. Combining Eq. 2.20 and Eq. 2.21 results in the following improved B&T formulation :

$$\langle R \rangle^2 - \langle R_0 \rangle^2 = 1224.15 \left(\frac{\sigma_{\text{R0}}}{\langle R_0 \rangle}\right)^{8.53} M_{\text{b}} \gamma_{\text{b}} t^{-0.78 \ln\left(\frac{\sigma_{\text{R0}}}{\langle R_0 \rangle}\right) + 0.34}. \tag{2.22}$$

Although the set ($\ln(\alpha) = 3.56$; $n = 0.56$) obtained for the BiM initial grain size distribution predicts well the evolution of $\langle R \rangle$, it does not follow the trend obtained for the log-normal initial grain size distributions (see Fig. 2.15). So the formulation of the B&T model given by Eq. 2.22 is only accurate for log-normal initial grain size distributions. By using $\alpha = \alpha_{\text{fit}}$ and $n = n_{\text{fit}}$ in Eq. 2.20, small $L^2_{\text{B\&T}}$ are obtained (see beige bars on Fig. 2.12). An interesting prospect of this study is to perform the same analysis for different bimodal distributions.

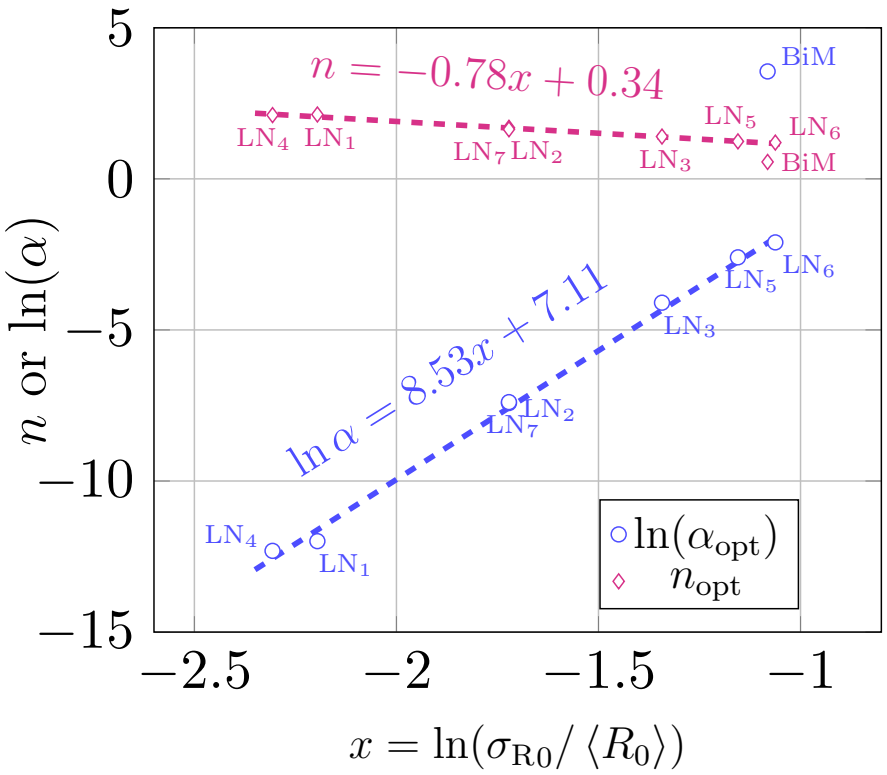

Fig. 2.15. *Optimized values α_{opt} and n_{opt} obtained by inverse analysis from the full field simulation results and linear relationships between the set of parameters ($ln(\alpha)$;n) and the ratio $ln(\sigma_{R0}/\langle R_0\rangle)$.*

Summary

This first chapter introduced the LS-FE formalism considered for full field simulations. Polycrystals are modeled using the LS method while boundary migration is performed by solving a set of partial differential equations using the FE method. Some limitations inherent to the LS method, such as vacuum, overlapping and loss of metric properties, were discussed and the considered treatments developed during previous studies [135, 138, 146] and considered in this formalism were presented.

Based on this LS-FE formalism, 3D-GG full field simulations were performed and results were used to discuss two analytical GG models during the transient regime: the Hillert/Abbruzzese and B&T models. More particularly, the influence of the initial grain size distribution characteristics on microstructure responses during the transient regime are discussed thanks to full field simulations considering an initial number of 8000 grains. It is worth noticing that these results were published in 2016 [173] and from this date, a new step in 3D-GG full field simulations was reached with the consideration of polycrystal of more than 500 000 grains [141, 169]. In [169], large-scale GG simulations were used to validate the ability of the classic B&T formulation during the steady state regime but the transient regime was not considered. In [141], authors showed that the classic B&T formulation is always consistent if the considered number of grains is high enough in the RVE, but since the GG simulation times are very high, the transient regime is not really studied. Even if the transient regime is not directly studied in these studies, these ultra large-scale GG models are primordial to understand the behavior of polycrystals at steady-state regimes of GG.

Results showed that Hillert/Abbruzzese model is versatile since it considers the initial grain size distribution of the microstructure. However this model relies on a first-order parameter β which needs to be finely calibrated in the transient regime. Numerical full field investigations have highlighted a new value for β, which is globally constant around 1.4 for all initial distributions in this regime. We have finally demonstrated that the calibrated Hillert/Abbruzzese model predicts finely $\langle R \rangle$ and the evolution of the distribution curves during the transient regime, even for the BiM distribution.

The classical B&T model does not take the initial grain size distribution into account, which makes it inaccurate during the transient regime. Based on full field simulation results, a new B&T formulation given in Eq. 2.22 was proposed in this regime. This new formulation proved to be able to predict accurately the evolution of $\langle R \rangle$ for any log-normal initial grain size distribution, regardless of σ_{R0} and $\langle R_0 \rangle$. On the other hand, this new model is not universal and needs to be improved in order to consider other kinds of initial grain size distribution, like bimodal distributions.

A main advantage of the LS-FE approach is the ability to model complex geometries, even at large deformations. Therefore in the next chapter, the LS-FE approach is extended for 3D modeling of DRX and PDRX at high strain levels and with relatively low computational costs.

Chapter 3

Modeling of dynamic and post-dynamic recrystallization by coupling a full field approach to phenomenological laws

Contents

3.1 Introduction 77

3.2 Modeling of dynamic and post-dynamic recrystallization 78

3.2.1 Initial polycrystal 78

3.2.2 Grain boundary migration 78

3.2.3 Strain hardening and recovery 78

3.2.4 Nucleation 81

3.3 Sensitivity study of the model 86

3.3.1 Dynamic recrystallization 86

3.3.2 Post-dynamic recrystallization 93

3.4 Comparison with predictions of a mean field model 95

3.4.1 Dynamic recrystallization 95

3.4.2 Post-dynamic recrystallization 102

Résumé en français

Le formalisme champ complet utilisé au CEMEF et présenté dans le chapitre précédent était jusqu'à présent dédié aux seuls mécanismes de croissance de grains et recristallisation statique. Dans ce chapitre, une extension de ce formalisme afin de modéliser les mécanismes de recristallisation dynamique et post-dynamique est présentée. Ces mécanismes sont modélisés en couplant la méthode Level-Set pour le suivi des joints de grains avec des lois phénoménologiques pour décrire les mécanismes d'écrouissage, restauration et germination. Contrairement à d'autres modèles de la littérature, ce modèle ne considère pas de plasticité cristalline afin de limiter son coût numérique. Un avantage majeur de ce modèle est lié au fait qu'il est capable d'atteindre de grandes déformations en trois dimensions et avec des temps de calcul relativement faibles. Finalement une comparaison entre ce nouveau modèle champ complet et un modèle champ moyen de la littérature permet de mettre en évidence les limites actuelles des modèles champ moyen.

This chapter presents a full field model of dynamic and post-dynamic recrystallization in 3D polycrystals, with an accurate description of grain topology at large deformations. This model is based on the Level-Set method in a finite element framework as introduced in chapter 2. Topological evolutions are simulated based on a kinetic law linking the velocity of the boundaries to the thermodynamic driving forces. Recrystallization is modeled by coupling a Level-Set approach to phenomenological laws describing strain hardening, recovery and nucleation. Although the proposed formalism does not consider crystal plasticity because of its computational costs, it enables to reach outstanding dynamic recrystallization computations in a front-capturing finite element framework comparatively to the state of the art.

3.1 Introduction

Literature already provides a large number of papers on full field modeling of DRX as presented at the end of the first chapter. However, a major drawback of these models is the difficulty to handle grain topology and morphology for large deformations [106, 130], which is a major limitation since many industrial processes go well further in deformation. Furthermore, crystal plasticity is generally used in DRX full field models since it predicts accurately the local evolution of dislocation density at the polycrystalline scale [101,110,111,115]. However, the use of crystal plasticity often leads to prohibitive computational costs. Finally, most of DRX full field models are developed in 2D because of numerical issues and computational costs [53, 106, 111]. Microstructure evolutions present a three-dimensional character, therefore results obtained from 2D models may not be representative of a real process. Some limitations of 2D models are related to the location of nuclei, their initial size or growth rates.

In the present work, we proposed a 3D model based on the Level-Set finite element framework (LS-FE) introduced in chapter 2. This model is proposed in context of unstructured tetrahedral mesh to model the DRX and PDRX phenomena with application to 304L steel. This latter is able to describe grain topology at large deformations (for instance $\varepsilon > 2$) with relatively low computational costs. The equations proposed and validated in a mean field model [49, 50] are used in this model to simulate nucleation, work hardening and recovery while the LS approach coupled to a remesher provides an accurate tracking of grain boundaries all along the simulation. The next section of this chapter introduces the modeling of the grain boundaries network and grain boundary kinetic. This section is followed by the presentation of the main constitutive equations for strain hardening, dynamic recovery and nucleation. Then, a sensitivity study of optimal model parameters (mesh size, initial number of grains, deformation step, time step and critical nucleus radius) on microstructure responses of the model is investigated. The subsequent section presents a comparison between our full field model and the mean field model of Beltran et al. [50] introduced in first chapter.

3.2 Modeling of dynamic and post-dynamic recrystallization

3.2.1 Initial polycrystal

As already seen in the chapter 2, the generation of polycrystals can be performed directly from experimental pictures or from statistical numerical methods such as Voronoï and Laguerre-Voronoï methods (see from Eq. 2.2 to Eq. 2.6). For GG simulations performed in the chapter 2, we made the assumption that the microstructure was free of stored energy to consider only grain growth due to capillarity effects. However, for modeling of DRX and PDRX, a stored energy field must be considered. Therefore, at the initial stage of the simulation, an energy field noted E, considered constant per grain and representative of a 304L steel, is initialized in the unstructured finite element mesh. This energy field can be generated either according to a particular distribution (Gaussian, log-normal, bimodal) or from experimental data. Furthermore, the energy field can be related to a dislocation density field ρ according to the following relationship :

$$E = \tau\rho, \tag{3.1}$$

where τ represents the unit dislocation line and is considered as material dependant. As already mentioned in previous chapters, a NR grain denotes a grain that is present from the first stage of simulation while a RX grain denotes a new grain appearing during the simulation. Thus, at initial stage of simulations, the polycrystal is only composed of NR grains.

3.2.2 Grain boundary migration

As detailed in chapter 1, grain boundaries migrate during a process at a high temperature, due to the jump in stored energy across grain boundaries and due to grain boundary curvature. Modeling of grain boundary migration in the LS-FE formalism was already presented in chapter 2 and is performed by solving the set of Eqs. 2.10.

3.2.3 Strain hardening and recovery

During plastic deformation, dislocation density increases in the microstructure due to strain hardening, resulting in an increase of the stored energy. However, a part of dislocations can also annihilate due to dynamic recovery. All these mechanisms were detailed in chapter 1. The modeling of strain hardening and recovery can be considered at different scales: at a local scale with crystal plasticity [53,111,130] or at a macroscopic scale with phenomenological laws [76,174,175]. In this model, phenomenological laws are considered to limit the computational cost of the 3D simulations, thus none resolution of a mechanical problem is considered. The deformation is simply modeled by applying a normal velocity on different faces of the RVE so as to respect a given strain rate and a velocity gradient. Each mesh node is thus displaced according to these velocities. During deformation, the faces of the RVE remain plane (homogeneous material

assumption) and the volume conservation of the RVE is ensured (incompressible material). Furthermore to ensure a good mesh quality, remeshing operations are performed every 0.2 of strain.

Considering N_g grains in the microstructure, the averaged dislocation density field obtained from Eq. 3.1 in each grain i noted ρ_i, is assumed to evolve according to the Yoshie-Laasraoui-Jonas law [76], as used in the model of Beltran et al. (Eq. 1.44) :

$$\frac{\partial \rho_i}{\partial \varepsilon} = K_1 - K_2 \rho_i, \tag{3.2}$$

where ε denotes the strain level, K_1 and K_2 are two constants representing the strain hardening and dynamic recovery term, respectively. At each time increment, this differential equation is solved with an Euler explicit method, i.e. :

$$\frac{\rho_i^{(t+\Delta t)} - {\rho_i}^t}{\Delta \varepsilon} = K_1 - K_2 {\rho_i}^t, \tag{3.3}$$

where $\Delta\varepsilon$ is equal to $\dot{\varepsilon} \times \Delta t$ with Δt the time step, leading to the final equation :

$$\rho_i^{(t+\Delta t)} = K_1 \Delta\varepsilon + (1 - K_2 \Delta\varepsilon) {\rho_i}^t. \tag{3.4}$$

When a grain boundary migrates, the swept volume is almost free of defects. This phenomenon is traduced by a decrease of the dislocation density in growing grains. Thus a minimal dislocation density ρ_0, which is material dependant, is attributed to swept volumes. Then the new dislocation density is averaged in each grain following the equation :

$$\rho_i^{(t+\Delta t)} V^{(t+\Delta t)} = {\rho_i}^t V^t + \Delta V \rho_0, \tag{3.5}$$

where ΔV represents the swept volume between the instants t and $(t+\Delta t)$. Fig. 3.1 shows the evolution of a dislocation density field in a 2D schematized grain between t and $(t+\Delta t)$ due to strain hardening, dynamic recovery and grain boundary migration.

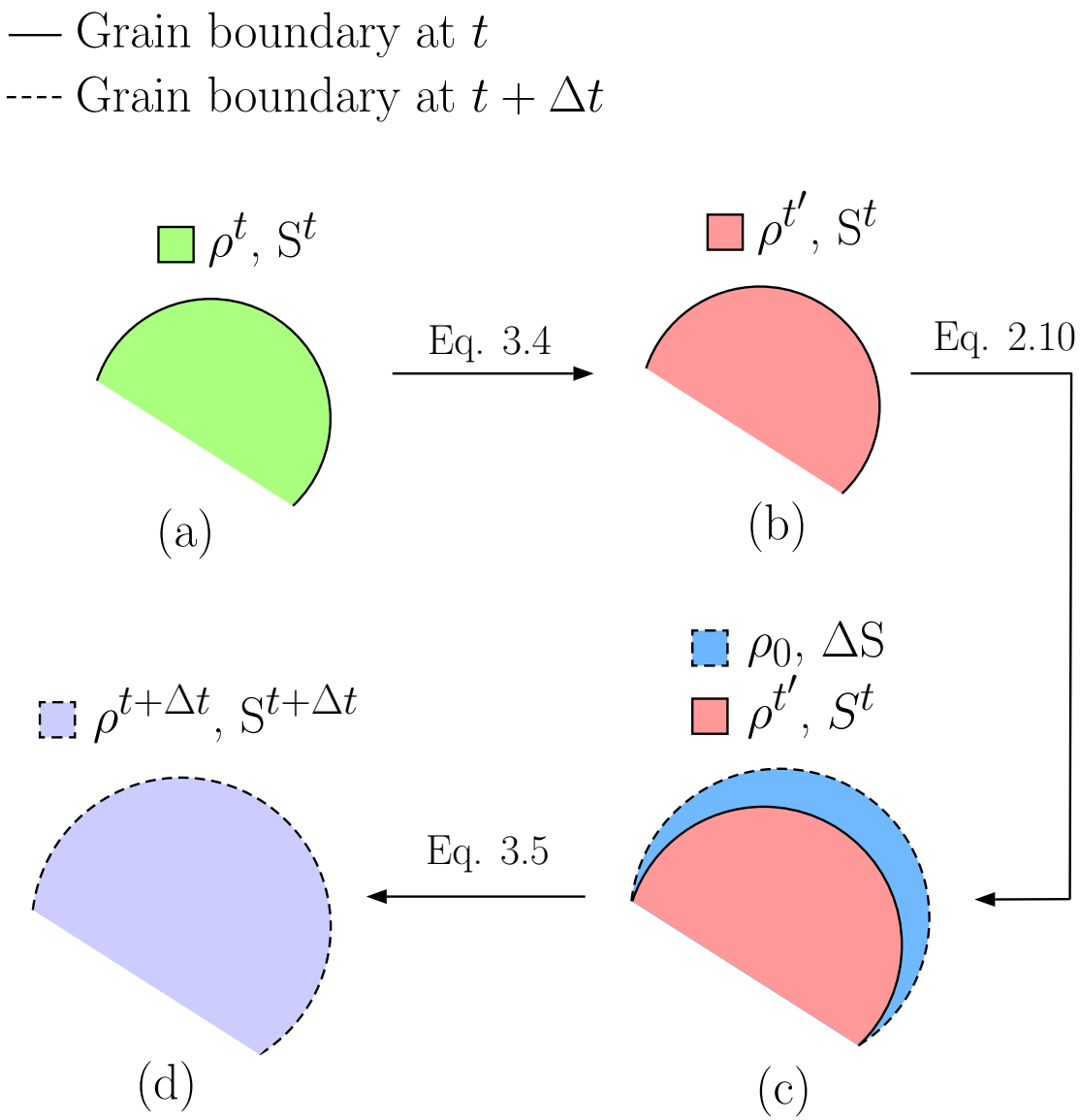

Fig. 3.1. *2D scheme illustrating the evolution of a dislocation density field of a single grain due to strain hardening and dynamic recovery (from (a) to (b)), grain boundary migration (from (b) to (c)) and decrease of dislocation density due to boundary migration (from (c) to (d)) between the instants t and $(t + \Delta t)$ of the simulation.*

PDRX is taken into account after deformation by modeling boundary migration given by the set of Eqs. 2.10 and the decrease of dislocation density due to boundary migration given by Eq. 3.5. Furthermore, the static recovery due to annihilation of dislocations is taken into account here using the same recovery law as used in the model of Beltran et al. (Eq. 1.45) :

$$\dot{\rho}_i = -K_s \rho_i, \tag{3.6}$$

where K_s is a temperature dependant parameter which represents the static recovery

term and a superposed dot denotes differentiation with respect to time. During PDRX, no nucleation of new grains is considered, thus the following section on nucleation only concerns DRX.

The mean flow stress σ_i in the i^{th} grain is computed during deformation from its average dislocation density ρ_i using the Taylor's equation (Eq. 1.47). Then the macroscopic flow stress σ is calculated as a volume average of the flow stresses in all grains :

$$\sigma = \frac{\sum \sigma_i V_i}{\sum V_i}. \tag{3.7}$$

3.2.4 Nucleation

When enough energy is accumulated in the material due to plastic deformation, some dislocation networks can develop within grains and tend to form new RX grains called nuclei, mainly located at grain boundaries [5]. In this model, nucleation is modeled by the SIBM mechanism, as considered in models of Cram & Zurob [70] and Beltran [50] introduced in first chapter. Different criteria need to be verified locally in order to obtain a substructure that becomes a nucleus: a mobile high-angle grain boundary has to be formed by the nucleation event, a high stored energy gradient across the grain boundary must be present in order to provide enough positive driving pressure for counter the capillarity effects applied on the nucleus. In the considered framework, since γ_b is assumed isotropic, only the stored energy and the critical nucleus radius are taken into account for nucleation event.

Nuclei location

The adopted strategy concerning the creation of new nuclei in a FE-LS framework is based on the recent developments of Scholtes et al. [143]. In the considered model, we assume that new nuclei of critical radius r_{cr} only appear close to grain boundaries. This restriction is taken into account by forcing the centers of new nuclei inside a layer $\pm L$ around grain boundaries, where $L = r_{cr}$ (see Fig. 3.2 for more details).

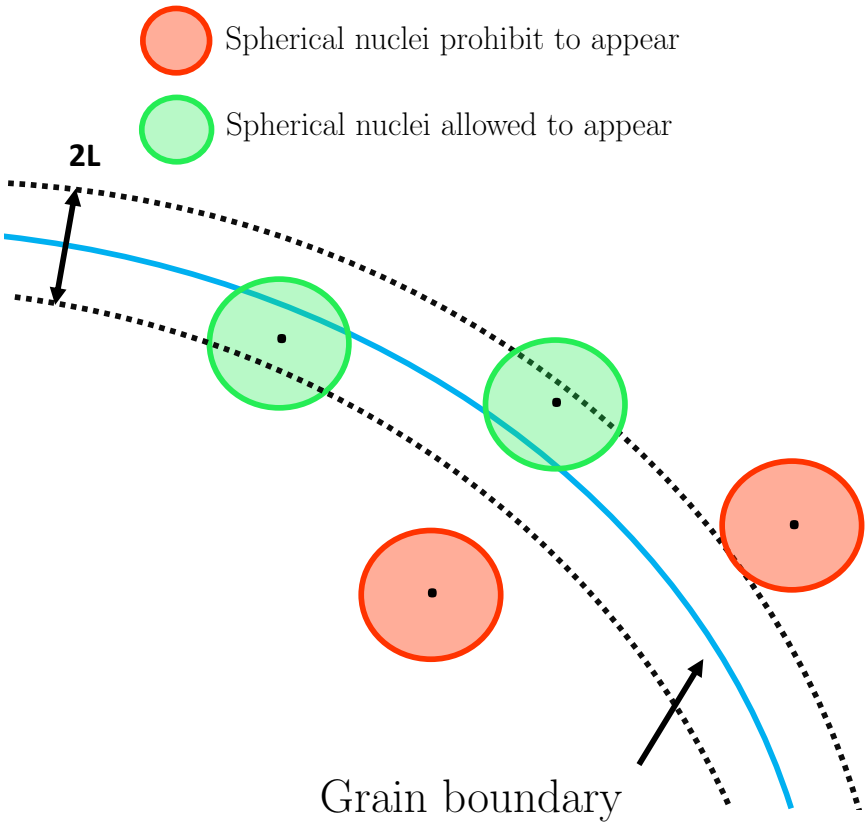

Fig. 3.2. *Examples of nuclei that are allowed (green color) and prohibit (red color) to appear depending on the distance from the grain boundary to their centers.*

Critical stored energy for nucleation

In the considered model, we assume that a new nucleus can appear if the averaged stored energy in its appearance surface reaches a critical value ρ_{cr}. This restriction is taken into account by averaging the energy in the volume occupied by the nucleus before its appearance, and by verifying if this averaged energy reaches ρ_{cr}. (see Fig. 3.3 for more details). If this condition is verified and if its position satisfies the condition presented previously, the new nucleus can be created with a stored energy ρ_0 and a radius r_{cr}.

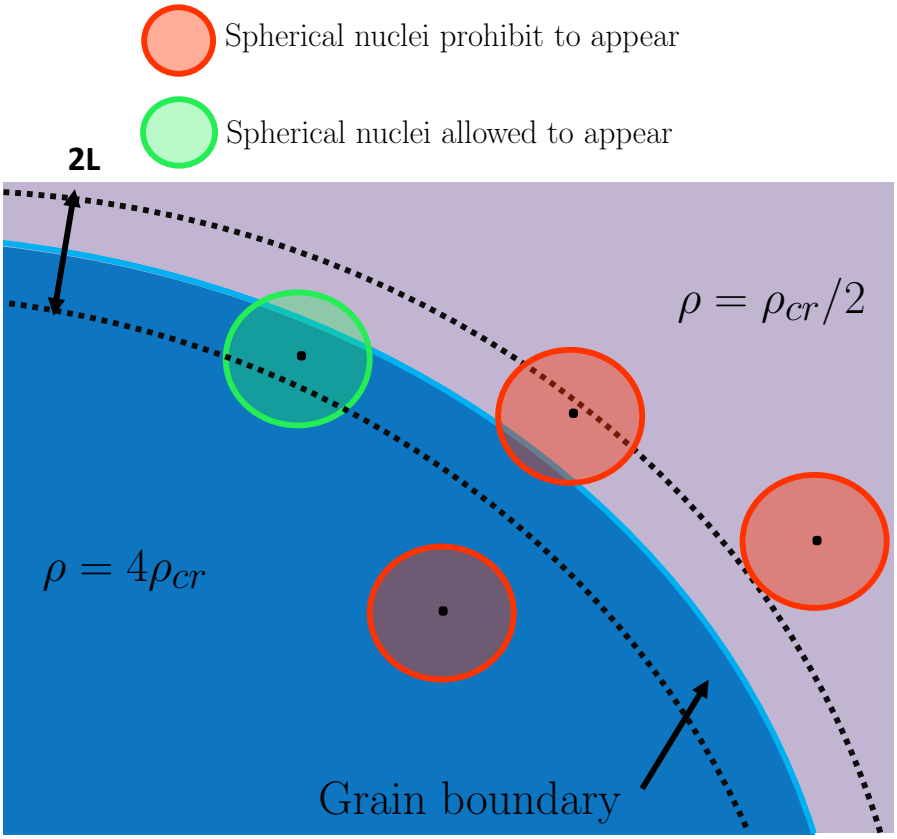

Fig. 3.3. *Examples of nuclei allowed (green) and prohibit (red) to appear depending on whether the averaged stored energy in the volume occupied by each nucleus before its appearance reached the critical dislocation density* ρ_{cr}.

To compute the critical dislocation density ρ_{cr}, the method used in [50] and already presented in first chapter is reproduced: a first value of ρ_{cr} is estimated thanks to Eq. 1.54 and an iterative calculation is performed according to Eq. 1.55, where the parameter K_3 is replaced here by the product $M_{\mathrm{b}}\delta\tau$, leading to :

$$\rho_{\mathrm{cr}} = \left(\frac{20K_1\gamma_{\mathrm{b}}\dot{\varepsilon}}{3M_{\mathrm{b}}\delta\tau^2}\right)^{1/3}, \tag{3.8}$$

$$\rho_{\mathrm{cr}} = \left[\frac{-2\gamma_{\mathrm{b}}\dot{\varepsilon}\dfrac{K_2}{M_{\mathrm{b}}\delta\tau^2}}{\ln\left(1-\dfrac{K_2}{K_1}\rho_{\mathrm{cr}}\right)}\right]^{1/2}. \tag{3.9}$$

The influence of the temperature on ρ_{cr} is taken into account in Eq. 3.9 thanks to the parameters K_2 and M_{b} while the influence of the strain rate on ρ_{cr} is taken into account in Eq. 3.9 thanks to the parameters K_1, K_2, $\dot{\varepsilon}$ and δ. It is assumed that ρ_{cr} increases

when decreasing temperature or increasing strain rate.

Nucleus critical radius

When a new nucleus appears in the microstructure, its critical radius must be high enough so that its stored energy counters the capillarity forces applied by the neighboring grains. This corresponds to the condition when the stored energy of the material is large enough to overcome the capillarity effects exerted by neighboring grains on the nucleus. This condition is approximated from the so-called Bailey-Hirsch criterion [36] already discussed in the first chapter (Eq. 1.8) and obtained by solving the equilibrium equation between force due to stored energy and force due to capillarity effects, i.e :

$$P_{\mathrm{e}} = P_c, \tag{3.10}$$

$$\tau(\rho_{\mathrm{cr}} - \rho_0) = \frac{2\gamma_{\mathrm{b}}}{r_{\mathrm{cr}}}. \tag{3.11}$$

By neglecting ρ_0, it leads to :

$$r_{\mathrm{cr}} = \omega \frac{2\gamma_{\mathrm{b}}}{\rho_{\mathrm{cr}}\tau}, \tag{3.12}$$

where $\omega > 1$ is a security factor ensuring that the created nucleus has a required driving force for growth. Indeed the Eq. 3.12 with ω = 1 is based on the assumption that a new nucleus is perfectly spherical but in the present model, depending on the mesh size, the nucleus cannot be perfectly spherical, which justifies the use of the security factor ω. The value of ω is investigated in the following.

Nucleation rate

The nucleation rate $\dot{V}$ representing a volume of nuclei per unit of time, is calculated according to a variant of the proportional nucleation model of Peczak and Luton [176] :

$$\dot{V} = K_{\mathrm{g}} \Phi \Delta \mathrm{t}, \tag{3.13}$$

where K_{g} is a probability coefficient related to the thermomechanical conditions, i.e. the temperature and the effective plastic strain rate and Φ represents the total boundary surface (in a necklace-type nucleation) or total volume (in a bulk-type nucleation) of grains verifying $\rho_i > \rho_{\mathrm{cr}}$.

For better understanding of the coupling between LS method and recrystallization governing laws, a flow chart summarizing the resolution method of the present model for a given process time is presented on Fig. 3.4.

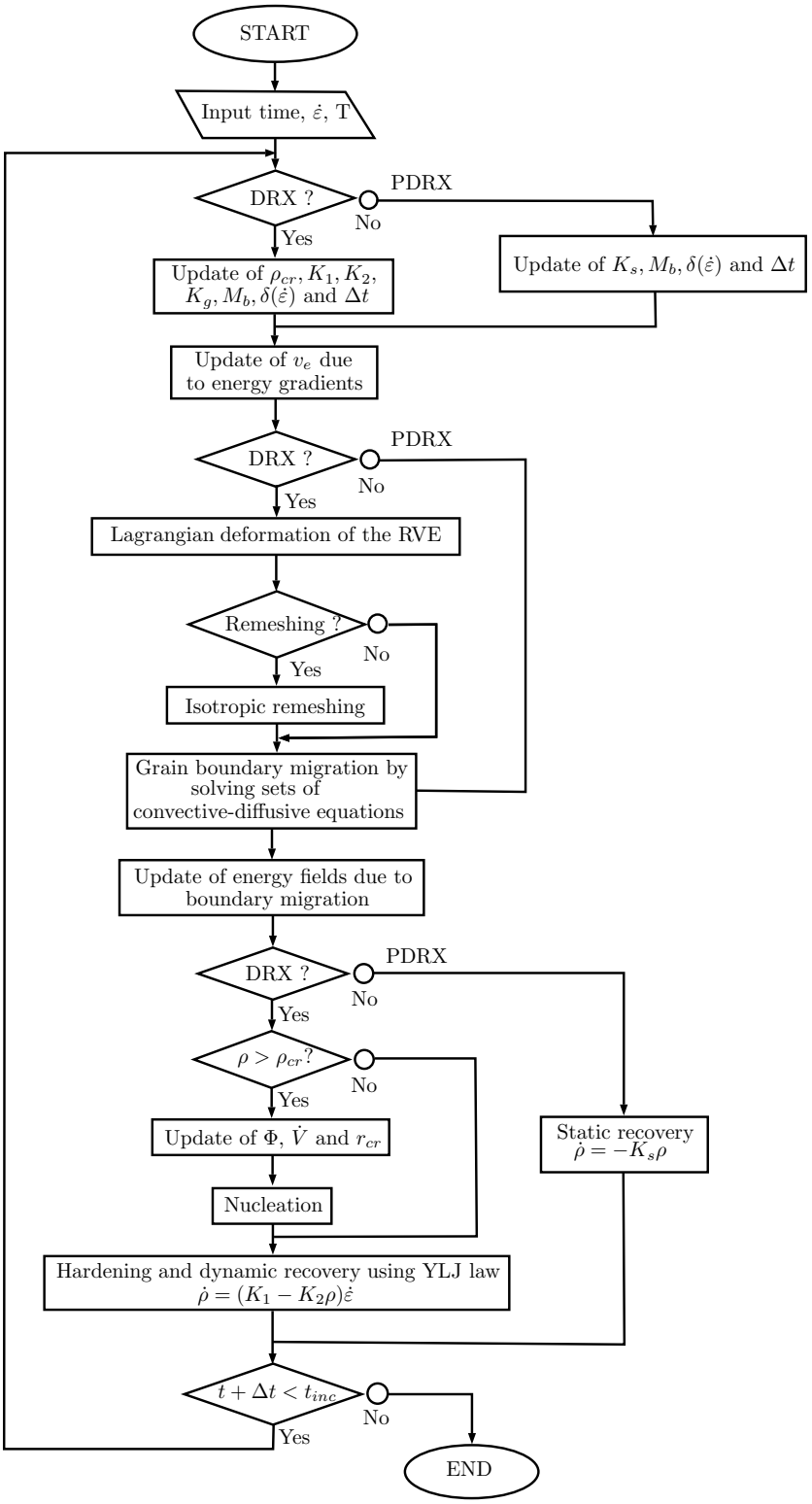

Fig. 3.4. *Scheme describing the resolution method of the present model for a given step time t_{inc}, strain rate $\dot{\varepsilon}$ and temperature T.*

3.3 Sensitivity study of the model

This model considers many parameters which have to be correctly initialized in order to model as accurately as possible the microstructure mechanisms, while keeping relatively low computational costs. This section is dedicated to a sensitivity study of initial parameters leading to converged results of DRX and PDRX.

3.3.1 Dynamic recrystallization

An identification of the optimal mesh size, initial number of grains, deformation step and critical nucleus radius of the DRX model leading to converged results while keeping low computational costs is done in this section.

Mesh size

A single nucleus is considered and the mesh size is calibrated so as to obtain a good description of this nucleus in terms of surface and volume. The isotropic mesh size must be small enough to correctly describe the nucleus mean curvature but also reasonable in order to limit the computational cost. Thus four spherical nuclei of radius 20μm are generated using four different mesh sizes and results are presented on Fig. 3.5. The quantity ξ corresponds to the ratio between the nucleus radius r_{cr} and the mesh size and is reported below each nucleus on Fig. 3.5. The quantity E_{v} corresponds to the L^1 error between the volume of the generated nucleus of radius r_{cr} (presented on Fig. 3.5) and the volume of a real sphere of radius r_{cr}. The error between the surfaces is also measured and noted E_{s}. These values are reported below each nucleus on Fig. 3.5.

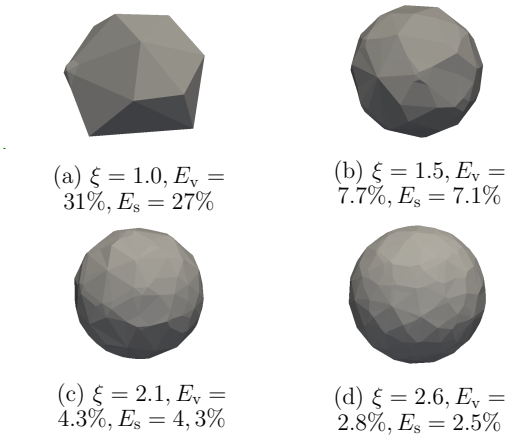

(a) $\xi = 1.0, E_{\text{v}} = 31\%, E_{\text{s}} = 27\%$

(b) $\xi = 1.5, E_{\text{v}} = 7.7\%, E_{\text{s}} = 7.1\%$

(c) $\xi = 2.1, E_{\text{v}} = 4.3\%, E_{\text{s}} = 4,3\%$

(d) $\xi = 2.6, E_{\text{v}} = 2.8\%, E_{\text{s}} = 2.5\%$

Fig. 3.5. *Four nuclei generated according to different mesh sizes. ξ corresponds to the ratio between the nucleus radius r_{cr} and the mesh size. E_v (resp. E_s) corresponds to the L^1 error between the volume (resp. surface) of the generated nucleus and the volume (resp. surface) of a sphere of same radius.*

It is observed that in each case, the E_{v} error is close to the E_{s} error. The nucleus presented on Fig. 3.5(a) has large E_{v} and E_{s} errors (31% and 27%, respectively). The three

other nuclei presented on Fig. 3.5(b), (c) and (d) give E_v and E_s errors lower than 10%, leading to a better description of the nuclei in these three cases. A ratio $\xi \simeq 2$ between the nucleus radius and the mesh size is chosen as a good compromise between a minimum number of mesh elements into the nucleus and low E_v and E_s errors. Thus, the future number of mesh elements in the full field simulations is always chosen so as to respect a ratio $\xi \simeq 2$.

Initial number of grains

Several full field simulations of DRX were performed using the considered model for a temperature of 1273K and a strain rate of 0.01s^{-1} during 300s. The deformation of the RVE is idealized at each increment by updating all mesh node coordinates at the instant $t+\Delta t$ thanks to the relations :

$$\begin{aligned} x^{t+\Delta t} &= x^t, \\ y^{t+\Delta t} &= (1+\dot{\varepsilon}\Delta t)y^t, \\ z^{t+\Delta t} &= (1-\dot{\varepsilon}\Delta t)z^t, \end{aligned} \tag{3.14}$$

with $(x^t;y^t;z^t)$ and $(x^t+\Delta t\ ;\ y^t+\Delta t\ ;\ z^t+\Delta t)$ the coordinates of a mesh node at the instants t and $t+\Delta t$ respectively, considering the $(0,\vec{x},\vec{y},\vec{z})$ Cartesian coordinate system (see Fig. 3.6), $\dot{\varepsilon}$ the strain rate following the direction of solicitation (i.e. direction $\vec{z}$) and Δt the time increment. These equations lead to an idealized channel-die case, where the six faces remain plane during the simulated process. Computations were performed on three nodes of 24 CPU processors each in order to compare computational costs. The variation of the initial number of grains is done by keeping the same initial mean grain radius ($\simeq 60\mu$m) and by varying the RVE size (from 0.14mm^3 to 0.34mm^3). The security factor ω (Eq. 3.12) is taken equal to 2, leading to a critical nucleus radius of 7μm. The mesh size is fixed to 3μm in order to validate the ratio $\xi \simeq 2$. The deformation step is taken low enough (2%) to ensure a good convergence of simulation results. Microstructures are presented on Fig. 3.6 and results in terms of RX fraction, mean grain radius (weighted by grain volume), mean dislocation density (weighted by grain volume), computational cost, grain radius distribution and dislocation density distribution are plotted on Fig. 3.7. The distributions are plotted at a true strain ε = 1. Only grains from 0 to 12 μm were considered on Fig. 3.7(e) since these grains represent more than 99% of the total number of grains in the microstructure. It is clearly observed that a total of 8 grains in the initial microstructure leads to results as close as with a number of 20 or 40 grains (see Fig. 3.7). Indeed our nucleation model considers a random nucleation on high energy grain boundaries. So during the DRX mechanism when all grains have a sufficient energy, nuclei appear everywhere at grain boundaries and the total number of grains rapidly increases in the microstructure, reducing the influence of the initial number of grains in this case. Two simulations with two different initial number of grains (8 and 27 grains) and exactly the same initial grain radius distribution and energy distribution are presented on Fig. 3.6. It is clearly observed at ε = 1.5 that the volumic fractions of nuclei are similar in the two cases. Thus it is assumed that the

accuracy of the results is sufficient here with an initial number of 8 grains.

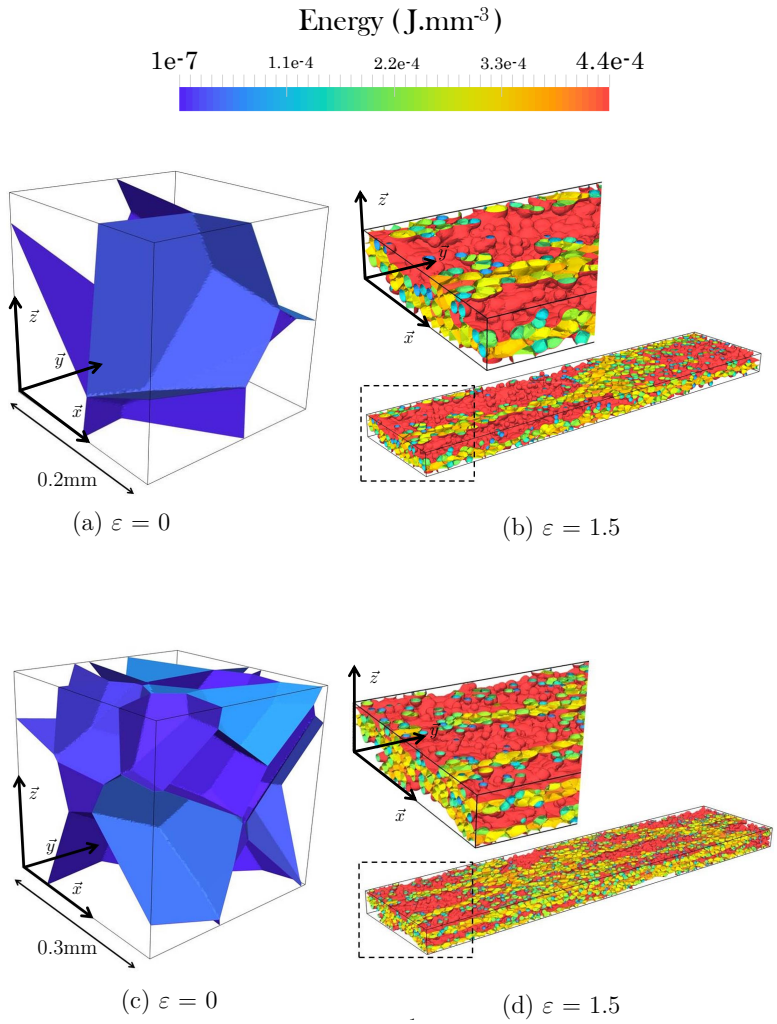

(a) $\varepsilon = 0$ (b) $\varepsilon = 1.5$

(c) $\varepsilon = 0$ (d) $\varepsilon = 1.5$

Fig. 3.6. *Two simulations using two different initial number of grains: 8 inital grains for a true strain $\varepsilon = 0$ (a) and $\varepsilon = 1.5$ (b). 27 initial grains for a true strain $\varepsilon = 0$ (c) and $\varepsilon = 1.5$ (d). The simulated process is a channel-die configuration at 1273K and a strain rate of $0.01s^{-1}$ during 150s.*

Furthermore, using 8 initial grains instead of 40 initial grains reduces the computational cost by a factor of 9, which is a non negligible time saving (see Fig. 3.7(d)). An initial number of 3 grains was also tested. However, this small number of grains led to artefacts (important influence of the boundary conditions, a too small number of grains to respect precisely the input grain size distribution and an insufficient total grain boundary surface for the appearance of new grains after few time increments) and therefore to non-physical results, in particular concerning the distributions (see Fig. 3.7(e) and (f)). Thus, a minimum initial number of 8 grains is chosen for future simulations.

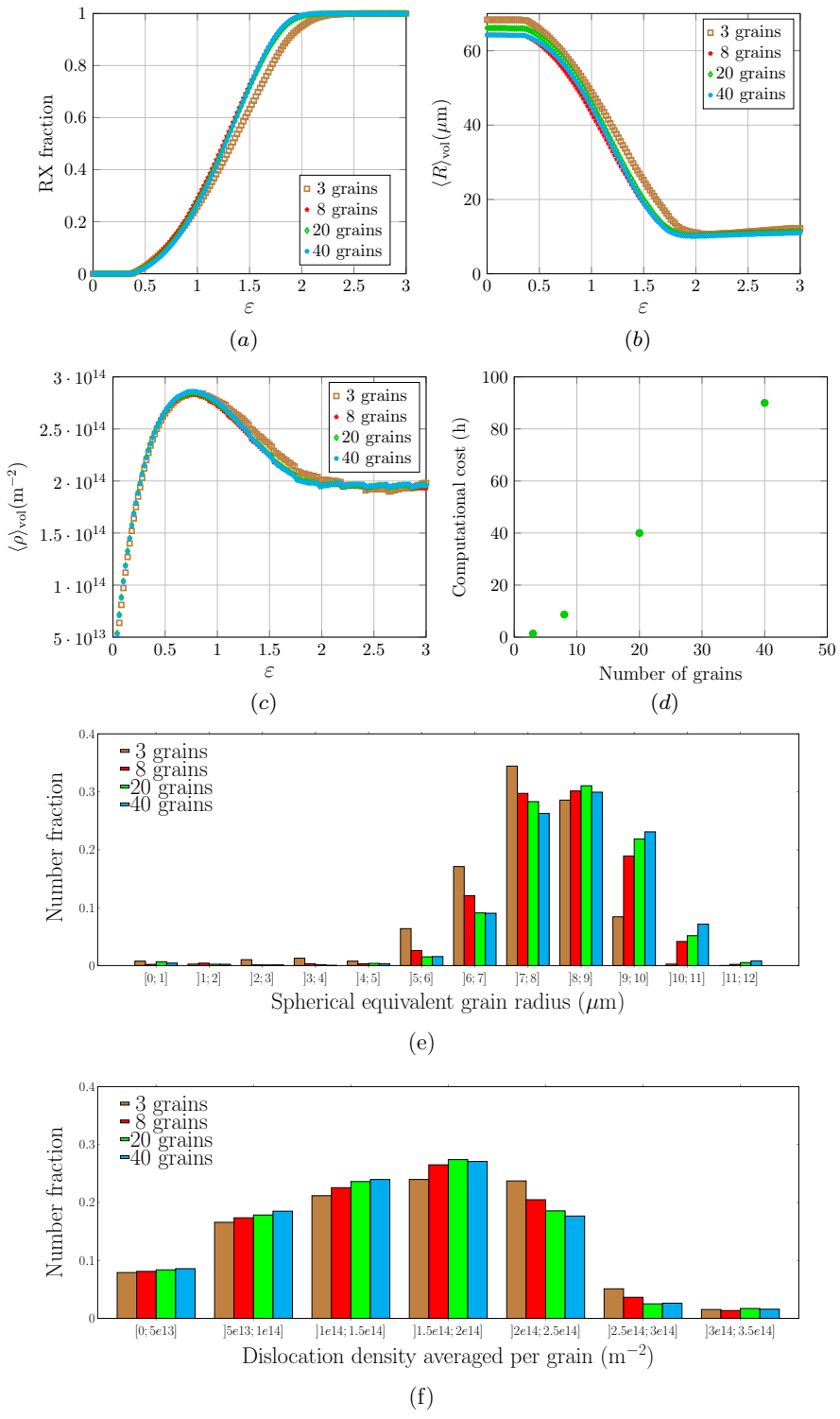

Fig. 3.7. *Sensitivity of the initial number of grains on polycrystal results. The simulated process is a channel-die compression at 1273K, at a strain rate of 0.01s^{-1} during 300s. The mean values are weighted by grain volume for a better representativeness of the curves at the onset of recrystallization.*

Deformation step

The strain hardening and dynamic recovery laws are directly related to the deformation step (see Eq. 3.2). Therefore a fixed time step is not enough to ensure convergence for any strain rate since the deformation step is given by the product between the time step and the strain rate. Thus, the idea of this section is to look for a deformation step that leads to converged results and then to use this ideal deformation step to deduce the associated time step.

According to the previous study, the initial number of grains is now fixed to 8 grains. The security factor ω and the mesh size are still fixed and equal to 2 and 3μm, respectively. To investigate the optimal deformation step, several simulations were done for four deformation steps (2%;5%;10%;20%). The same results as in the previous section (i.e. RX fraction, mean grain radius (weighted by grain volume), mean dislocation density (weighted by grain volume), computational cost, grain radius distribution and dislocation density distribution) were investigated on Fig. 3.8. When the deformation step decreases, all results converge toward the same trends. Furthermore, the computational cost is reduced by a factor of about 2 between 2% and 5% of deformation step while keeping close results (see computational cost on Fig. 3.8(d)). Thus a deformation step of 5% is chosen as a good compromise for all the future simulations.

Critical nucleus radius

The initial number of grains and deformation step are fixed to 8 and 5% respectively, and the influence of the critical nucleus radius, more particularly the security factor noted ω and used in Eq. 3.12, is thereafter investigated. Four different values of ω are tested (1;1.5;2;3) leading to the use of four different mesh sizes in order to respect the ratio $\xi \simeq 2$. The same results as in the previous section (i.e. RX fraction, mean grain radius (weighted by grain volume), mean dislocation density (weighted by grain volume), computational cost, grain radius distribution and dislocation density distribution) were investigated on Fig. 3.9. First, it is observed that the final mean grain radius $\langle R \rangle_{\text{vol}}$ and the grain radius distribution are highly influenced by the critical nucleus radius r_{cr}. This observation is important because it means that the final mean grain radius can be directly influenced by the security factor ω. By observing the four other curves, it is clearly observed that a security factor of 1 does not lead to converged results. This is due to the fact that a security factor of 1 leads to a critical nucleus radius too low to counter capillarity effects exerted by neighboring grains and thus the new nuclei do not survive, which explains the observed kinetic of RX fraction. In contrast, the two security factors of 1.5 and 2 lead to a good convergence of all presented results. Finally, a security factor of 3 does not lead to converged results in terms of RX fraction and $\langle \rho \rangle_{\text{vol}}$ because the critical nucleus radius is too large using this value and therefore results predicted by the model might be non-physical. Thus a security factor of 1.5 is chosen as the optimal value for the future simulations.

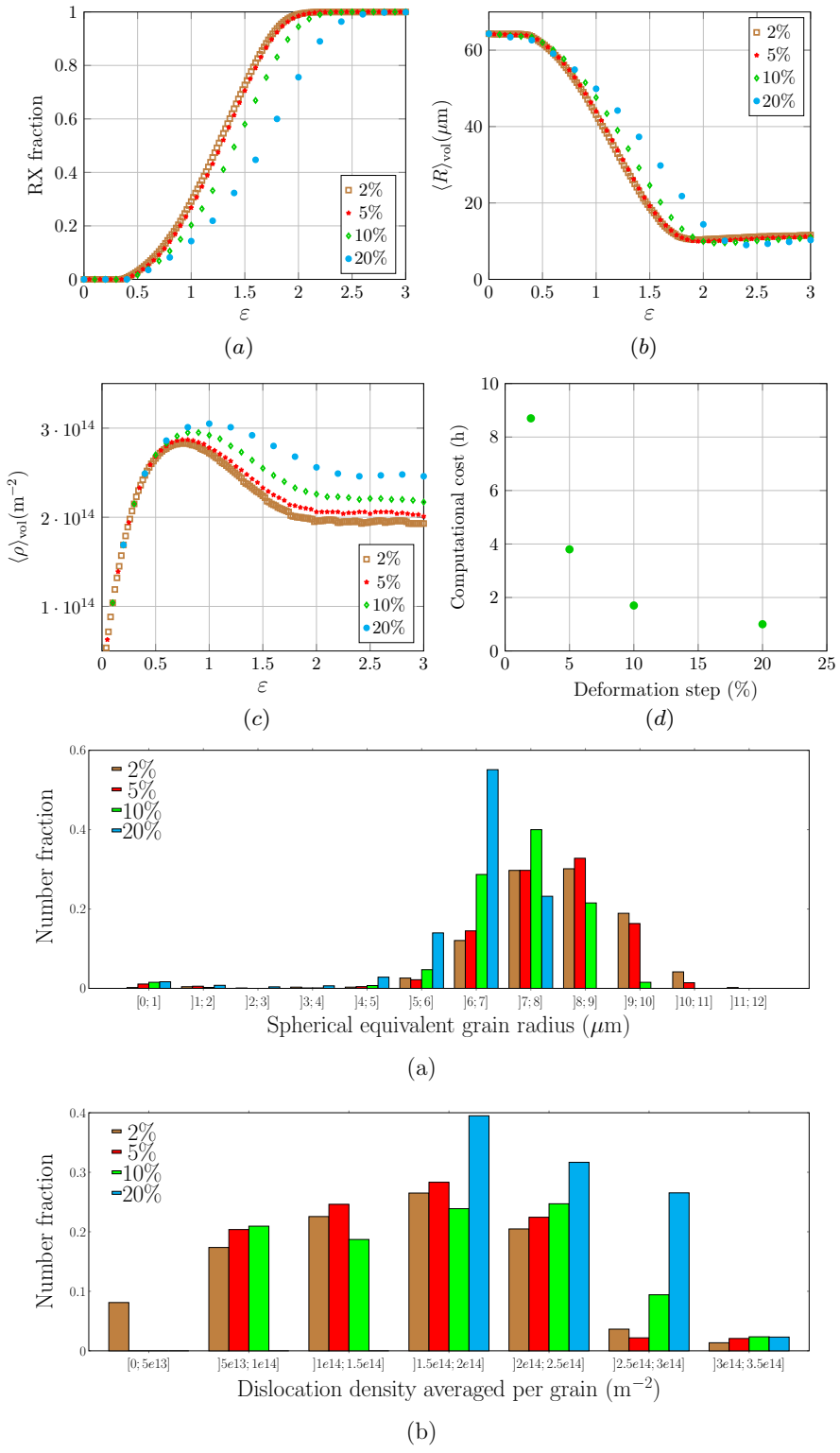

Fig. 3.8. *Sensitivity of the deformation step on polycrystal results. The simulated process is a channel-die compression at 1273K, at a strain rate of $0.01s^{-1}$ during 300s. The mean values are weighted by grain volume for a better representativeness of the curves at the onset of recrystallization.*

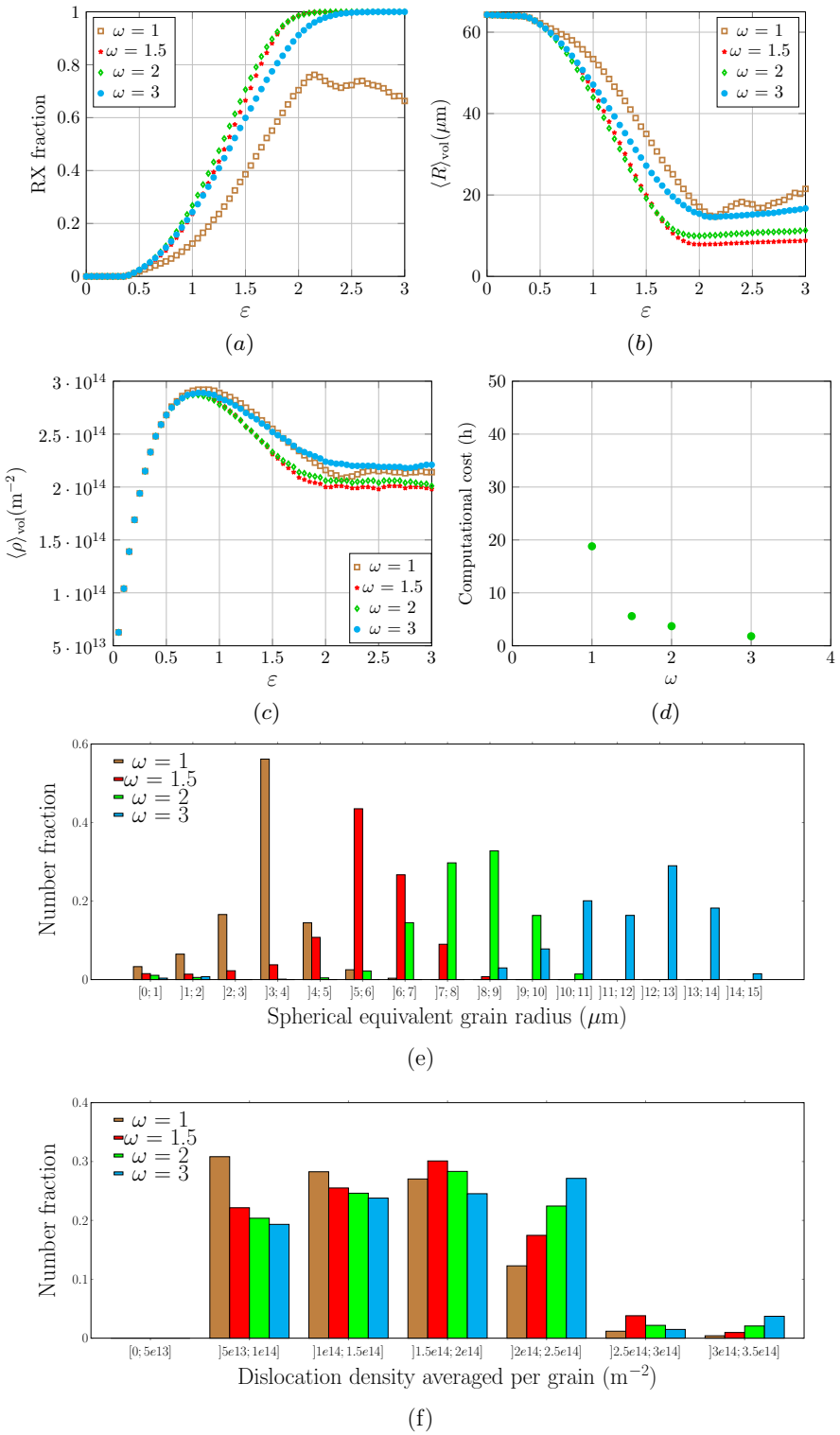

Fig. 3.9. *Sensitivity of the critical nucleus radius on polycrystal results. The simulated process is a channel-die compression at 1273K, at a strain rate of 0.01s^{-1} during 300s. The mean values are weighted by grain volume for a better representativeness of the curves at the onset of recrystallization.*

3.3.2 Post-dynamic recrystallization

Time step

The second convergence study concerns the ideal time step (Δt) used for PDRX simulations. If the displacement of a grain boundary is too high during Δt, the kinetic cannot be correctly captured. Thus, a solution is to adapt Δt as a function of a maximum displacement of grain boundaries. Let's consider the maximum displacement of a grain boundary $d_{\max}$ in a microstructure between t and $(t+\Delta t)$. This latter is given by the maximum velocity $v_{\max}$ in the microstructure between these two instants multiplied by the time increment Δt :

$$d_{\max} = v_{\max} \times \Delta t. \tag{3.15}$$

Furthermore, the highest value for $v_{\max}$ is reached if the smallest possible grain having the highest possible mean energy is surrounded by the largest possible grain having the lowest possible mean energy. Thus by using classical approximations for grain mean curvature, $v_{\max}$ is estimated as follow :

$$v_{\max} \simeq M_{\mathrm{b}} \left(\frac{2\gamma_{\mathrm{b}}}{\langle R \rangle} + \Delta E \right), \tag{3.16}$$

where $\Delta E = E_{\max}$ - $E_{\min}$. In context of anisotropy of M_{b} and/or γ_{b}, the same methodology could be used by using in Eq. 3.16 the maximum values of these physical parameters. Finally by combining Eqs. 3.15 and 3.16, the max displacement $d_{\max}$ is estimated at each step time by :

$$d_{\max} \simeq M_{\mathrm{b}} \left(\frac{2\gamma_{\mathrm{b}}}{\langle R \rangle} + \Delta E \right) \times \Delta t. \tag{3.17}$$

Then, it is necessary to find the ideal maximum displacement of grain boundaries in order to define the time step Δt at each increment thanks to Eq. 3.17. In this study, we define the ideal maximum displacement $d_{\max}$ as a percentage of mesh size and this choice is validated in the following.

Validation of the criterion for time step

To be representative of the PDRX mechanism, we assume four different simulations each representing a nucleus growing in a matrix (see Fig. 3.10). Each simulation is related to particular thermomechanical conditions (i.e. a couple of T and $\dot{\varepsilon}$) leading to a given critical nucleus radius r_{cr} (by using Eq. 3.12) and leading to a maximum dislocation density field in the matrix computed by the ratio K_1/K_2 which is the steady-state dislocation density according to Eq. 3.2 (since K_1 and K_2 depend on T and $\dot{\varepsilon}$). Furthermore, a dislocation density field ρ_0 = 1e11 m^{-2}, which is material dependant, is defined into the nucleus. We note R_{P} the ratio between the jump in stored energy (ΔE) across the boundary and the capillarity effect ($2\gamma_{\mathrm{b}}/r_{\mathrm{cr}}$). For each case, the mesh size is chosen so as to keep the ratio ξ between the nucleus radius and the mesh size

approximatively equal to 2 as demonstrated in the DRX sensitivity study of the previous section.

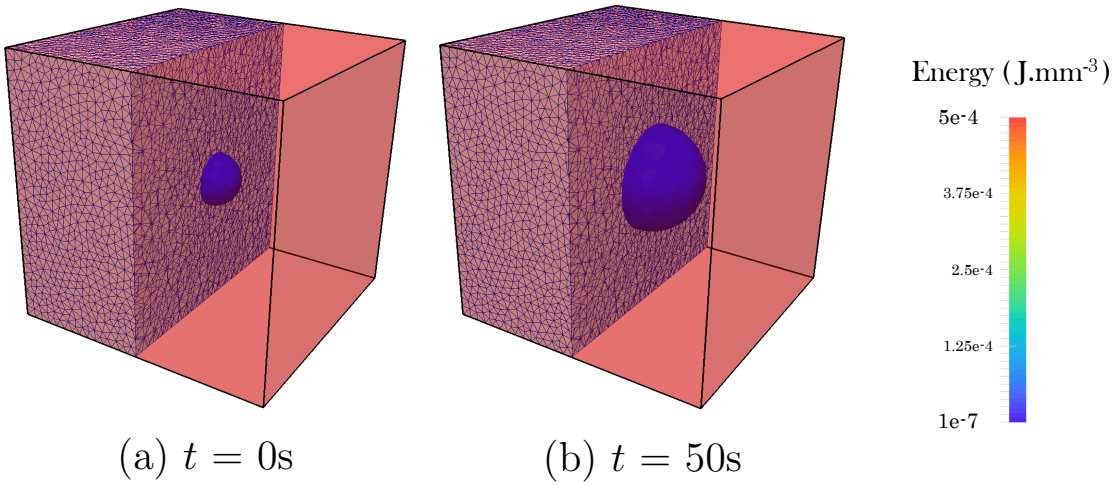

Fig. 3.10. *Growth of a nucleus immersed in a matrix. The critical nucleus radius is equal to 5.2µm. The energy in the nucleus and in the matrix are 1.47e-7 J.mm^{-3} and 4.9e-4 J.mm^{-3}, respectively.*

Different percentages of mesh size from 10% to 40% are investigated as maximum displacement $d_{\max}$. In every case, the evolution of the nucleus radius obtained by the numerical simulation is confronted to the analytical solution presented below :

$$r^{(t+\Delta t)} = r^t + M_b \Delta t \left(\Delta E - \frac{2\gamma_b}{r^t} \right), \tag{3.18}$$

The L^2 errors between the analytical solution and the numerical results are plotted on Fig. 3.11 for each case corresponding to a particular couple of thermomechanical conditions.

First, it is observed on Fig. 3.11 that the lowest errors are obtained for cases where the jump in stored energy across the grain boundary is dominant (i.e. highest values of R_P). This observation is logical and can be easily explained. The jump in stored energy term computed in the simulation is exact whereas the nucleus mean curvature is estimated by the Laplacian of the distance function and thus is mesh size dependant. Furthermore, as the mesh size is actually isotropic and non-refined around the grain boundary, a non-negligible error can appear on the capillarity term in the simulation. Thus when the jump in stored energy across the boundary is preponderant compared to the capillarity effects (i.e. high values of R_P), the error made on the estimation of the mean curvature is of second order in the velocity term and lower errors are observed with respect to the analytical solution.

Furthermore for a given nucleus size, the errors are observed dependant on the percentages of mesh size displacement (see Fig. 3.11). It is observed that the minimum

errors are globally obtained for the mesh size displacements of 10%, 20% or 30%. For a very small displacement, the error due to the reinitialization of the LS functions can be relatively high compared to the small displacement of the grain boundary, which can globally leads to inaccurate results. This aspect can explain that the 10%-case is globally less accurate than the 20%-case. For a large displacement (i.e. 40% of mesh size), the value of displacement seems too high during a single step time and thus the kinetic cannot be correctly captured. Indeed, our FE methodology remains of first order in time and important displacement during one time step can lead to non-physical results. Finally, 10%, 20% or 30% of mesh sizes give better results than 40% of mesh size. However, for reasons of computational costs, we retain a maximum displacement of mesh size $d_{\max}$ equal to 30% for the future PDRX simulations.

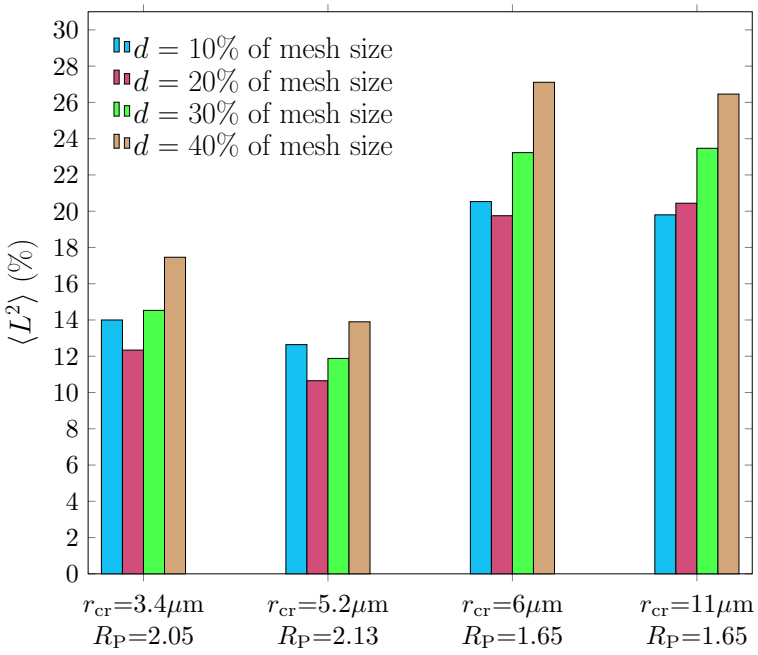

Fig. 3.11. *L^2 Error on the equivalent mean grain radius evolution between the full field simulations and the scheme defined by Eq. 3.18. r_{cr} is the critical nucleus radius. R_p is the ratio between the velocity due to capillarity effects and the velocity due to the jump in stored energy across the boundary. Each color corresponds to a specific displacement of mesh size performed at each increment of the model.*

3.4 Comparison with predictions of a mean field model

3.4.1 Dynamic recrystallization

This full field model is based on same phenomenological laws as an existing mean field model [49, 50] for nucleation, hardening and recovery. However, contrary to mean field models, this full field model presents the advantage to fully describe, in time and space, the grain boundary network thanks to the LS approach. Therefore, the idea of this sec-

tion is to compare this full field model with the mean field model of Beltran et al. [50] introduced in first chapter, in order to observe the influence of respecting the topology of the microstructure.

The governing laws of hardening, recovery and nucleation mechanisms are identical in the two considered mean field and full field models. The main limitation of the mean field model remains in the grain topology and the direct interactions between grains which is approximated while being explicitly considered in the full field model. Thus, we assume logically that the full field model is more accurate than the mean field model in the following comparisons.

The thermomechanical conditions considered in the two models are a hot deformation of a 304L steel at 1273K and $0.01s^{-1}$. The duration process is 300s in order to achieve a steady-state regime. In the same manner as previous simulations, a channel-die compression test is considered in the following full field simulation. The set of parameters used in the governing laws of the two models as well as the characteristics of the initial microstructures are representative of the considered 304L steel and are summarized in Tabs. 3.1 and 3.2, respectively [50, 170, 177]. Since simulations are also performed on an austenitic 304L steel, the values of M_0, γ_b and Q_m are identical to those used in 3D-GG simulations of chapter 2. A number of 8 initial classes is considered in the mean field model since this low number of initial classes showed same results as a large number of initial classes. The characteristics R_i and ρ_i of these 8 classes are identical to the characteristics of the 8 initial grains considered in the full field simulation. The number of grains N_i in each class of the mean field model is chosen in order to respect the input distribution.

	K_1	K_2	K_g	K_s	M_0	δ	γ_b	τ	Q_m
Unity	m^{-2}		m/s	s^{-1}	m^4/(J.s)		J/m^2	J/m	J/mol
Values	1.1e15	3.3	3.28e-8	0.001	1.56e-1	1.07	0.6	1.47e-9	2.8e5

Tab. 3.1. *Set of parameters used in governing laws of both mean field and full field models for the considered 304L steel [50, 170, 177]. The deformation conditions associated to these parameters are the following: T = 1273K; $\dot{\varepsilon} = 0.01s^{-1}$.*

	$\langle R \rangle$	σ_R	$\langle \rho_v \rangle$	σ_ρ
Unity	μm	μm	m^{-2}	m^{-2}
Values	60	10	6.5e13	1.25e13

Tab. 3.2. *Characteristics of the initial microstructure generated by the Laguerre-Voronoï tessellation algorithm and the associated energy field constant per grain generated from a Gaussian distribution.*

The full field simulation was performed on 3 nodes of 24 CPU processors. Four different instants of the full field simulation are presented on Fig. 3.12 with a color code

corresponding to the energy field constant per grain. The initial RVE measures $0.2mm^3$ and is composed of 8 grains at the early stage of the simulation while around 9000 grains are present in the RVE at the end of the simulation.

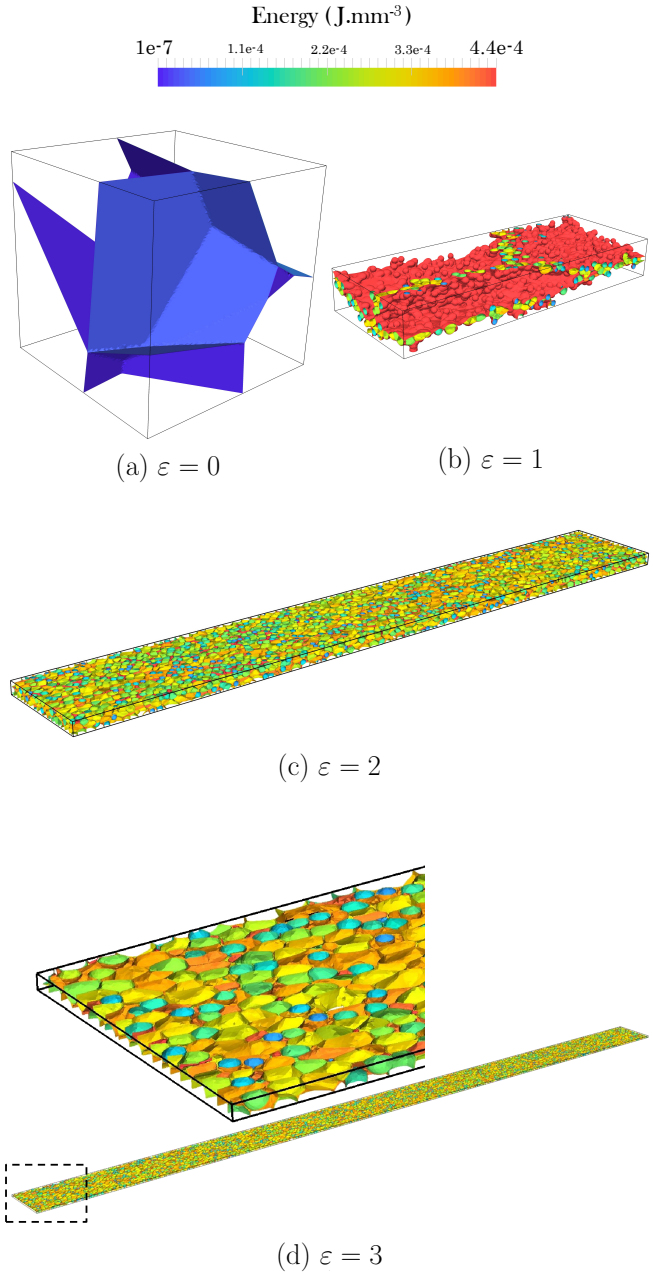

(a) $\varepsilon = 0$ (b) $\varepsilon = 1$

(c) $\varepsilon = 2$

(d) $\varepsilon = 3$

Fig. 3.12. *Four instants of a DRX simulation using the present full field model. The simulated process is a channel-die compression at 1273K at a strain rate of $0.01s^{-1}$ during 300s. Initial microstructure is composed of 8 grains while around 9000 grains are present at the end of deformation. Color code corresponds to the energy field constant per grain.*

Homogenized results in terms of mean dislocation density (weighted by grain volume) $\langle\rho\rangle_{\text{vol}}$, mean grain radius $\langle R\rangle$, mean grain radius (weighted by grain volume) $\langle R\rangle_{\text{vol}}$ and RX fraction are confronted between the two models on Fig. 3.13. First it is observed that the evolutions of the mean grain radius $\langle R\rangle$ predicted by the two models are similar during all the process duration (see Fig. 3.13(c)) and final values are slightly higher than the critical nucleus radius ($r_{\text{cr}} = 5.2\mu$m). The decrease of $\langle R\rangle$ at the onset of recrystallization ($\varepsilon \simeq 0.4$) is very fast and thus difficult to capture (see Fig. 3.13(c)), thus the mean grain radius (weighted by volume) $\langle R\rangle_{\text{vol}}$ is also plotted on Fig. 3.13(d). During the first minutes of process (up to $\varepsilon = 1$), the kinetics in terms of RX fraction, $\langle R\rangle_{\text{vol}}$ and $\langle\rho\rangle_{\text{vol}}$ are quasi similar between the two models (see Fig. 3.13(a), (b), (d)). However, at a true strain $\varepsilon > 1$, the kinetics are always faster for the full field results, meaning that the number of nuclei appearing in the microstructure is always larger in the full field case. A first cause explaining this difference can be the evolution of grain boundary surfaces from equiaxed to ellipsoidal shape, increasing the surface of grain boundaries and consequently increasing the nucleation rate in the full field case (Eq. 3.13).

Another cause explaining this difference can be a wrong estimation of the quantities γ_{RX} and γ_{NR} presented on Fig. 1.12 and used in the discussed mean field model. Therefore these two quantities were estimated from the full field simulation and compared with those computed in the mean field model. To estimate these quantities in the full field simulation, the surface fraction of each NR grain in contact with a RX grain is calculated and averaged to get the quantity γ_{NR} and vice versa for γ_{RX}. These values are measured at each instant of the full field simulation and are compared to the mean field model on Fig. 3.13(e) and (f). First, the increase of γ_{NR} observed on Fig. 3.13(e) is quite similar for the two models. Furthermore, this evolution is very fast from the moment where nuclei appear ($\varepsilon \simeq 0.4$). This fast increase is logical since nuclei mainly appear at grain boundaries, thus most of NR grains are in contact with RX grains as soon as nucleation starts. The decrease of γ_{RX} observed on Fig. 3.13(f) is perfectly similar for the two models up to a true strain $\varepsilon \simeq 0.9$. After this instant, the decrease of γ_{RX} is much faster in the mean field model. The quantity γ_{RX} is used in the mean field model to calculate the growth rate of nuclei, thus a faster decrease of γ_{RX} in the mean field case is a cause of the slower evolution of the RX fraction, $\langle\rho\rangle_{\text{vol}}$ and $\langle R\rangle_{\text{vol}}$ predicted by the mean field model (see Fig. 3.13(a), (b) and (d)).

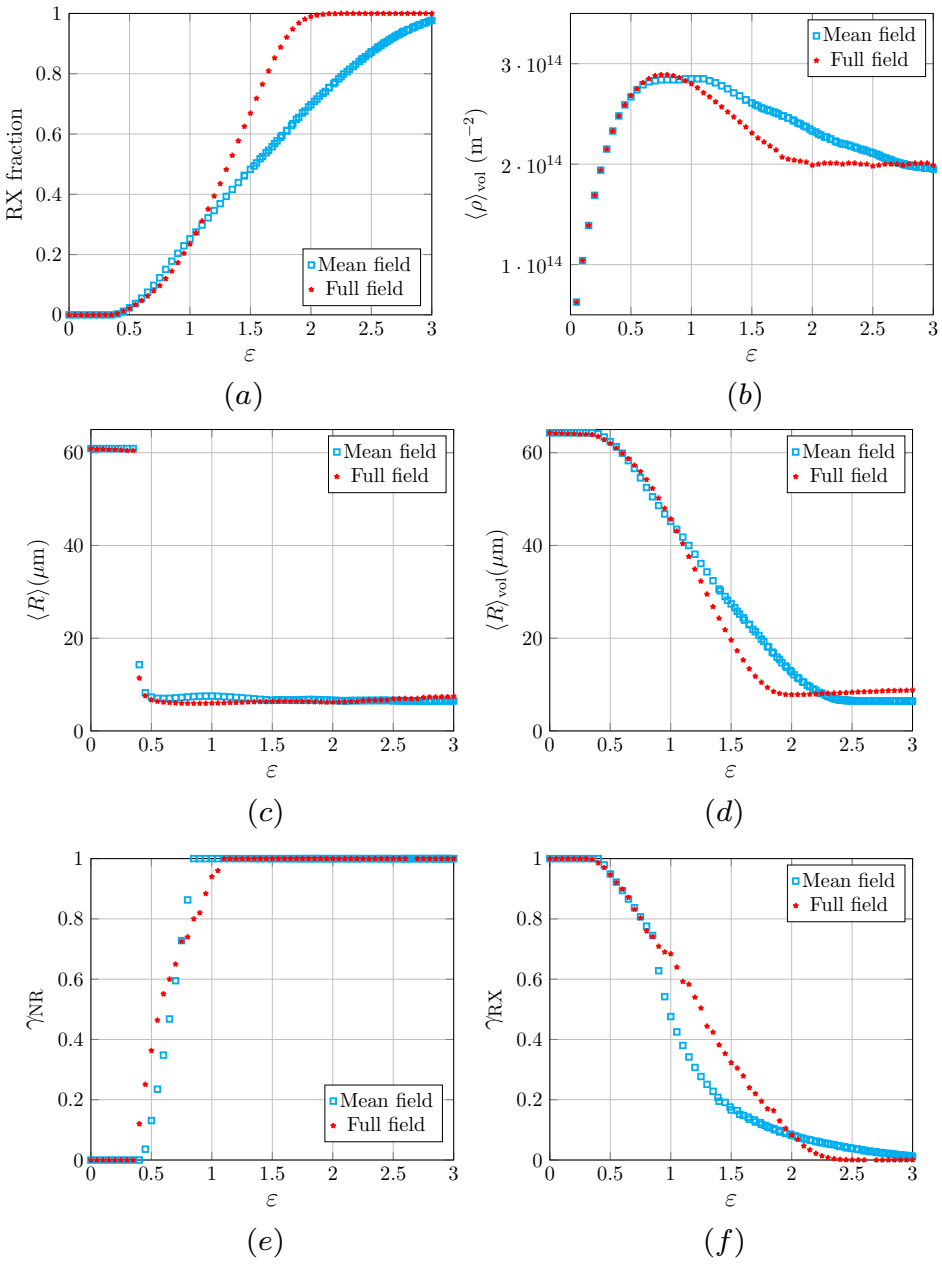

Fig. 3.13. *Comparisons of the macroscopic results obtained during a DRX process using the present full field model and the mean field model of Beltran et al. [50] introduced in first chapter. Compared results are: (a) RX fraction, (b) mean dislocation density (weighted by grain volume), (c) mean grain size, (d) mean grain size (weighted by grain volume), (e) averaged surface fraction of NR grains in contact with RX grains and (d) averaged surface fraction of RX grains in contact with NR grains. The simulated process is a channel-die compression at 1273K, at a strain rate of $0.01s^{-1}$ during 300s.*

Grain radius distributions and dislocation density distributions predicted by the two models are also compared at four instants of the simulations (see Fig. 3.14 and Fig. 3.15). The grain radius distributions are represented in volume fraction since after few

seconds of deformation, the number of nuclei is much higher than the number of initial grains. Thus a number fraction is not a discerning method to follow at the same time the small and large grains. The class width of histograms is 3μm for the grain radius distributions and 5e13m^{-2} for the dislocation density distributions.

The grain radius distributions predicted by the two models have still some similarities at a true strain $\varepsilon = 1$ (see Fig. 3.14(b)). However, at a true strain $\varepsilon = 2$, a volume fraction of large grains is observed in the mean field simulation whereas in the full field simulation, the microstructure is fully recrystallized and these large grains have disappeared (see. Fig. 3.14(c) and (d)). This difference is still due to the quantity γ_{RX} which decreases faster in the mean field case, leading to a slowly growth of RX grains at the expense of the NR grains. Finally, a vertical asymptote is observed in mean field predictions at a true strain $\varepsilon = 3$ at the steady-state regime whereas a more spread distribution is observed in the full field prediction (see Fig. 3.14(d)). This issue was already discussed in [83] and in chapter 1 and is due to the particularity of the boundary migration equation (Eq. 4.3) and the consideration of the same HEM for each grain.

Concerning the dislocation density distributions, the shapes of the curves are close at the three instants $\varepsilon = 1$, $\varepsilon = 2$ and $\varepsilon = 3$ of process (see Fig. 3.15(b), (c) and (d)). At each instant, the curve predicted by the full field simulation has a more pronounced peak compared to that predicted by the mean field simulation.

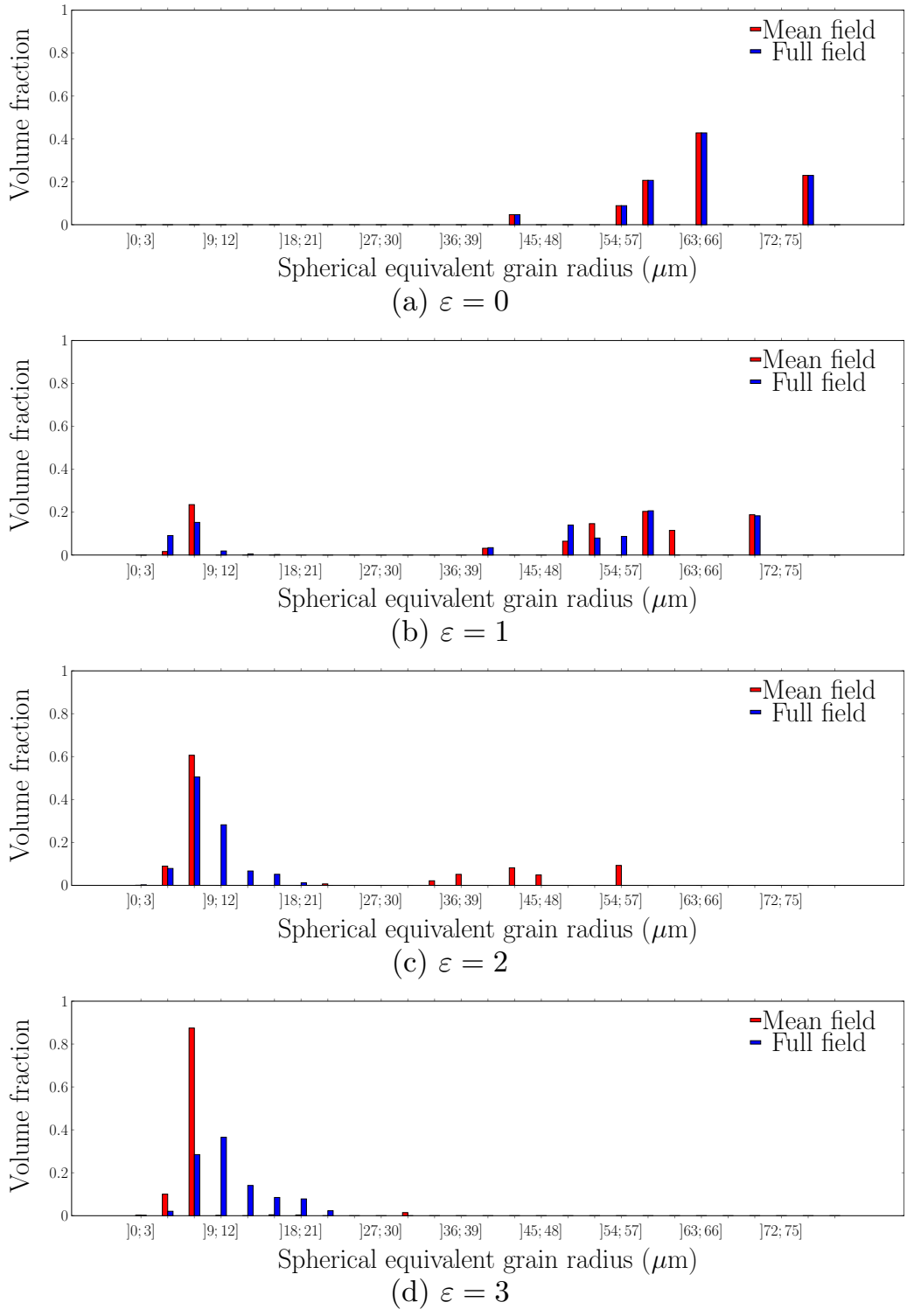

Fig. 3.14. *Comparisons, at different instants, of the grain radius distributions ((a) to (d)) obtained during a DRX process using the present full field model and the mean field model of Beltran et al. [50] introduced in first chapter. The simulated process is a channel-die compression at 1273K, at a strain rate of 0.01s^{-1} during 300s.*

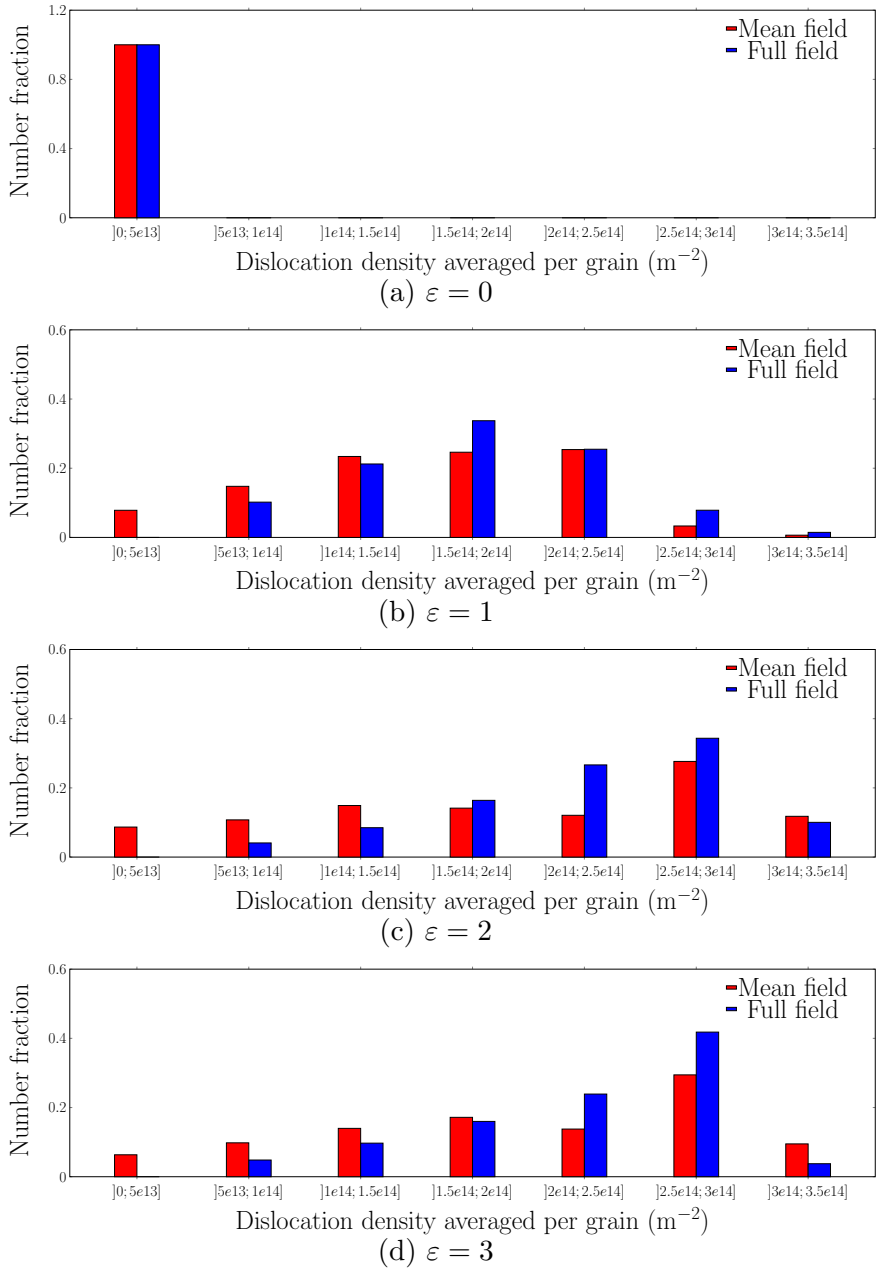

Fig. 3.15. *Comparisons, at different instants, of the dislocation density distributions ((a) to (d)) obtained during a DRX process using the present full field model and the mean field model of Beltran et al. [50] introduced in first chapter. The simulated process is a channel-die compression at 1273K, at a strain rate of 0.01s^{-1} during 300s.*

3.4.2 Post-dynamic recrystallization

A PDRX simulation is then considered using the two models in order to compare the results. To avoid accumulating differences from DRX, the initial state of the microstructure used in both models corresponds to the final state microstructure obtained after a

DRX simulation using the present full field model. The PDRX process is simulated by considering a 304L steel maintained at 1273K during 25min. The first two minutes of PDRX are presented on Fig. 3.16. It is observed a large decrease of energy in the material during the first minutes of PDRX. After these few minutes, the preponderant mechanism is the capillarity driven GG mechanism since the energy is low in the material and thus only the mean curvature of grains plays a primordial role on the pressure acting on grain boundaries.

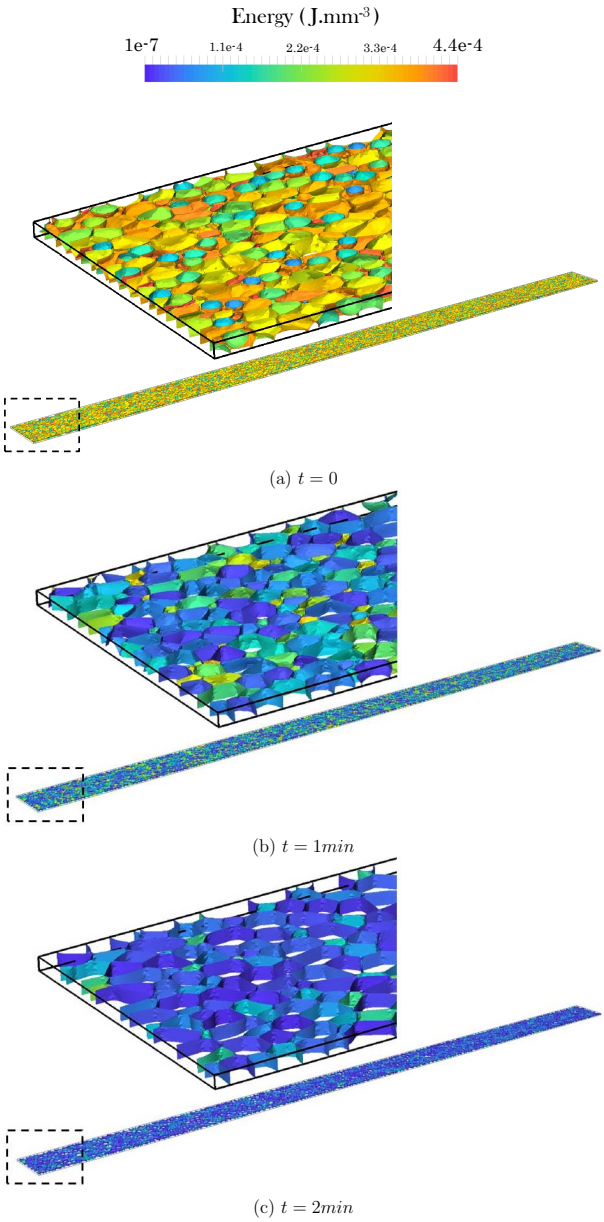

Fig. 3.16. *Three instants of the PDRX simulation using the present full field model. The simulated process is a heat treatment at 1273K during 25min. Initial microstructure is composed of 9000 grains while around 600 grains are present at the end of the heat treatment. Color code corresponds to the mean energy per grain.*

Comparisons of mean dislocation density (weighted by grain volume) $\langle\rho\rangle_{\text{vol}}$, mean grain radius $\langle R\rangle$ and mean grain radius (weighted by grain volume) $\langle R\rangle_{\text{vol}}$ predicted by the two models are presented on Fig. 3.17. The results obtained according to the two models are close. The evolutions of the curves are very pronounced at the early stage of the simulation since the energy is still high in the material. After few minutes, the energy is much more low in the material (see Fig. 3.16) and thus the grain boundary kinetic slows down, which is characterized by a slow evolution of $\langle R\rangle$ and $\langle R\rangle_{\text{vol}}$ after this instant on Fig. 3.17(b) and (c).

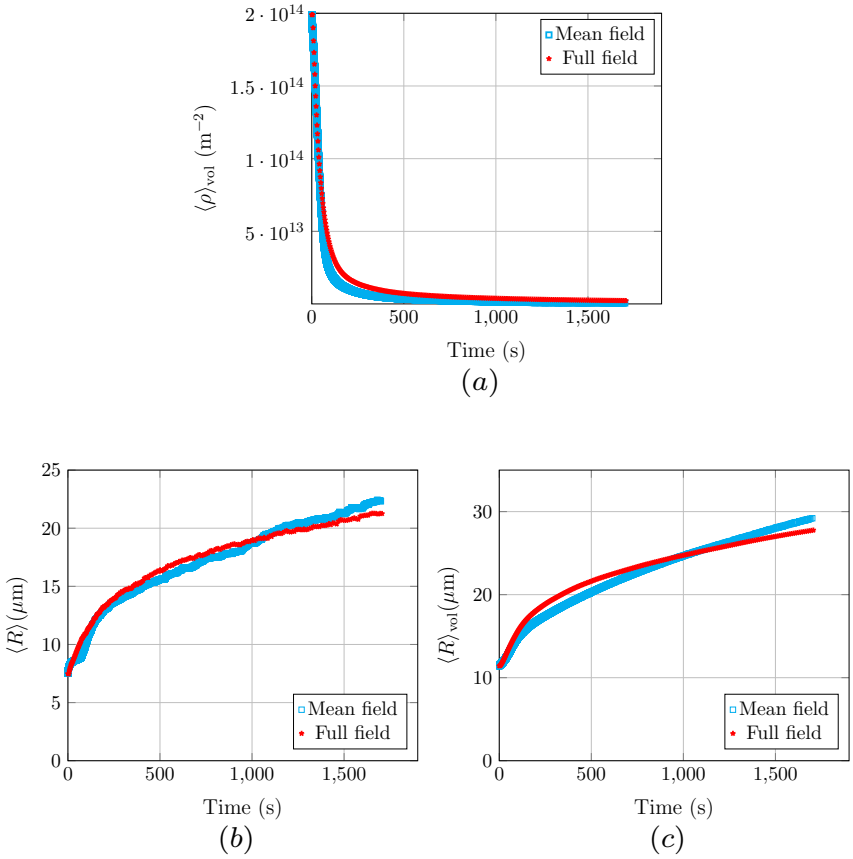

Fig. 3.17. *Comparisons of the macroscopic results obtained during a PDRX simulation using the present full field model and the mean field model of Beltran et al. [50] introduced in first chapter. Compared results are: (a) mean dislocation density (weighted by grain volume), (b) mean grain size and (c) mean grain size (weighted by grain volume). The simulated process is a heat treatment at 1273K during 25min.*

The grain radius distributions and dislocation density distributions are also presented and compared on Figs. 3.18 and 3.19. After 10 min of PDRX, the grain radius distributions are still very close between the two simulations (see Fig. 3.18(b)). However, after 20 min of PDRX, a single higher peak is appearing on the grain radius distribution of the mean field simulation (see Fig. 3.18(c)) and this peak is still observed after 25min of PDRX (see Fig. 3.18(d)). In the full field simulation, this single higher peak is not

observed during the simulation. Globally, it is observed that the grain radius distribution is correctly described by the mean field model. Concerning the dislocation density distributions, the results are identical in the two simulations since the energy quickly decreases in the material and thus after 10min of PDRX, all the grains have the same low energy and a single narrow peak is observed in the two models (see Fig. 3.19).

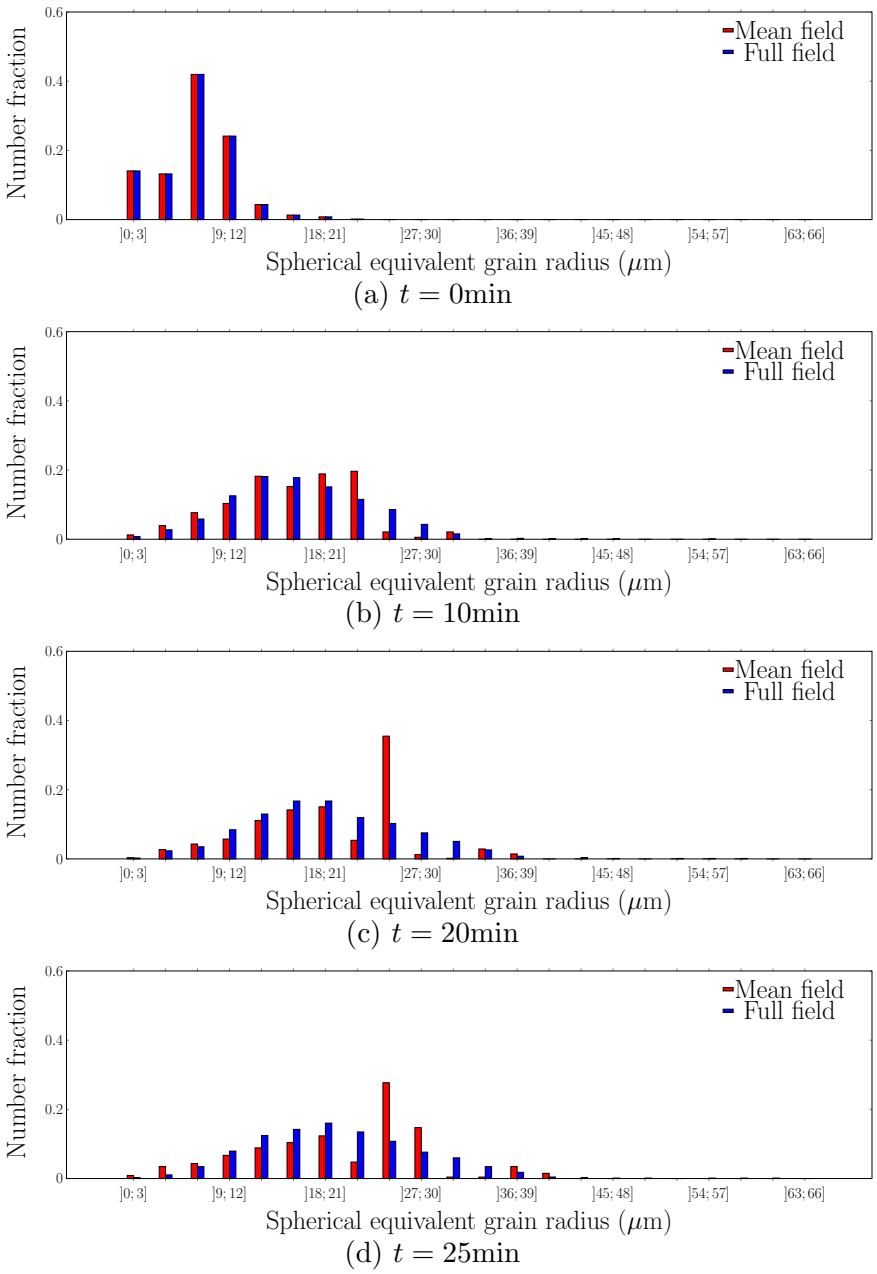

Fig. 3.18. *Comparisons, at different instants, of the grain radius distributions ((a) to (d)) obtained during a PDRX process using the present full field model and the mean field model of Beltran et al. [50] introduced in first chapter. The simulated process is a heat treatment at 1273K during 25min.*

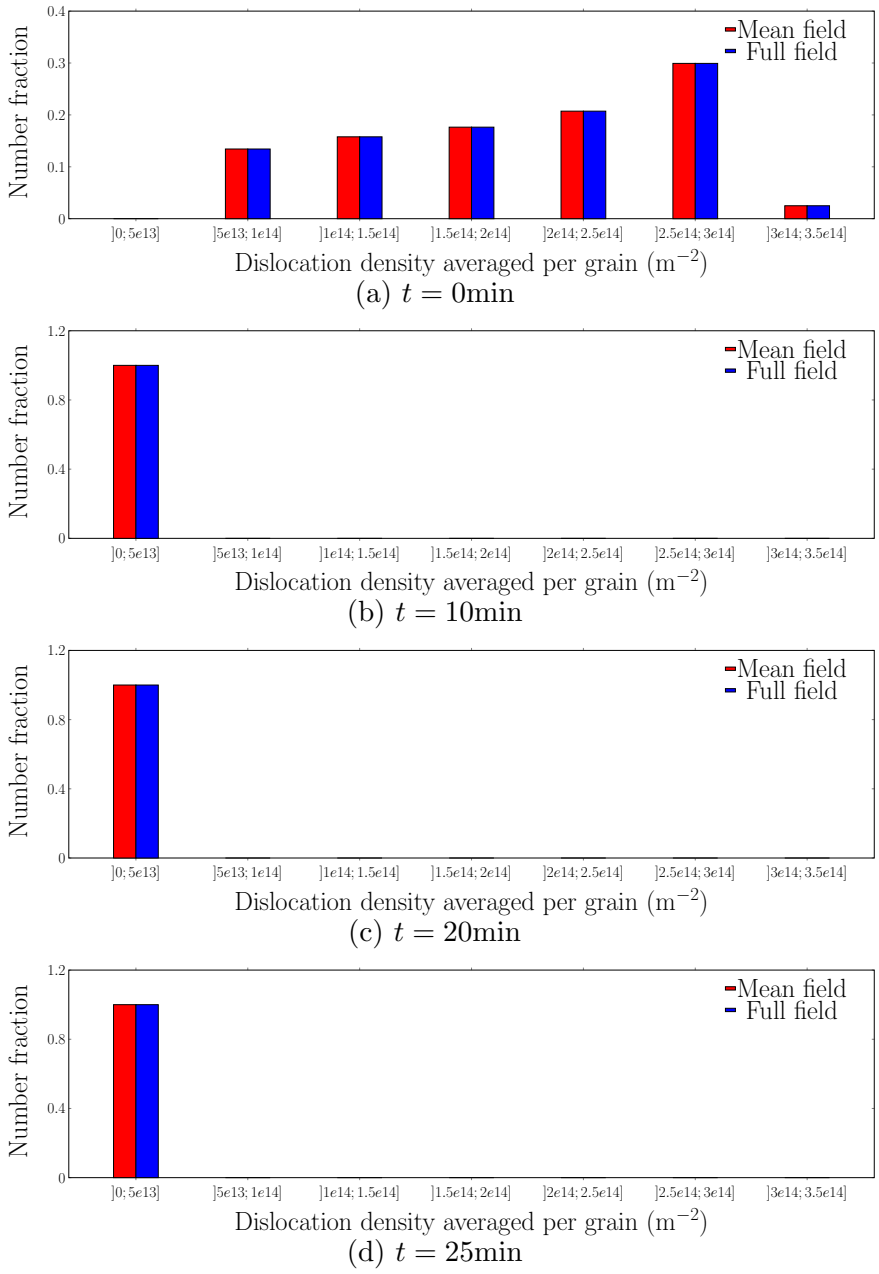

Fig. 3.19. *Comparisons, at different instants, of the dislocation density distributions ((a) to (d)) obtained during a PDRX process using the present full field model and the mean field model of Beltran et al. [50] introduced in first chapter. The simulated process is a heat treatment at 1273K during 25min.*

Summary

In this third chapter, a robust 3D model based on the LS-FE framework and coupled to analytical laws was presented. It is able to model DRX and PDRX occurring during and after hot deformation of metal alloys, respectively. The advantages of the considered model are large: (i) the model enables to perform 3D simulations; (ii) strain hardening, static and dynamic recovery are simulated thanks to phenomenological laws coming from a pre-existing mean field model [49, 50], which is not as accurate as with a crystal plasticity FE formulation, but considerably reduces the computational costs of the simulations; (iii) the considered 3D model is able to describe the grain boundary network using the LS method, even at large deformations (for instance $\varepsilon > 1$) in order to reproduce industrial processes and (iv) a sensitivity study has largely minimized computational costs, allowing the integration of the model in an industrial context through the DIGIMU® software package.

Results of DRX and PDRX simulations using this new numerical framework were also confronted with the prediction of a mean field model introduced in first chapter [49,50]. Results showed that the mean field model provides a poor description of the RX fraction and grain size distributions during hot deformation (i.e. during DRX regime). This difference reinforces the idea that the proposed full field model is much more powerful than a mean field model since it explicitly takes the grain boundary network into account. After hot deformation (i.e. during the PDRX regime), the whole results predicted by the mean field model, including the grain size distribution, are close to the full field predictions.

Differences between both mean field and full field predictions were explained by different reasons: first grains remain spherical all along the deformation in mean field simulations, whereas they evolve toward an ellipsoidal shape in full field simulations, increasing nucleation rate. Then some differences were observed on the term γ_{RX}, decreasing the kinetic in mean field case. Finally, the issue of grain size distributions predicted by mean field models was already discussed in [83] and in chapter 1. It is due to the grain boundary equation considered in mean field models and to the fact that each grain is immersed into the same HEM, imposing the same evolution for each grain. Smagghe [71] recently tackled this limitation by making each grain evolves with a random-selected grain as neighbor in his mean field model.

The next chapter proposes a new approach for mean field modeling of DRX and PDRX. This new approach tackles assumptions of existing mean field models discussed in this chapter by considering the evolution of grain shape from spherical to ellipsoidal one and by considering a particular neighborhood (composed of several selected grains as neighbors) for each grain.

Chapter 4

A new topological approach for the mean field modeling of dynamic and post-dynamic recrystallization : the NHM

Contents

4.1 Introduction 111

4.2 Mean field modeling of dynamic recrystallization 112

4.2.1 Constitutive laws 112

4.2.2 Neighborhood choice during DRX 113

4.2.3 Modeling of grain elongation 119

4.2.4 Comparison with DRX full field predictions 123

4.3 Mean field modeling of post-dynamic recrystallization 130

4.3.1 Constitutive laws 130

4.3.2 Neighborhood choice during PDRX 130

4.3.3 Comparison with PDRX full field predictions 131

Résumé en français

Dans ce chapitre, un nouveau modèle champ moyen pour la modélisation de la recristallisation dynamique et post-dynamique est présenté. Ce modèle, appellé "NHM" pour NeighborHood Model, contourne les hypothèses des modèles champ moyen standards en considérant un voisinage qui s'approche de la réalité. De plus, NHM modélise l'évolution de la forme des grains par des ellipsoïdes au cours de la déformation. Un avantage considérable de ce modèle est lié au fait qu'il est basé sur les mêmes lois constitutives que le modèle champ complet précedemment introduit, pour les mécanismes d'écrouissage, restauration et germination. De ce fait, le champ complet peut être utilisé comme référence afin de valider les améliorations apportées au champ moyen. De plus, étant donné que le champ moyen est très peu couteux numériquement, il peut être utilisé afin d'identifier de manière rapide par analyse inverse, les paramètres communs aux deux modèles. Les deux améliorations majeures de ce nouveau modèle sont détaillées dans la première partie de ce chapitre. Une étude de sensibilité est ensuite présentée afin de mieux comprendre l'influence des différents paramètres d'entrée sur les résultats. Finalement, les prédictions de NHM sont comparées aux prédictions du modèle champ complet. Les prédictions en termes de valeurs moyennes (taille de grain moyenne, fraction recristallisée, contrainte macroscopique etc.) et distributions de tailles de grains sont très proches entre les deux modèles, ce qui tend à valider cette nouvelle approche.

In this chapter, a new approach called "NHM" for NeighborHood Model is proposed for mean field modeling of dynamic and post-dynamic recrystallization. A first benefit of the NHM compared to the state of the art is based on a more precise description of the immediate vicinity and of the shape of each grain to describe microstructure evolution all along the hot deformation process. Another benefit of the NHM is related to the fact that constitutive equations (and consequently model parameters) are the same as used in the full field model of chapter 3, therefore the full field model can be used as a reference to validate the improvements made in the NHM. Furthermore the NHM can also be used to identify quickly by inverse analysis the model parameters used in both the NHM and the full field model. The NHM is first presented. Then, results provided by the NHM are compared to predictions of the full field model presented in chapter 3 and those of a former mean field formulation, in terms of recrystallization kinetics and grain size distributions. Predictions of the NHM are very close to full field predictions and the progress when compared to former the former mean field model formulation is obvious. Furthermore, the limitation of mean field models concerning the non-realistic shape of grain size distributions during dynamic recrystallization is solved in the NHM.

4.1 Introduction

Mean field models were introduced in first chapter as a compromise between phenomenological laws and full field models. In chapter 3, the proposed full field model was compared to the mean field model of Beltran et al. introduced in first chapter [50] using same constitutive laws and same model parameters (therefore only the microstructure representation differs). Is was conclude that this mean field model provides poor predictions in terms of recrystallization kinetics as well as grain size distributions. In particular prediction of grain size distributions is a major limitation inherent to many mean field models [48–50, 70] and already discussed in [71]. The many reason, already mentioned in chapters 1 and 3, is related to the fact that in real microstructures, each grain evolves depending on its own neighborhood, which is not the case in mean field models where each grain is immersed into the same HEM and follow the same evolution. Furthermore, kinetics of recrystallization are generally slower in mean field models due to the fact that grains remain spherical during the deformation while their surface should increase in reality, increasing the stored energy and the nucleation sites. Therefore, in this work a new topological approach for the mean field modeling of DRX and PDRX is proposed. Hereafter, this new model is called "NeighborHood Model (NHM)". The NHM is based on the same constitutive equations for DRX and PDRX as used in the full field model presented in chapter 3. The major novelty of the NHM is based on the consideration of a particular neighborhood for each grain instead of considering the whole average microstructure as HEM. In addition, the grain shape changes from spherical to ellipsoidal shape during deformation in the NHM, to take the increase of grain boundary surface into account. These two major improvements are first presented in this chapter. Then, the results of simulations related to hot deformation of a 304L austenitic steel provided by the NHM, the mean field model of Beltran et al. [50]

and the full field model of chapter 3 are compared.

4.2 Mean field modeling of dynamic recrystallization

4.2.1 Constitutive laws

Initial microstructures in mean field models are represented by spherical grains, each having a dislocation density ρ_i and a grain size R_i. As detailed in the first chapter, in several existing models [50,68], the concept of grain classes is used to reduce computational costs. This consists in gathering several similar grains in one single entity called " grain class", that is defined by a grain radius R_i, a dislocation density ρ_i and a number of grains N_i in the considered class. The main drawback to this consideration is that all the grains belonging to the same class follow the same behavior during the simulation. This concept of classes is used in the NHM to reduce computational costs. However, in this chapter, it is referred to grains instead of grain classes in order to facilitate the understanding of the NHM principle.

As already mentioned in previous chapters, a RX grain denotes a grain appearing during the simulation while a NR grain denotes a grain present from the first stage of simulation. Furthermore, a RX grain having just appeared is called nucleus. The constitutive laws for strain hardening, dynamic recovery and nucleation considered in the NHM are exactly the same as used in the full field model of chapter 3. Therefore the evolution of the average dislocation density ρ_i in each i^{th} grain during deformation is modeled by the Yoshie-Lasraoui-Jonas law [76] using Eq. 3.2 (also given by 1.44 in the first chapter), the critical dislocation density ρ_{cr} is calculated using Eqs. 3.8, 3.9 (also given by Eqs. 1.54, 1.55 in the first chapter), the critical radius of nuclei noted r_{cr} is calculated from the modified Bailey-Hirsch criterion using Eq. 3.12 (originally expressed by Eq. 1.8 in the first chapter) and the nucleation rate $\dot{V}$ representing a volume of nuclei per unit time, is calculated according to Eq. 3.13. However, boundary migration is not modeled by the same law since the local curvature cannot be computed without an explicit description of the microstructure in the NHM. Grain boundary migration is generally described in mean field models by the following equation :

$$\frac{dR_i}{dt} = M_{\text{b}} \left(\tau(\langle \rho \rangle_{\text{surf}} - \rho_i) + \beta \gamma_{\text{b}} \left(\frac{1}{R_{\text{cr}}} - \frac{1}{R_i} \right) \right), \tag{4.1}$$

leading to the following volume variation for the i^{th} grain :

$$\Delta V_i = \frac{dR_i}{dt} S_i \Delta t, \tag{4.2}$$

where S_i is the boundary surface of the i^{th} grain. In the second chapter, we showed that a value of β equal to 1.4 leads to more accurate results. M_{b} and γ_{b} are assumed to be isotropic (i.e. identical for all grain boundaries) as considered in the full field model

of chapter 3. To be coherent with the DRX full field models of chapter 3 and to tackle the assumption of averaged energy per grain, the parameter δ related to the strain rate dependence of grain boundary migration is also considered here (see chapter 2 section 1.2 for more explanations about this parameter), leading to the following relationship :

$$\Delta V_i = M_{\mathrm{b}} \left(\delta \tau (\langle \rho \rangle_{\mathrm{surf}} - \rho_i) + \beta \gamma_{\mathrm{b}} \left(\frac{1}{R_{\mathrm{cr}}} - \frac{1}{R_i} \right) \right) S_i \Delta t. \tag{4.3}$$

4.2.2 Neighborhood choice during DRX

In a real microstructure, each grain is surrounded by a number of neighbors (see Fig. 4.1(a)). This microstructure is described in mean field models by spherical grains (see Fig. 4.1(b)), each grain having a radius R_i and a dislocation density ρ_i. However a strong assumption made in mean field models [48, 50, 70] is that each grain has no neighbors but is surrounded by a HEM (see Fig. 4.1(c)). To be more realistic, the new proposed approach tackles this first limitation by considering a particular neighborhood for each grain, composed of a certain number of grains that are appropriately chosen (see Fig. 4.1(d)).

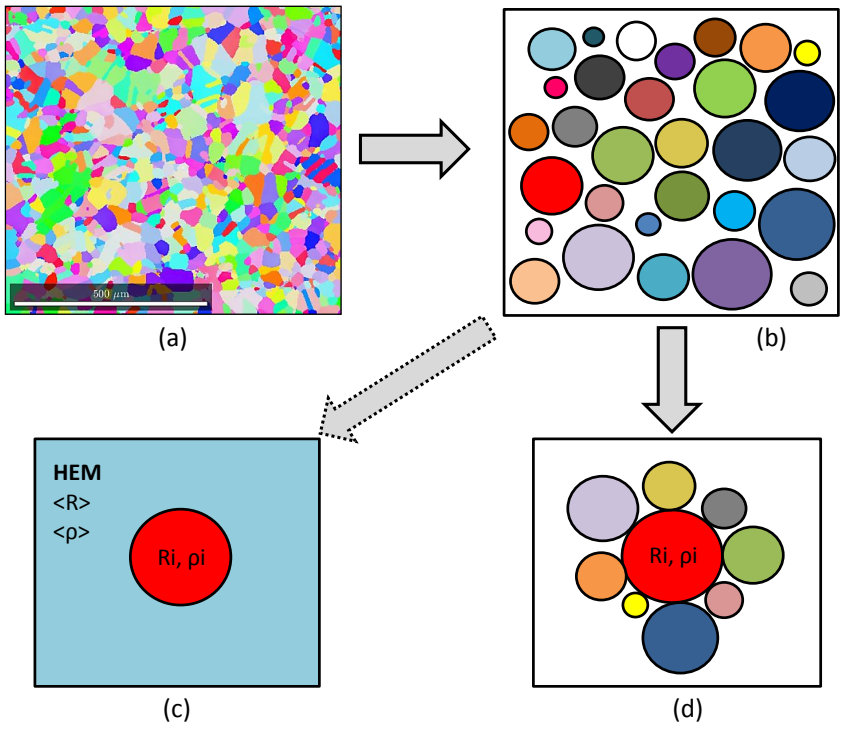

Fig. 4.1. *Representation of the microstructure in mean field models. (a) EBSD picture of an austenitic steel 304L microstructure, (b) representation of a microstructure in mean field models as a set of spherical grains, (c) standard mean field approach: each grain is surrounded by a homogeneous equivalent medium (HEM) composed of all grains in the microstructure and (d) the NHM: each grain is surrounded by a certain number of grains that compose its neighborhood.*

Representation of a grain's neighborhood in the NHM

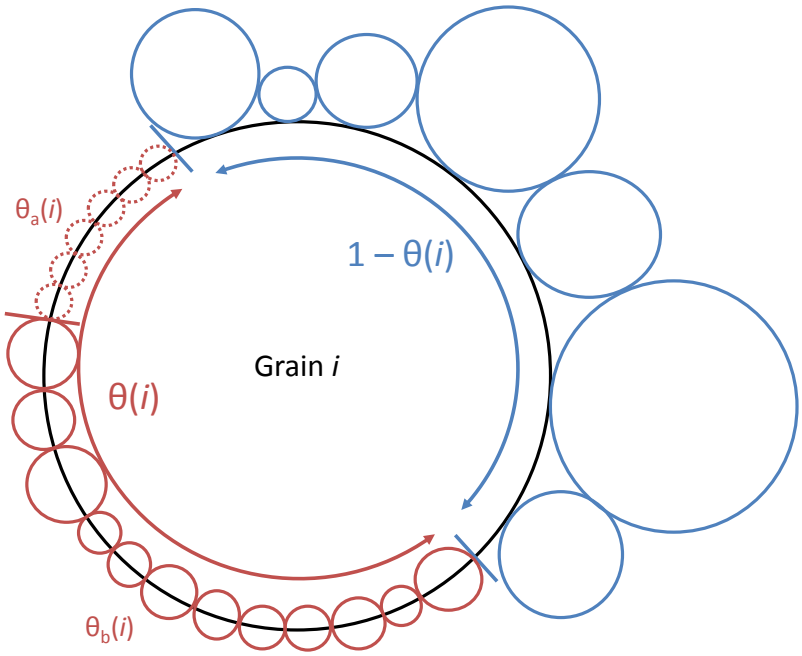

Fig. 4.2. *Representation of a grain in the NHM during the DRX regime. Each grain i has a surface fraction $\theta(i)$ in contact with RX grains represented in red color and a surface fraction $(1-\theta)(i)$ in contact with NR grains represented in blue color. $\theta(i)$ is also subdivided into two quantities $\theta_a(i)$ and $\theta_b(i)$ representing the surface fraction occupied by nuclei in dashed line and other RX grains in full line, respectively.*

As already considered in the full field model of chapter 3, necklace nucleation resulting from the SIBM mechanism, is considered here since this is the kind of nucleation observed in 304L during DRX [178,179]. Hereafter, the quantities $\theta(i)$ and (1-θ)(i) denote the surface fraction of the i^{th} grain in contact with RX and NR grains, respectively. The description of a grain with its neighborhood in the NHM is presented in 2D on Fig. 4.2. To enrich this description, the quantity $\theta(i)$ is subdivided into two other quantities noted $\theta_a(i)$ and $\theta_b(i)$ representing the surface fraction of any i^{th} grain in contact with nuclei and with other RX grains, respectively.
The 2D schematic surface of a grain i having RX grains appeared on its boundary is represented on Fig. 4.3(a). The quantity $S1(i)$ represents the boundary surface between the grain i and RX grains while $S2(i)$ represents the boundary surface of the grain i that is not in contact with RX grains. In this case, the boundary surface S_i of the grain i should be defined by $S_i = S1(i) + S2(i)$ and the surface fraction θ should be defined by $\theta = S1(i)/(S1(i) + S2(i))$ on Fig. 4.3(a). However, in mean field models [48, 50, 70] a surface such as the one presented on Fig. 4.3(a) is hard to consider, thus it is common to keep working with the assumption of spherical grains as represented on Fig. 4.3(b). In the NHM, the assumption of spherical grains presented on Fig. 4.3(b) is also considered. The quantity $S3(i)$ is defined as the total intersection surface between the considered

grain i and RX grains on its boundary (see Fig. 4.3(b)). Therefore the surface fraction θ is estimated in the NHM by :

$$\theta(i) \simeq \left(\frac{S3(i)}{S2(i)+S3(i)} \right). \tag{4.4}$$

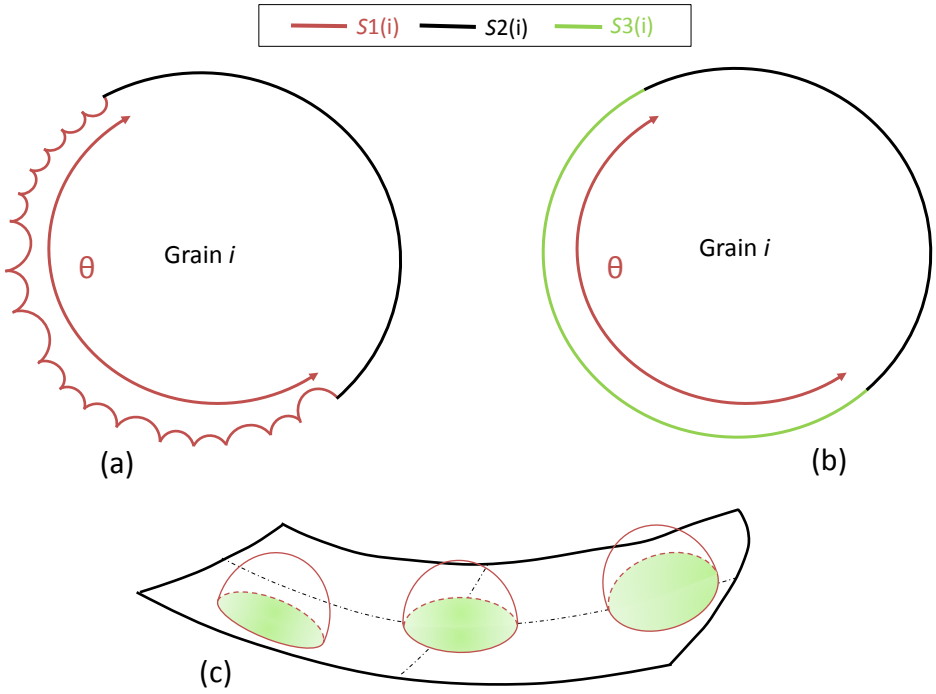

Fig. 4.3. *Schematic representation of (a) the surface of the grain i with RX grains on its boundary (b) the surface of the grain i as it is considered in the NHM (c) a 3D portion of a grain boundary with three nuclei as neighbors. The intersections are approximated by several circles in green color. S1(i) represents the boundary surface between the grain i and RX grains, S2(i) the boundary surface of the grain i that is not in contact with RX grains, S3(i) the total intersection surface between the grain i and RX grains, estimated by a sum of circles in the NHM.*

By doing the assumption that the grain i is large compared to RX grains, intersection surfaces between one RX grain and the grain i are approximated by circles in the NHM as represented on Fig. 4.3(c). Furthermore by doing the assumption that all RX grain sizes are approximated by the mean RX grain size $\langle R_{RX} \rangle$ with their center belonging to the boundary of i, each intersection can be finally defined by a circle of radius $\langle R_{RX} \rangle$ having a surface equal to $\pi \langle R_{RX} \rangle^2$. If $N_{RX}(i)$ denotes the number of RX grains appeared in the considered grain i, $S3(i)$ can be estimated by $\pi N_{RX}(i) \langle R_{RX} \rangle^2$, and θ can be finally approximated by :

$$\theta(i) \simeq \left(\frac{\pi N_{RX}(i) \langle R_{RX} \rangle^2}{S_i} \right). \tag{4.5}$$

The number of RX grains $N_{\mathrm{RX}}(i)$ appeared in the grain i increases during the simulation while the RX mean grain size $\langle R_{\mathrm{RX}} \rangle$ and the grain surface S_i are quasi-constant. To avoid values of $\theta(i)$ higher than 1, the final equation for $\theta(i)$ is defined as :

$$\theta(i) \simeq \min\left(\frac{\pi N_{\mathrm{RX}}(i)\langle R_{\mathrm{RX}}\rangle^2}{S_i}, 1\right). \tag{4.6}$$

Number of neighbors per grain

The numbers of neighbors occupying the $\theta_{\mathrm{a}}(i)$, $\theta_{\mathrm{b}}(i)$ and (1 - θ)(i) surface fractions of any i^{th} grain are noted $N_{\theta_{\mathrm{a}}}(i)$, $N_{\theta_{\mathrm{b}}}(i)$ and $N_{(1-\theta)}(i)$, respectively.

The number $N_{\theta_{\mathrm{a}}}(i)$, representing the number of nuclei in the i^{th} grain at the latest time increment, is directly known at any instant of the simulation from Eq. 3.13. The reasoning leading to Eq. 4.6 can also be considered for the nuclei and leads to :

$$\theta_{\mathrm{a}}(i) \simeq \min\left(\frac{\pi N_{\theta_{\mathrm{a}}}(i) r_{\mathrm{cr}}^2}{S_i}, 1\right). \tag{4.7}$$

As such, $\theta_{\mathrm{b}}(i)$ is deduced using the following relationship :

$$\theta_{\mathrm{b}}(i) = \theta(i) - \theta_{\mathrm{a}}(i). \tag{4.8}$$

Assuming that Eq. 4.7 is also available for θ_{b}, the number of RX neighbors $N_{\theta_{\mathrm{b}}}(i)$ of any i^{th} grain can be estimated by the following relation :

$$N_{\theta_{\mathrm{b}}}(i) \simeq \left(\frac{\theta_{\mathrm{b}}(i) S_i}{\pi \langle R_{\mathrm{RX}}\rangle^2}\right). \tag{4.9}$$

The number of NR neighbors $N_{(1-\theta)}(i)$ must also be estimated. As an approximation, the number of grains on the surface fraction $(1-\theta)(i)$ can be estimated using a law from literature for describing steady-state or quasi steady-state microstructures. Several kinds of law were proposed in the literature to estimate the number of neighbors of grains in steady-state or quasi steady-state 3D microstructures. DeHoff and Liu [180] proposed a linear relationship between the number of neighbors and the mean tangent diameter of grains in 3D microstructures, validated experimentally by Liu et al. [181]. Abbruzese and Campopiano [182] proposed a quadratic relationship between the number of neighbors and the normalized equivalent sphere radius of a grain in 3D microstructures. This relationship was validated by experimental investigations [181,183] and numerical studies [184–186]. All the resulting curves are presented on Fig. 4.4(a). The curves are globally close to each other. To reinforce this relationship, an additional GG numerical simulation was performed in 3D using the full field model of chapter 3. An equiaxed microstructure with an average grain size of 100μm was generated using a Laguerre-Voronoï algorithm [151] and a heat treatment at 1373K for 30min was simulated on a 304L steel. The resulting microstructure is composed of 2000 grains and the number of neighbors of each individual grain is plotted as a function of its normalized equivalent

sphere radius on Fig. 4.4(b) while the average number of neighbors is plotted as a function of the normalized equivalent sphere radius on Fig. 4.4(a). The curve on Fig. 4.4(a) resulting from the full field simulation is close to the other experimental and numerical curves of the literature, which reinforces the idea that a general polynomial equation can correctly estimate the number of grain neighbors as a function of their normalized equivalent sphere radius in steady-state or quasi steady-state 3D microstructures. This polynomial dependence is used in the NHM to estimate the number of grain neighbors $N_{(1-\theta)}(i)$ at a given stage of the deformation process. This relationship is given in Eq. 4.10.

$$N_{(1-\theta)}(i) = \left(4.06 \times \omega_i^2 + 4.22 \times \omega_i + 4.71\right) \times (1 - \theta(i)), \tag{4.10}$$

where ω_i is the normalized grain radius defined by $R_i/\langle R_{\mathrm{NR}} \rangle$.

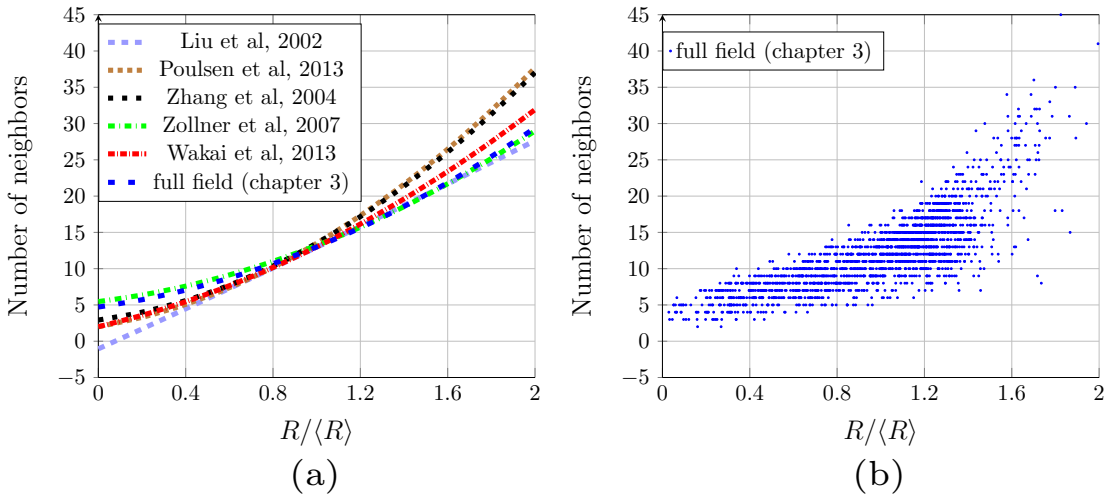

Fig. 4.4. *Number of neighbors as a function of the normalized equivalent sphere radius. All investigations were done on steady-state or quasi steady-state microstructures. a) Each blue dot represents a grain coming from simulations using the full field model of chapter 3 (b) Different curves issued from the literature and from the full field model. Those are obtained by least-square regression or by an average per topological classes.*

Thus the total number of neighbors of any i^{th} grain noted $N_{\mathrm{tot}}(i)$ is given by :

$$N_{\mathrm{tot}}(i) = N_{\theta_{\mathrm{a}}}(i) + N_{\theta_{\mathrm{b}}}(i) + N_{(1-\theta)}(i). \tag{4.11}$$

Criteria for choosing grain neighbors

As soon as the quantities $N_{\theta_{\mathrm{b}}}(i)$ and $N_{(1-\theta)}(i)$ are estimated for any i^{th} grain thanks to Eqs. 4.9 and 4.10, respectively, the neighbors are chosen according to the following criteria :

- the neighbors in $N_{\theta_a}(i)$ are the nuclei appeared on the grain boundary of the i^{th} grain during the last time step.
- The neighbors in $N_{\theta_b}(i)$ are chosen among the RX grains of the microstructure.
- The neighbors in $N_{(1-\theta)}(i)$ are chosen among the NR grains of the microstructure.

The choice of the neighbors in $N_{\theta_b}(i)$ and $N_{(1-\theta)}(i)$ is made by weighted each grain by its volume in order to be representative of real microstructures.

A bijection is imposed between a grain and its neighbors, meaning that if the i^{th} grain has the j^{th} grain as neighbor, the j^{th} grain has also the i^{th} grain as neighbor. Thus when the i^{th} grain grows of a quantity $\Delta V_{(i,j)}$ with respect to the j^{th} grain, the j^{th} grain shrinks of a quantity -$\Delta V_{(i,j)}$ with respect to the i^{th} grain in order to ensure the bijective as well as volume conservation.

It is also worth noticing that the surface fractions $\theta(i)$ and $(1-\theta)(i)$ are only used to identify the respective numbers of neighbors $N_{\theta_b}(i)$ and $N_{(1-\theta)}(i)$. Even so, after the random selection of the neighbors in $N_{\theta}(i)$ and $N_{(1-\theta)}(i)$, a small error can exist on the fractions $\theta(i)$ and $(1-\theta)(i)$. However, this is not a strong assumption since a grain boundary surface is never exactly spherical in reality.

Reformulation of boundary migration equation

Since this new approach considers a particular neighborhood for each grain, the Eq. 4.3 for grain boundary migration presented in the first section has to be reformulated. First, the volume change of the i^{th} grain is computed according to the following equation in the NHM :

$$\Delta V_i = \sum_{j=1}^{N_{\text{tot}}(i)} \Delta V_{(i,j)}, \tag{4.12}$$

where $\Delta V_{(i,j)}$ is the volume variation between the i^{th} grain and its j^{th} neighbors, defined by the equation :

$$\Delta V_{(i,j)} = M_b \left(\delta\tau(\rho_j - \rho_i) + \beta\gamma_b \left(\frac{1}{R_j} - \frac{1}{R_i} \right) \right) S_i \Psi_{(i,j)} \Delta t, \tag{4.13}$$

where ρ_j and R_j denote the dislocation density and grain radius of a neighbor j of the i^{th} grain. $\Psi_{(i,j)}$ is the radius fraction of a neighbor j with respect to other grain neighbors of i, aiming to redistribute the volume variation of the i^{th} grain on its neighbors depending on their size. This quantity is estimated by the following relation :

$$\Psi_{(i,j)} = R_j / \sum_{k=1}^{N_{\text{tot}}(i)} R_k. \tag{4.14}$$

Two flow charts summarizing the main algorithm of the NHM as well as the implementation performing boundary migration are presented for a single time step on Fig. 4.5(a) and (b), respectively.

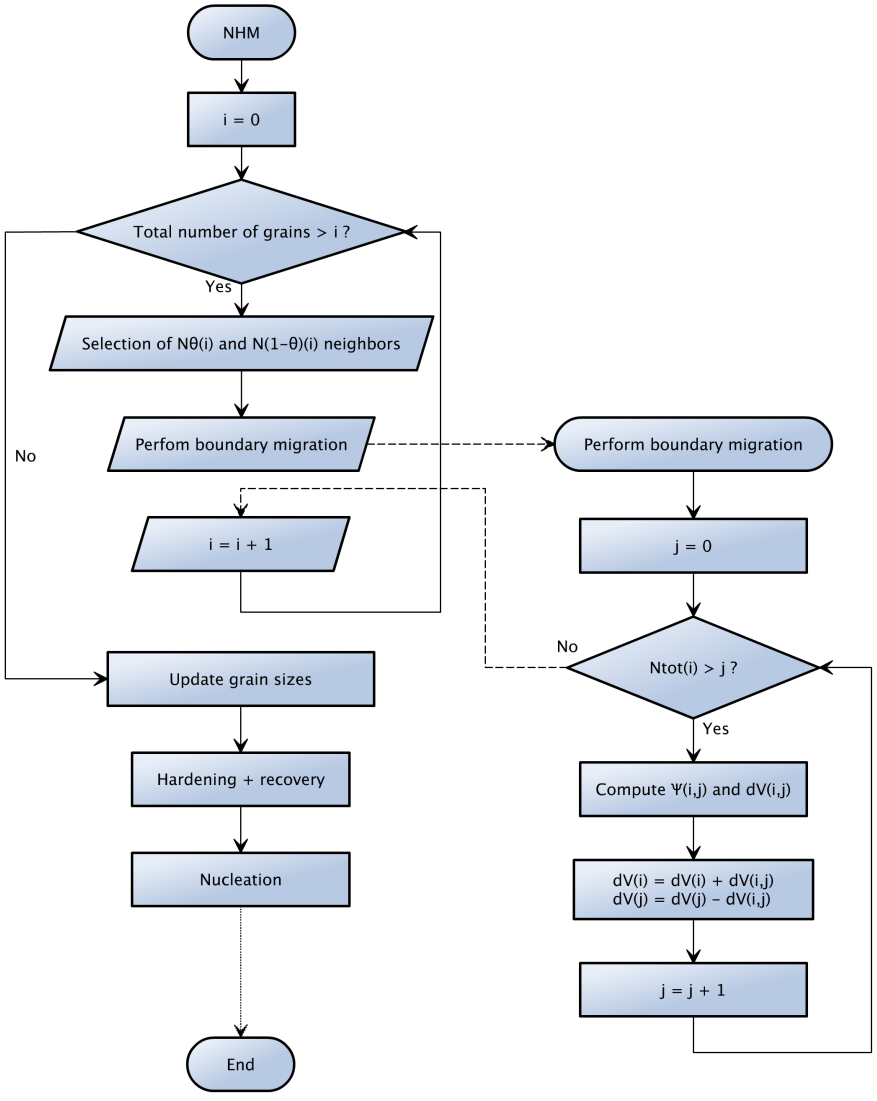

Fig. 4.5. *Flow charts representing (a) one time step of the main algorithm and (b) the way to perform boundary migration in the NHM.*

4.2.3 Modeling of grain elongation

To our knowledge, mean field models of the literature [48–50] assume that the grains remain spherical all along the deformation process. However, it is well-known that the

grain shape evolves during deformation. In the case of necklace type nucleation, the assumption of grains remaining spherical all along the deformation process is a strong assumption that can affect the nucleation rate. Indeed, the nucleation rate $\dot{V}$ depends on the grain surface (Eq. 3.13) which can be underestimated when elongated grains are supposed spherical. Full field models have the advantage of explicitly describing the grain shape evolution during deformation. To investigate the effect of grain shape evolution on the recrystallization kinetics, several DRX simulations were performed using full field model of chapter 3. These latter were performed at two strain rates ($0.01s^{-1}$ and $0.1s^{-1}$), with and without the topological deformation of the RVE. In both cases the dislocation density evolution as well as nucleation and grain boundary migration are modeled in the same manner. It is worth noticing that the simulation presented on Fig. 4.6(c) makes no physical sense but is only used here to illustrate the potential effect of grain shape evolution on the recrystallization kinetics during DRX with a necklace nucleation. Two snapshots of the simulations performed at a strain rate of $0.01s^{-1}$ with and without considering the topological deformation of the RVE are presented on Fig. 4.6. RX fraction, mean grain size, mean grain size (weighted by grain volume) and mean dislocation density (weighted by grain volume) are presented as a function of strain on Fig. 4.7 for the studied strain rates.

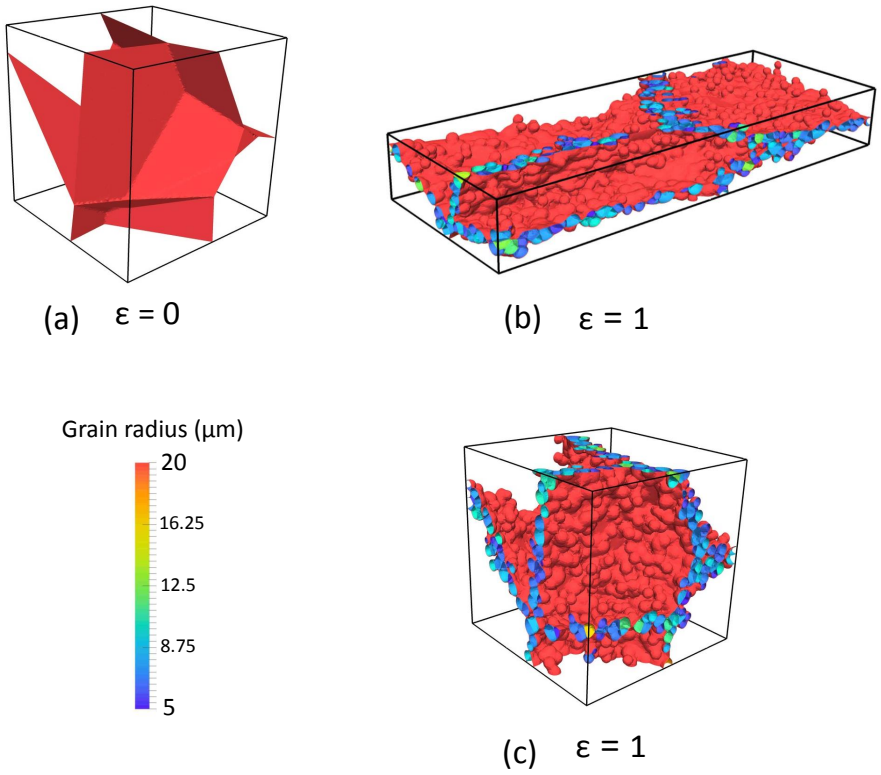

Fig. 4.6. *Microstructure evolution during a full field simulation of DRX performed at a strain rate of $0.01s^{-1}$ (a) at the initial stage of the simulations (b) at $\varepsilon = 1$ with representing the topological deformation of the RVE (c) at $\varepsilon = 1$ without the topological deformation of the RVE.*

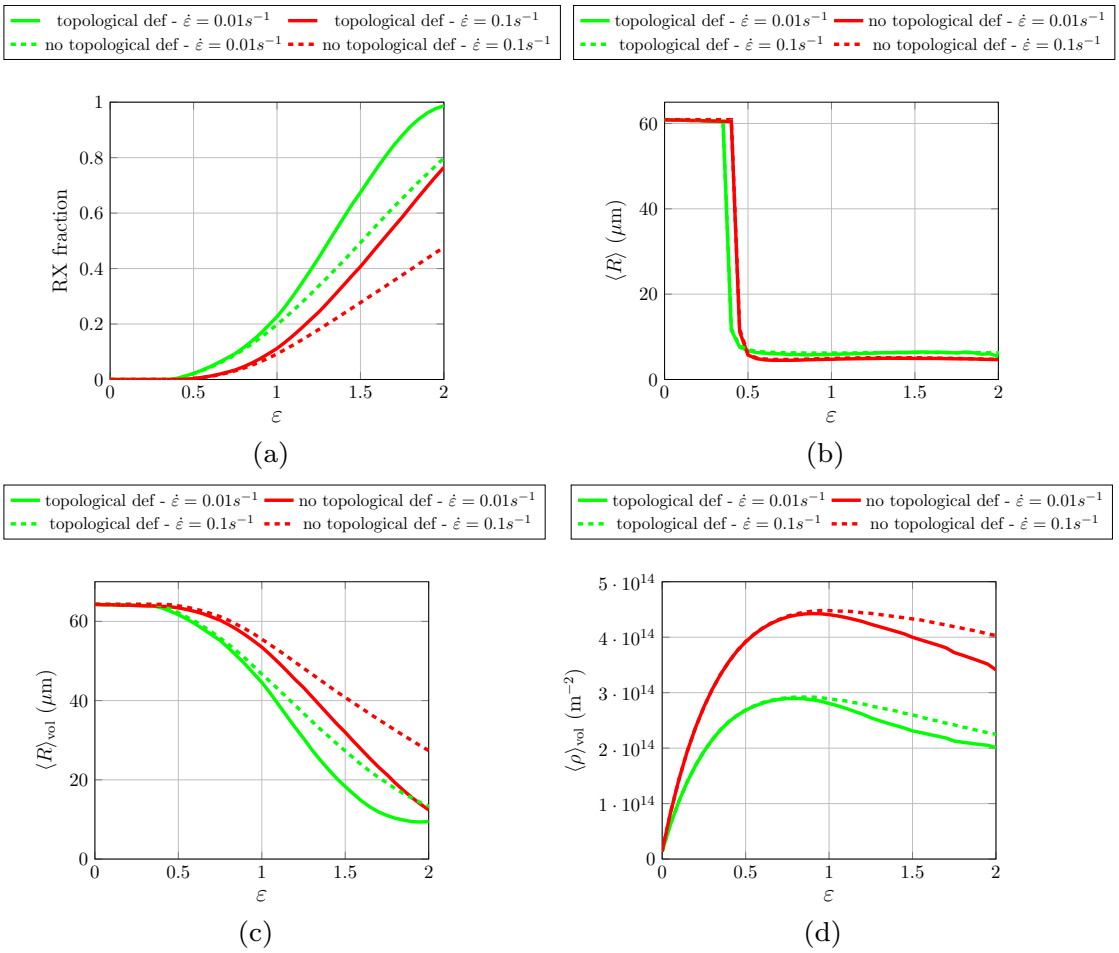

Fig. 4.7. *Comparisons of the results obtained with the full field model of chapter 3, with and without representing the topological deformation of the RVE. The conditions of deformation are a temperature of 1273K and two different strain rates of $0.01s^{-1}$ and $0.1s^{-1}$. The model parameters are those of a 304L steel.*

The consideration of the topological deformation of the RVE has a clear influence on the evolutions of the RX fraction, mean grain size (weighted by grain volume) and mean dislocation density (weighted by grain volume). This can be explained by the fact that when the topological deformation of the RVE is modeled, the grain shape evolves from equiaxed to elongated, which increases the grain boundary surface and thus the nucleation rate (Eq. 3.13). The following section aims to enrich the NHM by modeling evolution of grain shape from spherical to ellipsoidal shape during a dynamic process, in order to take the increase of boundary surface into account.

In this section, grains are assumed to evolve toward an ellipsoidal shape during the deformation process. Thus, for each ellipsoidal grain i, a local coordinate system $(\vec{e_1}^i, \vec{e_2}^i, \vec{e_3}^i)$ that is aligned in the three main directions of the ellipsoid is considered. Three values $(a(i), b(i), c(i))$ represent the three principal semi-axis lengths of the ellipsoidal grain i in its local coordinate system $(\vec{e_1}^i, \vec{e_2}^i, \vec{e_3}^i)$. Furthermore each grain

is associated with an orientation matrix M_i to express the canonical coordinate system $(\vec{x},\vec{y},\vec{z})$ in the local coordinate system $(\vec{e_1}^i,\vec{e_2}^i,\vec{e_3}^i)$. Therefore, each grain i is now defined in the NHM by three semi-axes $(a(i),b(i),c(i))$, a dislocation density ρ_i and a rotation matrix M_i. Thus its volume can be deduced by $V_i = (4/3)\pi a(i)b(i)c(i)$ and its equivalent sphere radius by $R_i = [(3V_i)/(4\pi)]^{1/3}$.

Considering any kind of solicitation, the macroscopic strain tensor $\mathbf{E}$ applied on the material in the canonical coordinate system $(\vec{x},\vec{y},\vec{z})$ can be written as follows :

$$\mathbf{E} = \begin{pmatrix} E_{xx} & E_{xy} & E_{xz} \\ E_{yx} & E_{yy} & E_{yz} \\ E_{zx} & E_{zy} & E_{zz} \end{pmatrix} .$$

Therefore the local strain tensor $\mathbf{L_i}$ in the coordinate system of a given ellipsoidal grain i can be obtained by the following relation :

$$\mathbf{L_i} = M_i \mathbf{E} M_i^t. \tag{4.15}$$

The obtained local strain tensor L_i can be written :

$$\mathbf{L_i} = \begin{pmatrix} \varepsilon_{11} & \varepsilon_{12} & \varepsilon_{13} \\ \varepsilon_{21} & \varepsilon_{22} & \varepsilon_{23} \\ \varepsilon_{31} & \varepsilon_{32} & \varepsilon_{33} \end{pmatrix} .$$

This local strain tensor can be used in the considered ellipsoidal grain to update its three semi-axes $(a(i),b(i),c(i))$. However the obtained strain tensor $\mathbf{L_i}$ is not necessarily diagonal and shear strain can be observed. In order to keep the grains ellipsoidal, only the terms in $\mathbf{L_i}$ that are in the diagonal are considered. This assumption means that if only shear strain components are observed in the local strain tensor $\mathbf{L_i}$ of a grain i, its three semi-axes $(a(i),b(i),c(i))$ do not change. If ε is small enough at each time increment, the evolution of $(a(i),b(i),c(i))$ can be expressed as follows :

$$\begin{aligned} a(i)^{(t+\Delta t)} &= a(i)^t(1+\varepsilon_{11}), \\ b(i)^{(t+\Delta t)} &= b(i)^t(1+\varepsilon_{22}), \\ c(i)^{(t+\Delta t)} &= c(i)^t(1+\varepsilon_{33}). \end{aligned} \tag{4.16}$$

When a grain grows due to boundary migration (Eq. 4.3), its three semi-axes $(a(i),b(i),c(i))$ must also be updated. In this model, growth of a grain is assumed isotropic, thus the three semi-axes $(a(i),b(i),c(i))$ of a grain i having undergone a variation volume are

updated following the relations :

$$\begin{aligned} a(i)^{(t+\Delta t)} &= a(i)^t \times^3 \sqrt{\frac{V_i^{(t+\Delta t)}}{V_i^t}}, \\ b(i)^{(t+\Delta t)} &= b(i)^t \times^3 \sqrt{\frac{V_i^{(t+\Delta t)}}{V_i^t}}, \\ c(i)^{(t+\Delta t)} &= c(i)^t \times^3 \sqrt{\frac{V_i^{(t+\Delta t)}}{V_i^t}}, \end{aligned} \tag{4.17}$$

where V_i^t and $V_i^{(t+\Delta t)}$ are the volume of the grain i at the instants t and $(t+\Delta t)$, respectively.

The evolution of principal lengths of a grain i during deformation leads to an increase of its boundary surface. The grain boundary surface of any ellipsoidal grain can be calculated using incomplete elliptic integral of the first and second kind. However to make it simpler and to decrease the computational cost, the surface of a grain i is estimated using the relation [187] :

$$S_i \simeq 2\pi(a(i)^{\mathrm{p}}b(i)^p + a(i)^p c(i)^p + b(i)^p c(i)^p)^{1/p}, \tag{4.18}$$

where $p = \ln(3)/\ln(2)$. This equation gives the surface of a general ellipsoid with a relative error $< 1.42\%$. With this approach, the grain boundary surface of all grains increases during deformation and the constitutive equation of nucleation rate (Eq. 3.13) is affected. This leads to an acceleration of the nucleation kinetics. Thanks to this new formulation, it is also possible to perform a DRX simulation from an initial microstructure composed of elongated grains, by defining particular initial values of $(a(i), b(i), c(i))$ for each grain i.

4.2.4 Comparison with DRX full field predictions

In the present section, the DRX full field model of chapter 3 is used to discuss the NHM results. As already said, this full field model is based on the same constitutive laws that are used in the NHM for strain hardening, recovery and nucleation. The only difference between the full field model and the present NHM is that the microstructure is explicitly described in the full field methodology which means that the comparison between both indicates if the new microstructure description proposed in the NHM is accurate. An illustrated case of a DRX simulation using the full field model is presented on Fig. 4.8. The simulated process is a channel-die compression on a 304L steel at a temperature of 1273K and a strain rate of $0.01\mathrm{s}^{-1}$.

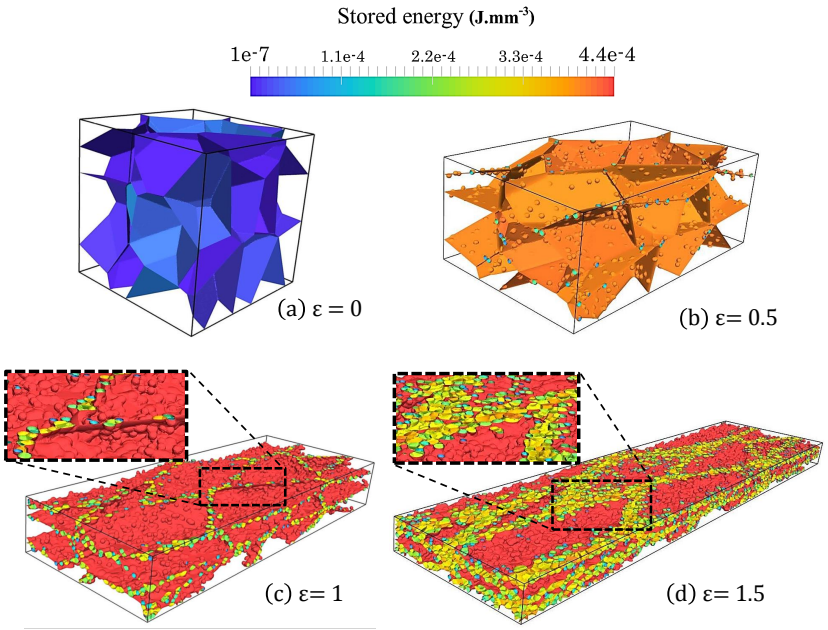

Fig. 4.8. *Illustrated case of a DRX simulation using the full field model of chapter 3. The simulated process is a channel-die compression on a 304L steel at a temperature of 1273K and a strain rate of* $0.01s^{-1}$.

The results in terms of RX fraction, mean grain radius, mean grain radius (weighted by grain volume) and mean dislocation density (weighted by grain volume) obtained from the mean field model of Beltran et al. [50], the NHM and full field simulations are compared on Fig. 4.9. The evolution of the RX fraction and mean grain size (weighted by grain volume) obtained with the model of Beltran et al. [50] are quasi-linear for the two considered strain rates (see Figs. 4.9(a) and (c)). With the present NHM, the RX fraction follows an Avrami evolution (i.e. with a "S" shape, see Fig. 4.9(a)), which is commonly observed in experimental investigations of DRX [156, 188]. Furthermore, evolutions of RX fraction, mean grain size (weighted by volume) and dislocation density (weighted by volume) described with the NHM are quite close to those described by the full field model. Finally, the evolution of the mean grain size (see Fig. 4.9(b)) is correctly described with both the NHM and mean field model of Beltran et al. [50]. It is also observed that the recrystallization kinetics are always faster in the full field case. This observation can be due to the fact that the surface $S1(i)$ is approximated by the surface $S3(i)$ in the NHM and model of Beltran et al. [50] with $S3(i) < S1(i)$ (see Fig. 4.3), whereas $S1(i)$ is explicitly taken into account in the full field case. Thus the total boundary surface Φ considered in the nucleation rate (Eq. 3.13) is always underestimated in the NHM and model of Beltran et al. [50], leading to slower kinetics of recrystallization.

As already mentioned, a known drawback of pre-existing mean field models if that they provide grain size distributions which do not match with experimental ones. The grain size distributions obtained with the full field model, the NHM and the model of Beltran et al. [50] are compared on Fig. 4.10. These distributions are compared

at four strain levels $\varepsilon = 0.5$, $\varepsilon = 1$, $\varepsilon = 1.5$ and $\varepsilon = 2$. The grain size distributions described by the NHM are globally close to grain size distributions obtained with the full field model. Furthermore, the grain size distributions obtained with the NHM are quite wide and spread, which is characteristic of experimental distributions observed during DRX [189]. The grain size distributions obtained with the model of Beltran et al. [50] are more tight, which is the characteristic shape observed in the grain size distributions predicted by standard mean field models [48, 50, 70] as already discussed previously.

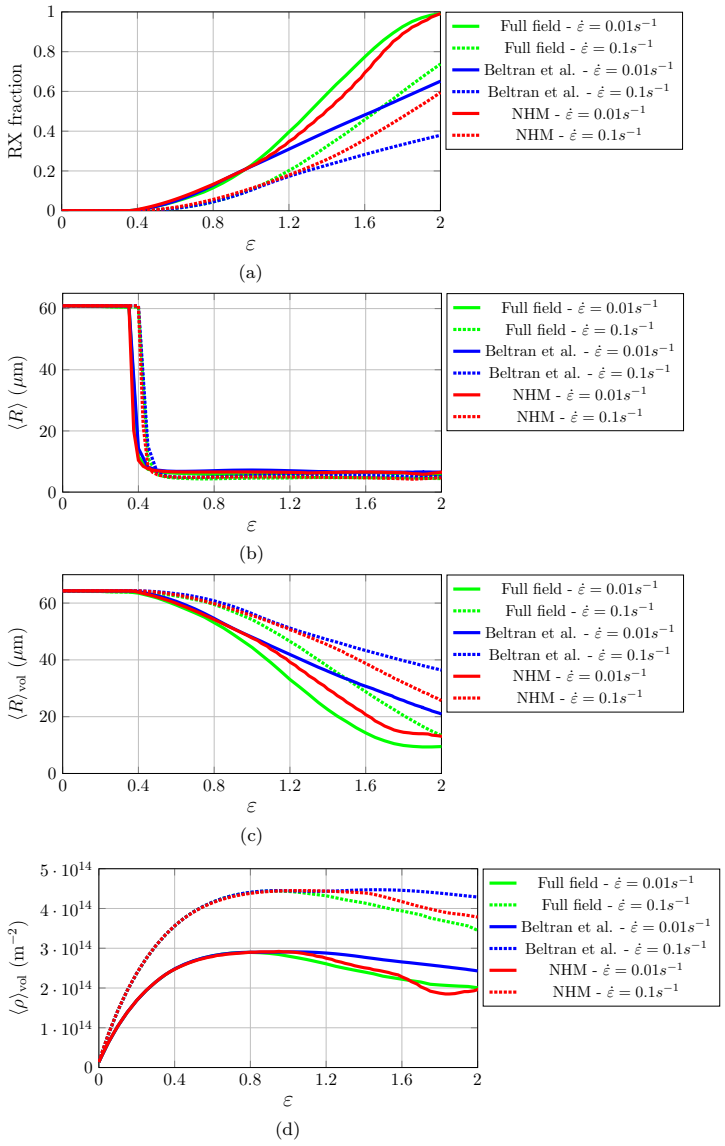

Fig. 4.9. *Comparison of the results obtained by three different models: the full field model of chapter 3, the mean field model of Beltran et al. [50] introduced in first chapter and the NHM proposed in this chapter. The simulated process is a channel-die compression at 1273K, at two different strain rates of $0.01s^{-1}$ and $0.1s^{-1}$.*

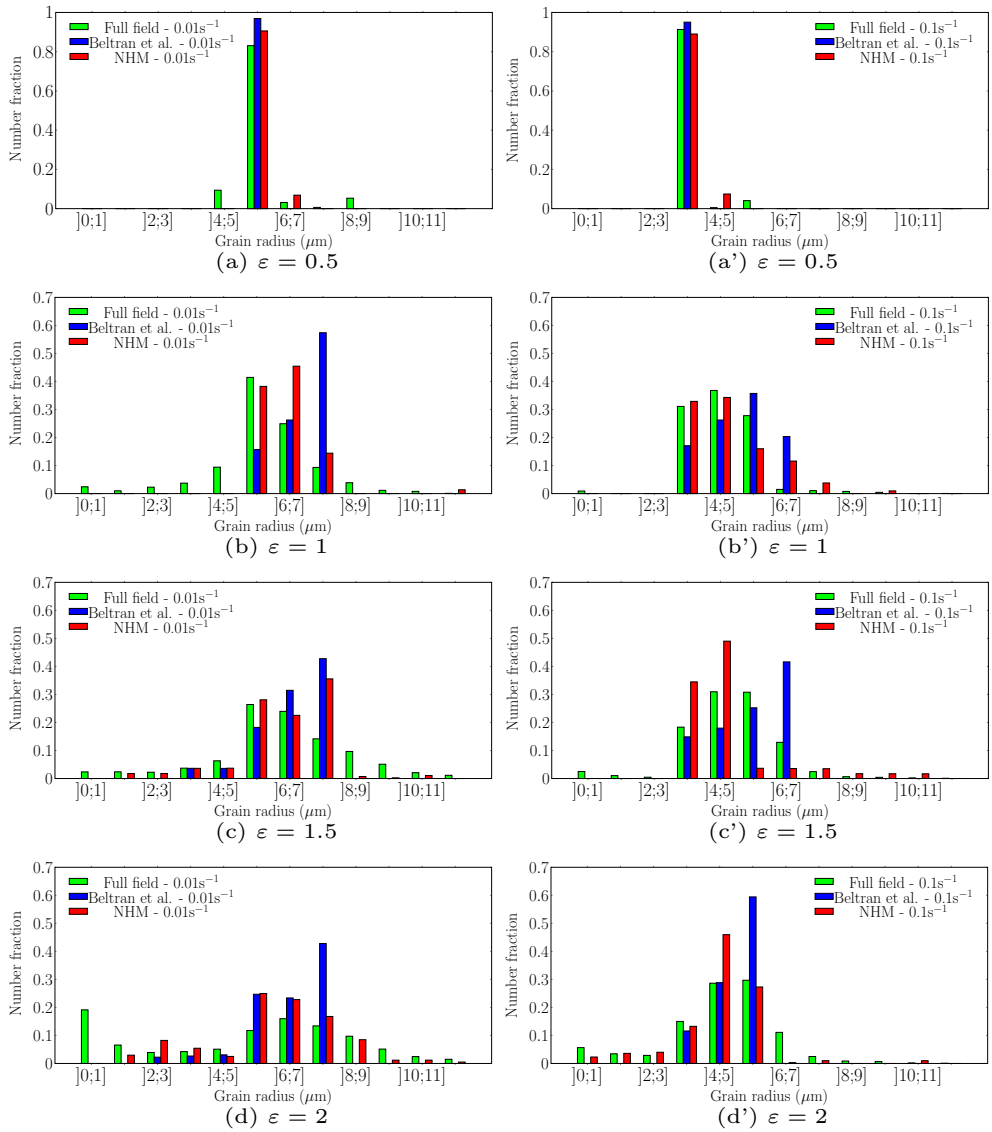

Fig. 4.10. *Comparison of the grain radius distributions obtained with the full field model of chapter 3, the mean field model of Beltran et al. [50] and the NHM. The simulated process is a channel-die compression at 1273K during 200s at two strain rates 0.01s^{-1} and 0.1s^{-1} and interrupted at different strain levels ((a) to (d)).*

As already mentioned, the great advantage of mean field models is their low computational costs. This gives them the possibility to be coupled with macroscopic FE simulations to predict microstructure evolutions throughout the processed product. Therefore, the computational cost of a single simulation is very important in order to perform a large number of simulations in a relatively short time. The computational cost of a NHM simulation mainly depends on the number of grain classes. Therefore, several simulations using the NHM were performed at a temperature of 1273K and a strain rate of 0.01s^{-1}, considering three different initial number of grain classes (8, 16 and 24 grain classes) but the same initial mean grain size. Resulting RX fraction, computa-

tional cost, mean grain radius (weighted by grain volume) as well as mean dislocation density (weighted by grain volume) evolutions are presented on Fig. 4.11. The obtained results are not really dependant on the initial number of classes (see Fig. 4.11(a), (c) and (d)). However, the computational cost seems to increase quite linearly with the initial number of classes (see Fig. 4.11(b)). Thus, a number of 8 initial grain classes is a good compromise between low computational cost and converged results. It is worth mentioning that for this case, the number of classes at the end of the simulation is around 90.

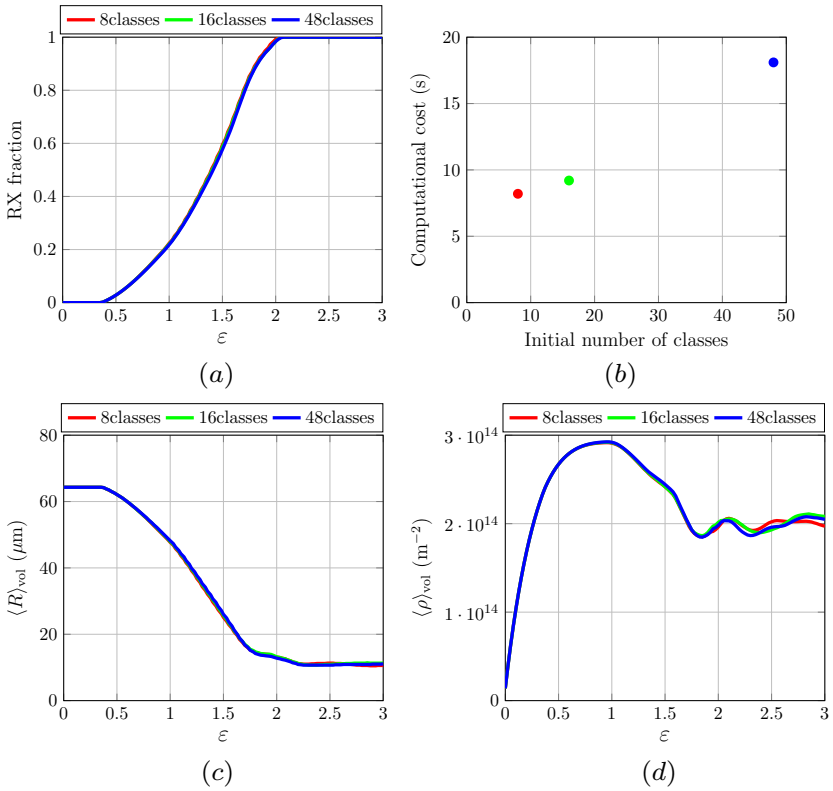

Fig. 4.11. *Sensitivity study of the initial number of grain classes on results obtained with the NHM: (a) recrystallized fraction (b) computational cost (c) mean grain radius (weighted by grain volume) (d) mean dislocation density (weighted by grain volume). Simulations were performed at a strain rate of $0.01s^{-1}$ and a temperature of 1273K.*

The number of grain classes in a simulation, and consequently the computational cost, is also affected by the deformation step. Therefore several simulations using the NHM were performed at the same thermomechanical conditions, with an initial number of 8 grain classes and by considering different deformation steps ($\Delta\varepsilon = 0.01$, $\Delta\varepsilon = 0.025$ and $\Delta\varepsilon = 0.05$). Results in terms of RX fraction, computational cost, mean grain radius (weighted by grain volume) as well as mean dislocation density (weighted by grain volume) are presented on Fig. 4.12. The RX fraction evolution predicted by the NHM with the three different deformation steps are quite similar (see Fig. 4.12(a)). However, the final value of the mean dislocation density (weighted by grain volume) and mean grain

size (weighted by grain volume) predcited by the NHM with a deformation step of 0.05 is a bit different from those predicted with a deformation step of 0.01 or 0.025, the latter being close to each other. It is also observed that the computational cost is very dependant on the deformation step (see Fig. 4.12(c)). A simulation using a deformation step of 0.025 leads to computational costs significantly lower than using a deformation step of 0.01. The influence of the deformation step on the computational cost comes from the fact that the deformation step has a strong influence on the apparition of new classes during the simulation. During nucleation, a new class is created at each deformation step, thus the smaller the deformation step, the more new classes are created during the simulation. A deformation step of 0.025 is retained as a good compromise between converged results and low computational costs. The time step is deduced by dividing the deformation step by the considered strain rate. However for very low strain rates, prohibitive time steps can be obtained. To avoid this problem, a maximal time step of 5s is considered in simulations.

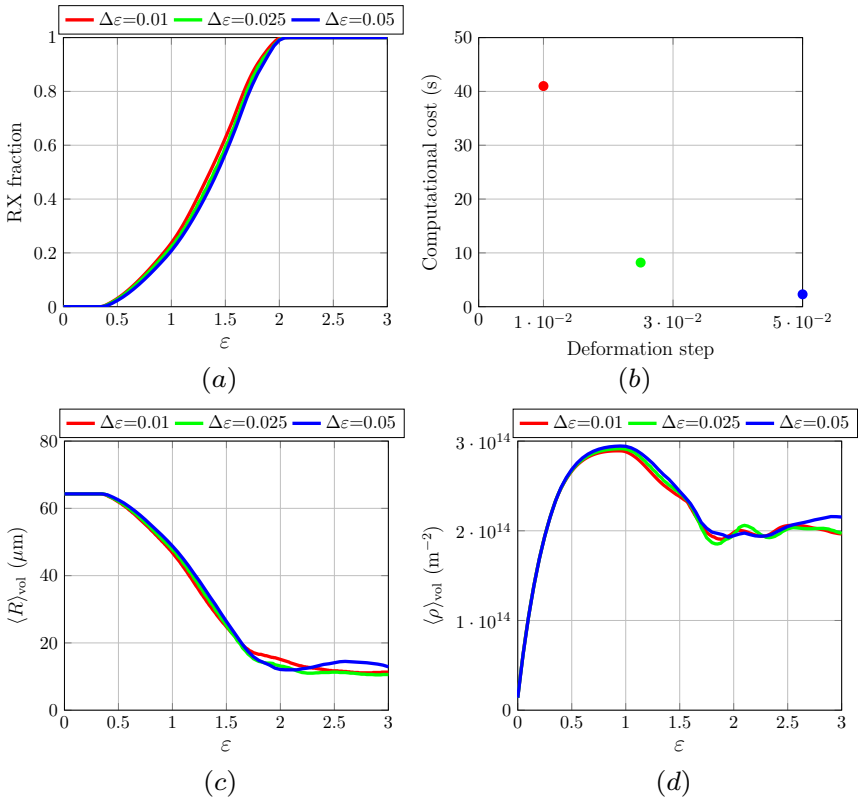

Fig. 4.12. *Sensitivity study of the deformation step on results obtained with the NHM: (a) recrystallized fraction (b) computational cost (c) mean grain radius (weighted by grain volume) (d) mean dislocation density (weighted by grain volume). Simulations were performed at a strain rate of* $0.01s^{-1}$ *and a temperature of 1273K.*

Finally, since the computational cost depends on the strain level, the Fig. 4.13 presents the evolution of the number of increments as well as the cumulated computational cost as a function of the true strain during a simulation at a temperature of 1273K and a strain

rate of $0.01s^{-1}$ using the NHM. A number of 8 initial classes as well as a deformation step of 0.025 were considered in the simulation. First the evolution of the number of increments is linear up to a strain level of 1.2 and then evolves faster. This increase is due to the strategy adopted in the model of Beltran et al. [50] and used in the NHM. The latter consists in adapting the deformation step in order to avoid grains with a negative volume, which can appear with Eq. 4.13 in the NHM. This adaptation means that each deformation step can be discretized in several increments during the simulation. The cumulated computational cost also increases as a function of the true strain during the simulation. This evolution is slow up to a strain level of 1.2 since the number of classes is still low at the beginning of the simulation. Then the evolution of the computation cost increases faster up to the end of the simulation. This increases is due to the fact that the number of increments as well as the number of classes are constantly increasing all along the simulation. The global computational cost of the NHM simulation is still very low ($\simeq$ 8s) at $\varepsilon = 3$, which is quite promising.

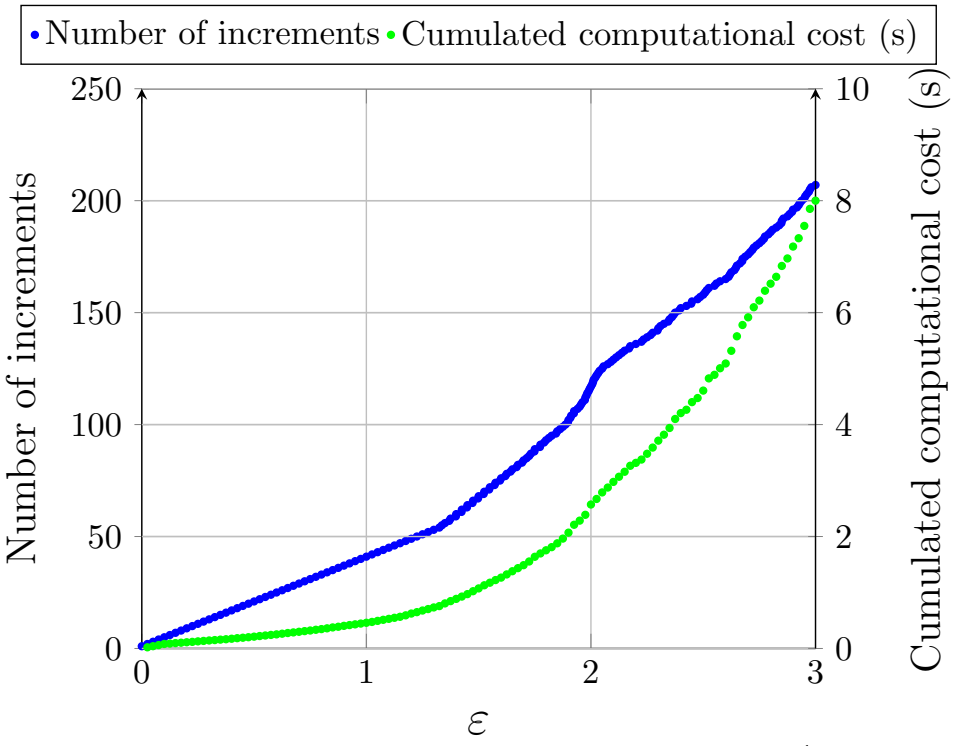

Fig. 4.13. *Number of increments and cumulated computation cost as a function of the true strain obtained during a simulation using the NHM at a strain rate of* $0.01s^{-1}$ *and a temperature of 1273K. A number of 8 initial grain classes and a deformation step of 0.025 were considered.*

4.3 Mean field modeling of post-dynamic recrystallization

4.3.1 Constitutive laws

Grain boundary migration

The grain boundary migration is modeled during the PDRX regime thanks to Eqs. 4.12, 4.13 and 4.14.

Recovery mechanism

The dislocation density is supposed to decrease during the PDRX regime by static recovery. The decrease of the average dislocation density in the i^{th} grain is modeled by the same static recovery equation as used in the mean field model of Beltran et al. [50](Eq. 1.45) and in the full field model of chapter 3 (Eq. 3.6).

Nucleation

In general, PDRX is composed of a static (where nucleation may take place) and metadynamic (no nucleation, just grain boundary migration) regimes. In this model and similarly to the mean field model of Beltran et al. [50] and the full field model of chapter 3, only metadynamic recrystallization is considered in the PDRX regime, hence no nucleation events take place and we considered that last nuclei appeared at the end of the DRX regime. Several authors already showed a good prediction of PDRX without considering nucleation during this regime [50, 190].

4.3.2 Neighborhood choice during PDRX

The choice of neighbors during PDRX is similar to that made during the DRX regime. Since nucleation is not considered during the PDRX regime, the surface fraction θ_a does not exist for the PDRX regime and therefore ($\theta = \theta_b$) as it can be seen on Fig. 4.14.

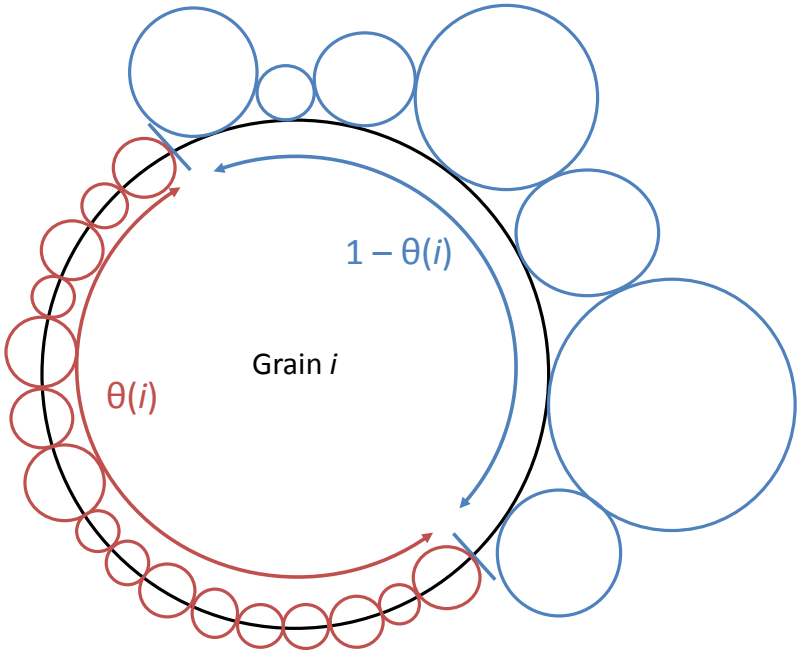

Fig. 4.14. *Representation of a grain in the NHM during the PDRX regime. Each grain i has a surface fraction $\theta(i)$ in contact with RX grains represented in red color and a surface fraction $(1-\theta)(i)$ in contact with NR grains represented in blue color.*

4.3.3 Comparison with PDRX full field predictions

To investigate the efficiency of the NHM during the PDRX regime, simulations were performed and compared using both the NHM and the full field model of chapter 3. The first simulation is composed of a channel-die compression on a 304L steel at a temperature of 1273K and a strain rate of $0.01s^{-1}$ during 200s in order to reach a fully recrystallized state. After deformation, the steel is maintained at 1273K during 1000s to simulate PDRX.

Results are presented on Fig. 4.15 in terms of RX fraction, mean grain size, mean grain size (weighted by grain volume) and mean dislocation density (weighted by grain volume). It is observed that results predicted by the NHM during the PDRX regime are very close to those predicted by the full field model. This good correlation between the two models in the PDRX regime is due to the good prediction of results in the DRX regime, since evolution in the DRX regime has a large influence on predictions in the PDRX regime. Furthermore, the grain size distributions predicted by the two models at the final stage of the PDRX regime are presented on Fig. 4.16. The grain size distribution predicted by the NHM is very close to that predicted by the full field model. However, a lower number of classes remains in the NHM at the end of the simulation, which explains the lower number of peaks in the distribution predicted by the NHM.

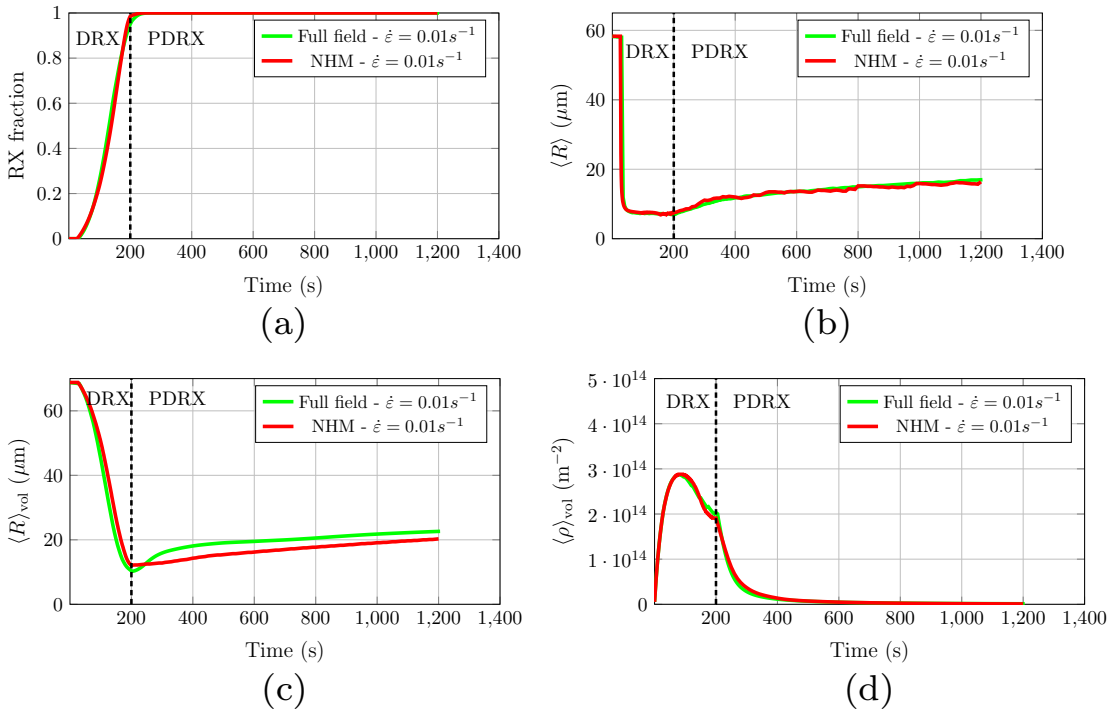

Fig. 4.15. *Comparison of the results obtained by the full field model presented in the previous chapter and the the NHM proposed in this chapter. Compared results are: (a) recrystallized fraction (b) mean grain size, (c) mean grain size (weighted by grain volume) and (d) mean dislocation density (weighted by grain volume). The simulated process is a channel-die compression at 1273K, at a strain rate of 0.01s^{-1} for 200s following by a hold at this same temperature for 1000s.*

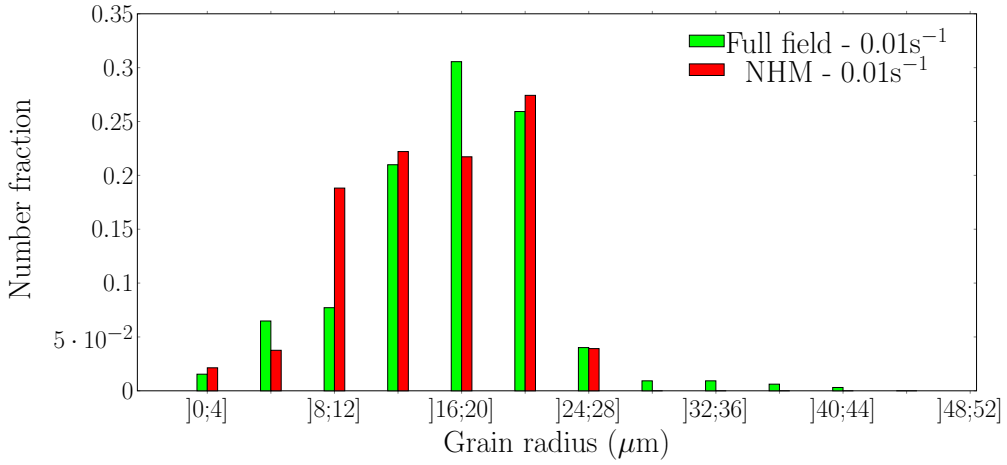

Fig. 4.16. *Comparison of the grain radius distributions predicted by the full field model presented in the previous chapter and by the NHM at the final stage of the PDRX regime. The simulated process is a channel-die compression at 1273K at a strain rates 0.01s^{-1} for 200s following by a hold at this same temperature for 1000s.*

Another interesting case to be studied is a half-fully recrystallized microstructure following by a hold to simulate a PDRX process. This case is particularly interesting since the microstructure is non-fully recrystallized and therefore it can be seen whether interactions between NR and RX grains are correctly taken into account in the NHM. To investigate this case, a channel-die compression is simulated using both the NHM and full field models, at 1273K and a strain rate of 0.01s^{-1} during 130s to reach a half-fully recrystallized state. Then the microstructure are maintained at this same temperature during 1000s to simulate PDRX. Results are presented on Fig. 4.17 in terms of RX fraction, mean grain size, mean grain size (weighted by grain volume) and mean dislocation density (weighted by grain volume). Is it still observed that averaged results predicted by the NHM are very close to those predicted by the full field model, meaning that the description of the neighborhood considered in the NHM during PDRX regime is a good approximation of full field models. The grain size distributions predicted by the two models at the final stage of the PDRX regime are also presented on Fig. 4.18. A good prediction of the grain size distribution is still observed with the NHM when compared to that predicted by the full field model.

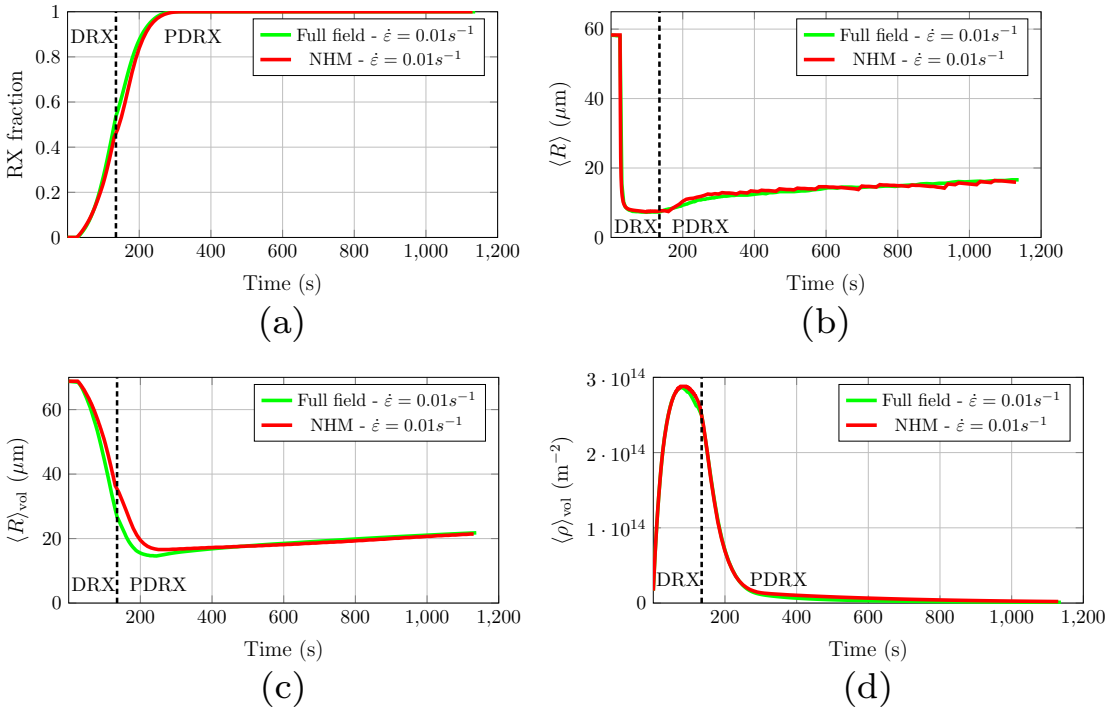

Fig. 4.17. *Comparison of the results obtained by the full field model presented in the previous chapter and the NHM proposed in this chapter. Compared results are: (a) recrystallized fraction (b) mean grain size, (c) mean grain size (weighted by grain volume) and (d) mean dislocation density (weighted by grain volume). The simulated process is a channel-die compression at 1273K, at a strain rate of $0.01s^{-1}$ for 130s following by a hold at this same temperature for 1000s.*

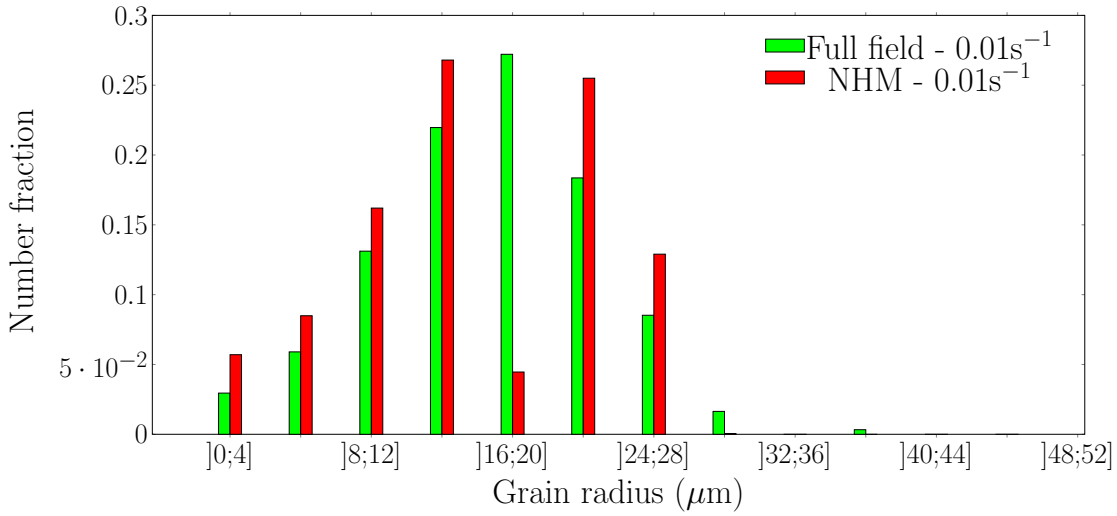

Fig. 4.18. *Comparison of the grain radius distributions predicted by the full field model presented in the previous chapter and by the NHM at the final stage of the PDRX regime. The simulated process is a channel-die compression at 1273K at a strain rates 0.01s^{-1} for 130s following by a hold at this same temperature for 1000s.*

Summary

In this chapter, a new topological approach called "NHM" for NeighborHood Model is proposed for the mean field modeling of DRX and PDRX. The latter is based on two main improvements as compared to the state of the art: (i) the consideration of a particular neighborhood for each grain and (ii) the modeling of grain shape evolution from spherical to ellipsoidal shape during a dynamic process, in order to take the increase of boundary surface into account.

On a first hand, the results obtained by the NHM during the DRX regime were compared to those obtained by a former mean field model [50] and non-negligible improvements were observed in terms of average quantities as well as grain size distributions. Furthermore, a sensitivity study performed during the DRX regime showed that the NHM is interesting in terms of numerical costs, which gives the opportunity to simulate the microstructure evolutions on an entire forged part issued from a FE calculation in few days.

On a second hand, multi-pass deformation routes (DRX + PDRX) were performed with the NHM and compared to full field predictions in terms of averaged quantities as well as grain size distributions. Two cases were simulated: the first case is composed of a DRX regime up to a fully recrystallized microstructure following by a holding at the same temperature during few minutes to simulate a PDRX regime. The second case is composed of a DRX regime up to a half-fully recrystallized microstructure also following by a holding at the same temperature during few minutes to simulate a PDRX regime. In both cases, the NHM correctly predicts averaged quantities (RX fraction, mean grain size and mean dislocation density) as well as grain size distributions when compared to full field predictions. Despite large advances in terms of predictions as compared to former mean field formulations, some improvements concerning the choice of neighbors can still be done based on experimental investigations.

A major advantage of NHM is related to the fact that it is based on the same constitutive equations as used in the full field model of chapter 3. Therefore, since NHM simulations are relatively fast, it can helps to identify some model parameters by inverse analysis and these latter can then be used in the full field model. In the next chapter, a procedure of identification of the four model parameters is presented. While the strain hardening K_1 and dynamic recovery K_2 parameters are identified based on stress-strain curves, the two others parameters related to strain rate dependence of boundary migration δ and to nucleation K_g need to be identified by inverse analysis on microstructural quantities. Therefore in this case, the NHM is primordial and allows to identify all K_g and δ parameters in few minutes based on experimental data.

Chapter 5

Identification of DRX model parameters for the 304L steel and comparison between model predictions and experimental results.

Contents

5.1 Thermomechanical testing 139

5.1.1 Compression process 140

5.1.2 Sample geometries 141

5.1.3 Finite element simulations 141

5.1.4 Repeatability study 145

5.2 Identification of strain hardening (K_1) and dynamic recovery (K_2) parameters 146

5.2.1 Stress-strain curves 146

5.2.2 Method for the identification of K_1 and K_2 148

5.3 Identification of the parameter describing the strain rate dependence of boundary migration (δ) and of the nucleation parameter $(K_{\mathbf{g}})$ 156

5.3.1 Microstructure investigations 156

5.3.2 Identification procedure for δ and K_{g} 168

5.4 Comparison between experimental data and results issued from the NHM after calibration 171

5.5 Comparison between experimental data and results issued from the NHM and the full field model after calibration 174

Résumé en français

Dans ce chapitre, des essais de compression à hautes températures ont été éffectués sur un acier 304L. Ceux-ci sont présentés afin de mettre en place une méthode de calibration robuste des deux modèles champ complet et champ moyen précédemment introduits. Les courbes contrainte-déformation obtenues permettent de déterminer les paramètres d'écrouissage et de restauration. Par ailleurs, les observations microstructurales permettent d'identifier par analyse inverse grâce au modèle champ moyen les paramètres liés à la mobilité des joints de grains et à la germination. Après identification de ces quatre paramètres pour différentes conditions thermomécaniques, les résultats prédits par les deux modèles sont comparés aux données expérimentales pour un nouveau couple de conditions thermomécaniques. Une très bonne prédiction des modèles est alors observée. Les distributions de tailles de grains sont également comparées aux données expérimentales et des populations de très petits grains observées sur les cartographies expérimentales ne sont pas correctement prédites par les modèles. Ceci est principalement relié au fait que les germes sont insérés avec une taille critique. Une discussion afin de remédier à ce problème est évoquée à la fin de ce chapitre.

In chapters 3 and 4, a new full field model and the NHM were proposed for modeling dynamic and post-dynamic recrystallization. In these two chapters, as a first approximation, model parameters identified by inverse analysis using the mean field model of Beltran et al. for a 304L steel were taken from literature [50]. Even though dynamic recrystallization is modeled through the physical mechanisms taking place, the identified parameters cannot be considered as model independent, because the identification process uses the implemented model. It is therefore necessary to identify the material parameters set using the new proposed models. In a first part of this chapter, compression tests performed at high temperatures on a 304L steel are presented. Then based on the obtained flow curves and microstructure evolutions, the four model parameters were identified at different temperatures and strain rates: stress-strain curves were used to identify the strain hardening (K_1) and dynamic recovery (K_2) parameters while microstructure evolutions were used to identify the strain rate dependence of boundary migration given by the parameter (δ) as well as nucleation parameter (K_g). Finally, the results issued from the NHM and the full field model after calibration were compared to experimental ones.

5.1 Thermomechanical testing

Thermomechanical tests performed on 304L steel samples are presented in this section. Among the classical mechanical tests, compression was chosen since this is the closest to industrial processes (especially forging). Different sets of conditions were chosen in terms of temperature and strain rate to investigate flow behaviors and microstructure evolutions. The steps of the compression tests are presented on Fig. 5.1: (A) the sample is put in the heated oven so its temperature increases, (B) the sample is kept at a high temperature for 30min to ensure the homogeneity of the desired temperature, (C) compression test is performed for a given strain rate and up to a given level of strain, (D) After plastic deformation the sample is quenched with the smallest possible delay (i.e. around 2s) to limit post-dynamic evolutions.

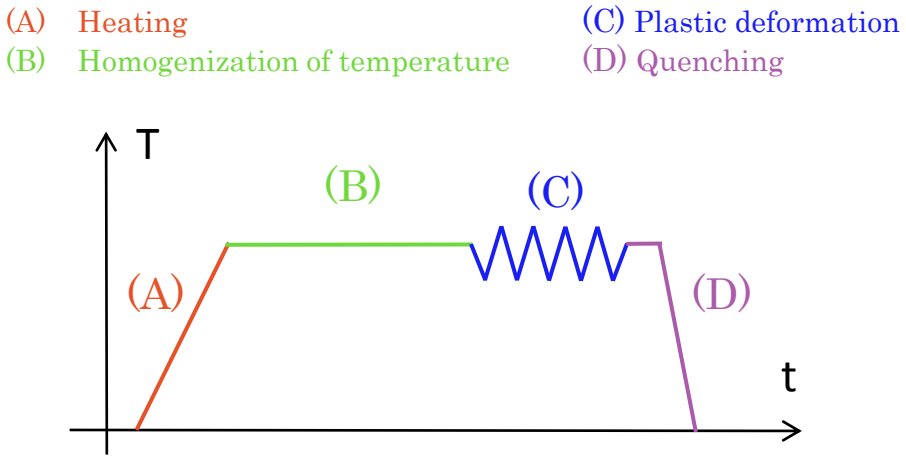

Fig. 5.1. *Thermomechanical path used for the hot compression tests.*

5.1.1 Compression process

The heating step is performed by using an oven with a power of 2000W. The maximal temperature that can be reached is around 1473K while the heating speed is around 773K per hour in average. The temperature gradient is controlled at any instant thanks to two sensors at the bottom and top of the oven. As soon as the oven reaches the desired temperature, the sample is inserted and is maintained during 30min before compression to make sure that the desired temperature is homogeneous inside the sample. After compression, the oven goes up and the sample is manually pushed into water to minimize post-dynamic evolutions. Since the quenching is performed manually, the duration between the end of deformation and cooling is around 2s, which will be considered to be short enough to avoid any significant post-dynamic evolution for the applied strain rate range.

The deformation step is performed by using a compression machine MTS Landmark 370-25. Compression is performed by controlling the displacement of the upper tool as a function of time, while the bottom tool remains static. The maximal force that can be reached is around 250kN while the maximal velocity of the upper tool is around 100mm/s. Lower and upper tools are made of the super-alloy Udimet 720 that keeps suitable mechanical properties at high temperatures. Furthermore, a silicon nitride (Si_3N_4) ceramic insert is also added on the tools extremities. A small quantity of molybdenum disulphide (MoS_2) is also added on the tools as lubricant to reduce friction and sticking at interfaces between the tools and the sample. The hot compression framework is schematized on Fig. 5.2.

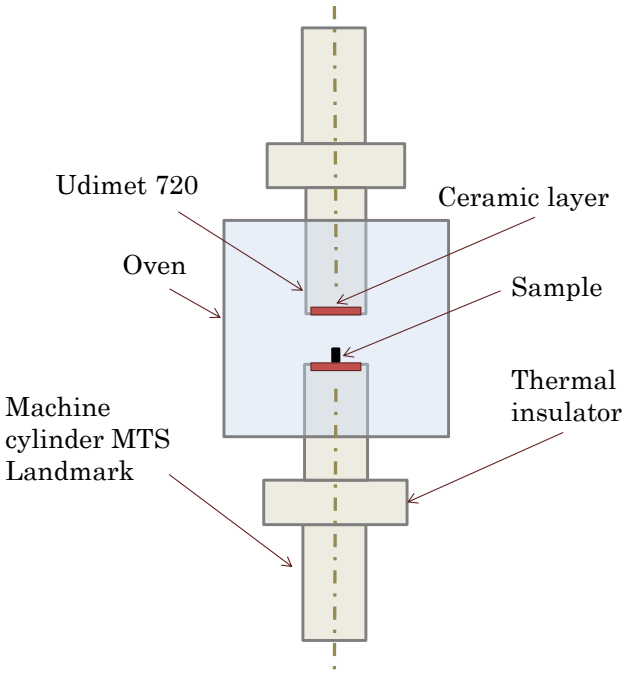

Fig. 5.2. *Compression framework for the dynamic tests.*

5.1.2 Sample geometries

Two different sample geometries were used for the compression tests: cylindrical and double-cone samples as presented on Fig. 5.3. Cylindrical samples were used for identifying the stress-strain curves and also for the microstructure analyses at low strain levels. Double-cone samples were used to analyze the microstructure states of the 304L steel at higher strain levels. An advantage of the double-cone samples is the ability to obtain a strain gradient along the radius while keeping a quasi-constant strain rate.

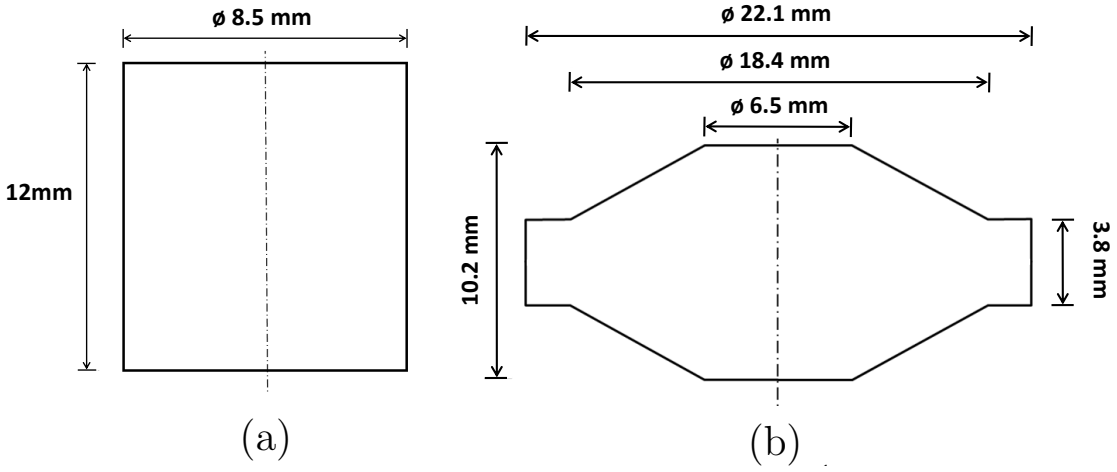

Fig. 5.3. *Sample geometries used for compression tests: (a) cylindrical and (b) double-cone.*

5.1.3 Finite element simulations

During compression tests, the strain and strain rate fields are heterogeneous inside samples due to friction at interfaces with tools, but also due to the geometry of double-cone samples. Microstructure investigations will be performed only at selected points of samples. In order to estimate the strain and strain fields and properly choose the areas to be analysed, compression tests were simulated using the Forge® finite element software to establish a link between boundary conditions imposed on the upper tool $(\dot{\varepsilon}, \varepsilon)$ and local thermomechanical history $(\dot{\varepsilon}_{\mathrm{VM}}, \varepsilon_{\mathrm{VM}})$ at each point of the deformed sample. Here $\dot{\varepsilon}$ and ε stand for the macroscopic strain rate and the true strain, respectively, and $\dot{\varepsilon}_{\mathrm{VM}}$ and $\varepsilon_{\mathrm{VM}}$ are the von Mises equivalent plastic strain rate and equivalent plastic strain, respectively, calculated by the relations :

$$\dot{\varepsilon}_{\mathrm{VM}} = \sqrt{\frac{2}{3}\dot{\varepsilon}_{ij} : \dot{\varepsilon}_{ij}}, \tag{5.1}$$

$$\varepsilon_{\mathrm{VM}} = \int_0^t \dot{\varepsilon}_{\mathrm{VM}} \mathrm{d}t, \tag{5.2}$$

where $\dot{\varepsilon}_{ij}$ are the components of the strain tensor. The procedure to perform FE simulations is the following: a 2D axisymmetric model is first built up in the software. Then,

samples with an initial height noted h_0 (h_0 = 12mm for cylindrical and 10.2mm for double-cone samples), are compressed up to a final height noted h_f ($h_f = 8.2^{\pm 0.05}$mm for cylindrical and $4.5^{\pm 0.15}$mm for double-cone samples, in accordance with final heights obtained during experimental tests). The true strain ε, considered to quantify the macroscopic deformation of sample, is deduced at any instant of the simulation by the following relation :

$$\varepsilon(t) = \ln\left(\frac{h(t)}{h_0}\right), \tag{5.3}$$

where $h(t)$ is the height of the sample at time t. The macroscopic strain rate $\dot{\varepsilon}$ imposed on a sample between two instants t_1 and t_2 can be deduced from the relation :

$$\dot{\varepsilon}_{(1-2)} = \frac{d\varepsilon}{dt_{(1-2)}} = \frac{v_{(1-2)}}{h_1}, \tag{5.4}$$

where h_1 is the height of the sample at the instant t_1 and $v_{(1-2)}$ is the constant velocity of the upper tool between t_1 and t_2. In this work, we tried to perform each compression test at a constant strain rate, therefore the tool velocity was piecewise constant, but frequently reduced during compression to compensate for the sample height reduction, so as to respect the imposed macroscopic strain rate.

A Hensel Spittel constitutive equation [191], representative of the considered 304L steel, is used in simulations :

$$\sigma = Ae^{m_1 T}\varepsilon^{m_2}\dot{\varepsilon}^{m_3}\varepsilon^{m_4/\varepsilon}, \tag{5.5}$$

where σ, ε and $\dot{\varepsilon}$ are respectively stress, strain and strain rate and T is the temperature in Celsius, $m_1 = -0.00383$ defines the material's sensitivity to temperature, $m_2 = 0.01246$ and $m_4 = -0.02413$ define the material's sensitivity to strain, $m_3 = 0.09912$ defines the material's sensitivity to the strain rate and $A = 8905.35$ is an additional fitting parameter. These values were extracted from the Forge® database. Elastic behavior is omitted in these simulations. To model friction at interfaces between samples and tools, a Coulomb's law is considered in the software. Friction coefficients were estimated by inverse analysis minimizing the error between experimental and numerical barrel shape obtained at end of compression process. We found a mean friction coefficient of 0.6 and this value was used for all the simulations.

After compression tests, microstructure is observed at different points of samples. For the cylindrical samples, the observation zone is located in the middle of the sample (Point A on Fig. 5.4). For the double-cone samples, two observations zones, located in the middle and at a distance to one third of the center (Points B and C on Fig. 5.5, respectively) are considered. As an illustration, the final stage of a simulated compression test performed on a cylindrical sample at T = 1273K and $\dot{\varepsilon}$ = 0.008s^{-1} is presented on Fig. 5.4. The ε_{VM} and $\dot{\varepsilon}_{VM}$ fields are presented on Fig. 5.4(a) and (b), respectively. It is observed that the maximal ε_{VM} value is reached at the point A and is around 0.65. Furthermore the $\dot{\varepsilon}_{VM}$ value at this instant of simulation and at this point is around 0.016s^{-1}, which is two times higher than $\dot{\varepsilon}$.

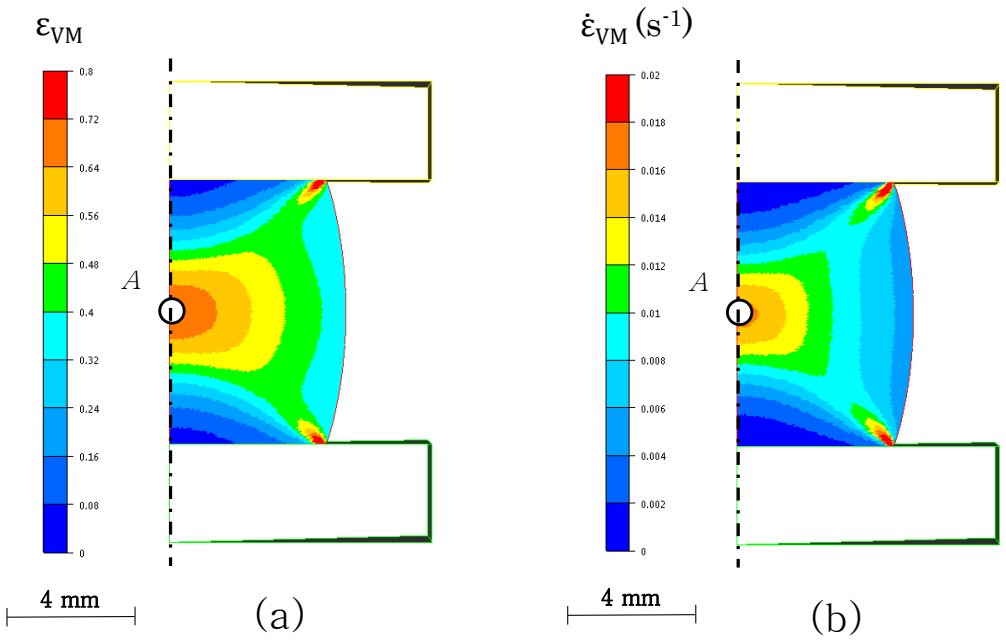

Fig. 5.4. *Finite element simulations performed on a cylindrical sample at $T = 1273K$ and $\dot{\varepsilon} = 0.008s^{-1}$ at the final stage of the simulation ($h_f \simeq 2/3h_0$). Presented fields are (a) equivalent plastic strain and (b) equivalent plastic strain rate.*

A simulated compression test performed at $T = 1273$K and $\dot{\varepsilon} = 0.01\text{s}^{-1}$ on a double-cone sample is also presented on Fig. 5.5 at the final stage of the simulation. At this instant, the ε_{VM} value at point B is around 1.35 while that at point C is around 1. Furthermore, the $\dot{\varepsilon}_{VM}$ value at point B is around 0.015s^{-1} while that at point C is around 0.01s^{-1}.

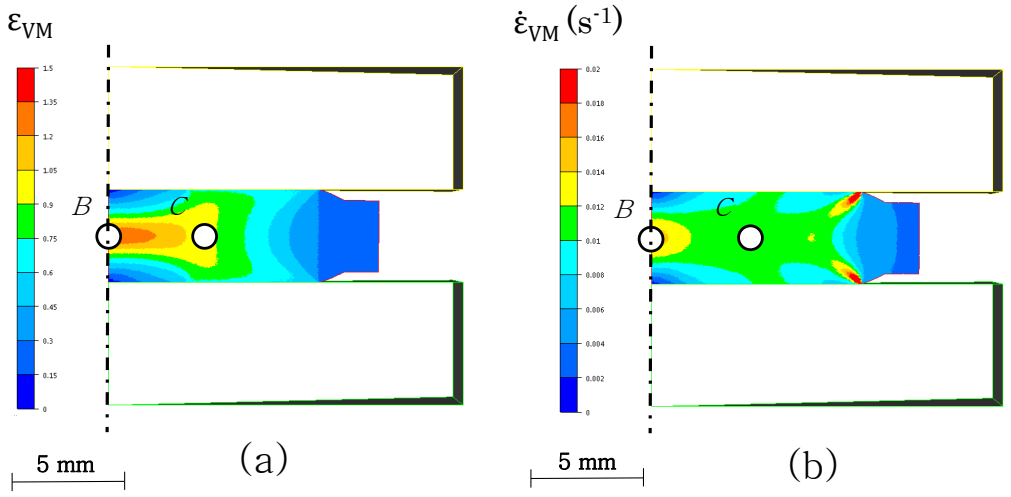

Fig. 5.5. *Finite element simulations performed on a double-cone sample at $T = 1273K$ and $\dot{\varepsilon} = 0.01s^{-1}$ at the final stage of the simulation. Presented fields are (a) equivalent plastic strain and (b) equivalent plastic strain rate.*

The FE simulations are also used to make sure that $\dot{\varepsilon}_{VM}$ is quasi-constant at points A, B

and C all along the compression tests. Therefore, the evolutions of $\dot{\varepsilon}_{VM}$ and ε_{VM} at these three points are plotted over time on Fig. 5.6(a) and (b), respectively. It is observed that the evolution of ε_{VM} is quasi linear in the three cases while the evolution of $\dot{\varepsilon}_{VM}$ is quite winding. The values of $\dot{\varepsilon}_{VM}$ are most of time between 0.01 and 0.02s^{-1} at the three points and are spread around a mean value of 0.014s^{-1}. We assumed in this work that $\dot{\varepsilon}_{VM}$ is almost constant over time in the three cases and equal to 0.014s^{-1}. Thus, for each given set of equivalent plastic strain rate $\dot{\varepsilon}_{VM}$ and temperature T, three levels of ε_{VM} were investigated (0.65, 1 and 1.35).

Different relations between the macroscopic strain rates $\dot{\varepsilon}$ imposed on the compression machine and the equivalent plastic strain rates $\dot{\varepsilon}_{VM}$ obtained at the three points A, B and C by simulations are reported in Tab. 5.1.

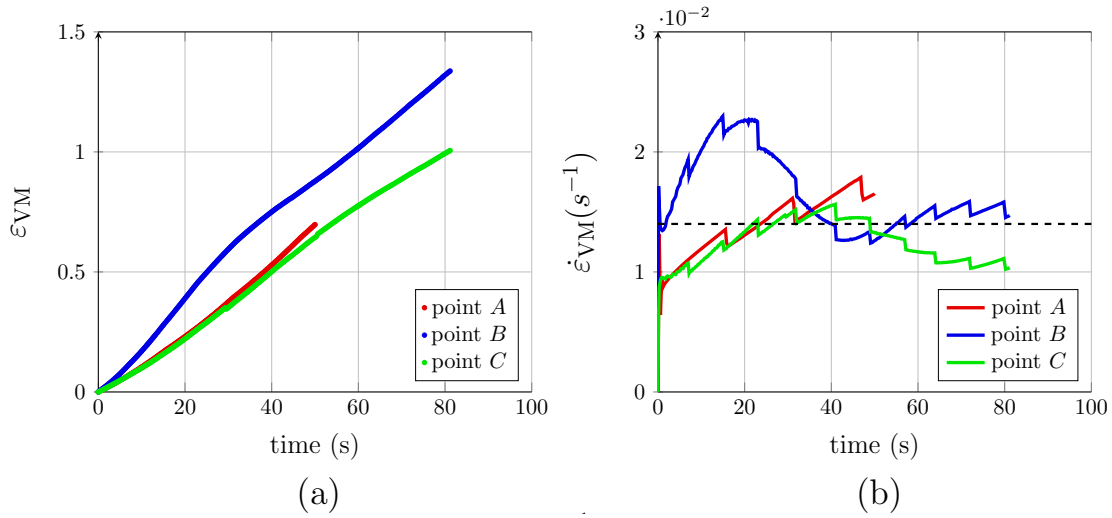

Fig. 5.6. *Evolution of (a) equivalent plastic strain and (b) equivalent plastic strain rate at the three points A, B and C obtained by finite element simulations of hot compression tests, as presented on Figs. 5.4 and 5.5.*

	cylindrical sample (point A)			double-cone sample (points B and C)		
$\dot{\varepsilon}(s^{-1})$	0.008	0.04	0.08	0.01	0.05	0.1
$\dot{\varepsilon}_{VM}(s^{-1})$	0.014	0.07	0.14	0.014	0.07	0.14

Tab. 5.1. *Relations between different imposed macroscopic strain rates $\dot{\varepsilon}$ and equivalent plastic strain rates $\dot{\varepsilon}_{VM}$ at the three points A, B and C. Since $\dot{\varepsilon}_{VM}$ slightly varies during a simulation (Fig. 5.6), values presented here are averaged on time. These results are obtained by finite element simulations, as presented on Figs. 5.4, 5.5 and 5.6.*

To summarize, the macroscopic thermomechanical conditions applied for the all experimental compression tests are reported in Tab. 5.2. The ranges of temperatures and macroscopic strain rates were chosen to be close to industrial processes conditions. For

each test, the equivalent plastic strain rates $\dot{\varepsilon}_{VM}$ in samples at points A, B and C were reported in Tab. 5.1.

		$\dot{\varepsilon}(s^{-1})$					
		0.008	0.01	0.04	0.05	0.08	0.1
T(K)	1273	✓	✓	✓	✓	✓	✓
	1323	✓	✓				
	1373	✓	✓				

✓: Tests performed only on cylindrical samples.
✓: Tests performed on both double-cone and cylindrical samples.

Tab. 5.2. *Sets of thermomechanical conditions in terms of macroscopic strain rates and temperatures applied for the compression tests.*

5.1.4 Repeatability study

Several compression tests performed on cylindrical samples were doubled in order to investigate the repeatability of results. The obtained stress-strain curves are presented on Fig. 5.7 where the true stress σ is plotted as a function of the true strain ε. The oscillations observed on the curves are related to the changes in the upper tool velocity to keep a quasi-constant macroscopic strain rate. For each set of thermomechanical conditions, both curves are close to each other, in particular at the lower temperatures, confirming the repeatability of the compression tests. Therefore, only single tests will be done for the other thermomechanical conditions.

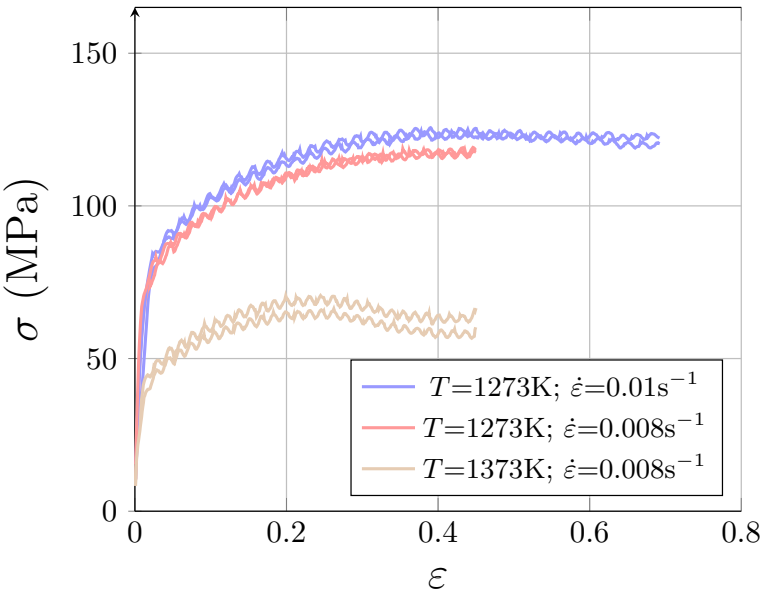

Fig. 5.7. *Compression tests for different sets of thermomechanical conditions to investigate the repeatability of the compression framework.*

5.2 Identification of strain hardening (K_1) and dynamic recovery (K_2) parameters

The method for the identification of K_1 and K_2 is based on stress-strain curves. Therefore the stress-strain curves obtained during the compression tests on 304L steel cylindrical samples are first presented. Then, the method of identification of K_1 and K_2 is introduced and all identified K_1 and K_2 parameters values are given.

5.2.1 Stress-strain curves

Influence of strain rate on mechanical behavior

The stress-strain curves obtained from the compression tests on cylindrical samples at T = 1273K and different macroscopic strain rates are presented on Fig. 5.8(a). For a better analysis of these curves, the elastic parts were removed on Fig. 5.8(b) and a smoothing was made using 7^{th} order polynomial functions. Few cylindrical samples were deformed up to 0.7 of true strain but these samples were not used for microstructure investigations.

The true stress decreases when decreasing the macroscopic strain rate, which is the classical trend observed in hot deformation of metal alloys. The yield stress and peak stress also decrease with decreasing macroscopic strain rate.

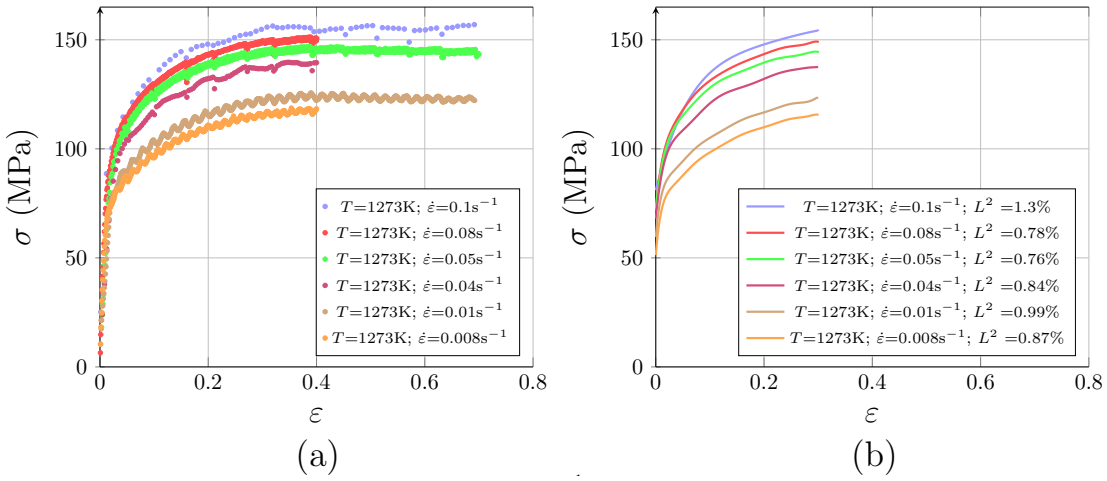

Fig. 5.8. *Stress-strain curves obtained from compression tests on cylindrical samples at different macroscopic strain rates and same temperature (1273K). (a) Raw curves and (b) 7^{th} order polynomial fitted curves.*

Influence of temperature on mechanical behavior

The influence of temperature on the flow behavior of 304L steel was investigated by performing compression tests on cylindrical samples deformed at T = 1273K, 1323K

and 1373K and $\dot{\varepsilon} = 0.08$ and 0.1s^{-1}. The corresponding raw and smoothed stress-strain curves are plotted on Fig. 5.9(a) and 5.9(b), respectively.

The increase of temperature leads to a decrease of the true stress, yield stress and peak stress, which is the classic dependence observed during hot deformation of metals.

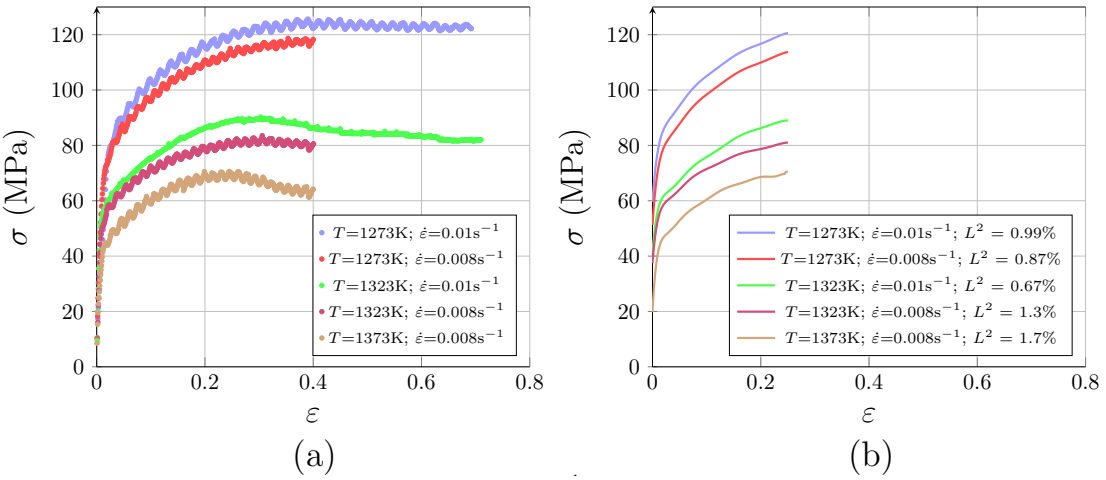

Fig. 5.9. *Stress-strain curves obtained from compression tests on cylindrical samples at different temperatures and close macroscopic strain rates. (a) Raw curves (b) 7^{th} order polynomial fitted curves.*

Relations between peak stress, flow stress and Zener-Hollomon parameter

It was previously observed that increasing macroscopic strain rate or decreasing temperature leads to an increase of peak stress and yield stress. The Zener-Hollomon parameter Z described in the first chapter was introduced to describe the effect of temperature and macroscopic strain rate on the flow behavior of a metal alloy. Three Arrhenius-type equations were proposed by Sellars et al. [192–194] to correlate the stress σ with the Zener-Hollomon parameter Z :

$$Z = A_1 \sigma^n, \tag{5.6}$$

$$Z = A_2 e^{\beta \times \sigma}, \tag{5.7}$$

$$Z = A_3 [\sinh(\alpha\sigma)]^m, \tag{5.8}$$

where Eq. 5.6 is preferred for low strains, Eq. 5.7 is preferred for high strains and Eq. 5.8 is employed for a wide range of strains. Several authors already investigated the dependence of the true stress on Z using these equations. For instance in [195], a dependence between the peak stress and Z was shown using these equations. In [196], a dependence between the true stress at steady-state and Z was also shown using these equations. In order to investigate the validity of Eq. 5.6 in the case of the 304L steel

studied here, the values of yield stress σ_0 were estimated from Fig. 5.8 and 5.9 and plotted as a function of $\ln(Z)$ on Fig. 5.10(a). In the same manner, the values of peak stress σ_p are identified and plotted as a function of $\ln(Z)$ on Fig. 5.10(b). A linear dependence of σ_p and σ_0 on the the quantity $\ln(Z)$ is observed, which is consistent with Eq. 5.6. The linear equations issued from Fig. 5.10 are reported below :

$$\sigma_0 = 13.038 \times \ln(Z) - 234.84, \tag{5.9}$$

$$\sigma_p = 19.729 \times \ln(Z) - 317.82, \tag{5.10}$$

where Eq. 5.9 is used in the following to estimate σ_0 values for all thermomechanical conditions applied in this work.

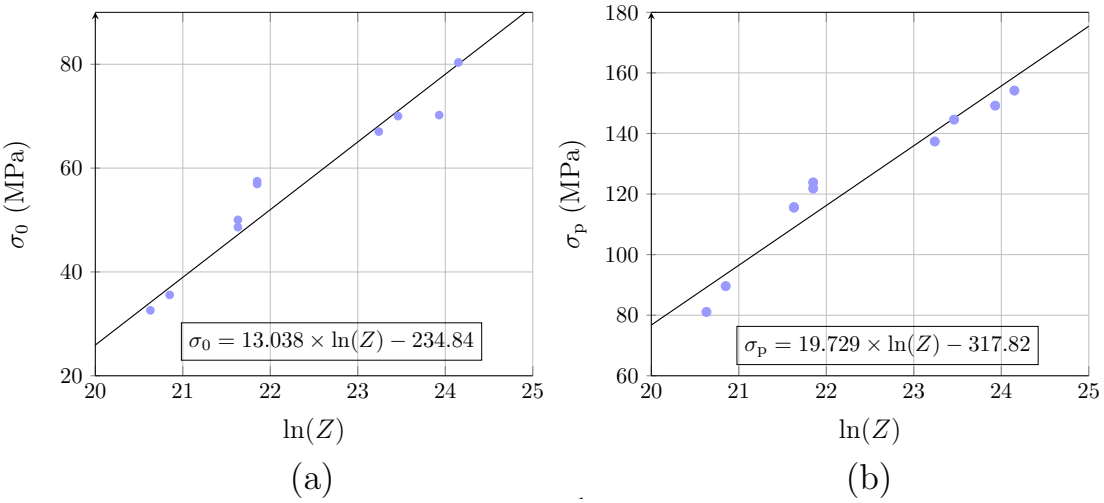

Fig. 5.10. *Relation between the Zener-Hollomon parameter and (a) yield stresses (b) peak stresses obtained from compression tests on cylindrical samples.*

5.2.2 Method for the identification of K_1 and K_2

The identification of K_1 and K_2 is based on two steps: first the method introduced by Jonas in [197] is used to obtain a first estimation of K_1 and K_2. Then an inverse analysis method is used to refine the identified parameters values. These two methods are explained and then applied on all stress-strain curves to identify K_1 and K_2 parameters values for each set of applied thermomechanical conditions. However, the procedure is only detailed on the stress-strain curve obtained at T=1273K and $\dot{\varepsilon} = 0.1s^{-1}$.

1st step: Jonas method

Jonas et al. [197] proposed an approach to identify K_1 and K_2 from a stress-strain curve. The method is explained and applied below to the stress-strain curve obtained from the compression test at 1273K and $0.1s^{-1}$. If irregularities and/or fluctuations are observed on the stress-strain curve, a fitting and/or smoothing can be beforehand required. The

raw as well as smoothed $(\sigma - \varepsilon)$ curves are presented on Fig. 5.11(a) and (b) respectively. In these two curves, the linear part was cut out. The yield stress is around 80MPa while the saturated stress is around 155MPa.

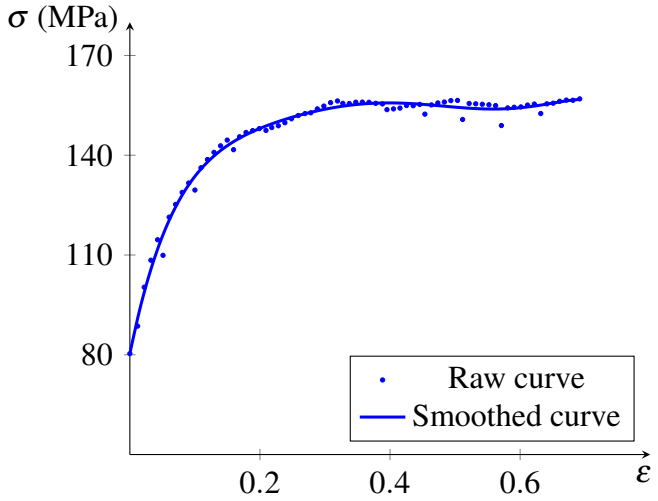

Fig. 5.11. *Stress-strain curves obtained from compression of a cylindrical 304L steel sample at a temperature of 1273K and a macroscopic strain rate of 0.1s^{-1}. The "elastic" portion was removed. The yield stress σ_0 is around 80MPa. Raw curve (dots) is superimposed onto the smoothed curve (full line).*

The true stress σ in a material subjected to uniaxial loading can be related to the mean dislocation density in the microstructure $\langle\rho\rangle$ according to the Taylor's equation [198] :

$$\sigma = \sigma_0 + M_T \alpha \mu b \sqrt{\langle\rho\rangle}, \tag{5.11}$$

where σ_0 is the uniaxial flow stress in the material under the absence of dislocation interactions, also considered as being the yield stress, α is a material-dependent constant that is mostly defined by the type of the formed substructure [199] ($\alpha = 0.15$ will be used in this work in accordance with the work of Bäcke [200]), M_T is the Taylor factor relating the shear flow stress of a single crystal to the uniaxial flow stress of a polycrystal ($M_T \simeq 3$ for f.c.c and b.c.c metals submitted to tension or compression [201], M_T = 3 will be used in this work), μ is the shear modulus at the deformation temperature (estimated from [202]) and b is the norm of the Burgers vector (b=2.5e-10m for ½<110> dislocations in the considered 304L steel [203]). The term $M_T \alpha \mu b$ was estimated to be 5N.m^{-1} at 1273K for the considered 304L steel. We assume here that the evolution of the mean dislocation density $\langle\rho\rangle$ follows Eq. 5.12 (originally proposed by YLJ [76]) :

$$\frac{\partial\langle\rho\rangle}{\partial\varepsilon} = K_1 - K_2\langle\rho\rangle, \tag{5.12}$$

with the maximum mean dislocation density value reached during deformation which is defined by the ratio of the strain hardening and dynamic recovery parameters K_1/K_2. Thus the saturated stress noted σ_s resulting from the balance between the production of

dislocations (strain hardening) and dislocation annihilation (dynamic recovery) can be expressed as :

$$\sigma_s = \sigma_0 + M_T \alpha \mu b \sqrt{K_1/K_2}. \tag{5.13}$$

In work of Jonas [197], the term σ_0 was neglected in Eq. 5.13 contrary to what is done in this work. By coupling the YLJ law (Eq. 5.12) with Taylor's equation (Eq. 5.11), the following relation can be obtained :

$$\frac{\partial \theta}{\partial \varepsilon} = \frac{M_T \alpha \mu b}{2\sqrt{\rho}}(K_1 - K_2 \rho), \tag{5.14}$$

where $\theta = (\sigma - \sigma_0)$. Then by multiplying 5.14 by θ, the following relation is obtained,

$$\theta \frac{\partial \theta}{\partial \varepsilon} = \frac{(M_T \alpha \mu b)^2}{2}(K_1 - K_2 \rho). \tag{5.15}$$

By combining Eq. 5.15 with Eq. 5.11, it leads to,

$$\theta \frac{\partial \theta}{\partial \varepsilon} = \frac{(M_T \alpha \mu b)^2 K_1}{2} - \frac{K_2 \theta^2}{2}. \tag{5.16}$$

Finally, by using Eq. 5.13 in Eq. 5.16, the following relation is obtained,

$$\theta \frac{\partial \theta}{\partial \varepsilon} = 0.5 K_2 (\sigma_s - \sigma_0)^2 - 0.5 K_2 \theta^2. \tag{5.17}$$

It is observed that Eq. 5.17 is a linear equation of $\theta \dfrac{\partial \theta}{\partial \varepsilon}$ as a function of θ^2. The slope of this linear equation is $-0.5K_2$ and the y-intercept is $0.5K_2(\sigma_s - \sigma_0)^2$. Therefore by plotting the quantity $\theta \dfrac{\partial \theta}{\partial \varepsilon}$ as a function of the quantity θ^2 using data issued from a stress-strain curve, the resulting slope and the y-intercept can be used to identify K_2 as well as σ_s. The corresponding plot of the smoothed stress-strain curve of Fig. 5.11(b) is shown on Fig. 5.12. A linear trend clearly appears, which can be fitted with the equation -4.277x + 25314. From that it can be deduced that K_2 = -4.277/-0.5 $\simeq$ 8.6 and σ_s = $\sqrt{25314/0.5K_2} + \sigma_0 \simeq$ 157 MPa.

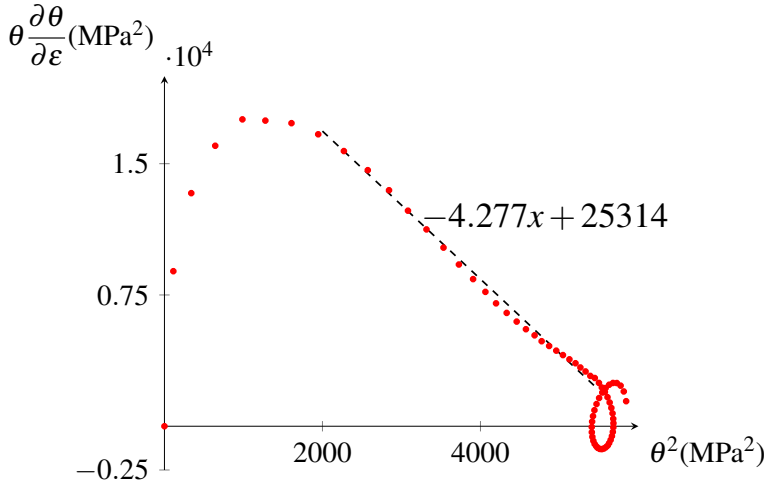

Fig. 5.12. *The quantity $\theta\dfrac{\partial\theta}{\partial\varepsilon}$ is plotted as a function of the quantity θ^2 using data from the smoothed stress-strain curve presented on Fig. 5.11.*

Then knowing K_2 and σ_s, K_1 can be deduced from Eq. 5.13 by :

$$K_1 = \left(\frac{\sigma_s - \sigma_0}{M_T \alpha \mu b}\right)^2 \times K_2, \tag{5.18}$$

and it comes that $K_1 \simeq$ 2e15 m^{-2}.

2nd step: Inverse analysis

An inverse analysis method is then used to refine the values of K_1 and K_2 obtained in the 1st step by the Jonas method. This refinement is particularly important if the linear trend is not clearly observed with the Jonas method.

The inverse analysis method is detailed here on the stress-strain curve of Fig. 5.11. Only the part of the curve which is defined by strain hardening and dynamic recovery must be used, i.e. beyond the yield stress and before nucleation occurs. Nucleation will be assumed to occur at 80% of the peak strain value ε_p.

This inverse analysis method consists in combining the YLJ equation (Eq. 5.12) with the Taylor's equation (Eq. 5.11) to obtain the following relation :

$$\sigma = \sigma_0 + M_T \alpha \mu b \sqrt{(\rho_0 - K_1/K_2)e^{(-K_2\varepsilon)} + K_1/K_2}. \tag{5.19}$$

Although the dislocation density at the onset of plastic deformation, noted ρ_0, is very low and can be neglected compared to the term K_1/K_2 in Eq. 5.19, we preferred to keep this term in this study. Then, the set of parameters $(K_1; K_2)$ that fit the portion of the stress-strain curve between the yield stress and the beginning of nucleation (i.e. 80% of the peak strain value) is identified by inverse analysis from Eq. 5.19 using

the solver of the Excel® software and the initial values of K_1 and K_2 identified in the previous section, i.e. $K_1 \simeq 2e15m^{-2}$ and $K_2 \simeq 8.6$ for the presented example. The new parameters $K_1 \simeq 1.5e15m^{-2}$ and $K_2 \simeq 6$ are obtained. The fitted stress-strain curves are plotted on Fig. 5.13 using the set (K_1;K_2) identified by the Jonas method and after refinement by inverse analysis. The fit is clearly improved when using inverse analysis in addition to Jonas method, in particular at the early stage of deformation range that is used for the parameter identification.

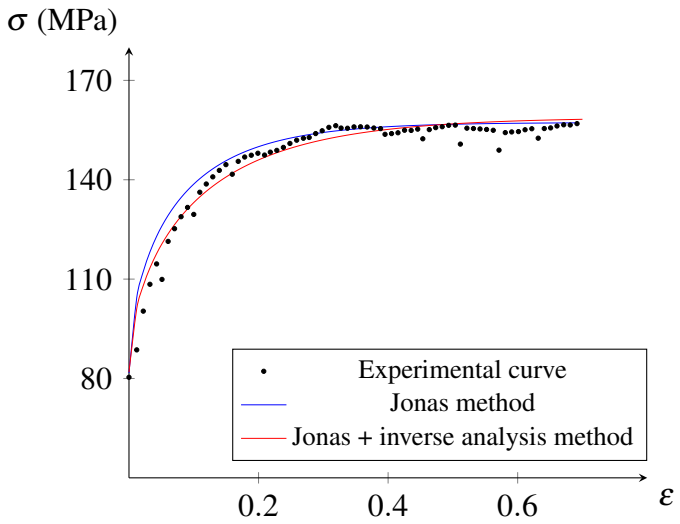

Fig. 5.13. *Comparison between the raw experimental stress-strain curve and the ones recalculated using K_1 and K_2 parameters obtained with Jonas method and after inverse analysis refinement. Thermomechanical conditions are T=1273K and $\dot{\varepsilon}$=0.1s^{-1}.*

The major advantage of starting with the Jonas method is related to the fact that K_2 is identified independently of K_1 contrary to the inverse analysis method where K_1 and K_2 are identified together. However a drawback of the Jonas method is that depending on the quality of the stress-strain curve, the linear trend can be more or less explicit and can affect the identification of K_1 and K_2, therefore refining parameters with inverse analysis method appeared to be primordial.

Identified parameter values

The procedure for parameter value identification presented above (Jonas + inverse analysis method) was performed on all stress-strain curves. The identified values of K_1 and K_2 are presented in Tab. 5.3. Furthermore, the resulting recalculated stress-strain curves obtained by using the identified K_1 and K_2 values in Eq. 5.19 are compared to the experimental curves on Fig. 5.14. Globally, the fitted curves are very close to experimental ones, which confirms the ability of this method to properly identify K_1 and K_2.

T(K)	$\dot{\varepsilon}(s^{-1})$	$K_1(m^{-2})$	K_2
1273	0.1	1.5e15	6
1273	0.08	2.2e15	8.1
1273	0.05	1.65e15	5.9
1273	0.04	1.63e15	7.3
1273	0.01	1.32e15	6.8
1273	0.01	1.07e15	5.4
1273	0.008	1.45e15	7.2
1273	0.008	1.42e15	7.7
1323	0.01	1.0e15	8.1
1323	0.008	1.1e15	12.1
1373	0.008	1.3e15	13.3
1373	0.008	1.2e15	13.7

Tab. 5.3. *Strain hardening (K_1) and dynamic recovery (K_2) parameters identified at different sets of thermomechanical conditions by coupling Jonas method and inverse analysis method.*

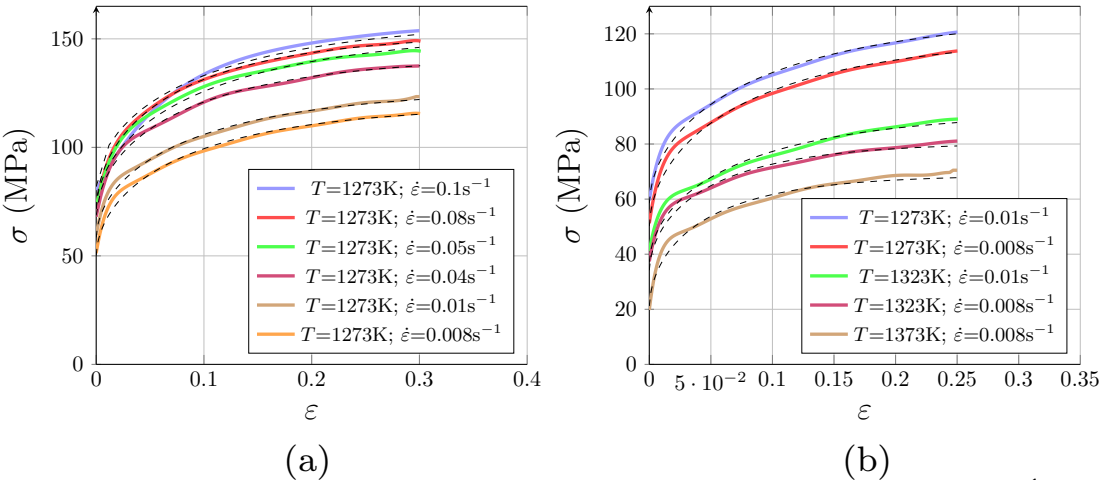

Fig. 5.14. *Fitted curves obtained by coupling the Jonas method and inverse analysis refinement are represented in dashed lines and are superimposed to the experimental ones in full lines. These fitted curves are obtained by combining Eq. 5.19 with identified K_1, K_2 values presented in Tab. 5.3. (a) Comparisons at same temperatures, (b) comparisons at close macroscopic strain rates and different temperatures.*

Physically, strain hardening is assumed to be only dependent on the strain rate while dynamic recovery is supposed to be dependent on both strain rate and temperature. Therefore K_1 is plotted as a function of macroscopic strain rate on Fig. 5.15(a) and K_2 is plotted as a function of Z on Fig. 5.15(b). The strain hardening parameter K_1 seems to be linearly correlated to $\dot{\varepsilon}$ while a logarithmic relationship can describe the dependence of the dynamic recovery parameter K_2 on the Zener-Hollomon parameter

Z. These correlations, described by Eqs. 5.20 and 5.21, are used in the following to interpolate the values of K_1 and K_2 for any set of thermomechanical conditions within the explored range (from 1273 to 1373K and 0.01 to 0.1s^{-1}, approximately).

$$K_1 = (69 \times \dot{\varepsilon} + 12) \times 1e14, \tag{5.20}$$

$$K_2 = -1.4 \times \ln(Z) + 40. \tag{5.21}$$

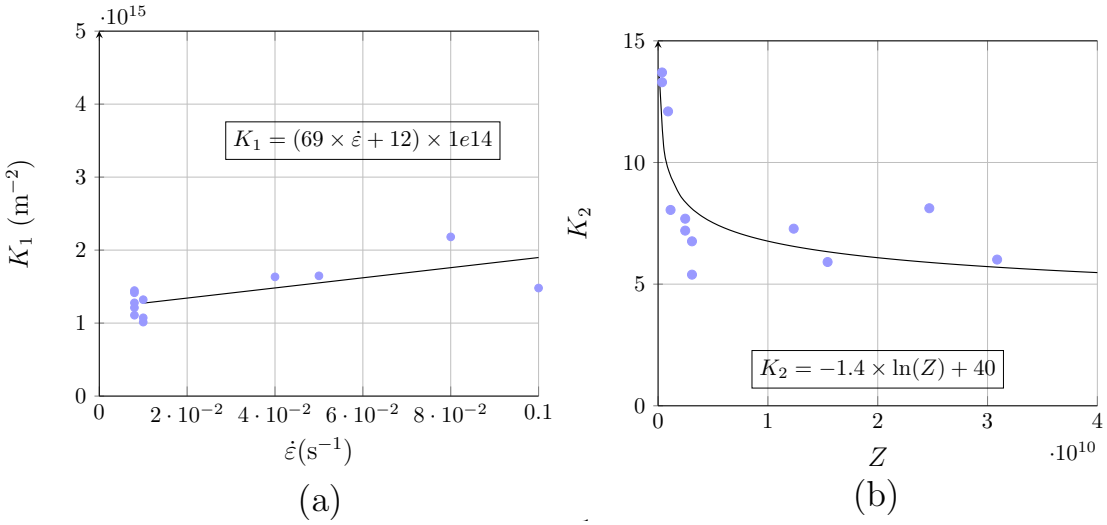

Fig. 5.15. *Dependence of (a) the strain hardening parameter K_1 as a function of the macroscopic strain rate and (b) the dynamic recovery parameter K_2 as a function of the Zener-Hollomon parameter.*

Sensitivity study

The influence of the quantity ρ_0 and of the product $M_T\alpha\mu b$ on the identified values of K_1 and K_2 was tested. To do that, different values of ρ_0 and $M_T\alpha\mu b$ were tested and K_1 and K_2 were identified for each configuration using the inverse analysis method. The stress-strain curve obtained at T=1273K and $\dot{\varepsilon}$=0.1s^{-1} was considered. The obtained values of the parameters K_1 and K_2 are reported in Tab. 5.4, where the L^2 errors calculated between the raw experimental and the fitted stress-strain curves in the domain of identification are also reported.

$\rho_0(\mathrm{m}^{-2})$	$M_\mathrm{T}\alpha\mu b(\mathrm{N.m}^{-1})$	$K_1(\mathrm{m}^{-2})$	K_2	L^2 (%)
1e11	6	1e15	6	2.2
1e11	5.5	1.2e15	6	2.2
1e11	5	1.5e15	6	2.2
1e11	4.5	1.8e15	6	2.2
1e11	4	2.3e15	6	2.2
2e12	4	1.5e15	5.9	2.3
1e12	4	1.5e15	6	2.3
5e11	4	1.5e15	6	2.2
5e10	4	1.5e15	6	2.2
1e10	4	1.5e15	6	2.2

Tab. 5.4. *Identification of K_1 and K_2 values for different values of ρ_0 and $M_T\alpha\mu b$, and corresponding L^2 errors between raw experimental and fitted stress-strain curves.*

An increase by 20% of the product $M_\mathrm{T}\alpha\mu b$ (from 5 to 6) has an important impact on the K_1 value (decrease by 33%). A decrease by 20% of the $M_\mathrm{T}\alpha\mu b$ value (from 5 to 4) leads to an increase of K_1 value by 53% which is far from being negligible. On the other hand the K_2 parameter does not seem to be affected by the $M_\mathrm{T}\alpha\mu b$ value. The L^2 errors are constant when the $M_\mathrm{T}\alpha\mu b$ value changes, meaning that for all tested values of $M_\mathrm{T}\alpha\mu b$, a good fit of the experimental stress-strain curve can be obtained. However, since the K_1 parameter is considered in other constitutive laws such as the computation of the critical dislocation density (Eq. 3.9), it is primordial to choose a value of $M_\mathrm{T}\alpha\mu b$ as physical as possible.

The initial dislocation density ρ_0 has no influence on the identified parameters values (Tab. 5.4) as long as ρ_0 is at least 1000 times smaller than the ratio K_1/K_2. For the tested ρ_0 values, the L^2 errors are quasi-constant whatever the ρ_0 value. If ρ_0 is neglected, the same parameters values as obtained with ρ_0 = 1e10 are obtained.

The yield stress σ_0 considered in this sensitivity study was around 80MPa. However, depending on the quality of the stress-strain curve, it can be quite difficult to evaluate its value. Therefore a sensitivity study was also performed on the yield stress by choosing other values around 80MPa and by observing the new values of K_1 and K_2 obtained by the inverse analysis method and reported in Tab. 5.5. The L^2 errors measured between the raw experimental and the fitted stress-strain curves in the domain of identification are also reported in Tab. 5.5. It turns out that an error on the lecture of σ_0 has a weak influence on the identified value of K_2, but a strong influence on K_1. This behavior is quite logical since σ_0 defines the early stage of plasticity, where the dislocation density is low and therefore the effect of dynamic recovery is neglected as compared to that of strain hardening. Therefore, a modification on the σ_0 value is mainly corrected by the strain hardening parameter K_1. An increase of σ_0 by 25% (from 80 to 100MPa) leads to a decrease by about 50% of the K_1 value but only by 12% of the K_2 value. The L^2 error is slightly affected by σ_0 but keeps being around 2%, meaning that a good fit can

be always obtained whatever the tested σ_0 value. However, since the choice of σ_0 has a strong influence on the identified K_1 value and since K_1 is used in other constitutive laws of models, it is important to choose σ_0 as accurately as possible.

σ_0(MPa)	K_1(m^{-2})	K_2	L^2(%)
100	7.3e14	5.3	2.2
88	1.2e15	6.1	1.8
80	1.5e15	6	2

Tab. 5.5. *Identification of K_1 and K_2 for different values of flow stress σ_0 and corresponding L^2 errors between experimental and fitted stress-strain curves.*

5.3 Identification of the parameter describing the strain rate dependence of boundary migration (δ) and of the nucleation parameter (K_g)

The identification of δ and K_g parameters, mainly used in Eqs. 2.10, 3.13 and 4.3, is made by inverse analysis based on microstructure quantities. Microstructure quantitative analysis is first presented, then, the inverse analysis method based on the NHM is described and finally all the identified values of δ and K_g are presented and discussed.

5.3.1 Microstructure investigations

After performing compression tests on cylindrical and double-cone 304L samples, the microstructure is characterized. Thanks to the FE simulations previously introduced, the sets of three equivalent plastic strain levels $\varepsilon_{\mathrm{VM}}$ corresponding to thermomechanical conditions (i.e. temperatures T and equivalent plastic strain rates $\dot{\varepsilon}_{\mathrm{VM}}$) at points *A*, *B* and *C* are reported in Tab. 5.6.

The first step, before performing microstructure characterization, is to prepare metalographic sections by cutting and polishing the compressed samples. The microstructures are then observed using the Electron BackScatter Diffraction (EBSD) technique to measure quantities such as RX fractions, mean grain sizes and to get grain size distributions.

T \ $\dot{\varepsilon}_{\mathrm{VM}}$	0.014s^{-1}	0.07s^{-1}	0.14s^{-1}
1273K	(0.65; 1; 1.35)	(0.65; 1; 1.35)	(0.65; 1; 1.35)
1323K	(0.65; 1; 1.35)		
1373K	(0.65; 1; 1.35)		

Tab. 5.6. *Sets of three equivalent plastic strain levels ε_{VM} corresponding to the observed microstructure at different values of equivalent plastic strain rate $\dot{\varepsilon}_{VM}$ and temperatures T. The $\dot{\varepsilon}_{VM}$ and ε_{VM} values were obtained from FE simulations.*

Samples preparation

Cylindrical and double cone samples are cut according to the schemes of Figs. 5.16(a) and 5.16(c), respectively. Then the sections schematized on Fig. 5.16(b) and Fig. 5.16(d) are polished.

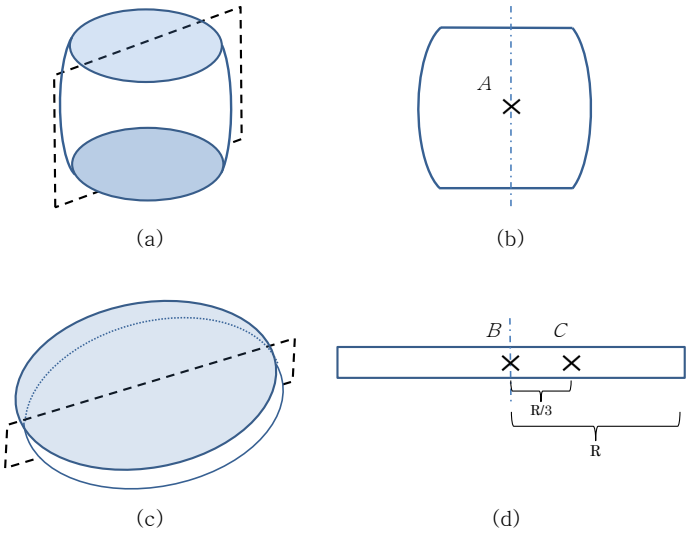

Fig. 5.16. *Cutting plane of (a) cylindrical and (c) double-cone samples. Microstructure is then observed at (b) the middle of the section (point A) for cylindrical samples and (d) the middle and at one third from center (points B and C) for double-cone samples.*

The polishing step is primordial in order to get a surface quality satisfying the EBSD technique requirements. The polishing procedure applied on the considered 304L steel samples is the following :

- 30s using a SiC paper P600 with a normal force of 2daN to obtain a plane surface and eliminate the hardening due to cutting.
- 60s using a SiC paper P1200 with a normal force of 2daN to eliminate hardening created by the previous step.
- 2min using a diamond solution of 6μm.
- 2min using a diamond solution of 3μm.
- 2min using a diamond solution of 1μm.
- 2min of chemical mechanical polishing using a solution of colloidal silica (OPS) with a normal pressure of 1.5daN in order to obtain a very clean surface for observations. In the surface is not clean enough, this last step is repeated as long as it is necessary.

EBSD analysis

The electron microscope used for microstructure characterization is a Zeiss Supra 40 FEG SEM (Field Emission Gun Scanning Electron Microscope), equipped with several detectors. In this work, the **Electron Backscatter Diffraction (EBSD)** detector was mostly used. EBSD provides crystalline orientation maps and is largely used when aiming at quantifying microstructure quantities such as the RX fraction and the grain size distribution. The EBSD acquisition setup is as follows. The polished 304L steel sample section is placed in the SEM with a tilt angle of 70° as presented on Fig. 5.17(a). The electron beam scans the surface of the sample over a regular grid (here square grid) with a fixed step size. The EBSD detector is a 2D detector that produced an image of the intensity fluctuations of backscattered electrons (BSE) in space. Those fluctuations arise from diffraction of the backscattered electrons which fulfil the Bragg condition with respect to the atomic planes. The diffraction diagram is composed of bands (each one corresponding to a different diffracting pane) called *Kikuchi bands* as presented on Fig. 5.17(b) [204]. The band positions are automatically detected via the Hough transform of the diagram and the angles between band pairs are measured. Then, an algorithm is applied to determine the crystallographic orientation that minimizes the mismatch between the measured band angles and the ones recalculated from the postulated orientation. The crystal orientation is thus theoretically determined for each point of the scan grid (actually, experimental data sets present a certain rate of non-indexed points, most often corresponding to diffraction diagrams of bad quality, along grain boundaries for example). *MTEX* toolbox [205] was used for the post-treatment of all EBSD orientation maps presented in the following.

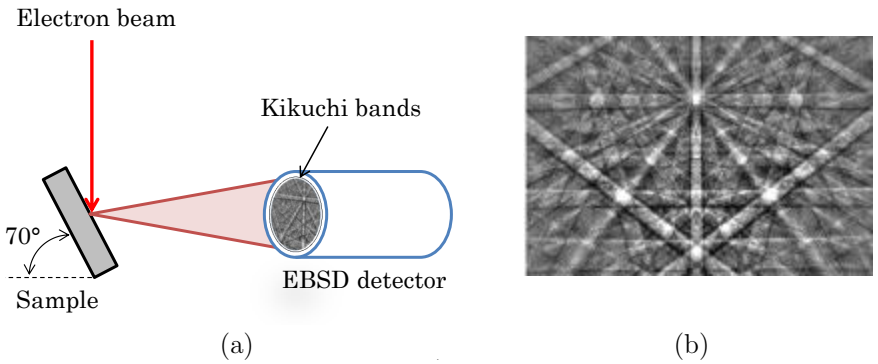

Fig. 5.17. *(a) Schematic illustration of the EBSD pattern in a SEM and (b) example of EBSD pattern made of Kikuchi bands [204].*

Grain size measurements

In the EBSD map analyses performed in this work, a grain is defined as a cluster of at least 3 pixels disoriented by less than 10°. As an illustration, the microstructure of the 304L steel at the initial state is presented on Fig. 5.18(a). Twin boundaries, represented as red lines on Fig. 5.18(a), are particular boundaries defined by a misorientation of 60°

around the crystallographic direction <111> in the considered 304L steel, like in any FCC material. In the grain detection, twin boundaries are considered as internal grain defects. Fig. 5.18(b) shows the grain boundary network used to detect grains, therefore excluding twin boundaries.

The same EBSD map is also shown within an orientation color-coding defined in the standard triangle on Fig. 5.18(d); the color refers in this case to the crystallographic direction that is parallel to the scanned section normal (so called Z direction). The orientation data of this map are also shown in the form of pole figures on Fig. 5.18(c). These pole figures show the stereographic projection of {001}, {110} and {111} plane normals in the sample frame along the *Z* direction. The color code is given in "multiple of random density" with a maximal value around 1.6, which shows that no dominant orientation exists in the initial microstructure.

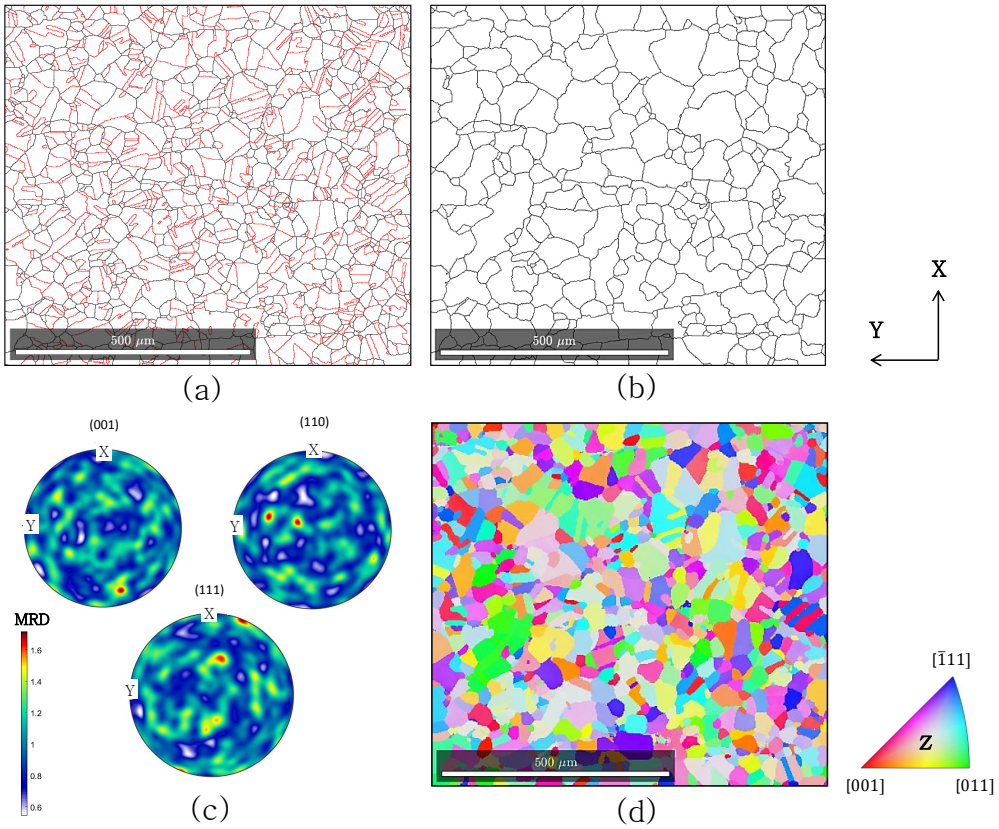

Fig. 5.18. *Microstructure generated from EBSD data with grain boundaries represented in black color and defined by a minimum disorientation of 10°. (a) Twin boundaries are represented in red color, (b) grain boundary network, excluding twin boundaries, (c) pole figures with color code given in "multiple of random density", (d) orientation map within a color coding showing the crystalline direction parallel to the section normal (Z direction), defined in the standard triangle.*

The grain size measurement is made by calculating each grain area converted into the equivalent circle radius by the relationship :

$$R_i = \sqrt{\frac{S_i}{\pi}}, \tag{5.22}$$

where R_i and S_i are the equivalent circle radius and the grain surface of the i^{th} grain, respectively. Then, the mean grain size is calculated as :

$$\langle R \rangle = \frac{1}{N} \sum_{i=1}^{N} R_i, \tag{5.23}$$

where N is the number of considered grains. The mean grain size (weighted by grain surface) $\langle R \rangle_{\text{surf}}$ can also be calculated by the following relationship :

$$\langle R \rangle_{\text{surf}} = \frac{1}{S_{\text{tot}}} \sum_{i=1}^{N} R_i S_i. \tag{5.24}$$

The 2D distributions of all grains sizes obtained from EBSD maps at point B after compression tests on double-cone samples are presented on Fig. 5.19. At this point, ε_{VM} reaches 1.35 at the end of compression tests.

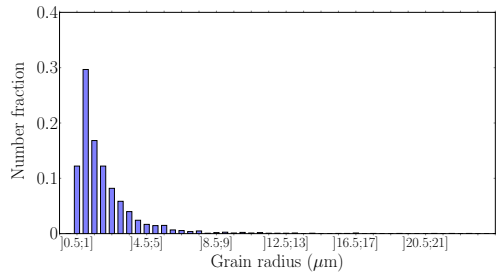

(a) T=1273K, $\dot{\varepsilon}_{\mathrm{VM}}$=0.14s^{-1}, $\varepsilon_{\mathrm{VM}} = 1$

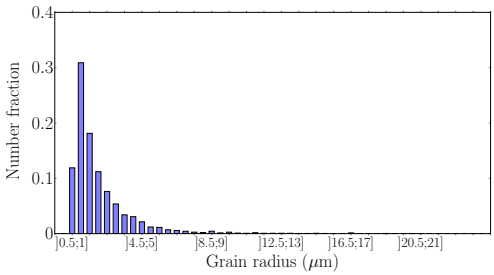

(b) T=1273K, $\dot{\varepsilon}_{\mathrm{VM}}$=0.07s^{-1}, $\varepsilon_{\mathrm{VM}} = 1$

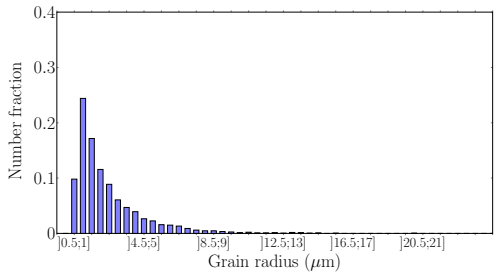

(c) T=1273K, $\dot{\varepsilon}_{\mathrm{VM}}$=0.014s^{-1}, $\varepsilon_{\mathrm{VM}} = 1$

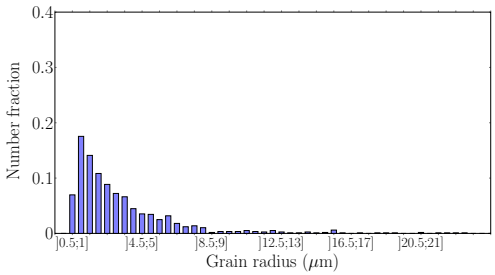

(d) T=1323K, $\dot{\varepsilon}_{\mathrm{VM}}$=0.014s^{-1}, $\varepsilon_{\mathrm{VM}} = 1$

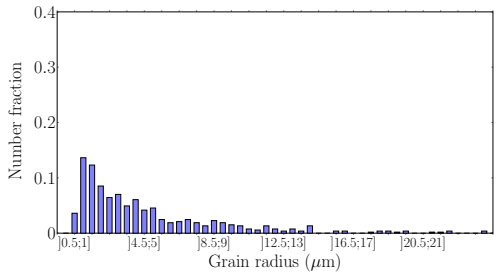

(e) T=1373K, $\dot{\varepsilon}_{\mathrm{VM}}$=0.014s^{-1}, $\varepsilon_{\mathrm{VM}} = 1$

Fig. 5.19. *2D distributions in number fraction of all grain sizes obtained from EBSD maps at point B at the end of hot compression tests on the 304L double-cone samples. The ε_{VM} value reaches 1.35 at this point at the end of the compression tests.*

Quantification of intra-granular disorientations

The presence of dislocations in strain-hardened grains induces intragranular crystal lattice rotations which can be measured by EBSD if the dislocation density is high enough. It is worth mentioning here that intragranular misorientations can only be converted into, or interpreted in terms of, geometrically necessary dislocations (GNDs). The other dislocations, so-called statistically stored, have indeed no cumulative effect on the crystal lattice orientation.
Based on EBSD data, different criteria can be used to quantify intra-granular misorientations, as detailed below.

- **The Kernel Average Misorientation (KAM)** is defined at each pixel as the mean

disorientation between this pixel and its neighbors located at a given distance :

$$\mathrm{KAM}(i) = \frac{1}{n}\sum_{j=1}^{n}\theta_{ij}, \tag{5.25}$$

where n is the number of neighbor pixels of i and θ_{ij} is the disorientation between pixels i and j. The neighbor pixels leading to a disorientation grower than 10° with the considered pixel are omitted.

The neighborhood choice can be limited to the 1st neighbors as presented on Fig. 5.20 but can also be extended to the 2nd or n^{th} neighbors.

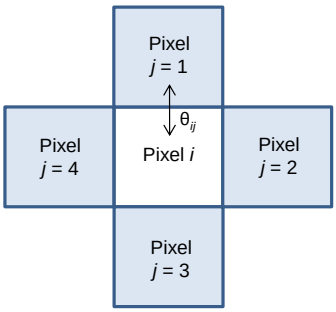

Fig. 5.20. *1st neighbor pixels for calculation of KAM.*

The major drawback of the KAM parameter is that it highly depends on the measurement step size and on the neighborhood extent.

- **The Grain Average Misorientation (GAM)** is defined in each grain as the average disorientation between all pairs of neighbor pixels in the grain :

$$\mathrm{GAM} = \frac{1}{N}\frac{1}{n}\sum_{i=1}^{N}\sum_{j=1}^{n}\theta_{ij}, \tag{5.26}$$

where n is the number of first neighbor pixels of i and N is the number of pixels in the grain. Thus, the GAM provides information about the grain average GND density. However, since it is calculated based on the disorientation between adjacent pixels, it depends on the distance between them, i.e. on the measurement step size, like the KAM.

- **The Grain Orientation Spread (GOS)** is also used to estimate the GND density in each grain of the microstructure. This latter is obtained by calculating the disorientation between each pixel and the mean grain orientation, and then by averaging all these values :

$$\mathrm{GOS} = \frac{1}{N-1}\frac{1}{N}\sum_{i=1}^{N}\sum_{j=1}^{N}\theta_{ij}, i \neq j. \tag{5.27}$$

Therefore, the GOS, like the GAM, has a constant value per grain, i.e. is a grain property. The advantage of this parameter is that it is not dependent on the measurement step size, contrary to the KAM and GAM values.

EBSD maps showing KAM, GAM and GOS values after hot compression to $\varepsilon_{\mathrm{VM}} = 1$ at T=1273K and $\dot{\varepsilon}_{\mathrm{VM}}$=0.07s^{-1} are presented on Fig. 5.21.

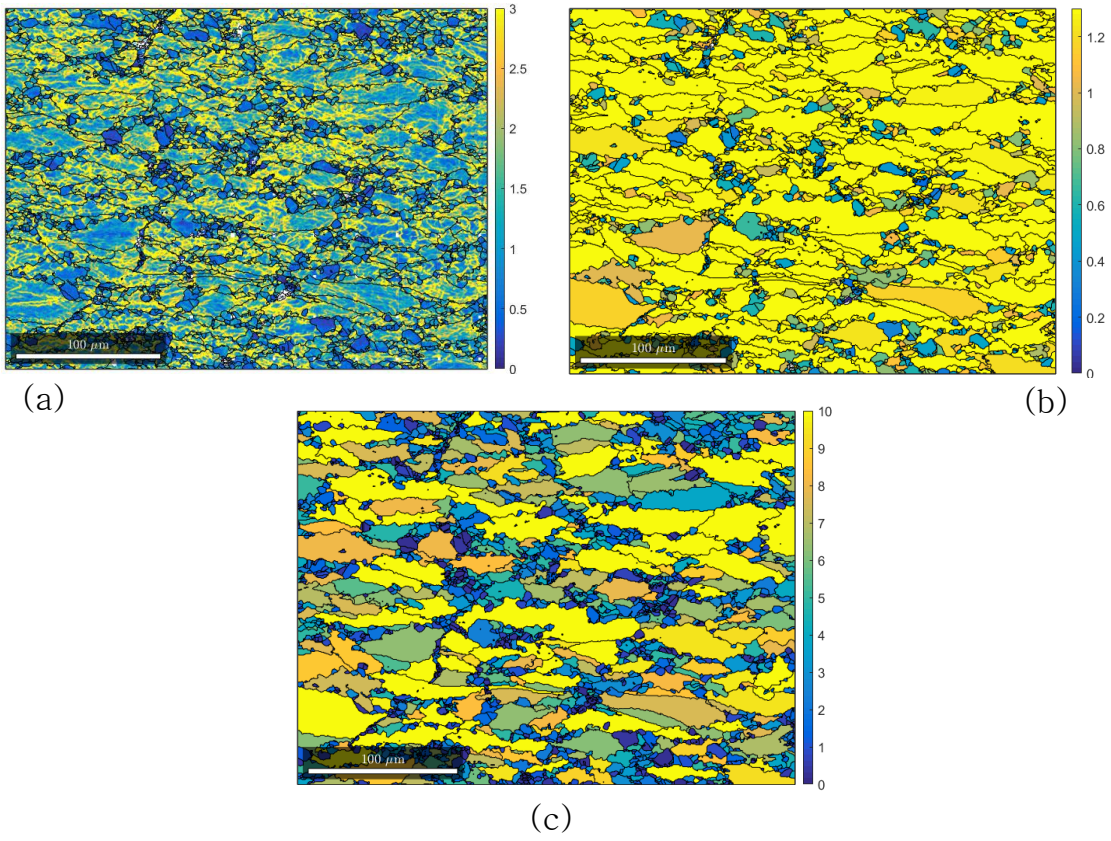

Fig. 5.21. *EBSD maps obtained from a 304L steel sample compressed to ε_{VM}=1 at T=1273K and $\dot{\varepsilon}_{VM}$=0.07s^{-1}. (a) Kernel Average Misorientation map, (b) grain Average Misorientation map and (c) grain Orientation Spread map. (Units: degrees)*

Recrystallized fraction measurement

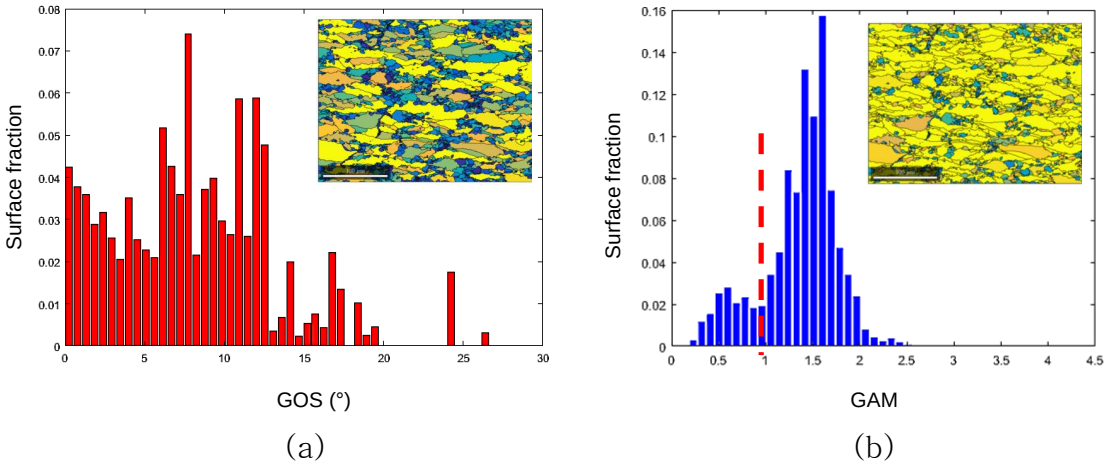

Fig. 5.22. *(a) GOS and (b) GAM distributions issued from an EBSD map whose the set of thermomechanical conditions is a temperature of 1273K, an equivalent plastic strain rate equal to 0.07s^{-1} and an equivalent plastic strain equal to 1 (same EBSD dataset as on Fig. 5.21).*

RX grains have globally a low dislocation density, leading to low intragranular disorientation levels, and therefore low GAM and GOS values. Thus, GAM or GOS criteria introduced previously could generally be used to separate the RX and NR grains. The GOS and GAM distributions issued from the EBSD map of Fig. 5.21 are plotted on Fig. 5.22 in order to discuss the choice of GOS or GAM criterion for separating NR and RX grains. Since two different kinds of grain, RX and NR, are present in the microstructure, the GOS and GAM distributions should be composed of two modes each corresponding to RX and NR grain populations. Hence, dissociating the two modes enables to determine the RX and NR area fraction. In the GOS distribution (Fig. 5.22(a)), the two modes are not clearly depicted and their separation is quite complex. On the other hand, the GAM distribution (Fig. 5.22(b)) has two distinct modes and a threshold value around 1° can be chosen to distinguish RX from NR grains. In the following, the GAM criterion will be used to quantify RX fractions.

To further validate the choice of the GAM criterion, GAM distributions at the same temperature T and equivalent plastic strain rate $\dot{\varepsilon}_{VM}$ that used for Fig. 5.22 but at three different levels of effective plastic strain ε_{VM} (0.65, 1 and 1.35) are plotted on Fig. 5.23. Two grain populations are also clearly observed on Fig. 5.23(c) with a GAM threshold around 1°, equal to that identified on Fig. 5.22. On Fig. 5.23(a), the two populations are nevertheless not clearly visible since the fraction of RX grains is still very low at this strain. However, since there is no objective reason to choose a different GAM threshold, the value of 1° will also be used for separating the two populations on this map. The EBSD maps showing the NR and RX grains separated thanks to a GAM threshold of 1° are also presented on Fig. 5.23. The GAM criterion will actually be coupled to a grain

size criterion in order to force the very small grains (with a radius lower than 1.5μm in this case) to be automatically considered as RX grains.

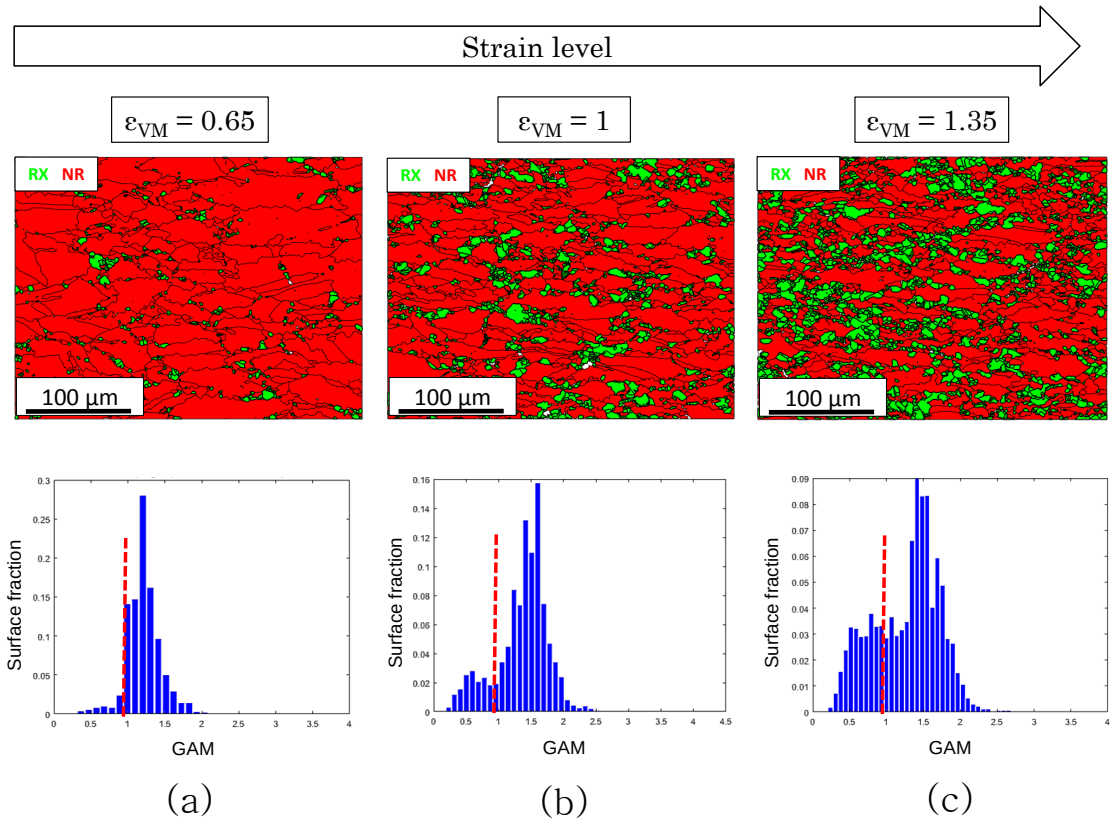

Fig. 5.23. *Identification of RX grains using a GAM threshold of 1 at three different values of equivalent plastic strain (a) ε_{VM} = 0.6, (b) ε_{VM} = 0.95 and (c) ε_{VM} = 1.35.*

Results

EBSD maps are presented on Fig. 5.24 for each compression test with the RX grains in green color. The GAM thresholds were identified for each set of thermomechanical conditions and were equal to $1^{\circ}(\pm 0.1)$ for all maps. The RX fraction noted X is calculated at any $\varepsilon_{\mathrm{VM}}$ value by the relationship :

$$X = \frac{\sum_{i=1}^{N_{\mathrm{RX}}} S_i}{S_{\mathrm{tot}}}, \tag{5.28}$$

where S_i is the surface of the i^{th} RX grain, S_{tot} is the total map surface and N_{RX} is the total number of RX grains.

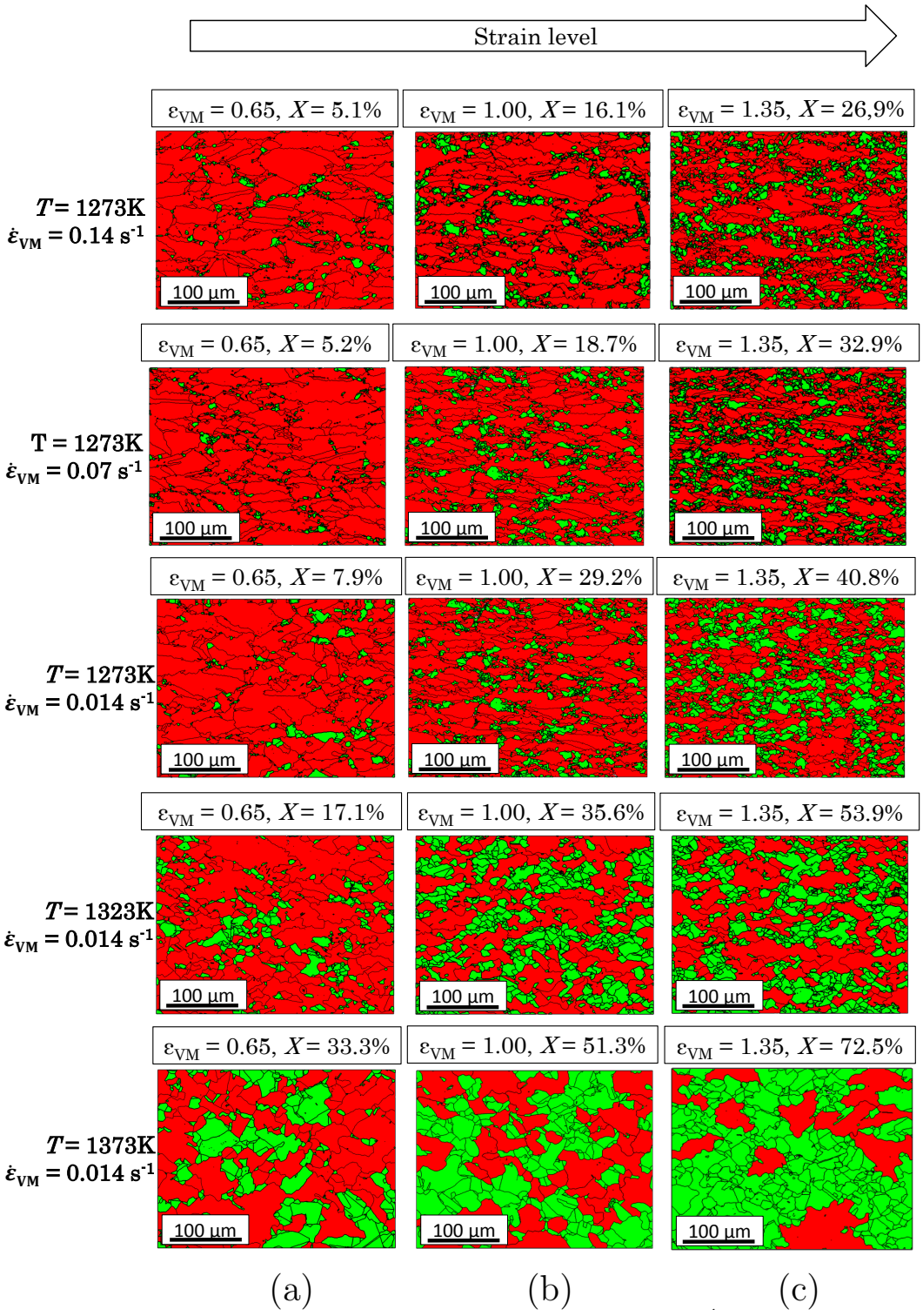

Fig. 5.24. *Microstructures (EBSD maps) of 304L steel samples compressed at different temperatures and strain rates to different equivalent plastic strain levels, with RX and NR grains represented in green and red colors, respectively. (a) ε_{VM} = 0.6, (b) ε_{VM} = 0.95 and (c) ε_{VM} = 1.35.*

By applying Eq. 5.28 on all EBSD maps, the RX fractions were estimated and reported on Fig. 5.24. Furthermore, RX fractions are also reported as a function of the equivalent plastic strain on Fig. 5.25(a). At a given level of equivalent plastic strain ε_{VM}, the RX fraction increases when increasing T and decreases with increasing $\dot{\varepsilon}_{VM}$, as expected. Furthermore, the RX fraction increases with ε_{VM}. The 2D mean radius values of RX grains noted $\langle R_{RX} \rangle$ are also reported on Fig. 5.25(b). This quantity $\langle R_{RX} \rangle$ increases with T and decreases with increasing $\dot{\varepsilon}_{VM}$, also as expected. Furthermore, $\langle R_{RX} \rangle$ is almost constant for a given set of thermomechanical conditions, whatever the applied ε_{VM}. A slight increase with strain is only observed at higher temperatures, which can be explained by a higher mobility of grain boundaries promoting the growth of RX grains. Finally, the 2D overall mean grain radius noted $\langle R \rangle$ are reported on Fig. 5.25(c). This quantity $\langle R \rangle$ increases with T and decreases with increasing $\dot{\varepsilon}_{VM}$. Furthermore, $\langle R \rangle$ decreases with increasing ε_{VM}, which is consistent with the increase of RX fraction as seen on Fig. 5.25(a) and the consumption of the large initial grains.

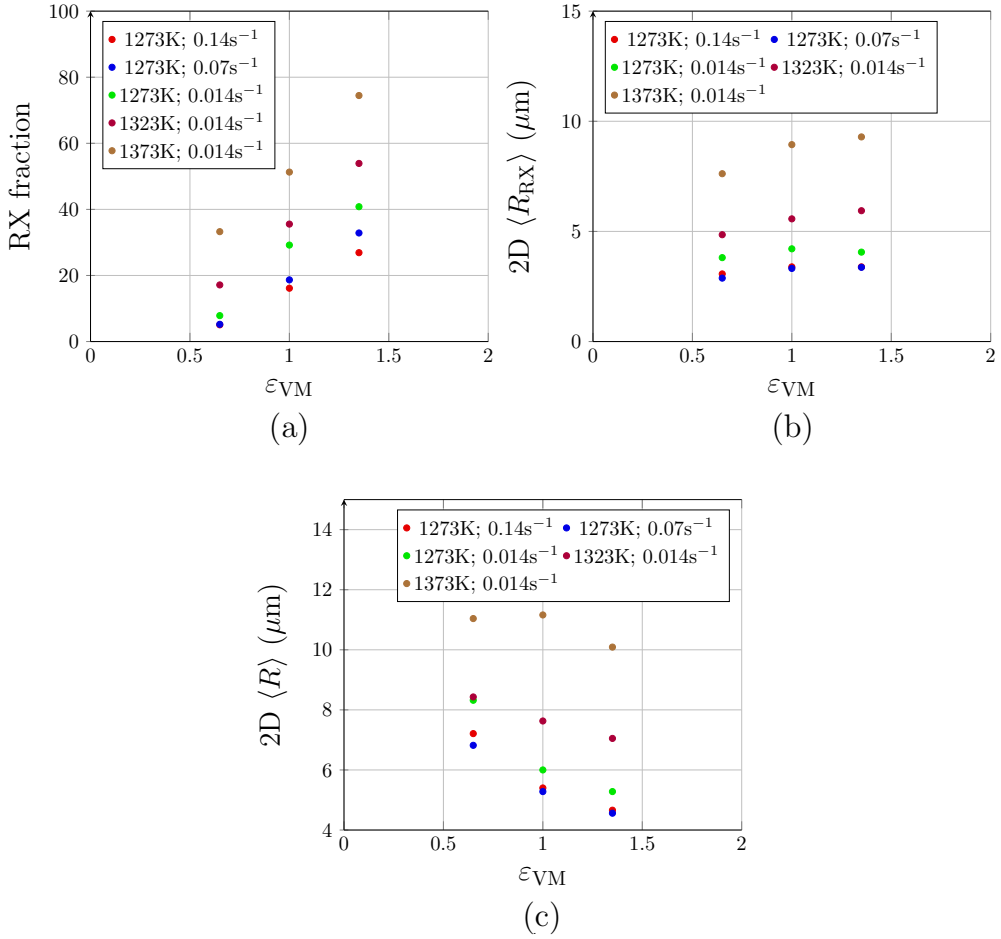

Fig. 5.25. *(a) Recrystallized fraction, (b) 2D mean RX grain radius and (c) 2D overall mean grain radius measured in 304L microstructures as a function of ε_{VM} for different sets of thermomechanical conditions.*

5.3.2 Identification procedure for δ and K_g

Inverse analysis using the NHM

The K_g parameter accounting for nucleation and the δ parameter accounting for the dependence of the grain boundary migration on strain rate were identified by inverse analysis using the NHM based on the microstructure quantities obtained from the EBSD maps shown above, following the procedure schematized on Fig. 5.26. For each set of thermomechanical conditions reported in Tab. 5.6 except that at 1323K and $0.014s^{-1}$ (kept for the discussion of the NHM after its calibration), K_1 and K_2 values are first estimated using Eqs. 5.20 and 5.21. Then, NHM simulations are launched in order to identify, by inverse analysis, the parameters values K_g and δ that fit best the microstructure quantities of: RX fraction, $\langle R \rangle_{surf}$ and $\langle R_{RX} \rangle_{surf}$. To be consistent with the NHM during inverse analysis procedure, 2D mean grain sizes obtained from experimental data were converted into 3D mean grain sizes using the Saltykov method [206]. Furthermore the overall mean grain sizes and the recrystallized mean grain sizes are here weighted by grain surface fraction since at the early stage of nucleation, a large number of very small RX grains appears in the microstructure, which decreases instantaneously the mean grain sizes to very small values. However, these high numbers of RX grains only represent a small surface fraction of the total microstructure, therefore to obtain more representative values of grain sizes and avoid an instantaneous decrease, mean grain sizes weighted by grain surfaces were used. Finally, it is worth noticing that RX fractions calculated from EBSD maps are *surface* fractions and are compared with RX *volume* fractions obtained from 3D simulations.

Identified parameter values

The obtained values of δ and K_g identified from all EBSD maps on points A, B and C are reported in Tab. 5.7. The parameter value δ appears to be only dependent on $\dot{\varepsilon}_{VM}$, which is quite logical since this latter accounts for the heterogeneity of dislocations inside grains. Thus to observe the evolution of δ, the values of δ are plotted as a function of $\dot{\varepsilon}_{VM}$ on Fig. 5.27(a). A linear trend is observed with the following equation :

$$\delta = 17.4 \times \dot{\varepsilon}_{VM} + 0.8. \tag{5.29}$$

The parameter K_g is dependent on both T and $\dot{\varepsilon}_{VM}$, although the effect of temperature on K_g seems much lower than the effect of strain rate. K_g values increase with increasing T and $\dot{\varepsilon}_{VM}$, which has a physical sense since nucleation is thermally activated and its probability increases with the quantity of dislocations. The values of K_g are plotted as function of Z on Fig. 5.27(b) but a dependence of K_g on Z is not clearly observed. The main reason is that Z increases with strain rate but decreases with temperature. To exclude the effect of the dislocation density on the nucleation rate considered in K_g, values of K_g were subdivided by $\dot{\varepsilon}_{VM}$ and were plotted as a function of Z on Fig. 5.27(c). In this case, a linear dependence can be identified between the ratio $K_g/\dot{\varepsilon}_{VM}$ and Z, with the following equation :

$$K_g = (-7 \times 10^{-17} \times Z + 4.2 \times 10^{-6}) \times \dot{\varepsilon}_{VM}. \tag{5.30}$$

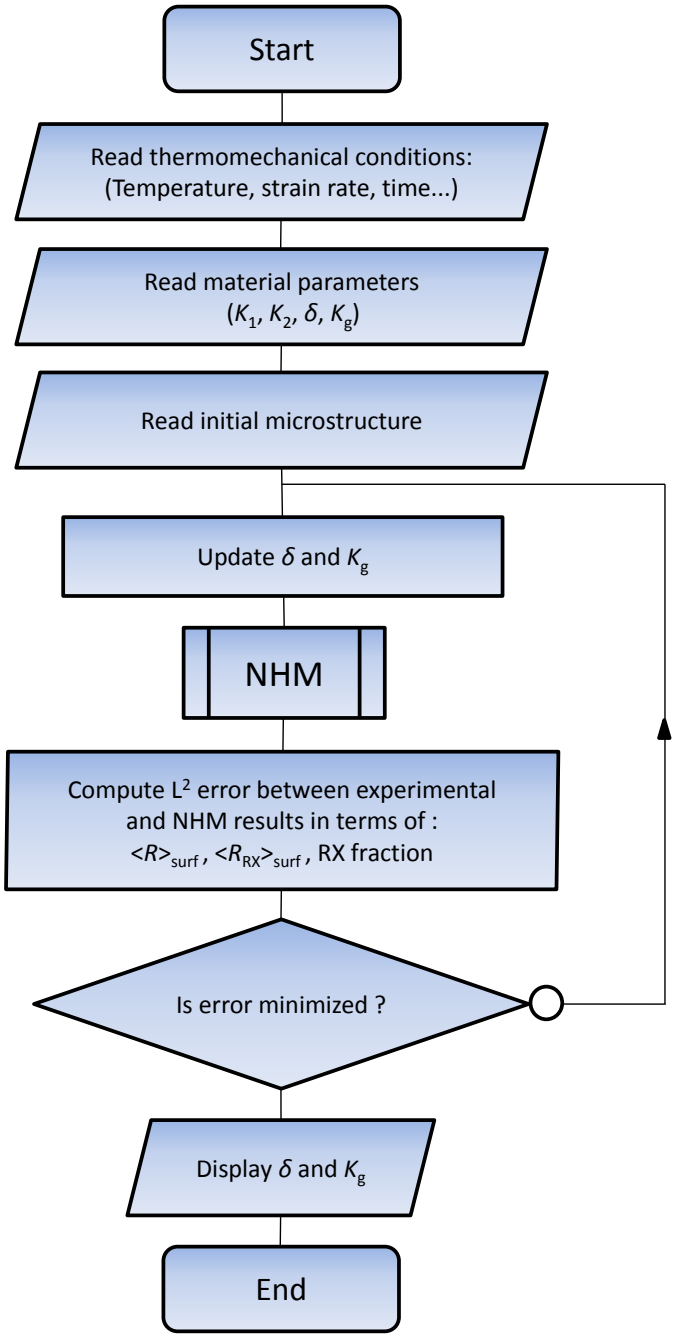

Fig. 5.26. *Inverse analysis procedure for the identification of the NHM parameters K_g and δ.*

This equation is used to interpolate values of K_g for any sets of thermomechanical conditions in the considered range (from 1273 to 1373K and 0.01 to 0.1s^{-1} approximately).

T(K)	$\dot{\varepsilon}_{VM}$ (s^{-1})	δ	K_g (m.s^{-1})
1273	0.14	3.3	1.8e-7
1273	0.07	2	1.7e-7
1273	0.014	1.2	5e-8
1373	0.014	1	6.3e-8

Tab. 5.7. *Values of δ and K_g parameters identified by inverse analysis on microstructure data using the NHM.*

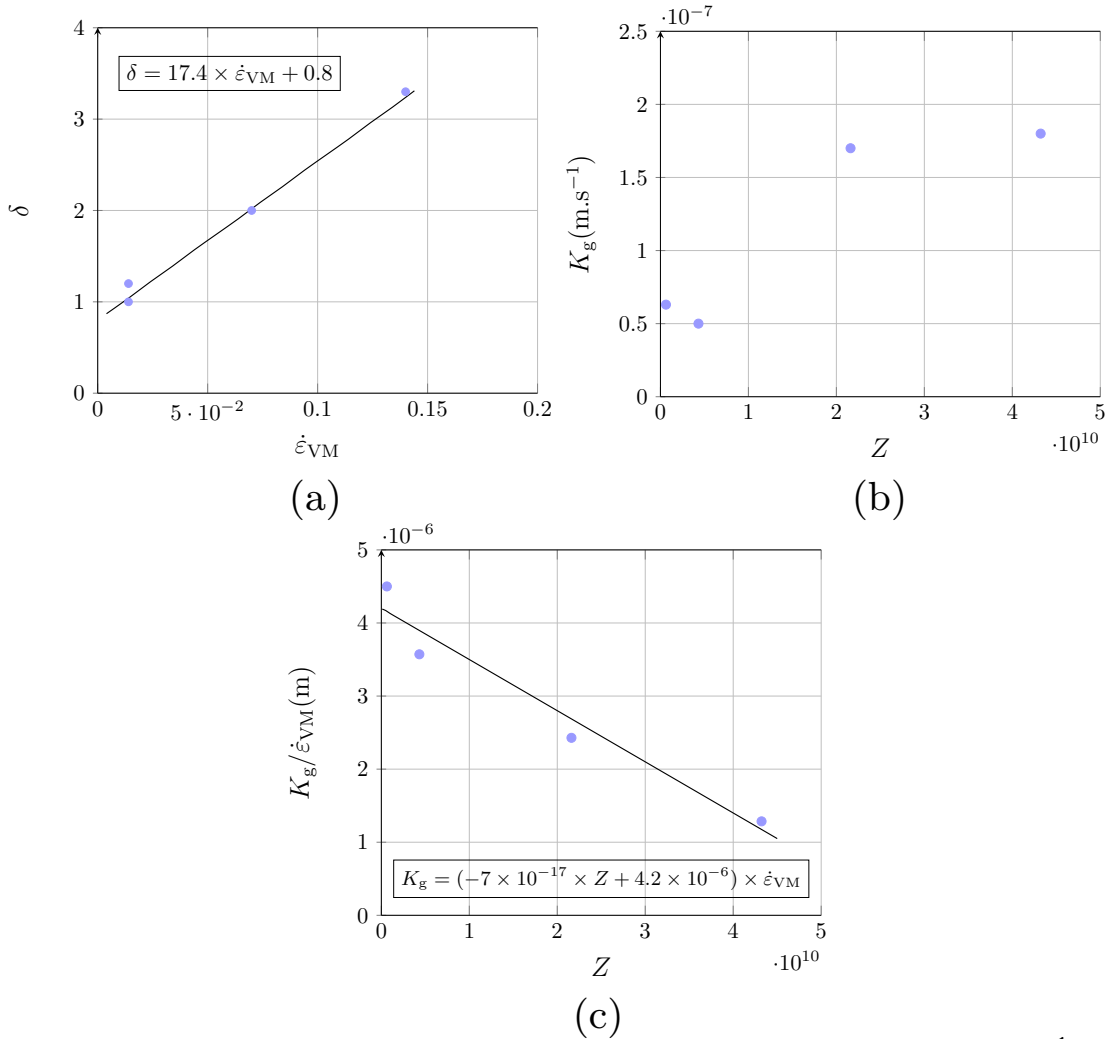

Fig. 5.27. *Representation of (a) the δ parameter as a function of strain rate, (b) the K_g parameter as a function of the Zener-Hollomon parameter and (c) the ratio $K_g/\dot{\varepsilon}_{VM}$ as a function of the Zener-Hollomon parameter.*

5.4 Comparison between experimental data and results issued from the NHM after calibration

The ability of the NHM to be fitted on experimental data is investigated in this part. Therefore the comparison between experimental data and NHM after calibration is presented on Fig. 5.28. These results are presented in terms of RX fraction, mean grain radius (weighted by surface), mean RX grain radius (weighted by surface), and macroscopic stress. The RX fraction is correctly fitted by the NHM, whatever the set of thermomechanical conditions. The comparison of mean grain radius is globally quite good but is a little bit overestimated by the NHM, except at 1373K where it is underestimated. Concerning the comparison of mean RX grain radius, results are satisfactory even if is a little bit underestimated by the NHM. Finally, the true stress evolution of the NHM is also quite close to the experimental one, even if the decrease in flow stress after the peak stress at a temperature of 1273K and a strain rate of $0.014s^{-1}$ is less pronounced with the NHM than in experimental data.

The fact that grain sizes are generally overestimated by the NHM can be explained by the security factor ω=1.5 used in the critical radius formulation (Eq. 3.12), which consequently increases the RX grain size. Indeed, this security factor is used to ensure the stability of the nuclei but defines the spatial resolution of the model. In the NHM it is not necessary since the stability of the nuclei is ensured directly through the critical size of the grain which respects the Bailey-Hirsch criterion. However, in the full field model, this security parameter is necessary because the calculation of the local curvature depends on the mesh size and therefore local curvature may be overestimated sometimes and the nuclei may shrink. Since both models, full field and the NHM, are built up with the same equations and parameters, we made the choice to keep this security factor in both the NHM and full field models since it allows to identify the parameters of full field model using the NHM while avoiding high calculation time. However, to highlight the fact that results issued from the NHM are better without using this security factor, the inverse analysis procedure was repeated with ω=1 and comparisons between the NHM and experimental data are presented in appendix *A* (Fig. 1), in terms of averaged quantities. It is worth noticing that experimental data are correctly fitted by the NHM without using this security factor (i.e. ω = 1), in particular mean grain sizes issued from the NHM (Fig. 1 from (c) to (f)) are now close to experimental data.

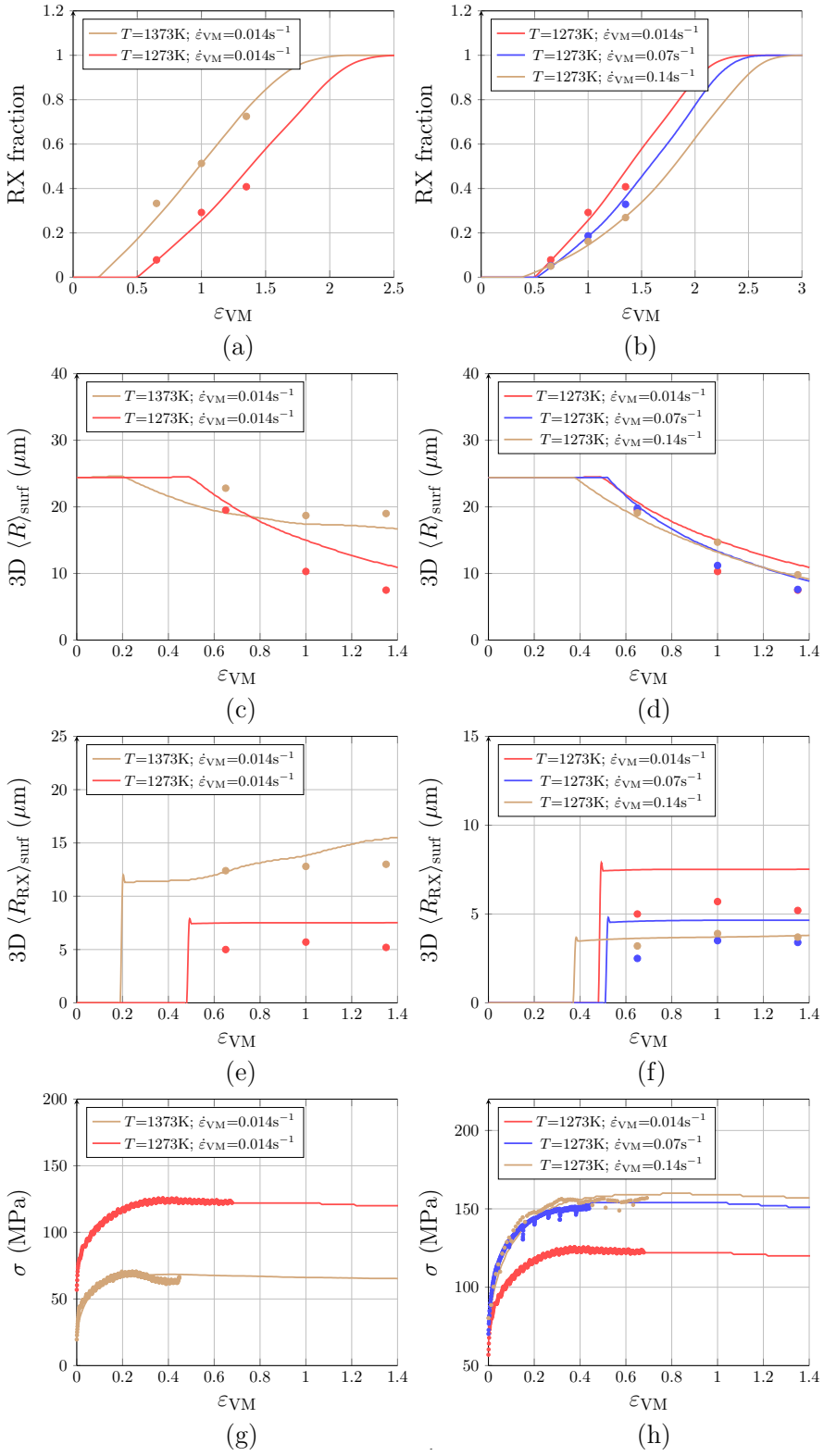

Fig. 5.28. *Comparison between experimental data and results issued from the NHM after calibration: (a) and (b) recrystallized fraction, (c) and (d) mean grain radius (weighted by grain surface), (e) and (f) mean recrystallized grain radius (weighted by grain surface) and (g) and (h) true stress.*

In order to discuss the NHM after calibration in the considered range of temperatures and strain rates (1273 to 1373K and 0.01 to 0.1s^{-1}, approximately), experimental data obtained at T=1323K and $\dot{\varepsilon}_{\mathrm{VM}}$=0.014s^{-1} are compared with the NHM predictions on Fig. 5.29. The parameters K_1 and K_2 used in the NHM at this set of thermomechanical conditions were identified from Eqs. 5.20 and 5.21, respectively, while the parameters δ and K_{g} were identified from Eqs. 5.29 and 5.30, respectively. Results predicted by the NHM are very close to experimental data, in particular for the RX fraction, the overall mean grain radius and the true stress. Concerning the mean RX grain radius, this latter is overestimated by the NHM. The reason is mainly due to the consideration of the security factor as already explained previously. Globally, these results show the versatility of the NHM to predict microstructure quantities in the considered range of thermomechanical conditions. In this context, an interesting prospect would be to perform additional compression tests out of the considered range of thermomechanical conditions, in order to investigate whether Eqs. 5.20, 5.21, 5.29 and 5.30 can be used to extrapolate the four model parameters.

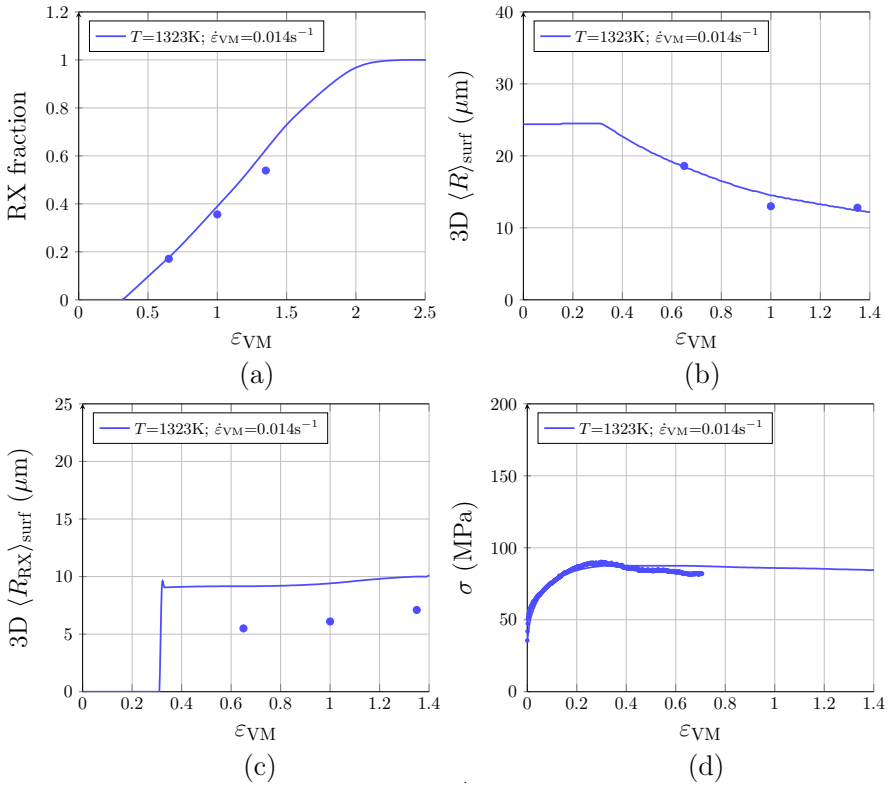

Fig. 5.29. *Comparison between experimental data and the NHM predictions at T=1323K and $\dot{\varepsilon}_{VM}$=0.014s^{-1} in terms of (a) recrystallized fraction, (b) mean grain radius (weighted by grain surface), (c) mean recrystallized grain radius (weighted by grain surface) and (d) true stress.*

5.5 Comparison between experimental data and results issued from the NHM and the full field model after calibration

The comparison between experimental data and results issued from by the NHM and the full field model after calibration is presented on Fig. 5.30 for two sets of thermo-mechanical conditions: T_1=1273K; $\dot{\varepsilon}_1$=0.14s^{-1} and T_2=1373K; $\dot{\varepsilon}_2$=0.014s^{-1}. Results are presented in terms of (a) RX fraction, (b) overall mean grain radius (weighted by grain surface), (c) mean RX grain radius (weighted by grain surface) and (d) true stress. Results issued from the NHM are close to those of the full field model. These results are interesting because they prove the consistency of both models, which means that the NHM can be used to identify with short computation times the full field model parameters.

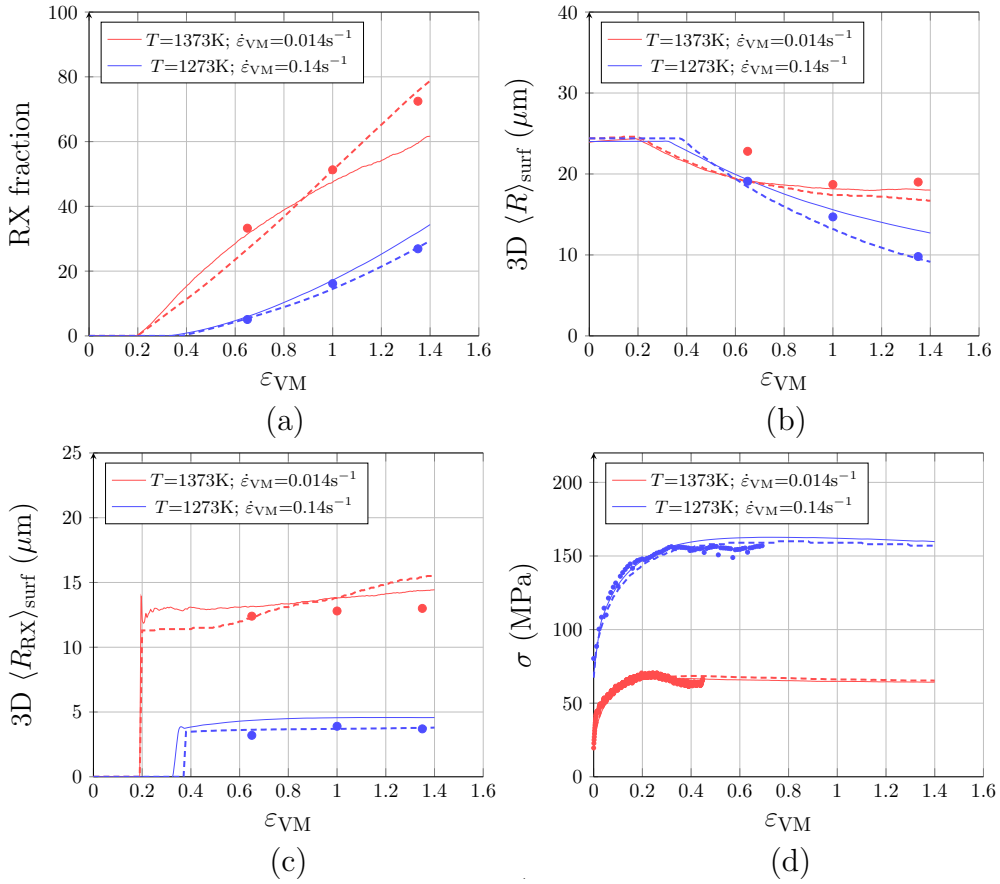

Fig. 5.30. *Comparisons between experimental data (dots) and those issued from the NHM (dashed lines) and the full field model (full lines) after calibration. (a) recrystallized fraction, (b) mean grain radius (weighted by grain surface), (c) mean recrystallized grain radius (weighted by grain surface) and (c) true stress.*

2D grain size distributions issued from the NHM and the full field model after calibra-

tion are also presented and compared to the experimental ones, for the two same sets of thermomechanical conditions: (T=1273K ; $\dot{\varepsilon}_{VM}$=0.14s^{-1}) on Fig. 5.31 and (T=1373K ; $\dot{\varepsilon}_{VM}$=0.014s^{-1}) on Fig. 5.32. All distributions are presented for three levels of equivalent plastic strain: (a) ε_{VM}=0.65, (b) ε_{VM}=1 and (c) ε_{VM}=1.35. Since the NHM considers 3D grains and an implicit microstructure, the inverse Saltykov method was used to transform 3D distributions into 2D distributions. In the case of the full field model, grains are also in 3D but the microstructure is explicit, therefore ten slices were extracted from the RVE and a 2D grain size distribution was built-up from each slice. Then the ten obtained 2D distributions were cumulated to obtain a 2D global distribution, as presented on Fig. 5.33 from (a) to (c).

The grain size distributions issued from the NHM are close to those of the full field model, which confirms the conclusions of chapter 4. However, some differences remain between the distributions issued from both models and the experimental ones. Small grains are always more numerous in experimental distributions compared to those from the models. This is due to the fact that in models, nuclei are inserted with a critical radius to make sure they survive whereas in experimental microstructures, a large number of very small RX grains is observed, a certain part of those grows and another disappears. This defines the spatial resolution of the models. Several alternatives may be tested to improve the spatial resolution of the NHM. For example one could consider a higher nucleation rate with a distribution of the nuclei size for which only part of them would survive because of capillarity forces, as used by Cram et al. [70]. Another possibility would be to omit the capillarity term exerted on nuclei in Eq. 4.13 in order to insert them with a very small size, the capillarity term being added later on each nucleus that reached the critical size. Finally, although in this work we chose to keep coherency between the full field and NHM models by keeping the same equations and the same parameters in both models, another alternative would be to decrease nuclei size in the NHM by using a security factor values $\omega = 1$ instead of 1.5. The grain size distributions issued from the NHM when using the two different security factors $\omega = 1$ and $\omega = 1.5$ are presented and compared to experimental ones in appendices B and C for two different sets of thermomechanical conditions (Fig. 2 and 3). The NHM results are better when using a security factor $\omega = 1$, in particular at T=1373K and $\dot{\varepsilon}_{VM} = 0.014$s^{-1}. Globally, it is worth noticing that grain size distributions issued from the NHM have a realistic shape, which is a major novelty compared to pre-existing mean field models [48–50]. Decreasing nuclei size in full field simulations is more complex because it leads to a decrease in mesh size and an increase in calculation time. Therefore an additional prospect would be to improve the consideration of nuclei in full field models.

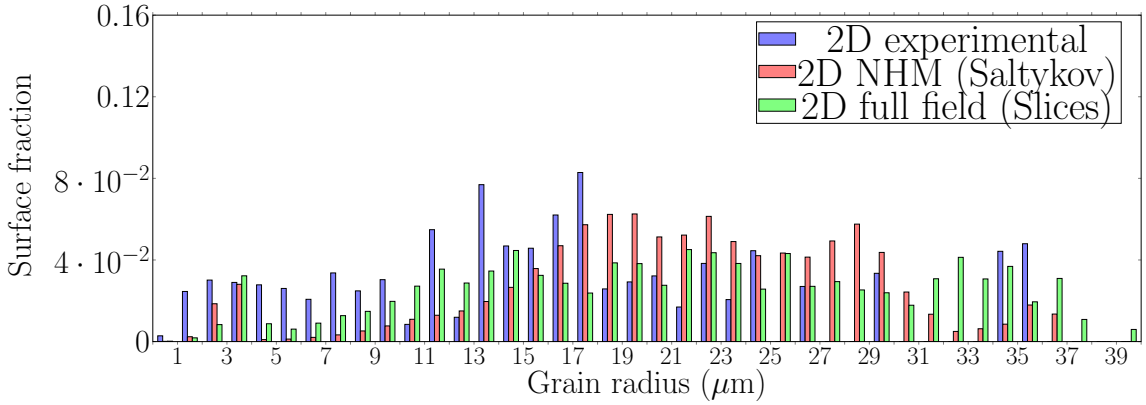

(a) T=1273K, $\dot{\varepsilon}_{\mathrm{VM}}$=0.14s^{-1}, $\varepsilon_{\mathrm{VM}}$=0.65, X_{expe}=5.1%

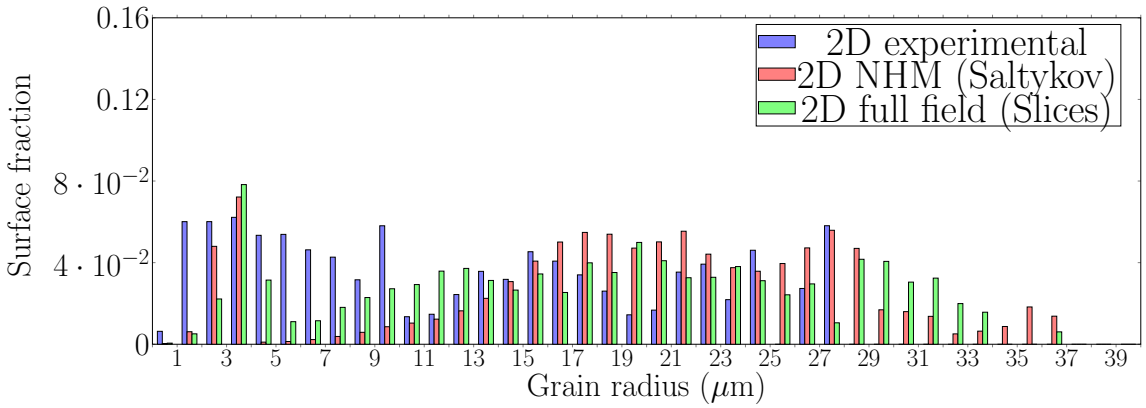

(b) T=1273K, $\dot{\varepsilon}_{\mathrm{VM}}$=0.14s^{-1}, $\varepsilon_{\mathrm{VM}}$=1, X_{expe}=16.1%

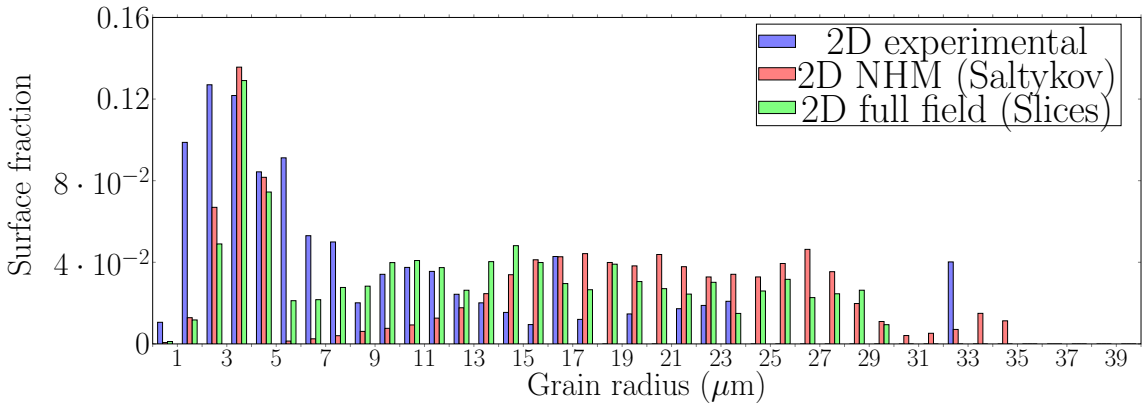

(c) T=1273K, $\dot{\varepsilon}_{\mathrm{VM}}$=0.14s^{-1}, $\varepsilon_{\mathrm{VM}}$=1.35, X_{expe}=26.9%

Fig. 5.31. *Comparison between experimental 2D grain size distributions and those issued from the NHM and the full field models at different values of equivalent plastic strain of (a) ε_{VM} = 0.65, (b) ε_{VM} = 1 and (c) ε_{VM} = 1.35 applied at T=1273K and $\dot{\varepsilon}_{VM}$=0.14s^{-1}.*

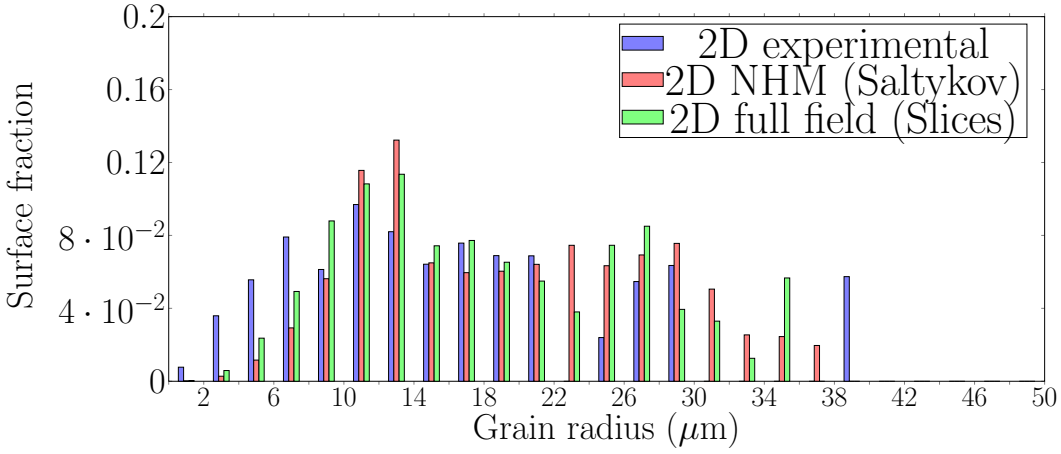

(a) T=1373K, $\dot{\varepsilon}_{\mathrm{VM}}$=0.014s^{-1}, $\varepsilon_{\mathrm{VM}}$=0.65, X_{expe}=33.3%

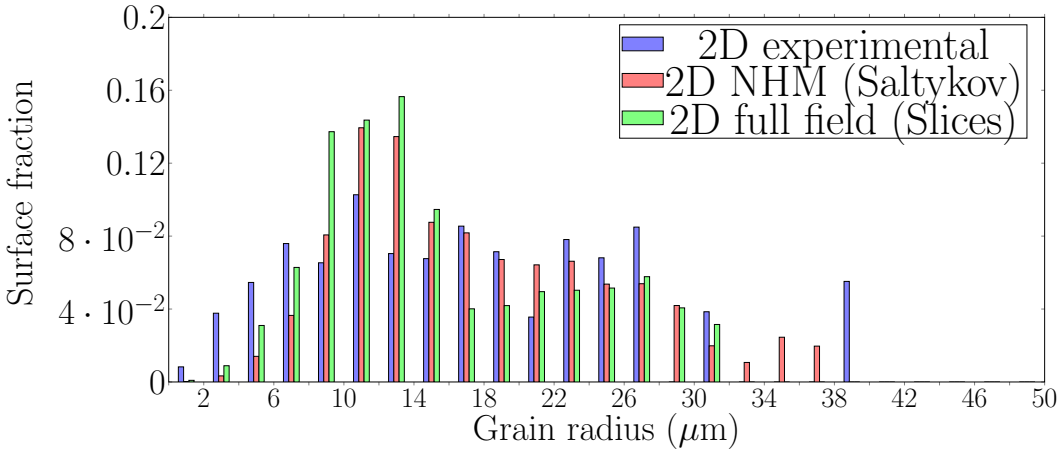

(b) T=1373K, $\dot{\varepsilon}_{\mathrm{VM}}$=0.014s^{-1}, $\varepsilon_{\mathrm{VM}}$=1, X_{expe}=51.3%

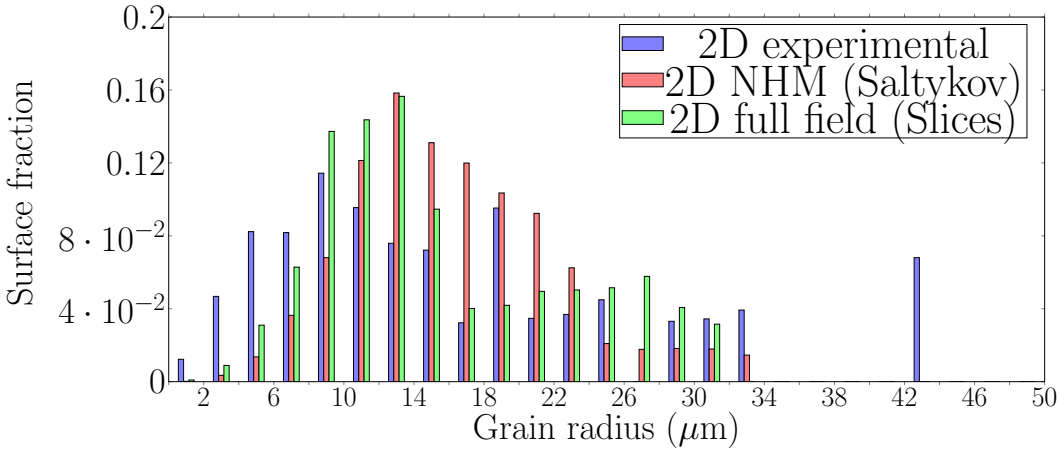

(c) T=1373K, $\dot{\varepsilon}_{\mathrm{VM}}$=0.014s^{-1}, $\varepsilon_{\mathrm{VM}}$=1.35, X_{expe}=72.5%

Fig. 5.32. *Comparison between experimental 2D grain size distributions and those issued from the NHM and the full field models at different values of equivalent plastic strain of (a) ε_{VM} = 0.65, (b) ε_{VM} = 1 and (c) ε_{VM} = 1.35 applied at T=1373K and $\dot{\varepsilon}_{VM}$=0.014s^{-1}.*

Finally, different slices were extracted from the 3D full field simulation RVEs at different ε_{VM} and are compared to EBSD maps on Fig. 5.33. The microstructures obtained by full field simulations are presented from (a) to (c) while the experimental ones are presented from (d) to (f). This kind of comparison is rare in the state of the art and only averaged quantities are generally compared. However, the major advantage of such comparisons is to figure out which should be the next model improvements for a still better prediction of microstructure mechanisms occurring during and after deformation. For instance, the RX grain size is uniform in the simulated microstructures ((a) to (c)) contrary to experimental microstructures. This limitation can be explained by the fact that all nuclei are inserted in simulations with the same initial size given by the Bailey-Hirsch condition. Another reason can be related to the fact that many nuclei are inserted simultaneously at each time increment in simulations, which can slow down their growth. The recrystallized grain shape is much more tortuous in experimental microstructures whereas more regular shapes are obtained with simulations. This arises from the assumption of uniform grain boundary energies and mobilities as well as the consideration of a uniform average dislocation density in each grain in the full field model. Despite those remarks, the comparison is quite satisfactory, and it shows the capacity of full field models to predicted realistic microstructures.

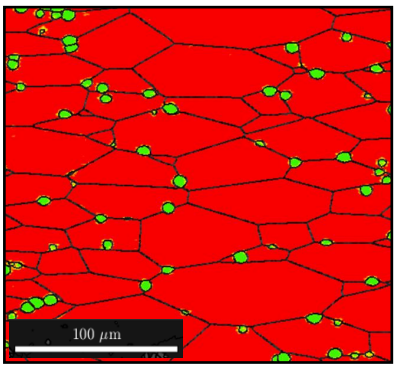

(a) Full field, $\varepsilon_{\mathrm{VM}} = 0.65$

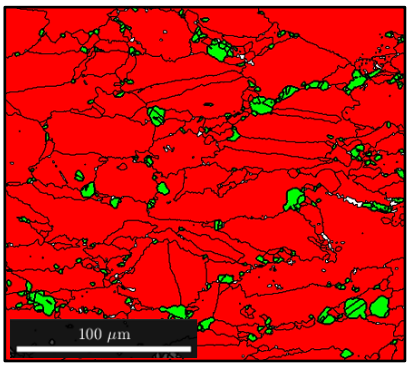

(d) Experimental, $\varepsilon_{\mathrm{VM}} = 0.65$

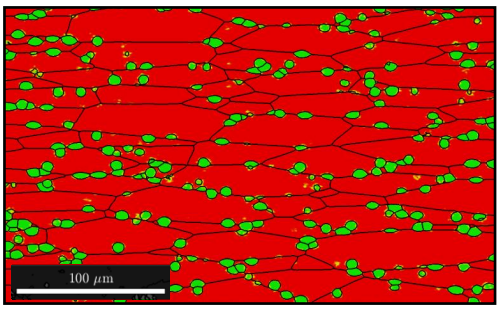

(b) Full field, $\varepsilon_{\mathrm{VM}} = 1$

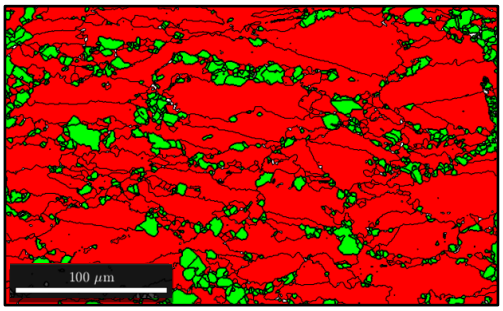

(e) Experimental, $\varepsilon_{\mathrm{VM}} = 1$

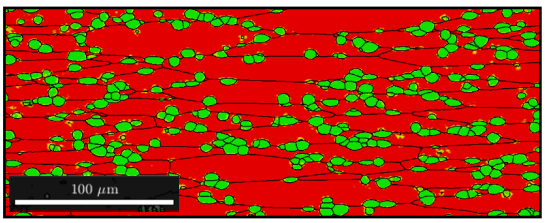

(c) Full field, $\varepsilon_{\mathrm{VM}} = 1.35$

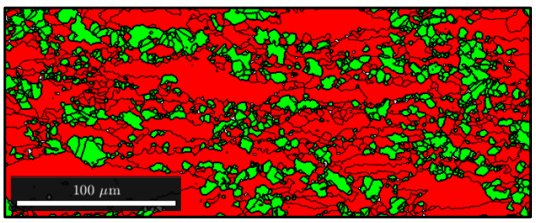

(f) Experimental, $\varepsilon_{\mathrm{VM}} = 1.35$

Fig. 5.33. *Comparisons between 2D microstructures obtained by slicing 3D full field simulations ((a) to (c)) and 2D experimental microstructures ((d) to (f)) obtained after compression tests at T=1273K and* $\dot{\varepsilon}_{VM}$*=0.014s*$^{-1}$.

Summary

In this chapter, different compression tests were performed on 304L steel samples at high temperatures and different strain rates. The flow behavior of the alloy, more precisely the stress-strain curves, were first obtained for different sets of thermomechanical conditions $(T, \dot{\varepsilon})$. Then using these stress-strain curves, the model parameters of strain hardening K_1 and dynamic recovery K_2 were identified at different temperatures and strain rates. Those values were correlated to the thermomechanical conditions to identify laws allowing for further interpolating these two parameters at any temperature and strain rate in the considered range (from 1273 to 1373K and 0.01 to 0.1s^{-1}, approximately) of thermomechanical conditions. Furthermore, the evolution of the K_1 and K_2 parameters with strain rate and temperature is in agreement with physical interpretations: strain hardening increases with strain rate while dynamic recovery increases with increasing temperature or decreasing strain rate.

Then the microstructures of the 304L steel samples submitted to the various thermomechanical conditions were characterized using the EBSD technique. Orientation maps were quantitatively analysed to get recrystallized fractions, mean grain sizes and grain size distributions. In parallel, the compression tests were simulated using the FORGE® finite element software to identify the exact local thermomechanical conditions corresponding to each map location in the samples.

Then these microstructure quantities were used to identify the two other model parameters, i.e. nucleation parameter K_{g} and parameter related to the strain rate dependence of boundary migration δ. This identification is made by inverse analysis using the NHM. It is worth reminding that both the full field model and the NHM are based on the same constitutive equations and consequently have the four same model parameters. Thus parameters can be identified very quickly by inverse analysis using the NHM and then be used in either the full field model or the NHM for DRX simulations.

After identification of all four parameters, the same simulations were performed using the NHM and full field models and the results were compared to experimental data. A good agreement was obtained between both models and between simulated results and experimental data. 2D slices were also taken out from 3D full field simulations and compared to experimental EBSD maps. Results are quite promising even though some improvements, such as the consideration of non-uniform grain boundary energy and mobility, or the consideration of non-uniform stored energy intragranular fields could help getting more realistic topologies. Using crystal plasticity calculations is the most obvious way to account for intragranular heterogeneities, but would be quite expensive from the computation time point of view.

Chapter 6

Conclusions and prospects

Context

This work was dedicated to the development of new approaches for modeling dynamic and post-dynamic recrystallization in three-dimensions, at large deformations and with relatively low computational costs. A huge number of models already exists in the state of the art, at three different main scales: phenomenological laws aiming to predict averaged quantities, mean field models which are based on an implicit description of microstructures and full field models which explicitly describe microstructures. Each of these modeling scales has its own advantages and drawbacks and should be used depending on the requirements. For instance thanks to their low computational costs, phenomenological laws as well as mean field models can easily be coupled to a finite element software in order to predict averaged quantities (e.g. mean grain size, recrystallized fraction) on an entire forged part. On the other hand, full field simulations generally lead to prohibitive computational costs, which do not allow them to be coupled with finite element software. However, since full field models are based on an implicit description of the microstructure, they are useful to study local phenomena.

The DIGIMU® software package is developed and commercialized by the Transvalor company in collaboration with the CEMEF research center. This software is based on a full field approach aiming to predict microstructure evolutions occurring during metallic material processing. More particularly, this software uses the Level-Set method in a finite element context. Even if this formalism is not the most rapid among all full field approaches, it has the major advantage of being versatile, therefore it can describe all microstructure mechanisms in a single and robust numerical framework. Furthermore, since this formalism is based on an implicit description of grain boundaries, it can describe three-dimensional complex geometries all along processes, even at large deformations. The DIGIMU® software package version pre-existing to this PhD work was able to handle only the mechanisms of grain growth and static recrystallization, and was limited to two-dimensional simulations.

Achievements

The first part of this study was dedicated to the improvement of two analytical grain growth models thanks to full field simulations. Existing analytical models for grain growth presented a good ability to predict microstructure evolutions in the steady-state grain growth regime. However, the transient regime is generally neglected in these models, but this regime can be primordial within an industrial context. The transient regime mainly depends on the characteristics of the initial grain size distribution. Therefore, full field grain growth simulations were performed considering different initial grain size distributions to investigate the ability of the classical Hillert/Abbruzzese and Burke & Turnbull analytical models to reproduce results in the transient regime. The Hillert/Abbruzzese model showed a good ability to describe microstructure evolutions during grain growth, whatever the initial grain size distribution. However, a fitting parameter of the grain boundary migration equation was recalibrated to be even closer to full field results. The Burke & Turnbull model was not able to model correctly microstructure evolutions during the transient regime, whatever the initial grain size distribution. Therefore, a new Burke & Turnbull formulation was proposed, taking the characteristics of the initial grain size distributions into account. This new Burke & Turnbull formulation showed a good ability to model microstructure evolutions during the transient regime, for any log-normal initial grain size distribution.

After showing the efficiency of using full field simulations to improve analytical models of grain growth, the focus was placed on full field modeling of dynamic and post-dynamic recrystallization which are more complex phenomena involving plasticity and stored energy driving forces. Three main criteria must be fulfilled: the new full field model must be able to run in three-dimensions, must provide low computational costs (necessary for an industrial use) and must be able to handle large deformations representative of industrial processes. Several conclusions were drawn from a large review of the existing full field approaches for dynamic and post-dynamic recrystallization. Phase-Field and Level-Set methods showed a good ability to model three-dimensional complex geometries even et large deformation when coupling with a good meshing/remeshing tool, which explains our choice of the Level-Set method. Some authors coupled the Level-Set or Phase-Field method with fast Fourier transform to perform large scale simulations in relatively low computational costs. However, the use of fast Fourier transform also requires regular grids, thus limiting the maximal deformation that can be reached. Therefore, after this review, the Level-Set method in a finite element framework appeared to be a justified choice for modeling of dynamic and post-dynamic recrystallization in three-dimensions. Many models are coupled to a crystal plasticity algorithm for modeling of strain hardening and dynamic recovery mechanisms appearing during deformation. However, since the use of crystal plasticity still leads to prohibitive computational costs and is not straightforward to implement, we preferred to start with phenomenological laws for describing the dislocation density evolution in our model.

The full field modeling of dynamic and post-dynamic recrystallization is really interest-

ing, in particular for the investigation of particular configurations such as heterogeneity of grain sizes, solicitations directions and heterogeneity of stored energy. Although a large number of improvements made in previous studies enables to perform full field simulations of dynamic and post-dynamic recrystallization within few hours using the Level-Set method in a finite element framework, computational costs are still too high to predict microstructure evolutions on an entire forged part. Therefore, mean field approaches appear as a good compromise between full field models and phenomenological laws. However, existing mean field models were still based on many assumptions that need to be tackled. In the fourth chapter, a new mean field approach called "NHM" for NeighborHood Model was proposed for modeling of dynamic and post-dynamic recrystallization. This approach tackles some assumptions of pre-existing mean field models by achieving two major improvements; this was done with the help of full field simulations. The two major improvements are: the consideration of a particular neighborhood for each grain and the consideration of the grain shape evolution from spherical to ellipsoidal one during deformation. Another major advantage is related to the fact that both the full field model and the NHM proposed in this work are based on the same constitutive equations for strain hardening, recovery and nucleation of recrystallized grains. Therefore, the same model parameters are considered and the NHM can be used to identify the model parameters very quickly by inverse analysis, parameters that can then be used either in the NHM or in the full field model.

The last chapter is dedicated to the calibration of the NHM and the full field model. Jonas [197] already proposed a method for the identification of the strain hardening K_1 and dynamic recovery K_2 parameters based on the analysis of stress-strain curves, between the yield stress and the onset of dynamic recrystallization. However, this method is more or less accurate depending on the quality of the experimental curve. Furthermore, no method existed concerning the identification of the two other parameters δ (dependence of the grain boundary migration on strain rate) and K_g (nucleation) since these two are related to our models. Therefore, a new calibration procedure was proposed to identify all four model parameters based on compression tests performed on 304L steel samples. The identification of K_1 and K_2 is based on the analysis of stress-strain curves using the Jonas method coupled to an inverse analysis algorithm. Then the identification of δ and K_g is made by inverse analysis using the NHM and based on experimental microstructure quantities. After calibration, results issued from both the full field model and the NHM were compared together and to experimental data in terms of averaged quantities and grain size distributions. Results demonstrate a good ability of both models to fit and predict experimental data in the considered range of thermomechanical conditions. Two-dimensional sections extracted from the representative elementary volumes of full field simulations also show reasonable agreement with experimental electron backscatter diffraction maps, even though this comparison showed that some model improvements are still necessary to get more realistic recrystallized grain shapes and grain size distributions.

Prospects

A major prospect is the coupling of the full field model proposed in this work with a crystal plasticity algorithm. Simulation results considering crystal plasticity could be compared to those obtained with the actual full field model to investigate the assumption/simplification related to the use of phenomenological laws for strain hardening and dynamic recovery. Previous studies [207] as well as an ongoing PhD work [208] at CEMEF aim at developing a robust framework for this coupling. Such implementation is not straightforward and many aspects need to be discussed on this topic. Indeed in the actual full field model, the stored energy is averaged per grain, therefore the jump in stored energy is easily computed at grain boundaries. When using a crystal plasticity algorithm, a local stored energy is obtained at every mesh element (or mesh node in the P1 formulation). Then to calculate the jump in stored energy across the boundary, this energy can be either averaged per grain as considered in the actual model or averaged per boundary, which is supposed to be the more accurate. However, averaging per boundary raises several questions, in particular to compute jump in stored energy at triple junctions. A recent paper discussed this topic [155]. Other questions such as the attribution of a particular orientation to nuclei were also discussed in [207] but need to be further improved according to the state of the art.

Despite of large improvements made to accelerate the full field simulations, a major part of process time is lost into the reinitialization procedure as well as in solving transport equations. An interesting prospect would probably be to develop an hydride method between Level-Set and Vertex approaches. Nodes would then be considered on grain boundaries and multiple junctions as in the Vertex method, while Level-Set functions would be considered to manage physical fields and grain boundary migration. An ongoing PhD work [209] at CEMEF aims to implement this hydride method. This aspect could potentially limit drastically the numerical cost of a classical non-conform Level-Set finite element strategy by increasing the resolution precision while avoiding local remeshing. An illustration of this hybrid method in two-dimensions is represented on Fig. 6.1 with a velocity field accounting for capillarity effects (i.e. which depends on the grain boundary curvatures).

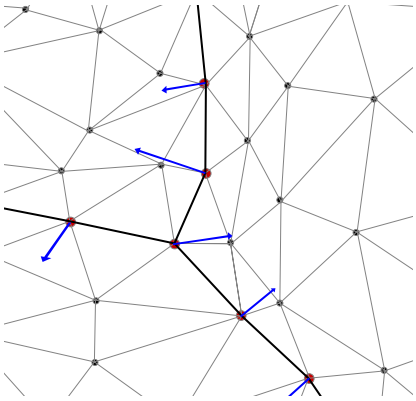

Fig. 6.1. *Illustration of the hybrid method in 2D, by coupling Level-Set and Vertex approaches, as considered in the PhD work of Florez [209] at CEMEF. Velocity field is represented by blue arrows at every node of grain boundaries.*

In most of mean field models for dynamic and post-dynamic recrystallization, grains are defined by an equivalent sphere radius and averaged dislocation density. In this work, a first step was reached with the NHM where three semi-axes of ellipsoid grains and a particular neighborhood were additionally considered per grain, which considerably refines results. A next improvement in the NHM would be to consider a crystallographic texture, for instance by considering a Taylor factor per grain. Based on such factor, it would be possible to make each grain harden differently during deformation. Another perspective would also be to consider a sub-grains population per grain, aiming to model for instance bulk nucleation. In this context, the work of Cram and Zurob [70] is very interesting and could be used as a first step in this prospect.

Finally many prospects concern experimental investigations. Comparisons between the NHM, the full field model and experimental data were made at the end of chapter 5 after calibration of the two models and comparison was good in the considered range of thermomechanical conditions. For the sake of an industrial use, additional tests outside the considered range of conditions would be beneficial to also enlarge the validity range of the laws describing the dependence of the model parameters on thermomechanical conditions. Furthermore, calibration and comparison were only performed for the dynamic recrystallization regime since no tests were performed with a post-dynamic holding time during this PhD work. A prospect would be then naturally to perform post-dynamic tests and propose a calibration method to identify the static recovery parameter K_s.

Appendix A: Influence of the safety factor on averaged quantities

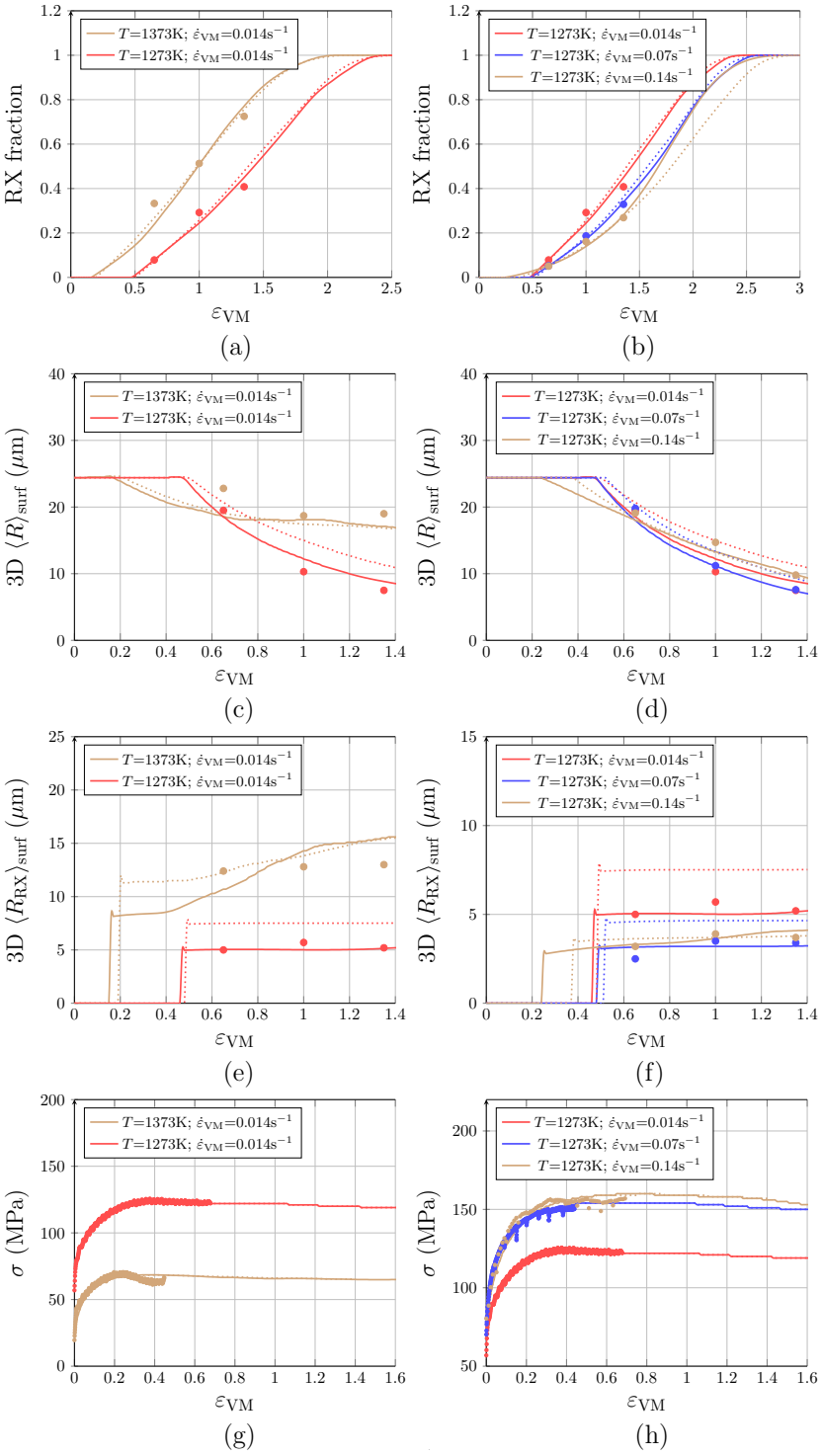

Fig. 1. *Comparison between experimental data (dots) and NHM predictions after calibration using two different safety factor values for nucleus size: $\omega = 1$ (full lines) and $\omega = 1.5$ (dashed lines). Results are presented in terms of: (a) and (b) recrystallized fraction, (c) and (d) mean grain radius (weighted by grain surface), (e) and (f) mean recrystallized grain radius (weighted by grain surface) and (g) and (h) true stress.*

Appendix B: Influence of the safety factor on grain size distributions

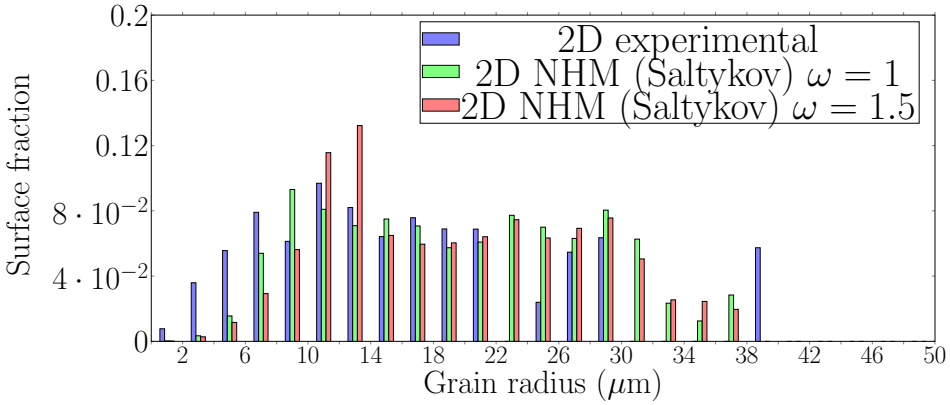

(a) T=1373K, $\dot{\varepsilon}_{\mathrm{VM}}$=0.014s^{-1}, $\varepsilon_{\mathrm{VM}}$=0.65, X_{expe}=33.3%

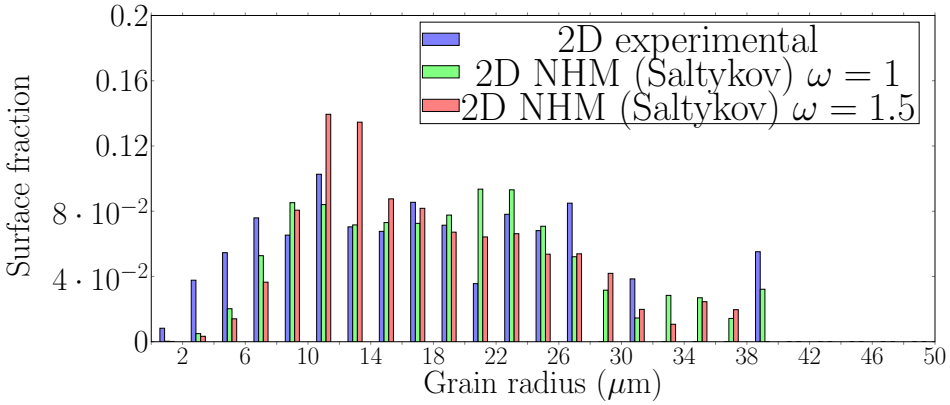

(b) T=1373K, $\dot{\varepsilon}_{\mathrm{VM}}$=0.014s^{-1}, $\varepsilon_{\mathrm{VM}}$=1, X_{expe}=51.3%

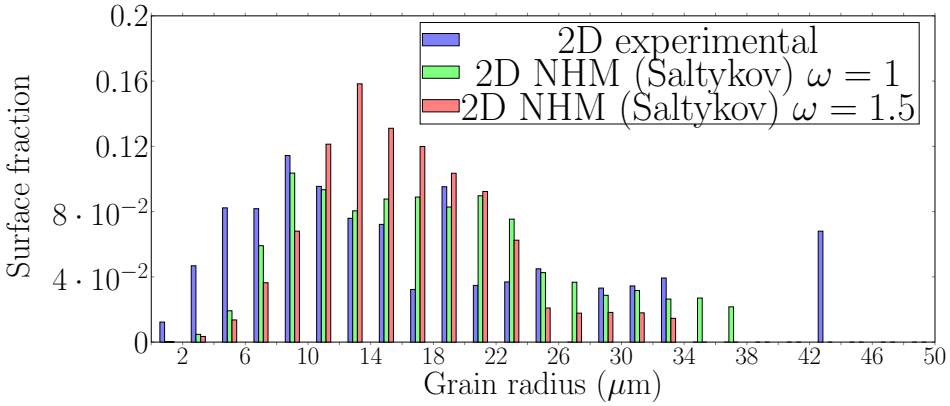

(c) T=1373K, $\dot{\varepsilon}_{\mathrm{VM}}$=0.014s^{-1}, $\varepsilon_{\mathrm{VM}}$=1.35, X_{expe}=72.5%

Fig. 2. *Comparison between 2D grain size distributions from experimental tests and those predicted by NHM after calibration using two different safety factor values for nucleus size: ω = 1 and ω = 1.5. Results are presented at three different equivalent plastic strain: (a) ε_{VM} = 0.65, (b) ε_{VM} = 1 and (c) ε_{VM} = 1.35. The corresponding set of thermomechanical conditions is T=1373K and $\dot{\varepsilon}_{VM}$=0.014s^{-1}.*

Appendix C: Influence of the safety factor on grain size distributions

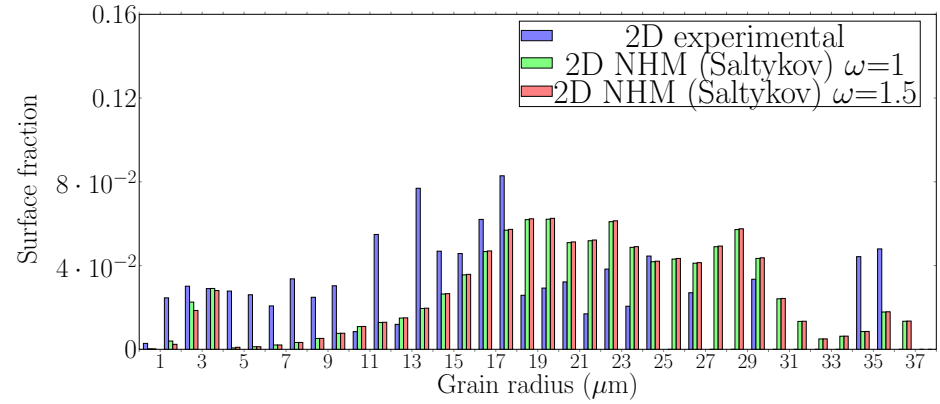

(a) T=1273K, $\dot{\varepsilon}_{\mathrm{VM}}$=0.14s^{-1}, $\varepsilon_{\mathrm{VM}}$=0.65, X_{expe}=5.1%

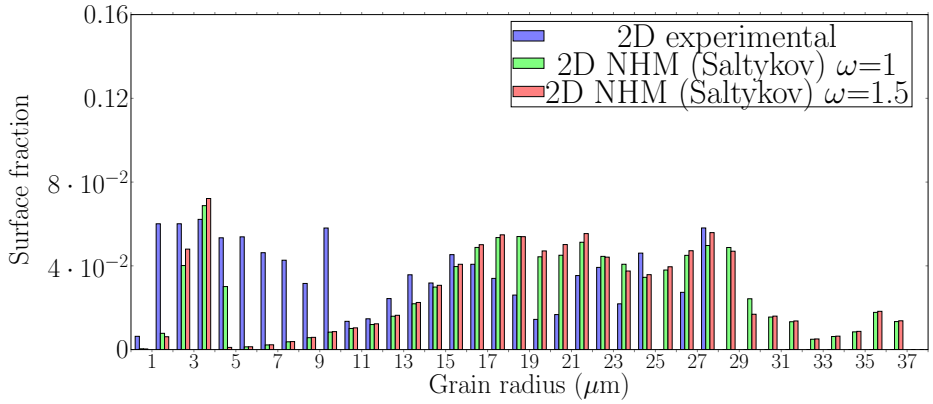

(b) T=1273K, $\dot{\varepsilon}_{\mathrm{VM}}$=0.14s^{-1}, $\varepsilon_{\mathrm{VM}}$=1, X_{expe}=16.1%

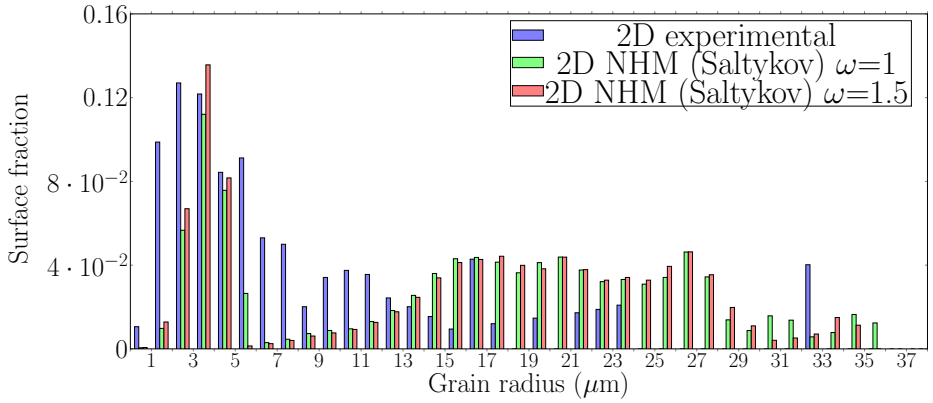

(c) T=1273K, $\dot{\varepsilon}_{\mathrm{VM}}$=0.14s^{-1}, $\varepsilon_{\mathrm{VM}}$=1.35, X_{expe}=26.9%

Fig. 3. *Comparison between 2D grain size distributions from experimental tests and those predicted by NHM after calibration using two different safety factor values for nucleus size: ω = 1 and ω = 1.5. Results are presented at three different equivalent plastic strain: (a) ε_{VM} = 0.65, (b) ε_{VM} = 1 and (c) ε_{VM} = 1.35. The corresponding set of thermomechanical conditions is T=1273K and $\dot{\varepsilon}_{VM}$=0.14s^{-1}.*

Bibliography

[1] T. Sakai, J. J. Jonas, Dynamic recrystallization: Mechanical and microstructural considerations, Acta Metallurgica 32 (2) (1984) 189–209.

[2] M. Luton, C. Sellars, Dynamic recrystallization in nickel and nickel-iron alloys during high temperature deformation, Acta Metallurgica 17 (8) (1969) 1033–1043. doi:10.1016/0001-6160(69)90049-2.

[3] C. M. Sellars, Recrystallization of Metals during Hot Deformation, Philosophical Transactions of the Royal Society A: Mathematical, Physical and Engineering Sciences 288 (1350) (1978) 147–158. doi:10.1098/rsta.1978.0010.

[4] T. Sakai, Dynamic recrystallization microstructures under hot working conditions, Journal of Materials Processing Technology 53 (1-2) (1995) 349–361. doi:10.1016/0924-0136(95)01992-N.

[5] F. J. Humphreys, M. Hatherly, Recrystallization and related annealing phenomena (2nd edition), Elsevier, 2004.

[6] A. Momeni, K. Dehghani, G. R. Ebrahimi, Modeling the initiation of dynamic recrystallization using a dynamic recovery model, Journal of Alloys and Compounds 509 (39) (2011) 9387–9393. doi:10.1016/j.jallcom.2011.07.014.

[7] D. Li, Q. Guo, S. Guo, H. Peng, Z. Wu, The microstructure evolution and nucleation mechanisms of dynamic recrystallization in hot-deformed Inconel 625 superalloy, Materials and Design 32 (2) (2011) 696–705. doi:10.1016/j.matdes.2010.07.040.

[8] H. Jiang, L. Yang, J. Dong, M. Zhang, Z. Yao, The recrystallization model and microstructure prediction of alloy 690 during hot deformation, Materials and Design 104 (2016) 162–173. doi:10.1016/j.matdes.2016.05.033.

[9] Z. Wan, Y. Sun, L. Hu, H. Yu, Experimental study and numerical simulation of dynamic recrystallization behavior of TiAl-based alloy, Materials & Design 122 (2017) 11–20. doi:10.1016/j.matdes.2017.02.088.

[10] K. Huang, R. Logé, A review on dynamic recrystallization phenomena in metallic materials, Materials & Design 111 (2016) 548–574. doi:10.1016/j.matdes.2016.09.012.

[11] X. G. Fan, H. Yang, P. F. Gao, R. Zuo, P. H. Lei, The role of dynamic and post dynamic recrystallization on microstructure refinement in primary working of a coarse grained two-phase titanium alloy, Journal of Materials Processing Technology 234 (2016) 290–299. doi:10.1016/j.jmatprotec.2016.03.031.

[12] M. H. Maghsoudi, A. Zarei-Hanzaki, P. Changizian, A. Marandi, Metadynamic recrystallization behavior of AZ61 magnesium alloy, Materials and Design 57 (2014) 487–493. doi:10.1016/j.matdes.2013.12.051.

[13] J. A. Spitznagel, R. Stickler, Correlation between precipitation reactions and bulk density changes in type 18-12 austenitic stainless steels, Metallurgical Transactions 5 (6) (1974) 1363–1371. doi:10.1007/BF02646622.

[14] K. C. Mills, Recommended values of thermophysical properties for selected commercial alloys, Woodhead, 2002.

[15] S. Towfighi, D. Romilly, J. Olson, Elevated temperature material characteristics of AISI 304L stainless steel, Materials at High Temperatures 30 (2) (2013) 151–155. doi:10.3184/096034013X13717290689579.

[16] F. C. Campbell, Elements of metallurgy and engineering alloys, ASM International, 2008.

[17] Z. C. S. Smith, Introduction to Grains, Phases, and Interfaces-an Interpretation of Microstructure, Trans. AIME 175 (1948) 15–51.

[18] W. T. Read, W. Shockley, Dislocation Models of Crystal Grain Boundaries, Physical Review 78 (3) (1950) 275–289. doi:10.1103/PhysRev.78.275.

[19] F. J. Humphreys, M. Hatherly, Recrystallization and related annealing phenomena (1st edition), Pergamon, 1996.

[20] D. Wolf, A read-shockley model for high-angle grain boundaries, Scripta Metallurgica 23 (10) (1989) 1713–1718. doi:10.1016/0036-9748(89)90348-7.

[21] A. Mallick, S. Vendantam, Phase field study of the effect of grain boundary energy anisotropy on grain growth, Computational Materials Science 46 (1) (2009) 21–25. doi:10.1016/J.COMMATSCI.2009.01.026.

[22] D. L. Olmsted, E. A. Holm, S. M. Foiles, Survey of computed grain boundary properties in face-centered cubic metalsII: Grain boundary mobility, Acta Materialia 57 (13) (2009) 3704–3713. doi:10.1016/j.actamat.2009.04.015.

[23] V. V. Bulatov, B. W. Reed, M. Kumar, Grain boundary energy function for fcc metals, Acta Materialia 65 (2013) 161–175. doi:10.1016/j.actamat.2013.10.057.

[24] J. Fausty, N. Bozzolo, D. Pïno Muñoz, M. Bernacki, A novel Level-Set Finite Element formulation for grain growth with heterogeneous grain boundary energies, submitted to Materials & Design.

[25] C. Herring, Surface Tension as a Motivation for Sintering, in: Fundamental Contributions to the Continuum Theory of Evolving Phase Interfaces in Solids, Springer Berlin Heidelberg, Berlin, Heidelberg, 1999, pp. 33–69. doi:10.1007/978-3-642-59938-5{_}2.

[26] P. R. Rios, F. Siciliano Jr, H. R. Z. Sandim, R. L. Plaut, A. F. Padilha, Nucleation and growth during recrystallization, Materials Research 8 (3) (2005) 225–238. doi:10.1590/S1516-14392005000300002.

[27] C. S. Smith, Discussion on paper by Mr.J.S.Bowles and Dr. W. Boas. "The effect of crystal arrangements on 'secondary recrystallization' in metals", Journal of the Institute of Metals 74 (1948) 742:758.

[28] H. Hu, Direct observations on the annealing of Si-Fe crystals in the electron microscope., Transactions of the Metallurgical Society of AIME 224 (1) (1962) 75–84.

[29] H. Hu, Recrystallization by subgrain coalescence, in: G. Thomas, J. Washburn (Eds.), Interscience: Electron Microscopy and Strength of Crystals, 1963, pp. 564–573.

[30] A. R. Jones, B. Ralph, N. Hansen, Subgrain Coalescence and the Nucleation of Recrystallization at Grain Boundaries in Aluminium, Proceedings of the Royal Society A: Mathematical, Physical and Engineering Sciences 368 (1734) (1979) 345–357. doi:10.1098/rspa.1979.0134.

[31] R. Sandström, B. Lehtinen, E. Hedman, I. Groza, S. Karlsson, Subgrain growth in Al and Al-1% Mn during annealing, Journal of Materials Science 13 (6) (1978) 1229–1242. doi:10.1007/BF00544729.

[32] P. A. Beck, P. R. Sperry, Strain Induced Grain Boundary Migration in High Purity Aluminum, Journal of Applied Physics 21 (2) (1950) 150–152. doi:10.1063/1.1699614.

[33] K. Li, P. Yang, The Formation of Strong {100} Texture by Dynamic Strain-Induced Boundary Migration in Hot Compressed Ti-5Al-5Mo-5V-1Cr-1Fe Alloy, Metals 7 (10) (2017) 412. doi:10.3390/met7100412.

[34] D.-F. Li, D.-Z. Zhang, S.-D. Liu, Z.-J. Shan, X.-M. Zhang, Q. Wang, S.-Q. Han, Dynamic recrystallization behavior of 7085 aluminum alloy during hot deformation, Trans. Nonferrous Met. Soc. China 26 (2016) 1491–1497. doi:10.1016/S1003-6326(16)64254-1.

[35] K. Kashihara, Y. Takeuchi, T. Shibayanagi, Characteristics of Strain-Induced Boundary Migration as Evaluated by the Crystal Rotation Axis Method in (001) [100] and (112) [11 1 1] Aluminum Bicrystal Deformed by Plane-Strain Compressiondoi:10.2320/matertrans.L-MG200952.

[36] J. E. Bailey, P. B. Hirsch, The Recrystallization Process in Some Polycrystalline Metals, Proceedings of the Royal Society A: Mathematical, Physical and Engineering Sciences 267 (1328) (1962) 11–30. doi:10.1098/rspa.1962.0080.

[37] S. Bellier, R. Doherty, The structure of deformed aluminium and its recrystallizationinvestigations with transmission Kossel diffraction, Acta Metallurgica 25 (5) (1977) 521–538. doi:10.1016/0001-6160(77)90192-4.

[38] P. A. Beck, The Formation of Recrystallization Nuclei, Journal of Applied Physics 20 (6) (1949) 633–634. doi:10.1063/1.1698446.

[39] R. W. Cahn, A New Theory of Recrystallization Nuclei, Proceedings of the Physical Society. Section A 63 (4) (1950) 323–336. doi:10.1088/0370-1298/63/4/302.

[40] A. Cottrell, Theory of Dislocations, in: Progress in Metal Physics, 1953, pp. 4:251–255.

[41] E. Brünger, X. Wang, G. Gottstein, Nucleation mechanisms of dynamic recrystallization in austenitic steel alloy 800H, Scripta Materialia 38 (12) (1998) 1843–1849. doi:10.1016/S1359-6462(98)00124-9.

[42] C. Zener, J. H. Hollomon, Effect of Strain Rate Upon Plastic Flow of Steel, Journal of Applied Physics 15 (1) (1944) 22–32. doi:10.1063/1.1707363.

[43] W. Roberts, B. Ahlbom, A nucleation criterion for dynamic recrystallization during hot working, Acta Metall 26 (1978) 801–813.

[44] A. Kolmogorov, On the Statistical Theory of Crystallization of Metals, Izv. Akad. Nauk SSSR, Ser. Mat. 3 (1937) 355–359.

[45] M. Avrami, Kinetics of Phase Change. I General Theory, The Journal of Chemical Physics 7 (12) (1939) 1103–1112. doi:10.1063/1.1750380.

[46] W. Johnson, R. Mehl, Reaction Kinetics in Processes of Nucleation and Growth, Transactions of the American Institute of Mining and Metallurgical Engineers 135 (1939) 416–442.

[47] M. Hillert, On the theory of normal and abnormal grain growth, Acta Metallurgica 13 (3) (1965) 227–238. doi:10.1016/0001-6160(65)90200-2.

[48] F. Montheillet, O. Lurdos, G. Damamme, A grain scale approach for modeling steady-state discontinuous dynamic recrystallization, Acta Materialia 57 (5) (2009) 1602–1612. doi:10.1016/j.actamat.2008.11.044.

[49] P. Bernard, S. Bag, K. Huang, R. Logé, A two-site mean field model of discontinuous dynamic recrystallization, Materials Science and Engineering: A 528 (24) (2011) 7357–7367. doi:10.1016/j.msea.2011.06.023.

[50] O. Beltran, K. Huang, R. Logé, A mean field model of dynamic and post-dynamic recrystallization predicting kinetics, grain size and flow stress, Computational Materials Science 102 (2015) 293–303. doi:10.1016/j.commatsci.2015.02.043.

[51] C. E. Krill, L. Q. Chen, Computer simulation of 3-D grain growth using a phase-field model, Acta Materialia 50 (12) (2002) 3059–3075. doi:10.1016/S1359-6454(02)00084-8.

[52] M. Bernacki, Y. Chastel, T. Coupez, R. Logé, Level set framework for the numerical modelling of primary recrystallization in polycrystalline materials, Scripta Materialia 58 (12) (2008) 1129–1132. doi:10.1016/J.SCRIPTAMAT.2008.02.016.

[53] Y. Mellbin, H. Hallberg, M. Ristinmaa, A combined crystal plasticity and graph-based vertex model of dynamic recrystallization at large deformations, Modelling and Simulation in Materials Science and Engineering 23 (4) (2015) 045011. doi:10.1088/0965-0393/23/4/045011.

[54] A. D. Rollett, D. Raabe, A hybrid model for mesoscopic simulation of recrystallization, Computational Materials Science 21 (1) (2001) 69–78. doi:10.1016/S0927-0256(00)00216-0.

[55] S. Hafez Haghighat, A. KarimiTaherib, An analytical and experimental investigation on the normal grain growth in metals using the Monte Carlo method, Materials & Design 28 (9) (2007) 2533–2539. doi:10.1016/J.MATDES.2006.09.006.

[56] D. Raabe, Introduction of a scalable three-dimensional cellular automaton with a probabilistic switching rule for the discrete mesoscale simulation of recrystallization phenomena, Philosophical Magazine A 79 (10) (1999) 2339–2358. doi:10.1080/01418619908214288.

[57] Y. Lin, Y.-X. Liu, M.-S. Chen, M.-H. Huang, X. Ma, Z.-L. Long, Study of static recrystallization behavior in hot deformed Ni-based superalloy using cellular automaton model, Materials & Design 99 (2016) 107–114. doi:10.1016/J.MATDES.2016.03.050.

[58] S.-I. Kim, Y.-C. Yoo, Dynamic recrystallization behavior of AISI 304 stainless steel, Materials Science and Engineering: A 311 (1-2) (2001) 108–113. doi:10.1016/S0921-5093(01)00917-0.

[59] S. Venugopal, S. L. Mannan, P. Rodriguez, Optimum design of a hot extrusion process for AISI type 304L stainless steel using a model for the evolution of microstructure, Modelling and Simulation in Materials Science and Engineering 10 (3) (2002) 253–265. doi:10.1088/0965-0393/10/3/301.

[60] A. Dehghan-Manshadi, M. Barnett, P. Hodgson, Hot Deformation and Recrystallization of Austenitic Stainless Steel: Part I. Dynamic Recrystallization, Metallurgical and Materials Transactions A 39 (6) (2008) 1359–1370. doi:10.1007/s11661-008-9512-7.

[61] S.-H. Cho, Y.-C. Yoo, Metadynamic recrystallization of austenitic stainless steel, Journal of Materials Science 36 (17) (2001) 4279–4284. doi:10.1023/A:1017995122420.

[62] P. Uranga, A. Fernandez, B. Lopez, J. Rodriguez-Ibabe, Transition between static and metadynamic recrystallization kinetics in coarse Nb microalloyed austenite, Materials Science and Engineering: A 345 (1-2) (2003) 319–327. doi:10.1016/S0921-5093(02)00510-5.

[63] A. Dehghan-Manshadi, M. Barnett, P. Hodgson, Recrystallization in AISI 304 austenitic stainless steel during and after hot deformation, Materials Science and Engineering: A 485 (1-2) (2008) 664–672. doi:10.1016/j.msea.2007.08.026.

[64] J. Burke, D. Turnbull, Recrystallization and grain growth, Prog. Met. Phys. 3 (1952) 220.

[65] R. Darvishi Kamachali, I. Steinbach, 3-D phase-field simulation of grain growth: Topological analysis versus mean-field approximations, Acta Materialia 60 (6-7) (2012) 2719–2728. doi:10.1016/J.ACTAMAT.2012.01.037.

[66] A. Cruz-Fabiano, R. Logé, M. Bernacki, Assessment of simplified 2D grain growth models from numerical experiments based on a level set framework, Computational Materials Science 92 (2014) 305–312. doi:10.1016/j.commatsci.2014.05.060.

[67] K. Lücke, R. Brandt, G. Abbruzzese, Normal and Abnormal Grain Growth as Transient Phenomena, Tech. rep. (1998).

[68] G. Abbruzzese, I. Heckelmann, K. Lücke, Statistical theory of two-dimensional grain growthI. The topological foundation, Acta Metallurgica et Materialia 40 (3) (1992) 519–532. doi:10.1016/0956-7151(92)90401-Y.

[69] K. Lücke, I. Heckelmann, G. Abbruzzese, Statistical theory of two-dimensional grain growthII. Kinetics of grain growth, Acta Metallurgica et Materialia 40 (3) (1992) 533–542. doi:10.1016/0956-7151(92)90402-Z.

[70] D. G. Cram, H. S. Zurob, Y. J. M. Brechet, C. R. Hutchinson, Modelling discontinuous dynamic recrystallization using a physically based model for nucleation, Acta Materialia 57 (17) (2009) 5218–5228. doi:10.1016/j.actamat.2009.07.024.

[71] G. Smagghe, modélisation de la recristallisation lors du forgeage à chaud de lacier 304L une approche semi-topologique pour les modèles en champs moyens, Ph.D. thesis, Mines de Saint-Etienne (2017).

[72] W. Chao, L. I. U. Guoquan, Reanalysis of the 3D quasi-stationary grain size distribution based on Hillert grain growth rate equation, Ser. E Technological Sciences 47 (1) (2004) 112–120.

[73] P. R. Rios, T. G. Dalpian, V. S. Brandao, J. A. Castro, A. C. L. Oliveira, Comparison of analytical grain size distributions with three-dimensional computer simulations and experimental data, Scripta Materialia 54 (9) (2006) 1633–1637. doi:10.1016/j.scriptamat.2006.01.007.

[74] R. Darvishi Kamachali, A. Abbondandolo, K. F. Siburg, I. Steinbach, Geometrical grounds of mean field solutions for normal grain growth, Acta Materialia 90 (2015) 252–258. doi:10.1016/j.actamat.2015.02.025.

[75] A. Laasraoui, J. J. Jonas, Prediction of Steel Flow Stresses at High Temperatures and Strain Rates, Tech. rep.

[76] A. Yoshie, H. Morikawa, Y. Onoe, K. Itoh, Formulation of static recrystallization of austenite in hot rolling process of steel plate., Transactions of the Iron and Steel Institute of Japan 27 (6) (1987) 425–431. doi:10.2355/isijinternational1966.27.425.

[77] A. L. Cruz-Fabiano, Modelling of crystal plasticity and grain boundary motion of 304L steel at the mesoscopic scale, Ph.D. thesis, Mines ParisTech (2013).

[78] O. Bouaziz, P. Buessler, Iso-work Increment Assumption for Heterogeneous Material Behaviour Modelling, Advanced Engineering Materials 6 (12) (2004) 79–83. doi:10.1002/adem.200300524.

[79] U. Kocks, H. Mecking, Physics and phenomenology of strain hardening: the FCC case, Progress in Materials Science 48 (3) (2003) 171–273. doi:10.1016/S0079-6425(02)00003-8.

[80] D. Turnbull, Theory of Grain Boundary Migration Rates, Trans Am Inst Min Metall Eng (5) (1951) 191–661.

[81] S. V. Raj, G. M. Pharr, A Compilation and Analysis of Data for the Stress Dependence of the Subgrain Size, Materials Science and Engineering 81 (1986) 217–237.

[82] D. Piot, G. Smagghe, J. J. Jonas, C. Desrayaud, F. Montheillet, G. Perrin, A. Montouchet, G. Kermouche, A semitopological mean-field model of discontinuous dynamic recrystallization Toward a correct and rapid prediction of grain-size distribution, Journal of Materials Science 53 (2018) 15–16. doi:10.1007/s10853-018-2137-3.

[83] D. Piot, G. Damamme, F. Montheillet, Mesoscopic Modeling of Discontinuous Dynamic Recrystallization: Steady-State Grain Size Distributions, Materials Science Forum 706-709 (2012) 234–239. doi:10.4028/www.scientific.net/MSF.706-709.234.

[84] G. Smagghe, D. Piot, F. Montheillet, G. Perrin, A. Montouchet, G. Kermouche, The Issue of Grain Size Distribution Using Mean Field Models for Dynamic and Post-Dynamic Recrystallization, Materials Science Forum 879 (2016) 1794–1799. doi:10.4028/www.scientific.net/MSF.879.1794.

[85] R. B. Potts, C. Domb, Some generalized order-disorder transformations, Mathematical Proceedings of the Cambridge Philosophical Society 48 (01) (1952) 106. doi:10.1017/S0305004100027419.

[86] M. P. Anderson, D. J. Srolovitz, G. S. Crest, P. S. Sahni, Computer simulation of grain growth-I. kinetics, Acre meroll 32 (5) (1984) 783–791.

[87] D. Srolovitz, M. Anderson, P. Sahni, G. Grest, Computer simulation of grain growth-II. Grain size distribution, topology, and local dynamics, Acta Metallurgica 32 (5) (1984) 793–802. doi:10.1016/0001-6160(84)90152-4.

[88] D Srolovitz, M. Anderson, G Grest, P Sahni, Computer simulation of grain growth-III. Influence of a particle dispersion, Acta Metallurgica 32 (9) (1984) 1429–1438. doi:10.1016/0001-6160(84)90089-0.

[89] G. Grest, D. Srolovitz, M. Anderson, Computer simulation of grain growth-IV. Anisotropic grain boundary energies, Acta Metallurgica 33 (3) (1985) 509–520. doi:10.1016/0001-6160(85)90093-8.

[90] D. Srolovitz, G. Grest, M. Anderson, Computer simulation of grain growth-V. Abnormal grain growth, Acta Metallurgica 33 (12) (1985) 2233–2247. doi:10.1016/0001-6160(85)90185-3.

[91] D. Srolovitz, G. Grest, M. Anderson, A. D. Rollett, Computer simulation of recrystallization-II. Heterogeneous nucleation and growth, Acta Metallurgica 36 (8) (1988) 2115–2128. doi:10.1016/0001-6160(88)90313-6.

[92] A. Rollett, D. Srolovitz, M. Anderson, R. Doherty, Computer simulation of recrystallization-III. Influence of a dispersion of fine particles, Acta Metallurgica et Materialia 40 (12) (1992) 3475–3495. doi:10.1016/0956-7151(92)90062-J.

[93] A. D. Rollett, M. J. Luton, D. J. Srolovitz, Microstructural simulation of dynamic recrystallization 40 (1) (1992) 43–55.

[94] S. Esche, Monte Carlo Simulations of Grain Growth in Metals, Applications of Monte Carlo Method in Science and Engineering (Cmc) (2011) 581–610. doi:10.5772/14942.

[95] P. Peczak, A Monte Carlo study of influence of deformation temperature on dynamic recrystallization, Acta Metallurgica et Materialia 43 (3) (1995) 1279–1291. doi:10.1016/0956-7151(94)00280-U.

[96] J. Li, H. Xu, T. Mattila, J. Kivilahti, T. Laurila, M. Paulasto-Kröckel, Simulation of dynamic recrystallization in solder interconnections during thermal cycling, Computational Materials Science 50 (2) (2010) 690–697. doi:10.1016/J.COMMATSCI.2010.09.035.

[97] J. von Neumann, The general and logical theory of automata, in: W. Aspray and A. Burks (eds.), Papers of John von Neumann on Computing and Computer Theory , vol. 12 in the Charles Babbage Institute Reprint Series for the History of Computing, MIT Press, Cambridge, 1963.

[98] S. Wolfram, Theory and applications of cellular automata : Advanced Series on Complex Systems, Singapore, 1986.

[99] S. Kundu, M. Dutta, S. Ganguly, S. Chandra, Prediction of phase transformation and microstructure in steel using cellular automaton technique, Scripta Materialia 50 (6) (2004) 891–895. doi:10.1016/j.scriptamat.2003.12.007.

[100] R. Chen, Q. Xu, B. Liu, Cellular automaton simulation of three-dimensional dendrite growth in Al-7Si-Mg ternary aluminum alloys, Computational Materials Science 105 (2015) 90–100. doi:10.1016/j.commatsci.2015.04.035.

[101] L. Hongwei, S. Xinxin, Y. He, A three-dimensional cellular automata-crystal plasticity finite element model for predicting the multiscale interaction among heterogeneous deformation, DRX microstructural evolution and mechanical responses in titanium alloys, International Journal of Plasticity 87 (2016) 154–180. doi:10.1016/J.IJPLAS.2016.09.008.

[102] D. Raabe, Recrystallization Simulation by Use of Cellular Automata, in: Handbook of Materials Modeling, Springer Netherlands, Dordrecht, 2005, pp. 2173–2203. doi:10.1007/978-1-4020-3286-8{_}113.

[103] H. Hallberg, Approaches to Modeling of Recrystallization, Metals 1 (1) (2011) 16–48. doi:10.3390/met1010016.

[104] K. Kremeyer, Cellular Automata Investigations of Binary Solidification, Journal of Computational Physics 142 (1) (1998) 243–263. doi:10.1006/JCPH.1998.5926.

[105] H. Hallberg, M. Wallin, M. Ristinmaa, Simulation of discontinuous dynamic recrystallization in pure Cu using a probabilistic cellular automaton, Computational Materials Science 49 (1) (2010) 25–34. doi:10.1016/j.commatsci.2010.04.012.

[106] L. Madej, M. Sitko, A. Legwand, K. Perzynski, K. Michalik, Development and evaluation of data transfer protocols in the fully coupled random cellular automata finite element model of dynamic recrystallization, Journal of Computational Science 26 (2018) 66–77. doi:10.1016/J.JOCS.2018.03.007.

[107] R. Ding, Z. Guo, Coupled quantitative simulation of microstructural evolution and plastic flow during dynamic recrystallization, Acta Metarialia 49 (2001) 3163–3175.

[108] H. Hallberg, B. Svendsen, T. Kayser, M. Ristinmaa, Microstructure evolution during dynamic discontinuous recrystallization in particle-containing Cu, Computational Materials Science 84 (2014) 327–338. doi:10.1016/j.commatsci.2013.12.021.

[109] M. Sitko, L. Madej, Development of Dynamic Recrystallization Model Based on Cellular Automata Approach, Key Engineering Materials 622-623 (2014) 617–624. doi:10.4028/www.scientific.net/KEM.622-623.617.

[110] W. Chuan, Y. He, L. H. Wei, Modeling of discontinuous dynamic recrystallization of a near-α titanium alloy IMI834 during isothermal hot compression by combining a cellular automaton model with a crystal plasticity finite element method, Computational Materials Science 79 (2013) 944–959. doi:10.1016/j.commatsci.2013.08.004.

[111] E. Popova, Y. Staraselski, A. Brahme, R. K. Mishra, K. Inal, Coupled crystal plasticity - Probabilistic cellular automata approach to model dynamic recrystallization in magnesium alloys, International Journal of Plasticity 66 (2015) 85–102. doi:10.1016/j.ijplas.2014.04.008.

[112] A. Soares, A. Ferro, M. Fortes, Computer simulation of grain growth in a bidimensional polycrystal, Scripta Metallurgica 19 (12) (1985) 1491–1496. doi:10.1016/0036-9748(85)90157-7.

[113] H. Frost, C. Thompson, C. Howe, J. Whang, A two-dimensional computer simulation of capillarity-driven grain growth: Preliminary results, Scripta Metallurgica 22 (1) (1988) 65–70. doi:10.1016/S0036-9748(88)80307-7.

[114] K. Nakashima, T. Nagai, K. Kawasaki, Scaling behavior of two-dimensional domain growth: Computer simulation of vertex models, Journal of Statistical Physics 57 (3-4) (1989) 759–787. doi:10.1007/BF01022831.

[115] Y. Mellbin, H. Hallberg, M. Ristinmaa, Recrystallization and texture evolution during hot rolling of copper, studied by a multiscale model combining crystal plasticity and vertex models, Modelling and Simulation in Materials Science and Engineering 24 (7) (2016) 075004. doi:10.1088/0965-0393/24/7/075004.

[116] E. A. Lazar, J. K. Mason, R. D. MacPherson, D. J. Srolovitz, A more accurate three-dimensional grain growth algorithm, Acta Materialia 59 (17) (2011) 6837–6847. doi:10.1016/j.actamat.2011.07.052.

[117] K. Pikoś, J. Tarasiuka, K. Wierzbanowski, B. Bacroix, Generalized vertex model of recrystallization Application to polycrystalline copper, Computational Materials Science 42 (4) (2008) 584–594. doi:10.1016/J.COMMATSCI.2007.09.014.

[118] Y. Mellbin, H. Hallberg, M. Ristinmaa, An extended vertex and crystal plasticity framework for efficient multiscale modeling of polycrystalline materials, International Journal of Solids and Structures 125 (2017) 150–160. doi:10.1016/J.IJSOLSTR.2017.07.009.

[119] J. Warren, W. Boettinger, Prediction of dendritic growth and microsegregation patterns in a binary alloy using the phase-field method, Acta Metallurgica et Materialia 43 (2) (1995) 689–703. doi:10.1016/0956-7151(94)00285-P.

[120] R. Kobayashi, Modeling and numerical simulations of dendritic crystal growth, Physica D: Nonlinear Phenomena 63 (3-4) (1993) 410–423. doi:10.1016/0167-2789(93)90120-P.

[121] N. Moelans, B. Blanpain, P. Wollants, Quantitative analysis of grain boundary properties in a generalized phase field model for grain growth in anisotropic systems, Physical Review B 78 (2) (2008) 024113. doi:10.1103/PhysRevB.78.024113.

[122] L.-Q. Chen, W. Yang, Computer simulation of the domain dynamics of a quenched system with a large number of nonconserved order parameters: The grain-growth kinetics, Physical Review B 50 (21) (1994) 15752–15756. doi:10.1103/PhysRevB.50.15752.

[123] D. Fan, L. Chen, Computer simulation of grain growth using a continuum field model, Acta Materialia 45 (2) (1997) 611–622. doi:10.1016/S1359-6454(96)00200-5.

[124] I. Steinbach, F. Pezzolla, B. Nestler, M. Seeßelberg, R. Prieler, G. Schmitz, J. Rezende, A phase field concept for multiphase systems, Physica D: Nonlinear Phenomena 94 (3) (1996) 135–147. doi:10.1016/0167-2789(95)00298-7.

[125] H. Garcke, B. Nestler, B. Stoth, On anisotropic order parameter models for multiphase systems and their sharp interface limits, Physica D: Nonlinear Phenomena 115 (1-2) (1998) 87–108. doi:10.1016/S0167-2789(97)00227-3.

[126] N. Moelans, A. Godfrey, Y. Zhang, D. Juul Jensen, Phase-field simulation study of the migration of recrystallization boundaries, Physical Review B 88 (5) (2013) 054103. doi:10.1103/PhysRevB.88.054103.

[127] T. Takaki, T. Hirouchi, Y. Hisakuni, A. Yamanaka, Y. Tomita, Multi-Phase-Field Model to Simulate Microstructure Evolutions during Dynamic Recrystallizationdoi:10.2320/matertrans.MB200805.

[128] T. Takaki, Y. Hisakuni, T. Hirouchi, A. Yamanaka, Y. Tomita, Multi-phase-field simulations for dynamic recrystallization, Computational Materials Science 45 (4) (2009) 881–888. doi:10.1016/J.COMMATSCI.2008.12.009.

[129] T. Takaki, C. Yoshimoto, A. Yamanaka, Y. Tomita, Multiscale modeling of hot-working with dynamic recrystallization by coupling microstructure evolution and macroscopic mechanical behavior, International Journal of Plasticity 52 (2014) 105–116. doi:10.1016/J.IJPLAS.2013.09.001.

[130] L. Chen, J. Chen, R. A. Lebensohn, Y. Z. Ji, T. W. Heo, S. Bhattacharyya, K. Chang, S. Mathaudhu, Z. K. Liu, L. Q. Chen, An integrated fast Fourier transform-based phase-field and crystal plasticity approach to model recrystallization of three dimensional polycrystals, Computer Methods in Applied Mechanics and Engineering 285 (2015) 829–848. doi:10.1016/j.cma.2014.12.007.

[131] P. Zhao, T. Song En Low, Y. Wang, S. R. Niezgoda, An integrated full-field model of concurrent plastic deformation and microstructure evolution: Application to 3D simulation of dynamic recrystallization in polycrystalline copper, International Journal of Plasticity 80 (2016) 38–55. arXiv:1509.04953, doi:10.1016/j.ijplas.2015.12.010.

[132] H. Hallberg, A modified level set approach to 2D modeling of dynamic recrystallization, Modelling and Simulation in Materials Science and Engineering 21 (8) (2013) 085012. doi:10.1088/0965-0393/21/8/085012.

[133] M. Bernacki, H. Resk, T. Coupez, R. E. Logé, Finite element model of primary recrystallization in polycrystalline aggregates using a level set framework, Modelling and Simulation in Materials Science and Engineering 17 (6) (2009) 064006. doi:10.1088/0965-0393/17/6/064006.

[134] K. Hitti, Direct numerical simulation of complex Representative Volume Elements (RVEs): Generation, Resolution and Homogenization.

[135] B. Scholtes, Development of an efficient level set framework for the full field modeling of recrystallization in 3D, Ph.D. thesis, MINES ParisTech (2016).

[136] M. Shakoor, Three-dimensional numerical modeling of ductile fracture mechanisms at the microscale, Ph.D. thesis, Mines ParisTech (2016).

[137] S. Osher, J. A. Sethian, Fronts propagating with curvature-dependent speed: Algorithms based on Hamilton-Jacobi formulations, Journal of Computational Physics 79 (1) (1988) 12–49. doi:10.1016/0021-9991(88)90002-2.

[138] B. Merriman, J. K. Bence, S. J. Osher, Motion of Multiple Junctions: A Level Set Approach, Journal of Computational Physics 112 (2) (1994) 334–363. doi:10.1006/JCPH.1994.1105.

[139] H.-K. Zhao, T. Chan, S. Osher, A Variational Level Set Approach to Multiphase Motion*, JOURNAL OF COMPUTATIONAL PHYSICS 127 (1996) 179–195.

[140] M. Elsey, S. Esedoglu, P. Smereka, Diffusion generated motion for grain growth in two and three dimensions, Journal of Computational Physics 228 (21) (2009) 8015–8033. doi:10.1016/j.jcp.2009.07.020.

[141] C. Mießen, N. Velinov, G. Gottstein, L. A. Barrales-Mora, A highly efficient 3D level-set grain growth algorithm tailored for ccNUMA architecture, Modelling and Simulation in Materials Science and Engineering 25 (8) (2017) 084002. doi:10.1088/1361-651X/aa8676.

[142] B. Merriman, J. K. Bence, S. J. Osher, Motion of Multiple Junctions: A Level Set Approach, Journal of Computational Physics 112 (2) (1994) 334–363. doi:10.1006/jcph.1994.1105.

[143] B. Scholtes, R. Boulais-Sinou, A. Settefrati, D. Pino Muñoz, I. Poitrault, A. Montouchet, N. Bozzolo, M. Bernacki, 3D level set modeling of static recrystallization considering stored energy fields, Computational Materials Science 122 (2016) 57–71. doi:10.1016/J.COMMATSCI.2016.04.045.

[144] A. Agnoli, N. Bozzolo, R. E. Logé, J.-M. Franchet, J. Laigo, M. Bernacki, Development of a level set methodology to simulate grain growth in the presence of real secondary phase particles and stored energy Application to a nickel-base superalloy, Computational Materials Science 89 (2014) 233–241. doi:10.1016/j.commatsci.2014.03.054.

[145] L. Madej, Digital/virtual microstructures in application to metals engineering A review, Archives of Civil and Mechanical Engineering 17 (4) (2017) 839–854. doi:10.1016/J.ACME.2017.03.002.

[146] M. Shakoor, B. Scholtes, P.-O. Bouchard, M. Bernacki, An efficient and parallel level set reinitialization method Application to micromechanics and microstructural evolutions, Applied Mathematical Modelling 39 (23-24) (2015) 7291–7302. doi:10.1016/j.apm.2015.03.014.

[147] M. A. Groeber, M. A. Jackson, DREAM.3D: A Digital Representation Environment for the Analysis of Microstructure in 3D, Integrating Materials and Manufacturing Innovation 3 (1) (2014) 5. doi:10.1186/2193-9772-3-5.

[148] S. Dancette, A. Browet, G. Martin, M. Willemet, L. Delannay, Automatic processing of an orientation map into a finite element mesh that conforms to grain boundaries Related content Automatic processing of an orientation map into a finite element mesh that conforms to grain boundaries, Modelling Simul. Mater. Sci. Eng 24 (2016) 55014–55028. doi:10.1088/0965-0393/24/5/055014.

[149] M. S. Wu, J. Guo, Analysis of a Sector Crack in a Three-Dimensional Voronoi Polycrystal With Microstructural Stresses, Journal of Applied Mechanics 67 (1) (2000) 50. doi:10.1115/1.321151.

[150] R. Quey, P. Dawson, F. Barbe, Large-scale 3D random polycrystals for the finite element method: Generation, meshing and remeshing, Computer Methods in Applied Mechanics and Engineering 200 (17-20) (2011) 1729–1745. doi:10.1016/j.cma.2011.01.002.

[151] K. Hitti, P. Laure, T. Coupez, L. Silva, M. Bernacki, Precise generation of complex statistical Representative Volume Elements (RVEs) in a finite element context, Computational Materials Science 61 (2012) 224–238. doi:10.1016/j.commatsci.2012.04.011.

[152] Z. Fan, Y. Wu, X. Zhao, Y. Lu, Simulation of polycrystalline structure with Voronoi diagram in Laguerre geometry based on random closed packing of spheres, Computational Materials Science 29 (3) (2004) 301–308. doi:10.1016/j.commatsci.2003.10.006.

[153] H. Telley, T. M. Liebling, A. Mocellin, The Laguerre model of grain growth in two dimensions I. Cellular structures viewed as dynamical Laguerre tessellations, Philosophical Magazine B 73 (3) (1996) 395–408. doi:10.1080/13642819608239125.

[154] B. Scholtes, M. Shakoor, A. Settefrati, P.-O. Bouchard, N. Bozzolo, M. Bernacki, New finite element developments for the full field modeling of microstructural evolutions using the level-set method, Computational Materials Science 109 (2015) 388–398. doi:10.1016/J.COMMATSCI.2015.07.042.

[155] D. N. Ilin, N. Bozzolo, T. Toulorge, M. Bernacki, Full field modeling of recrystallization: Effect of intragranular strain gradients on grain boundary shape and kinetics, Computational Materials Science 150 (April) (2018) 149–161. doi:10.1016/j.commatsci.2018.03.063.

[156] M. Zouari, R. E. Loge, O. Beltran, S. Rousselle, N. Bozzolo, Multipass forging of Inconel 718 in the delta-Supersolvus domain: assessing and modeling microstructure evolution, in: EUROSUPERALLOYS, Giens, France, 2014. doi:10.1051/matecconf/20141412001.

[157] M. Elsey, S. Esedoglu, P. Smereka, Large-scale simulation of normal grain growth via diffusion-generated motion, Proceedings of the Royal Society A: Mathematical, Physical and Engineering Sciences 467 (2126) (2011) 381–401. doi:10.1098/rspa.2010.0194.

[158] A. L. Cruz Fabiano, Modelling of crystal plasticity and grain boundary migration of 304L steel at the mesoscopic scale, Ph.D. thesis, Mines ParisTech (2014).

[159] A. Agnoli, Origin of inhomogeneous grain growth in Inconel 718 forgings, Ph.D. thesis, Mines ParisTech (2013).

[160] Y. Jin, B. Lin, M. Bernacki, G. Rohrer, A. Rollett, N. Bozzolo, Annealing twin development during recrystallization and grain growth in pure nickel, Materials Science and Engineering: A 597 (2014) 295–303. doi:10.1016/j.msea.2014.01.018.

[161] S. Florez, Progress report: A new FE framework for the modeling of complex moving interfaces, Tech. rep., MINES ParisTech (CEMEF) (2018).

[162] M. Fatima Vaz, M. Fortes, Grain size distribution: The lognormal and the gamma distribution functions, Scripta Metallurgica 22 (1) (1988) 35–40. doi:10.1016/S0036-9748(88)80302-8.

[163] B. Raeisinia, C. W. Sinclair, A representative grain size for the mechanical response of polycrystals, Materials Science and Engineering A 525 (1-2) (2009) 78–82. doi:10.1016/j.msea.2009.06.045.

[164] T. Luther, C. Könke, Polycrystal models for the analysis of intergranular crack growth in metallic materials, Engineering Fracture Mechanics 76 (15) (2009) 2332–2343. doi:10.1016/j.engfracmech.2009.07.006.

[165] J. K. Mason, E. A. Lazar, R. D. MacPherson, D. J. Srolovitz, Geometric and topological properties of the canonical grain-growth microstructure, Physical Review E 92 (6) (2015) 063308. doi:10.1103/PhysRevE.92.063308.

[166] Y. Suwa, Y. Saito, H. Onodera, Parallel Computer Simulation of Three-Dimensional Grain Growth Using the Multi-Phase-Field Model, Materials Transactions 49 (4) (2008) 704–709. doi:10.2320/matertrans.MRA2007225.

[167] S. G. Kim, D. I. Kim, W. T. Kim, Y. B. Park, Computer simulations of two-dimensional and three-dimensional ideal grain growth, Physical Review E 74 (6) (2006) 061605. doi:10.1103/PhysRevE.74.061605.

[168] A. Baskaran, D. Crist, D. Lewis, Effect of initial variance of microstructures on grain growth under mean curvature, Modelling and Simulation in Materials Science and Engineering 25 (6) (2017) 065010. doi:10.1088/1361-651X/aa763c.

[169] E. Miyoshi, T. Takaki, M. Ohno, Y. Shibuta, S. Sakane, T. Shimokawabe, T. Aoki, Ultra-large-scale phase-field simulation study of ideal grain growth, npj Computational Materials 3 (1) (2017) 25. doi:10.1038/s41524-017-0029-8.

[170] M. El Wahabi, J. Cabrera, J. Prado, Hot working of two AISI 304 steels: a comparative study, Materials Science and Engineering: A 343 (1-2) (2003) 116–125. doi:10.1016/S0921-5093(02)00357-X.

[171] R. Darvishi Kamachali, I. Steinbach, 3-D phase-field simulation of grain growth: Topological analysis versus mean-field approximations, Acta Materialia 60 (6-7) (2012) 2719–2728. doi:10.1016/j.actamat.2012.01.037.

[172] N. Petch, The cleavage strength of polycrystals, The Journal of the Iron and Steel Institute 174 (1953) 25–28.

[173] L. Maire, B. Scholtes, C. Moussa, N. Bozzolo, D. Pino Muñoz, M. Bernacki, Improvement of 3D mean field models for capillarity-driven grain growth based on full field simulations, Journal of Materials Science 51 (24) (2016) 10970–10981. doi:10.1007/s10853-016-0309-6.

[174] U. F. Kocks, Laws for Work-Hardening and Low-Temperature Creep, Journal of Engineering Materials and Technology 98 (1) (1976) 76. doi:10.1115/1.3443340.

[175] H. Mecking, U. Kocks, Kinetics of flow and strain-hardening, Acta Metallurgica 29 (11) (1981) 1865–1875. doi:10.1016/0001-6160(81)90112-7.

[176] P. Peczak, M. J. Luton, The effect of nucleation models on dynamic recrystallization I. Homogeneous stored energy distribution, Philosophical Magazine Part B 68 (1) (1993) 115–144. doi:10.1080/13642819308215285.

[177] K. Huang, Towards the modelling of recrystallization phenomena in multi-pass conditions: application to 304L steel, Ph.D. thesis (2012).

[178] S.-I. Kim, B.-C. Ko, C.-M. Lee, S.-K. Hwang, Y.-C. Yoo, Evolution of dynamic recrystallisation in AISI 304 stainless steel, Materials Science and Technology 19 (12) (2003) 1648–1652. doi:10.1179/026708303225008284.

[179] L. Gavard, F. Montheillet, Dynamic recrystallization and grain refinement in a high purity 304L type austenitic stainless steel, Matériaux & Techniques 88 (5-6) (2000) 65–68. doi:10.1051/mattech/200088050065.

[180] R. T. DeHoff, G. Q. Liu, On the relation between grain size and grain topology, Metallurgical Transactions A 16 (11) (1985) 2007–2011. doi:10.1007/BF02662401.

[181] G. Liu, H. Yu, X. Qin, Three-dimensional grain topologysize relationships in a real metallic polycrystal compared with theoretical models, Materials Science and Engineering: A 326 (2) (2002) 276–281. doi:10.1016/S0921-5093(01)01497-6.

[182] G. Abbruzzese, A. Campopiano, Topological aspects of grain growth microstructure: The two-dimensional and three-dimensional cases., in: STERMAT94, Proceedings of the 4th International Conference on Stereology and Image Analysis in Material Science, Wisla, Poland, 1994.

[183] C. Zhang, M. Enomoto, A. Suzuki, T. Ishimaru, Characterization of three-dimensional grain structure in polycrystalline iron by serial sectioning, Metallurgical and Materials Transactions A 35 (7) (2004) 1927–1933. doi:10.1007/s11661-004-0141-5.

[184] S. O. Poulsen, P. W. Voorhees, E. M. Lauridsen, Three-dimensional simulations of microstructural evolution in polycrystalline dual-phase materials with constant volume fractions, Acta Materialia 61 (2013) 1220–1228. doi:10.1016/j.actamat.2012.10.032.

[185] D. Zöllner, P. Streitenberger, Normal Grain Growth: Monte Carlo Potts Model Simulation and Mean-Field Theory, in: Micro-Macro-interaction, Springer Berlin Heidelberg, Berlin, Heidelberg, 2008, pp. 3–18. doi:10.1007/978-3-540-85715-0{_}1.

[186] F. Wakai, N. Enomoto, H. Ogawa, Three-dimensional microstructural evolution in ideal grain growthgeneral statistics, Acta Materialia 48 (6) (2000) 1297–1311. doi:10.1016/S1359-6454(99)00405-X.

[187] G. P. Michon, Final answers (2004) See Thomsen's formulas and Cantrell's comments.

[188] G. Shen, S. L. Semiatin, R. Shivpuri, Modeling microstructural development during the forging of Waspaloy, Metallurgical and Materials Transactions A 26 (7) (1995) 1795–1803. doi:10.1007/BF02670767.

[189] G. Smagghe, D. Piot, F. Montheillet, A. Montouchet, M. Bernacki, J. Jonas, G. Kermouche, An extended mean field approach for modelling realistic grain size distribution evolutions during Discontinuous Dynamic RX and Post-Dynamic RX, in: 6th International Conference on Recrystallization and Grain Growth: Recrystallization II: Dynamic Recrystallization, Pittsburgh, Pennsylvania, USA, 2016.

[190] M. Zouari, N. Bozzolo, R. E. Loge, Mean field modelling of dynamic and post-dynamic recrystallization during hot deformation of Inconel 718 in the absence of δ phase particles, Materials Science and Engineering: A 655 (2016) 1–17. doi:10.1016/j.msea.2015.12.102.

[191] A. Hensel, T. Spittel, Kraft- und Arbeitsbe darf bildsamer Formgebungsverfahren, 1978.

[192] C. M. Sellars, W. J. M. Tegart, La relation entre la résistance et la structure dans la deformation à chaud, Mémoires Scientifiques de la Revue de Metallurgie 63 (1966) 731–746.

[193] J. J. Jonas, C. M. Sellars, W. J. M. Tegart, Strength and structure under hot-working conditions, Metallurgical Reviews 14 (1) (1969) 1–24. doi:10.1179/mtlr.1969.14.1.1.

[194] C. M. Sellars, W. J. M. Tegart, Hot Workability, International Metallurgical Reviews 17 (1) (1972) 1–24. doi:10.1179/imtlr.1972.17.1.1.

[195] O. O. Tairu, P. O. Aiyedun, O. T. Tairu, Relationship between Yield stress and yield Strength on Various Grade of steel Being Hot rolled, IOSR Journal of Mechanical and Civil Engineering Ver. I 11 (1) (2014) 2320–334.

[196] A. Y. Churyumov, V. V. Teleshov, Quantitative description of the flow-stress dependence of aluminum alloys at the stage of steady flow upon hot deformation on the ZenerHollomon parameter, Physics of Metals and Metallography 118 (9) (2017) 905–912. doi:10.1134/S0031918X17090046.

[197] J. J. Jonas, X. Quelennec, L. Jiang, The Avrami kinetics of dynamic recrystallization, Acta Materialia 57 (2009) 2748–2756. doi:10.1016/j.actamat.2009.02.033.

[198] G. Taylor, Royal Society Yarrow Professor F.R.S., The Mechanism of Plastic Deformation of Crystals.

[199] E. V. Kozlov, N. A. Koneva, Internal fields and other contributions to flow stress, Materials science & engineering (A234-236) (1997) 982–985.

[200] L. Bäcke, Modeling the Microstructural Evolution during Hot Deformation of Microalloyed Steels, Ph.D. thesis, Royal Institute of Technology (KTH), Sweden (2009).

[201] D. Hull, D. Bacon, Introduction to Dislocations(Fifth Edition).

[202] L. Gavard, Recristallisation dynamique d'aciers inoxydables austénitiques de haute pureté, Ph.D. thesis, Ecole Nationale Supérieure des Mines de Saint-Etienne et l'Institut Polytechnique de Grenoble (2001).

[203] N. Yazdipour, C. Davies, P. Hodgson, Microstructural modeling of dynamic recrystallization using irregular cellular automata, Computational Materials Science 44 (2) (2008) 566–576. doi:10.1016/j.commatsci.2008.04.027.

[204] A. Winkelmann, Nolze Gert, Analysis of Kikuchi band contrast reversal in electron backscatter diffraction patterns of silicon, Ultramicroscopy 110 (3) (2010) 190–194. doi:10.1016/J.ULTRAMIC.2009.11.008.

[205] F. Bachmann, R. Hielscher, P. E. Jupp, W. Pantleon, H. Schaeben, E. Wegert, IUCr, Inferential statistics of electron backscatter diffraction data from within individual crystalline grains, Journal of Applied Crystallography 43 (6) (2010) 1338–1355. doi:10.1107/S002188981003027X.

[206] R. Heilbronner, D. Bruhn, The influence of three-dimensional grain size distributions on the rheology of polyphase rocks, Journal of Structural Geology 20 (6) (1998) 695–705.

[207] R. Boulais-Sinou, B. Scholtes, D. Pino Muñoz, C. Moussa, I. Poitrault, I. Bobin, A. Montouchet, M. Bernacki, Full field modeling of dynamic recrystallization in a global level set framework, application to 304L stainless steel, Proceedings of Numiform 2016: The 12th international conference on numerical methods in industrial forming processes.

[208] D. Ruiz, Deal with high anisotropies of interface properties and crystal plasticity in context of the level set method - Application to polycrystal microstructures, Ph.D. thesis (2017).

[209] S. Florez, Development of new meshing/remeshing capabilities to describe large 3D real or representative polycrystals and grain boundary motion in context of non-uniform finite element mesh., Ph.D. thesis (2017).

Résumé

Les propriétés finales des alliages métalliques sont directement liées à la microstructure de fin de mise en forme. Les mécanismes de recristallisation dynamique (DRX) et post-dynamique (PDRX) jouent un rôle important sur les évolutions microstructurales intervenant pendant et après les étapes de déformation à chaud. Dans ce contexte, un défi majeur pour les industriels et les chercheurs est de prédire la microstructure obtenue en fonction des conditions de mise en forme. Cela implique de bien connaître les mécanismes de DRX et PDRX et leur cinétique.

Les modèles en champ complet permettent de modéliser explicitement la microstructure des alliages métalliques et ses possibles évolutions à l'échelle du polycristal. Ces modèles sont précis comparativement aux modèles œuvrant aux plus grandes échelles, mais ils sont généralement très couteux en termes de temps de calcul. Les modèles à champ moyen sont quant à eux basés sur une description implicite de la microstructure, conduisant à des temps de calcul considérablement réduits, mais ils reposent sur un grand nombre d'hypothèses, notamment topologiques.

Cette thèse propose un nouveau modèle champ complet de DRX/PDRX et croissance de grains, capable de fonctionner en 2D comme en 3D, et une nouvelle approche en champ moyen, s'appuyant sur ces simulations en champ complet. La nouvelle approche champ moyen prend notamment mieux en compte les effets topologiques pour une meilleure prédiction des distributions de tailles de grains. Ce travail inclut une procédure de calibration et une validation des deux modèles s'appuyant sur une campagne d'essais expérimentaux sur un acier austénitique 304L.

Mots Clés

Modèle en champ complet, modèle en champ moyen, level-set, recristallisation, métallurgie numérique, acier 304L

Abstract

Final properties of metal alloys are directly related to their microstructure, inherited from the processing route. Dynamic (DRX) and post-dynamic recrystallization (PDRX) mechanisms play a primordial role in microstructure evolutions occurring during and after hot-deformation. Within this context, predicting microstructures depending on the applied thermomechanical conditions is a major challenge for both industrials and researchers. This requires a good knowledge of recrystallization mechanisms and kinetics.

Full field models are based on an explicit description of the microstructure of a metallic alloy, and its possible evolutions at a polycrystalline scale. These models are accurate compared to models operating at larger scales, but they generally lead to prohibitive numerical costs. On the other hand, mean field models are based on an implicit description of the microstructure, leading to considerably reduced numerical costs, but they are based on many assumptions, notably with regards to topology.

The outcome of this PhD work is a new full field model of DRX/PDRX and grain growth, working in 3D as well as in 2D, and a new DRX/PDRX mean field approach which better accounts for topological effects, and provides better predictions for grain size distributions. This work also includes a calibration procedure and a validation of these two new models, using experimental data obtained from compression tests performed on the 304L austenitic steel.

Keywords

Full field model, mean field model, level-set, recrystallization, numerical metallurgy, 304L steel